Landscape changes, cave site formation and human occupation during the Late Pleistocene: a geoarchaeological study from the Ach and Lone valleys (Swabian Jura, SW Germany)

Dissertation

der Mathematisch-Naturwissenschaftlichen Fakultät
der Eberhard Karls Universität Tübingen
zur Erlangung des Grades eines
Doktors der Naturwissenschaften

(Dr. rer. nat.)

vorgelegt von

Alvise Barbieri

aus Venedig/Italien

Tübingen

2017

Gedruckt mit Genehmigung der Mathematisch-Naturwissenschaftlichen Fakultät der Eberhard Karls Universität Tübingen.

Tag der mündlichen Qualifikation:	28.09.2017
Dekan:	Prof. Dr. Wolfgang Rosenstiel
1. Berichterstatter:	Prof. Dr. Christopher E. Miller
2. Berichterstatter:	Prof. Dr. Nicholas J. Conard

Acknowledgements

The work that is presented in this dissertation is the result of a nearly 5 year long process that has involved many people.

I would like to thank my advisors Prof. Nicholas Conard and Prof. Christopher Miller for having supported me through these years. In particular I would like to thank Prof. Miller for having offered me the possibility to conduct this research.

I am also grateful to Prof. Joachim Kind and Thomas Beutelspacher from Denkmalpflege Baden-Württemberg, who gave me the possibility to study the sequence of Hohlenstein-Stadel and supported the survey campaigns I conducted in Ach and Lone valleys. Thanks to Peter Leach, who initiated me into the world of GPR. Dr. Jens Hornung from the University of Darmstadt, who offered me training, access to equipment as well as many helpful suggestions and comments. Dr. Carsten Leven, who supported me with the coring and EC-logging campaigns in Ach and Lone valleys. Prof. Hartmut Schulz, who hosted me in the Sand Laboratory of the Department of Geosciences at the University of Tübingen. I would like to thank Dr. Greg Hodgins, Marcus Lee and the staff of the AMS Laboratory of the University of Arizona in Tucson for having offered me an amazing working and life experience. Thanks also to Michael Toffolo, for his help with the FTIR, Maria Malina, for the access to her field descriptions and databases, Panos Kritikakis, for the thin section production, and Dr. Peter Kühn, for helping me with the identification of clay coatings.

I would like to give my thanks to the municipalities of Sindelfingen, Bissingen and Rammingen as well as the owners of the properties on which I conducted my survey. I am grateful to the many people that helped me with the field work, Haydar B. Martínez, Felix Bachover, Geraldine Quénéhervé, Viola Schmid, Peter Kloos, Clemens Schmid, Elmar Schmaltz, Matthias Czechowski, Lucia Leierer and Jen Ort.

Thanks also to Alessandra, Cosimo, Maria, Magnus, Saad and all the friends and colleagues here not mentioned that were close to me during these years.

I dedicate this work to my mother, my father, my sister and Flora, my girlfriend, for having being there for me and with me during the happy and difficult moments of these years.

Table of Contents

Summary	xiv-xv
Zusammenfassung	xvi-xvii
1 Introduction	1
1.1.1 Geology and Geomorphology of the Swabian Jura	3
Jurassic system	3
Pre-Jurassic	5
Cretaceous-Paleogene	5
Eocene	7
Neogene	7
Quaternary – Pleistocene	10
Quaternary – Holocene	19
1.1.2 Geological questions addressed with this dissertation	19
1.2.1 Archaeological investigations in the Ach and Lone valleys	20
1.2.2 The prehistoric record of the Ach and Lone valleys	21
Middle Paleolithic	21
Aurignacian	23
Gravettian	26
Magdalenian colonization in between two phases of depopulation	29
1.2.3 Archaeological questions addressed with this dissertation	33
Middle to Upper Paleolithic transition	33
Gravettian to Magdalenian transition	33
2 Methods	35
2.1 GPR and EC-logging	35

2.2 Augering and Grain size analysis 39

2.3 Coring and sediment description 39

2.4 Micromorphology 41

2.5 FTIR 41

2.6 Dating 42

3 Results from the Lone Valley opposite from Hohlenstein 46

3.1 Previous research at the site 46

3.2 Results 48

3.2.1 Micromorphological results from Holenstein-Stadel 48

Unit M 49

Unit K/M to Unit Au 49

Unit SKS to Unit GL2A 52

3.2.2 Results from the Lone Valley in front of Hohlenstein 53

Depth to Bedrock 56

HS-GU1 57

HS-GU2 61

HS-GU3 63

HS-GU4 67

HS-GU5 70

HS-GU6 71

HS-GU7 73

HS-GU8 77

HS-GU9 78

HS-GU10 80

HS-GU11 83

HS-GU12 85

HS-GU13 87

HS-GU14 88

HS-GU15 90

3.3 Data interpretation 92

3.3.1 Site formation processes at Hohlenstein-Stadel 92

3.2.2 Interpretation of the data from the Lone Valley 97

I. Phases of soil formation, soil erosion and possibly river incision (pre-Quaternary and Pleistocene?) 97

II. Phases of soil formation, soil and sediment erosion, river deposition (around 25.000 14C BP) 98

III. Increasing deposition of loess (LGM?) 101

IV. Alternating phases of soil formation, soil erosion and hillside mass-wasting (Late Glacial to Holocene?) 102

V. River incision and floodplain aggradation (Late Glacial to Holocene?) 104

4 Results from The Lone Valley downhill from Bockstein 106

4.1 Previous research at Bockstein 106

4.2 Results 108

Depth to Bedrock 108

BS-GU1 110

BS-GU2 111

BS-GU3 114

BS-GU4 117

BS-GU5 118

4.3 Data Interpretation 120

I. Bedrock weathering, possible colluviation, river deposition (before 32.000 14C BP) 120

II. Soil formation and soil erosion (before 32.000 14C BP-26.000 14C BP) 120

III. Potential minor cave erosion (before 32.000 ^{14}C BP-26.000 ^{14}C BP) 121

IV. Potential river deposition (32.000-26.000 ^{14}C BP) 122

V. Landscape instability, cave erosion, increasing loess deposition, soil formation (26.000 14C BP-20.000 14C BP) 123

VI. Hillside instability and river erosion (Late Glacial to Holocene) 124

5 Results from The Ach Valley in front Hohle Fels 126

5.1 Previous research at Hohle Fels and in the Ach Valley 126

5.2 Results 129

Depth to Bedrock 130

HF-GU1 133

HF-GU2 135

HF-GU3 138

HF-GU4 139

HF-GU5 141

HF-GU6 143

HF-GU7 145

5.3 Data interpretation 147

I. River incision, soil and cave erosion (after 28.000 14C BP) 147

II. Increasing loess deposition (LGM?) 149

II. Hillside and cave erosion (possibly Late Glacial) 151

III. Lateral fluvial erosion (Early to Mid-Holocene) 152

6 Implications of landscape and environmental changes for the interpretation of the archaeological record of the Ach and Lone valleys 154

6.1 Less intensive phosphatization of the Early Aurignacian deposit inside Hohlenstein-Stadel 154

6.2 Landscape changes in Ach and Lone valleys 156

6.2.1 Fragmented clay coatings as indicators for landscape change 156

6.2.2 Cave erosion, loess accumulation, human depopulation around the LGM 162

6.2.3 Differential preservation of the Gravettian deposits in Ach and Lone valleys 165

6.2.4 River incision, minor cave erosion, Bergkies deposition and Magdalenian recolonization 168

6.3 Occurrence of archaeological material in The Lone and Ach Valleys 171

6.4 Summing up 173

6.5 Further Prospects 175

Refererences 177

Appendix I - Processing of the geophysical data and 3D Modelling 192

7.1 DTM data 192

Hohlenstein 192

Bockstein 194

Hohle Fels 194

7.2 Processing of GPR data 194

7.3 Import in GOCAD 202

The GPR data 202

The coring data 203

The EC-logging data 204

References 204

Appendix II - Surface mapping in The Lone Valley 205

8.1 Methods 205

8.1.1 Core recovering and sediment description 205

8.1.2 Grain size analysis 205

8.1.3 Data management 207

8.2 Results 211

8.3 Conclusions 212

References 215

Appendix III – Descriptions of the Geological Layers 216

References 243

List of Figures

1.1 Geological map of the Swabian Jura 3

1.2 White Jura sequence 4

1.3 Rhine drainage system capturing the Northern Danube tributaries 8

1.4 Map of localities mentioned in the main text 15

1.5 Cave sites with *Bergkies* deposit 18

1.6 Main cave sites in Ach and Lone valleys 22

2.1 GPR 35

2.2 EC-logging 38

2.3 Coring 40

2.4 Micromorphology 42

2.5 ^{14}C dating at the AMS Laboratory at the University of Arizona in Tucson 43

3.1 Cave sites in The Lone Valley 47

3.2 Hohlenstein-Stadel 48

3.3 Phosphate features from Hohlenstein-Stadel and *Vorplatz* 50

3.4 Fine fraction aggregates from Hohlenstein-Stadel 51

3.5 Shift in sediment source at the *Vorplatz* 53

3.6 Survey area opposite from Hohlenstein 54

3.7 Cross correlation of the cores collected from the area opposite from Hohlenstein 55

3.8 Bedrock topography 57

3.9 HS-GU1 58

3.10 Tentative reconstruction of HS-GU1 topography 59

3.11 Micromorphological features from HS-GU1 60

3.12 Transition from HS-GU2 to HS-GU3 62

3.13 HS-GU3 63

3.14 Tentative reconstruction of HS-GU3 topography 64

3.15 The laminated bedding of HS-GU3 in core 12 66

3.16. HS-GU4 and HS-GU5 68

3.17. Reworked aggregates from HS-GU4 69

3.18. Examples of “snowballs” from GL 64 (HS-GU5) 71

3.19. HS-GU6 72

3.20. HS-GU7 73

3.21 Lateral extension of HS-GU7 74

3.22 Micromorphological results from HS-GU7 75

3.23 HS-GU8 76

3.24 Clay and calcite pedofeatures from HS-GU8 77

3.25 HS-GU9 79

3.26 Sedimentary and pedogenic features from HS-GU9 81

3.27 HS-GU10 82

3.28 Micromorphological results from HS-GU10 82

3.29 HS-GU11 and 12 83

3.30 Pedofeatures from HS-GU11 84

3.31 Bedding of HS-GU12 in the geophysical data 86

3.32 Bedding of HS-GU12 in thin section 87

3.33 HS-GU13 87

3.34 HS-GU14 88

3.35 Terrace truncation 89

3.36 HS-GU15 90

3.37 The stratigraphic position of HS-GU15 91

3.38 Micromorphological result from HS-GU15 92

3.39 Site formation processes at Hohlenstein-Stadel 93

3.40 The Lone Valley at Hohlenstein 103

4.1. Bockstein in the Lone Valley 106

4.2 Bockstein cave complex 107

4.3 GPR data from Grid 1, nearby core 33 109

4.4 Cross-correlation of the cores collected in front of Bockstein 110

4.5. BS-GU1 111

4.6 BS-GU2 112

4.7 Micromorphological results from BS-GU2 113

4.8 BS-GU3 and 4 115

4.9 FTIR spectra representative for shell specimens from BS-GU3 116

4.10 Micromorphological evidence for cave erosion in BS-GU3 117

4.11 Calcite pedofeatures from BS-GU3 and BS-GU4 118

4.12 BS-GU5 119

4.13 Bedding of BS-GU5 in the geophysical data 119

4.14 The Lone Valley at Bockstein 122

5.1 Site location in the Ach Valley 126

5.2 Profile 2 from Hohle Fels 128

5.3 Core CSS1 128

5.4 Survey area in front of Hohle Fels 129

5.5 Sedimentary structures within HF-GU1, in the geophysical data 130

5.6 Cross-correlation of the cores collected in front of Hohle Fels 131

5.7 HF-GU1 132

5.8 *Vorplatz* and floodplain deposits in the geophysical data 133

5.9 Micromorphological results from HF-GU1 135

5.10 HF-GU2 and HF-GU3 136

5.11 Micromorphological results from HF-GU2 137

5.12 FTIR spectra from the dated bone fragment from HF-GU3 138

5.13 Micromorphological results from HF-GU3 139

5.14 HF-GU4 140

5.15 HF-GU5 141

5.16 Micromorphological results from HF-GU5 142

5.17 HF-GU6 and 7 144

5.18 FTIR spectra of the dated charcoal and sediment samples from HF-GU6 145

5.19 Micromorphological results from HF-GU6 146

5.20 The Ach Valley in front of Hohle Fels 149

5.21 The position of HF-GU2 in relation to previous river valley incision 150

6.1 Timetable 159

6.2 Landscape formation processes 161

6.3 Cave properties and preservation of the Gravettian record in Ach and Lone valleys 166

7. 1 DTM of the area opposite from Hohlenstein 193

7. 2 DTM of the area surrounding Hohle Fels 194

7. 3 GPR data processing 197

7.4 Assigning geographic coordinates to GPR data – part one 198

7.5. Assigning geographic coordinates to GPR data – part two 199

8.1 Location of described cores and outcrops in The Lone Valley 205

8.2 Surface mapping 207

8.3 Data Management 209

8.4 Analysis of the surface mapping data 213

8.5 Sedimentological map of the Lone Valley 215

List of Tables

1.1. Summary of Swabian Geological History 6

1.2 Summary of the last Apline Glaciation 12

2.1 Samples selected for 14C measurement 44

3.1. Depth to bedrock based on EC-logging data 56

3.2 Radiocarbon determination of ID 19 (HS-GU4) 67

3.3 Frequency of the main components and its relevance for the site formation model 95

4.1 Radiocarbon determinations from core 31 114

5.1 Radiocarbon determinations from core 37 138

Summary

In the Swabian Jura (Southwest Germany) the Ach and Lone valleys host a number of cave sites, which have been repeatedly occupied by groups of hominins since at least the last interglacial. From the excavation of these Prehistoric cave deposits generations of archaeologists have discovered deep sequences and spectacular finds that help to illuminate the evolution of our species and the extinction of Neanderthals.

The current understanding of the relationship between caves, cave deposits, human occupation and landscape evolution in the Ach and Lone valleys relies on data coming almost exclusively from cave sites and rockshelters. Conversely, the few geological studies that focused on the geomorphological evolution of the Ach and Lone valleys were mostly designed to answer questions unrelated to the study of the human occupation of this region.

This dissertation intends to bridge the gap existing (not only in the Ach and Lone valleys) between the geoarchaeological study of cave deposits and the reconstruction of past landscapes. To this end, we investigated the deposits accumulated inside the cave site of Hohlenstein-Stadel (in the Lone Valley) with micromorphological analysis and Fourier Transformed Infrared Spectroscopy (FTIR) methods. Additionally we studied the sediment archives preserved in the Ach and Lone valleys by means of coring, geophysics, micromorphology, FTIR and ^{14}C dating. By integrating our results with previous studies we have been able to evaluate the impact of landscape and environmental changes on the sedimentary and diagenetical processes that occurred inside the cave sites of this region. Our findings give insights into the relation between landscape changes and human migrations in the Swabian Jura.

Previous studies have argued that the early Aurignacian deposits at the sites of Hohle Fels and Geißenklösterle are characterized by deposition of fresh loess, less intensive phosphatization, and the formation of ice lenses. These data support the hypothesis that modern humans entered the Ach Valley in the course of a period characterized by cold climate. Our micromorphological analysis showed that inside Hohlenstein-Stadel (in the Lone Valley) the transition from the Middle Paleolithic to early Aurignacian deposits displays decreasing phosphatization. However, at Hohlenstein-Stadel we did not observe features diagnostic for ground freezing (such as ice lenses). Therefore at this site the less

intensive phosphatization of the early Aurignacian deposits cannot be regarded as secure indicator of a colder climatic period.

The data we collected from Ach and Lone valleys suggest that this region has been variably shaped by phases of soil formation, soil denudation, loess accumulation and river valley incision. Our study revealed that these changes in the landscape might have shaped significantly the archaeological record originally accumulated inside the cave sites of this region. Accordingly to a widely accepted model, Southwest Germany was abandoned by Gravettian groups around 26.000 ^{14}C BP. After a major chronostratigraphic gap Magdalenians recolonized the region starting 13.500 ^{14}C BP. Such chronostratigraphic gap (12.500 ^{14}C years) have been regarded as indicative of the depopulation that the region experienced during the LGM. Our data, however, show that the beginning of this long-lasting phase of apparent depopulation coincides with the occurrence of erosional phases at some cave sites of Ach and Lone valleys. Although the relation between cave erosion and Gravettian emigration needs to be further verified, we hypothesize that human groups might have been present in this region also during the period 26.000-13.500 ^{14}C BP and erosional processes might have cancelled the archaeological evidence for such occupations.

Zusammenfassung

Die Höhlen im Ach- und Lonetal der Schwäbischen Alb (Südwest Deutschland), wurden seit dem letzten Interglazial wiederkehrend von Menschen bewohnt. Generationen von Archäologen entdeckten in den Sedimenten dieser prähistorischen Fundstellen lange Phasen stratigraphischer Sequenzen und spektakuläre Funde, welche dazu beitrugen die Evolution unserer eigenen Spezies und der Ausrottung des verwandten Neandertalers

Das derzeitige Wissen über Höhlen, deren Sedimente, menschlicher Besiedlung und Landschaftsentwicklung stützt sich fast ausschließlich auf Daten aus dem inneren der Höhlen oder den unmittelbaren Bereichen unterhalb von Felsdächern. Dem entgegen stehen nur wenige geowissenschaftlichen Studien, welche sich auf die geomorphologische Entwicklung des Ach- und Lonetal fokussieren und deren Fragestellungen keinen direkten Bezug zur menschlichen Besiedlung in dieser Region haben.

Diese Dissertation beabsichtigt die Lücke zwischen der Mikromorphologie von Höhlensedimenten und der Entwicklung von Paläolandschaften zu schließen. Zu diesem Zweck wurden die Sedimente der Höhle Hohlenstein-Stadel (Lonetal) mit Methoden der Mikromorphologie und Fourier-Transform-Infrarotspektroskopie (FTIR) untersucht. Zusätzlich wurden die Sedimentarchive des Ach- und Lonetals mittels Erdbohrungen, Rammkernbohrungen, Geophysikalischen Methoden, Mikromorphologie, FTIR und 14C Datierung ausgewertet. Durch die Integration dieser neuen Resultate und jenen aus vorangegangen Studien, konnten die Wirkung der Landschaft- und Umweltveränderungen auf die diagenetischen Prozesse innerhalb der Höhlen im Untersuchungsgebiet evaluiert werden. Diese neuen Erkenntnisse leisten einen signifikanten Beitrag zu den Erklärungsmodellen für die Ankunft der ersten modernen Menschen, wie auch deren Verschwinden während des Letzteiszeitlichen Maximums (LGM) in der Schwäbischen Alb.

Frühere Studien führen an, dass die aurignacienzeitlichen Ablagerungen der Fundplätze Hohle Fels und Geißenklösterle vor allem durch die Ablagerung von Löss, einer geringen Phosphatanreicherung und der Bildung von Eislinsen aus. Dies unterstützt die These, dass die ersten modernen Menschen während einer klimatisch kalten Periode in das Achtal einwanderten. Dem gegenüber stehen die mikromorphologischen Ergebnisse dieser

Arbeit, die für den Übergang von Mittelpaläolithikum zu Aurignacien in Hohlenstein-Stadel (Lonetal) eine abnehmende Phosphatanreicherung aufweisen. Allerdings finden sich dort keine Spuren von Bodenvereisung wie etwa die Bildung von Eislinsen. Deshalb findet sich kein direkter Hinweis in dieser Höhle, der die These einer Kälteperiode bei Ankunft der ersten menschlichen Bewohner stützen würde.

Die gesammelten Daten aus dem Ach- und Lonetal legen nahe, dass die Region durch Phasen von Bodenbildung, Bodendenudation, Lössablagerung und fluvialer Erosion geprägt wurde. Die Ergebnisse dieser Studie deuten an, dass diese Veränderungen in der Landschaft außerhalb einen erheblichen Einfluss auf den archäologischen Befund im Inneren der Höhlen hatten. Nach einem mehrheitlich anerkannten Modell finden sich in Südwest Deutschland spätestens ab 26.000 14C BP keine Gruppen der Gravettien-Kultur mehr. Dieser Zeitpunkt markiert eine Unterbrechung der menschlichen Besiedlung in dieser Region, die erst wieder im Magdalénien ab 13.500 14C BP nachgewiesen werden kann. Diese chronostratigraphische Lücke von 12.500 14C Jahren wird gemeinhin mit den unwirtlichen Bedingungen des LGM korreliert. Nach unseren Ergebnissen deckt sich der Beginn dieser vermeintlichen Periode niedriger oder nicht vorhandener menschlicher Population mit dem Einsetzen errosiver Phasen in einigen Höhlen des Ach- und Lonetal. Obwohl ein endgültiger Nachweis eines Zusammenhanges zwischen Erosion in der Höhle und der Auswanderung während des Gravettien weiterer Forschung bedarf, sehen wir die Möglichkeit einer menschlichen Präsenz im fraglichen Zeitraum von 26.000 bis 13.500 14C BP in der Region, deren archäologische Spuren jedoch durch die errosiven Prozesse überprägt bzw. ausgelöscht wurden.

Contribution

Field notes and profile drawings from the cave site of Hohlenstein-Stadel are from Prof. Joachim Kind and Thomas Beutelspacher (Denkmalpflege Baden-Württemberg). Field notes and profile drawings from Hohle Fels are from Maria Malina.

Prof. Christopher Miller and Dr. Christoph Wißing collected the micromorphological samples from the *Vorplatz* of Hohlenstein-Stadel.

The recovering of cores and EC-logging was performed by Dr. Carsten Leven, Matthias Czechowski and myself, Alvise Barbieri.

Dr. Felix Bachover, Dr. Geraldine Quénéhervé and Elmar Schmaltz collected the DGPS points used by myself to locate the geophysical and coring data in Lone and Ach valleys.

FTIR measurements performed on the core samples selected for ^{14}C dating was conducted by Dr. Michael Toffolo.

^{14}C dating was performed at the AMS laboratory of the University of Arizona in Tucson by the lab staff and myself.

All the remaining sampling and analyses included in this dissertation have been conducted by myself, Alvise Barbieri.

1 Introduction

The Swabian Jura of southwestern Germany represents a key region for the study of the evolution of our species and the extinction of the endemic Neanderthals. Most of the evidence for the presence of Middle and Late Pleistocene hominins in this region comes from the cave sites of the Ach and Lone valleys. Although it is likely that most of the activities carried out by Paleolithic humans took place in the open-air (e.g. Münzel 1997; Çep and Waiblinger 2001; Niven 2007), there is relatively little evidence of the occurrence of Paleolithic open-air sites in the Swabian Jura (Bouls et al. 1999, Schneidermeier 1999; Floss et al. 2012). Conard and Bolus (2006) have argued that such bias toward cave sites results from the history of research, which focused for over a century on the study of Prehistoric caves. Additionally, they (Conard and Bolus, 2006) also hypothesized that the record of human occupation in the region has been affected by landscape changes, which might have led to the erosion or deep burial of open-air sites.

The current understanding of the relationship between caves, cave deposits, human occupation and landscape evolution in the Ach and Lone valleys relies mainly on indirect data. Riek (1934, 1957, 1973), Laville and Hahn (1981), Campen (1990, 1995) have considered the variation in lithological properties (e.g., fine vs coarse fraction) throughout the cave sequences of Ach and Lone valleys as indicative of climatic fluctuations. Among these authors, particularly Campen (1995) has remarked on the potential chronological, climatic and geomorphological significance of a specific type of cave deposit (*Bergkies*). More recently, Schiegl (et al. 2003), Goldberg (et al. 2003) and Miller (2015) have studied the sequence of the caves of Hohle Fels and Geißenklösterle with micromorphological analysis. Miller (2015) has argued that specific features within the cave deposits (e.g., degree of phosphatization and clay redistribution) are indicative of climatic and environmental changes. Goldberg (et al. 2003) and Miller (2015) have also shown that a significant part of the cave deposits is actually composed of sediments such as loess, clay, and soil aggregates that entered the caves from the outside landscape. Furthermore, the occurrence of disconformities in the sequences of Hohlenstein-Stadel (in the Lone valley) and Hohle Fels (in the Ach Valley) indicate that the sedimentation active inside these caves might have been shaped (to some extent) by changes in the surrounding landscape (Jahnke 2013, Miller 2015). Considering the relevance of the Paleolithic record of the

Swabian Jura in the framework of European Prehistory, the possibility that erosional events might have affected the caves of this region urges further study.

In the literature few publications are useful for reconstructing the land evolution of the Ach and Lone valleys during the middle and late Pleistocene. Dongus (1974) published a geomorphological map of the eastern Swabian Jura. Brost (et al. 1987) conducted geoelectric and seismic measurements in the Ach and Schmiech valleys in order to reconstruct the onset of the Ach and Schmiech rivers. German (1995) studied the origin of the Schmiechener See. Schneidermeier (1999) performed coring and geochemical analyses in the Lone Valley with the intent of identifying new open air sites. Plenty of cores also have been collected for hydrological purposes from the Schmiech, Ach and Blau valleys since the 1960s (e. g. Groschopf 1963 and 1969). Nevertheless, all these geological studies were designed to answer questions that, in most cases, are not related to the study of the Prehistoric sites of this region. Therefore, the results of these geological investigations can only be linked with difficulty to the results from previous geoarchaeological and archaeological research conducted inside the caves of the Ach and Lone valleys.

The problem of linking cave deposits with external environments appears common in Paleolithic studies and it results from the history of research in the fields of Geoarchaeology and Quaternary geosciences (Barbieri et al. 2018). As a consolidated practice initiated in the late 1970s (Goldberg 1979), the study of the processes that led to the formation of cave sequences is usually carried out by micromorphologists who make observations over tens of centimeters and meters. On the other hand, the reconstruction of regional geomorphological processes is commonly achieved by quaternary geoscientists who focus on loess sequences (e.g. Terhorst et al. 2014), lake deposits (e.g. Litt et al. 2001) and river terraces (e.g. Vanderberghe 2015).

In this dissertation we present our results from the geoarchaeological analysis of the sediments accumulated inside the cave of Hohlenstein-Stadel and our paleolandscape reconstruction of the Ach and Lone valleys. These results have been summarized in two dedicated publications (Barbieri and Miller in press and Barbieri et al. 2018, respectively). In this monograph we present in greater detail background (chapter 1), results (chapters 3, 4, 5), interpretations and archaeological implications (chapter 6) of our research. By

integrating our results with previous analyses performed on cave and open-air deposits we were able to evaluate how past environments impacted the formation of the archaeological record today preserved in the cave sites of this region.

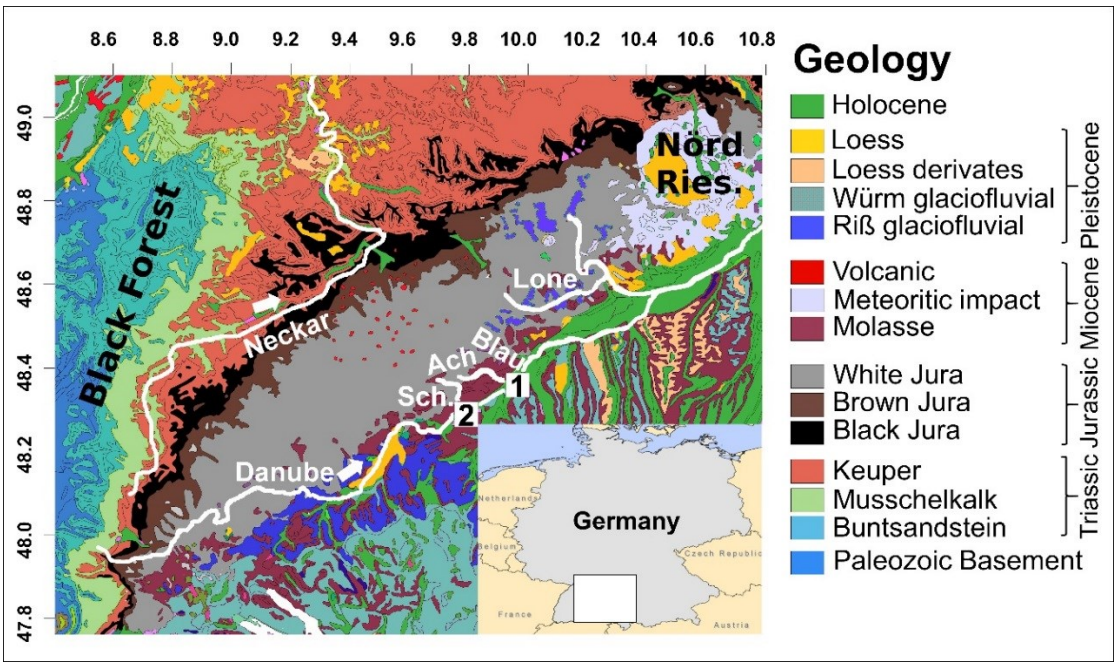

Fig. 1.1. Geological map of the Swabian Jura. ***1***, the city of Ulm, ***2***, the town of Schelklingen. This map was complied with data published in the Geologische Karte Deutschland 1:1000000, which is available online at http://www.bgr.bund.de/EN/Home/homepage_node_en.html. Loess and loess derivates are located accordingly to Sauer et al. 2016. The map is projected in the WGS 84 coordinate system. The labels along the upper and left axes indicate the WGS 84 coordinates. Figure from Barbieri et al. 2018.

1.1.1 Geology and Geomorphology of the Swabian Jura

Jurassic system

The *Schwäbische Alb* or Swabian Jura is a hilly, karstic region (between 500 to 1500 m amsl) in South-West Germany delimited by the Neckar drainage to the north, The Danube Valley to the south, the mountains of the Black Forest to the west, and the depression of the Nördlinger Ries in the east (Fig. 1.1 and Table 1.1. Barbieri et al. 2018).

All together Frankonian, French, Polish, Swiss and Swabian Jura share a significant part of their geological history. In particular, the predominant bedrock present in the whole area is made of limestones, mudstones, marls and sandstones formed between 195 and

145.5 millions of years ago (from here on Ma), in the Jurassic period (Geyer and Gwinner 1991).

Based on stratigraphic evidence, the Jurassic system has been divided into three main bodies. The lower one, called Black Jura (*Schwartzer Jura*), is composed of alternating dark gray sandstones, limestones, mudstones and marls, which are the result of marine sedimentation with significant terrigenous inputs. The following Brown Jura (*Brauner Jura*) is richer in oolitic limestones and was formed when a marginal sea of the Thethys Ocean was present in South Germany. Finally, the uppermost White Jura (*Weißer Jura*) is formed by marls and limestones rich in corals and sponges, indicative of a warm reef located in the regressive Tethys Basin (Figure 1.2, Geyer and Gwinner 1991 and Schall 2002).

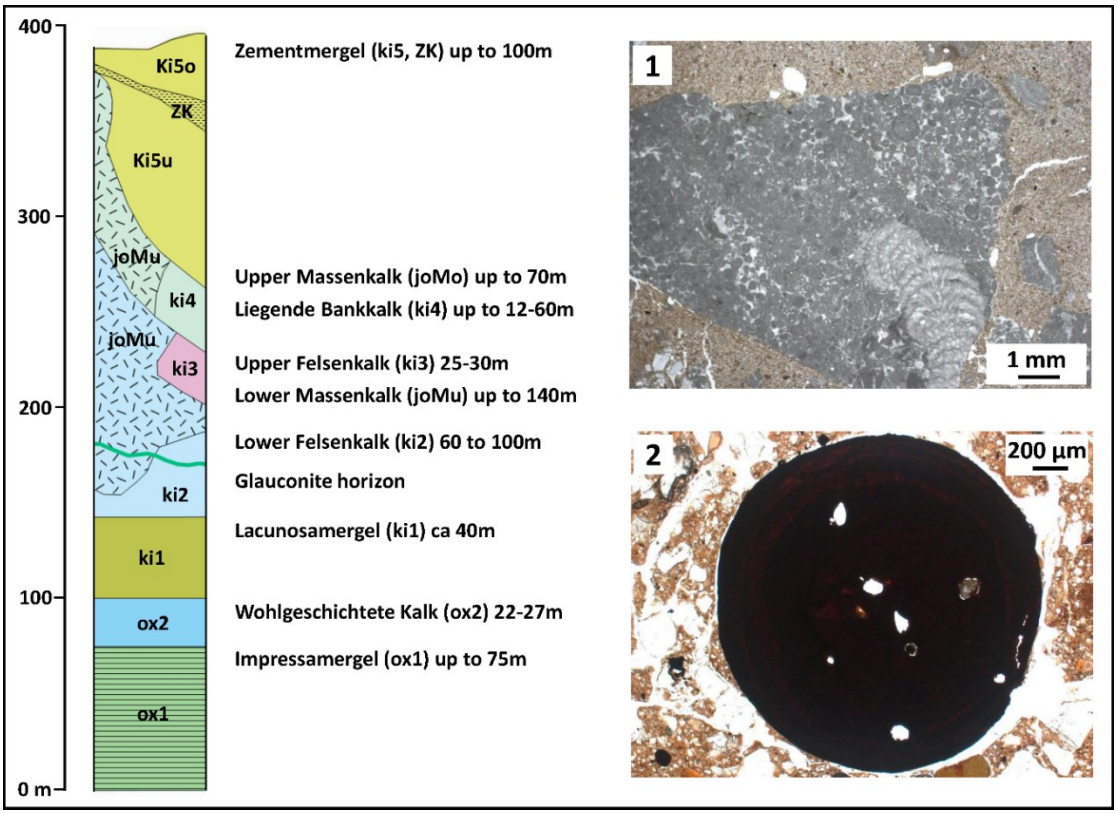

Fig. 1.2. White Jura sequence, Bohnerz and fresh Massenkalk fragments. ***On the left***, schematic stratigraphy of the White Jura (modified from Schall 2002). ***1***, detail of fresh Massenkalk fragment embedded in fresh, reworked loess (*Bergkies*) from the *Vorplatz* of Hohle Fels. ***2***, Bohnerz in Middle Paleolithic sediment recovered from Hohlenstein-Stadel.

The bedrock in the area of our research (Ach and Lone valleys, see below) is largely formed by upper White Jura formations (Geyer and Villinger 2001, Temmler et al. 2003, Mall and Geyer 2004. Fig.1.2). *Lacunosamergel*, *Wohlgeschichtete Kalk* and *Impressamergel* Formations are mainly present along the Swabian escarpment and north of the Jura, where they have been exposed by erosional processes. *Zementmergel*, *Lacunosamergel* and *Impressamergel* are laminated with limestones rich in corals and echinoderms and represent the aquicludes of karst water (Schall et al. 2002). The Upper and Lower *Massenkalk* are rich in belemnites, crinoids, algae, sponges, corals, stromatolites and thromobolites (Figure 1.2, detail 1). They result from cycles of sea deepening/shallowing, erosions, and landslides from the continent into the reef environment (Pawellek and Aigner 2003). In contrast the iron/manganese nodules, the glauconite horizon and the laminated marls present in the *Felsenkalk*, *Wohlgeschichtete* and *Bankkalk* formations are likely the result of a more pronounced continental influence. More in general the limestones of the White Jura contain usually more than 95% of $CaCO_3$ and are composed of sparitic and micritic calcite. Dolomite veins are also well documented in the whole region (Geyer and Gwinner 1991).

Pre-Jurassic

Rocks older than the Jurassic period have been documented exclusively at the borders of the Swabian Jura. Paleozoic crystalline rocks, like granites, are present to the west, in the Black Forest (Fig. 1.1). Triassic formations (such as *Buntsandstein*, *Muschelkalk* and *Keuper*), which are rich in siliceous rocks and marls, are common in the area north of the *Alb* (Figure 1.1, Geyer and Gwinner 1991).

Cretaceous-Paleogene

In the course of the Cretaceous, the opening of the North-Atlantic and South African oceans caused the subduction of the African plate under the European. As a result of these tectonic processes, the rocks which formed during the Jurassic period emerged above sea level, becoming a non-accentuated peneplain (Ufrecth 2008a). In this new setting the Swabian Jura was affected by episodic sedimentation, which was controlled by significant sea level fluctuations (Ufrecth 2008a). The *Bohnerz*-Formation originated in the course of this dramatic landscape change. This formation is composed of pea-sized iron concretions (*Bohnerz*. Fig. 1.2, detail 2) embedded in kaolinite clay and well sorted,

rounded quartz sand (Ufrecth 2008a). The *Bohnerz* are defined as limonite (Schall 2002) or goethite (Reiff 1993) concretions. Kaolinite and *Bohnerz* likely formed in the same environment in the passage between Cretaceous and Paleogene during a phase of ferralitic weathering combined with strong decalcification, desilification and mineral transformations. The resulting clay residuals would have then concentrated into round concretions. However, quartz was likely eroded by Cretaceous paleorivers from the Renish-Bohemian Shield or from the Alpine Foreland Basin (Ufrecht 2008a). Today, apart from rare exceptions, the *Bohnerz*-Formation is not preserved anymore in place but it is commonly found as infilling in karst systems and dry valleys where it has been admixed with Quaternary sediments.

Era	Period	Epoch	Start (Ma)	Geological Processes in Swabia	
Cenozoic	Quaternary	Holocene	0,01	Dry valleys. Landslides.	
		Pleistocene	2,59	Glaciations. Southward migration of the Danube drainage.	
	Neogene	Pliocene	5,33	Onset of The Danube River. Southwards migration of the Lone drainage.	
		Miocene	23,03	Swabian Alb as a kuesta. Volcanic activity. Onset of Lone River and karst system.	
	Paleogene	Oligocene	65,95	Since Eocene opening of the ECRIS. Continental Sedimentation in Swabia.	
		Eocene			
		Paleocene			
Mesozoic	Cretaceous		145,50	Beginning of Alpine Orogeny. Sedimentation of limestones, marls, sandstones, flysch and molasse.	
	Jurassic	Late	195,00	Marine Sedimentation	White Jura. Outcrops in the Alb.
		Middle			Brown Jura. Outcrops along the Northern Alb flank.
		Early			Black Jura. Outcrops North from the Alb and along its Northern flank.
	Triassic	Late	251,00		Keuper. Outcrops between Alb and Rhine valley.
		Middle			Muschelkalk. Outcrops in Black Forest and North from the Alb.
		Early			Buntsandstein. Outcrops in Black Forest.
Neoproterozoic & Paleozoic			650,00	Variscan/Hercynian and Caledonian orogeny. Paleozoic Basement composed of crystalline and metamorphic rocks. Outcrops in Black Forest.	

Table 1.1. Summary of Swabian Geological History.

Eocene

The collision between the African and Eurasian plates caused the Alpine orogeny, the regression of the Tethys Sea and the activation of the European Cenozoic Rift System (ECRIS, Bourgeois et al. 2007). These modification of the lithosphere significantly impacted the geomorphological evolution of the Swabian Jura. Molasse and flysch deposits eroded from the Alps and filled the regressive Tethys Sea (Geyer and Gwinner 1991). The Rhine Rift Valley, which starts near Basel and it is interrupted about 300 km northward by the Hercynian Rhenish Massif, is part of the ECRIS (Illies and Greiner 1979). Vosges, to the West, and the Black Forest, to the East, are the horsts of the rift system, and interestingly some authors have suggested that the uplift of the Black Forest would have taken place much later, even in the Quaternary. However further work has denied the relevance of Holocene and modern tectonic activity on the whole Black Forest area (Demoulin et al. 1998).

Neogene

In the Miocene the tectonic transformations of the lithosphere produced a southward tilt of the Swabian Jura. Since then, the north flank of the Swabian Jura has been deeply carved by rivers draining into the Rhine Graben. The deep incision in these paleo-valleys has exposed "softer" rocks located in the lower part of the Jurassic and Triassic sequences (Fig. 1.1), and once exposed these layers were more easily removed. This differential erosion resulted in the formation of escarpments originally located in the area of Würzburg, north of Swabia. However, during the Miocene through the Pliocene the higher erosion rate of the Rhine basin forced these escarpments to retreat towards the southeast (Fig. 1.3). In particular, the escarpment delimiting the north flank of the modern Swabian Jura is the result of this major erosional process which has governed the changes in the drainage system of the whole area (Fig. 1.3, Strasser et al. 2009, Schall 2002, Geyer and Gwinner 1991).

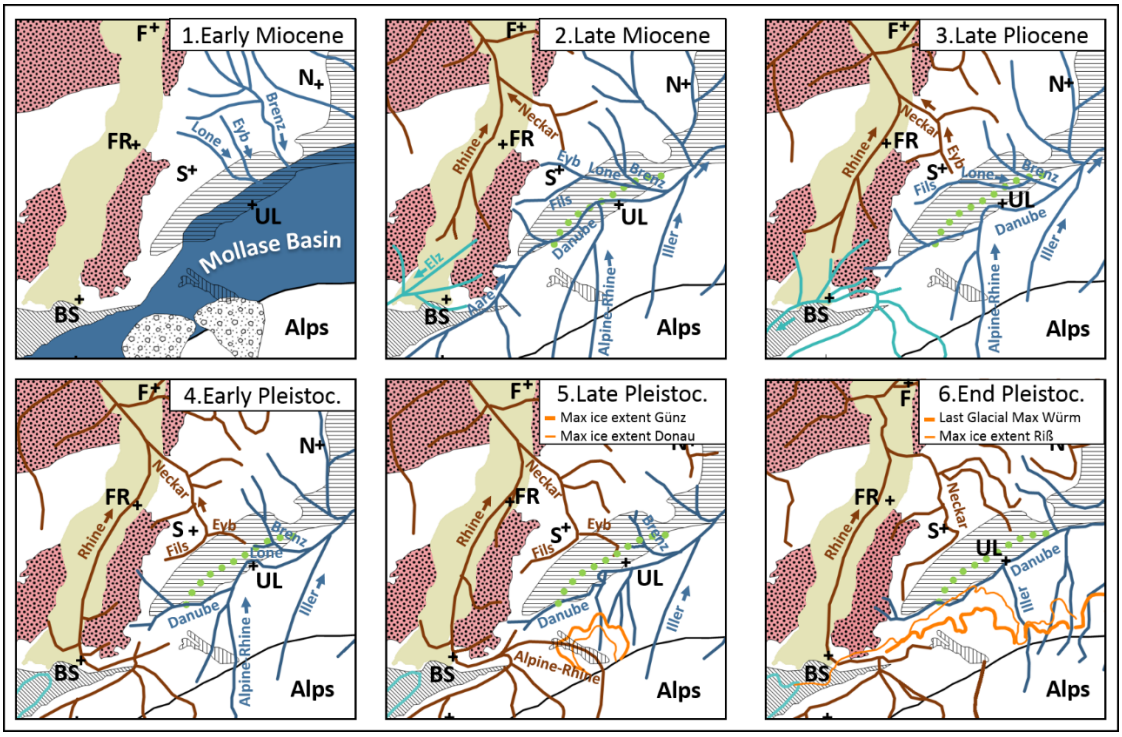

Fig. 1.3. Rhine drainage system capturing the Northern Danube tributaries. ***1. Early Miocene***, paleo-rivers draining the Swabian Alb into the Molasse Sea. ***2. Late Miocene***, Onset of Danube and Rhine drainage system. ***3. Late Pliocene***, Neckar captures Eyb from the Lone. The Danube loses also the Aare. ***4. Early Pleistocene***, Lone lost most of its original drainage. ***5. Late Pleistocene***, after Günz and Donau Ice Ages Alpine-Rhine migrated towards the Rhine Rift Valley. ***6. End Pleistocene***, during the Riß glaciation the ice reached Sigmaringen (North of the Danube). After Riß Glacial the Danube migrated southwards leaving the Alb between Schelklingen and Blaubeuren. List of Abbreviations: **BS**, Basel; **F**, Frankfurt; **Fr**, Freiburg; **N**, Nuremberg; **S**, Stuttgart; **UL**, Ulm. Maps mainly based on data from Geyer and Gwinner 1991, Berger et al. 2005, Strasser et al. 2009, Eberle et al. 2010, Fiebig et al. 2011.

In the Early Miocene, when the formation of the escarpments was just beginning, the large majority of the rising Swabian hills was drained southwards, directly into the regressive sea of the Marine Molasse (Strasser et al. 2009). Remarkably, a significant portion of this river system was occupied by the Paleo-Lone (*Ur-Lone*), which drained an area up to 5000 km^2, from Heilbronn to the Black Forest (Schall 2002. Fig. 1.3, detail 1). The sediments deposited by these paleo-rivers together with the uplift of the whole area caused the regression of the Marine Molasse Sea, which gave rise to brackish lakes and the onset of shallow karstification (Strasser et al. 2009). During this time period pisolites together with relicts of soils and sediments containing bones, Bohnerz, kaolinite and quartz started to accumulate in the karst system (Schall 2002, Strasser et al. 2009).

In the Middle Miocene the ongoing tilting and uplifting of the Jura became more pronounced (Strasser et al. 2009, Schall 2002, Dongus 1974). Around 16 to 5 Ma, due to tectonic dynamics and molasse deposition, the sea retreated permanently from South Germany and left behind a distinctive break-in-slope in the southern part of the Swabian Jura, which corresponds to the former coastline (*Klifflinie*, Geyer and Gwinner 1991). The tectonic dynamics of this period also resulted in the formation of volcanoes in the northern part of the Swabian Jura and just north of the Swabian hills. One of the most well-known volcanic systems in the area is the Urach-Kirchheimer, which was active about 16 Ma (Ufrecht 2008b). Volcanic tuff coming from these volcanos has also been documented in the non-volcanic area of Blaubeuren (Schreiner 1989). In the Middel Miocene the Neckar River, tributary of the Rhine, eroded the Swabian escarpments and captured the headwaters of the Paleo-Lone at Heilbronn. From here northwards the water still drained in the same valley but it flowed in the opposite direction into the Rhine Graben. In this phase both shallow and penetrative karstification spread throughout the whole region (Strasse et al. 2009).

In the Late Miocene the uplift of the Swabian Jura became even more pronounced (Bourgeois et al. 2007, Strasse et al. 2009). Alluvial sediments accumulated at the southern foot of the *Alb* (*Jura Nagelfluh*. Schall 2002, Ziegler and Fraefel 2009), while the Neckar expanded even further south, reaching Plochingen (Fig. 1.3, detail 2. Schall 2002, Ziegler and Fraefel 2009, Strasse 2009). At the very end of the Miocene or at the begin of the Pliocene, the Paleo-Danube was finally set flowing towards the East, along the southern foothills of the Swabian Jura. Alluvial gravels of the Paleo-Danube (*Donauschotter*) dated to this period have been largely documented in the area north of Blaubeuren (Schall 2002).

Towards the passage between Pliocene and Pleistocene the southwards expansion of the Neckar drainage likely pushed the Paleo-Danube to include the Alpine rivers in its drainage (Fig. 1.3, detail 3. Strasser et al. 2009). This change in the catchment is also confirmed by the composition of the Pliocene *Donauschotter*, which are rich in quartz, sandstones and carbonatic rocks from the Alps (Gwinner 1989, Geyer and Villinger 2001, Villinger 2003).

Quaternary - Pleistocene

For the Early Pleistocene, between 2.6 Ma to 790 ka before the present (Ka), six major glaciations have been documented in the Baden-Württemberg area, namely Biber, Donau, Günz, Haslach and Mindel (Habbe 2007). Some authors have also referred to these glaciations with the general term "Pre-Riß Glaciations" (Schielein et al. 2011). Geomorphological features and sedimentary archives dated to the Early Pleistocene are usually located south from the present course of the Danube (*Altendmoränen*, *Deckenschotter*. Habbe 2007, Villinger 2003, Gwinner 1989, Geyer and Villinger 2001). Notable exceptions are represented by river deposits and geomorphological features from Schelklingen and Blaubeuren, which indicate that during the Donau-Günz and Günz-Haslach interglacials the Danube River carved this part of the Alb to a depth of 10 m (Kaufmann and Romanov 2008). Furthermore, some cave sequences from the northern flank of the Swabian Jura show that former tributaries of the Lone River were captured by the Neckar in the Mindel-Haslach interglacial (Strasser et al. 2009). After this major event the drainage of the Lone River achieved probably its present day configuration (Fig. 1.3, detail 5. Schall 2002, Strasser et al. 2009). Dongus (1974), Brost (et al. 1987) and German (et al. 1995) suggest that the Lone and Ach valleys possibly underwent phases of incisions and flood plain aggradation during more recent periods of the Pleistocene.

The interglacial between the Mindel and Riß complex marks the beginning of the Middle Pleistocene (Habbe 2007), which stretches from 790 ka to about 130 ka (Eberle et al. 2010, Geyer and Gwinner 1991). In recent years the first major cold phase of the Riß complex has been considered a separate glaciation, which has been named in Baden-Württemberg the Hoßkirch Glacial (Habbe 2007, Fiebig et al. 2011). As a whole, the Riß Glacial is regarded as the most significant glaciation of the Pleistocene in Central Europe. At their maximum extent, the Alpine glaciers covered large parts of the Alp´s foreland joining the Swiss glaciers (Hantke 1978, Habbe 2007 and Fiebig et al. 2011). Interestingly the ice sheet also reached the Swabian Jura between Sigmaringen and Balingen, where terminal moraines and erratics have been documented (Fig. 1.3, detail 6. Hantke 1974, 1978, Geyer and Gwinner 1991). Riß-aged moraines have also been described in the southern Black Forest as part of the Feldberg glacier, which was likely separated from the Alpine and Swiss glaciers (Hantke and Rahm 1976, Eberle et al. 2010, Fiebig et al. 2011). In this period the Danube and its tributaries were flowing on a lower terrace system

(Hochterrasse) several tens of meters below the previous Deckenschotter deposit (Schielein et al. 2011).

The Riß-Würm Interglacial, also called Eemian, corresponds to the Marine Isotope Stage (MIS) 5e and dates the beginning of the Late Pleistocene, which spans from about 130 ka to 11.6 ka (Geyer and Gwinner 1991). In Swabia during this generally warm and humid interglacial, the permafrost was largely replaced by decalcified and iron oxide-rich soils, usually defined as *terra rossa* or *terra fusca* (Pfeffer 2004, Eberle et al. 2010). At the same time deciduous forest spread in the region. Additionally, this phase has been characterized by significant erosion and river migrations (Habbe 2007), in particular the Danube finally left the Jura between Schelklingen and Blaubeuren and migrated south (Groschopf 1963, Gwinner 1989, German et al. 1995. Fig. 1.3, detail 6 and Fig. 1.4). Since this migration, this part of the Jura has been drained by three smaller rivers, the Ach, Blau and Schmiech (German et al. 1995). Remarkably after the migration of the Danube the bottom of these three river valleys was 30 to 40 m deeper than today (German et al. 1995).

A detailed and widely accepted chronostratigraphic sequence has been formalized for the last glaciation of North Germany, which is named Weichselian (Brauer et al. 1999, Litt et al. 2001, Neugebauer et al. 2012). However, given its geographic position, the Swabian Jura was likely more impacted by the processes that shaped the Alpine foreland in the course of the Würm Glaciation. Data helpful to reconstruct the phasing of this glaciation appear very fragmented (Heiri et al. 2014), and the correlation between the stadials and interstadials of Würm and Weichselian glaciations is still debated (Litt et al. 2001).

In the Alps and their foreland, the beginning of the early Glacial is marked by a stadial (corresponding to the MIS5d, around 109 Ka), which was responsible for the collapse of the broadleaf deciduous forest which spread during the Eemian (Ivy-Ochs et al. 2008, Müller et al. 2013. Table 1.2). The dramatic decrease in vegetation coverage was responsible for hydrological instability, as documented by the paleo-landslides reported at the site of Unterangerberg, in Austria (Starnberger et al. 2013. Fig. 1.4). This cold phase was followed by a first interstadial, a second but less pronounced cold phase, and finally a second interstadial (MIS5a). During both the first and second interstadials the landscape was quickly recolonized by boreal forest and some deciduous trees. This sudden

recolonization suggests that these species might have survived the two previous stadials in refugia (Müller et al. 2003). The glacier extension during the early Würm remains controversial. In the Eastern Alps, evidence from the area around Hopfgarten (Austria, Fig. 1.4) implies that glaciers most likely did not reach the main Alpine valleys during the two cold stages of the early Würm (Ivy-Ochs et al. 2008. Table 1.2).

Epoch	Glacial Phase		Colder/Warmer	MIS	Starting	Relevant Geological Aspects
Holocene			Pre-Boreal	1	11.7 Ka	Progressive amelioration.
Late Pleistocene	Late Glacial		Eegen Stadial		12.680 cal BP	Distinct Cold Phase.
			Allerød ?		Uncertain	
			Older Dryas ?		13.500 cal BP	Possible cooling down.
			Bølling ?		Uncertain	
			Oldest Dryas ?		14.000 cal BP	Possible cooling down.
			Meiendorf Interstadial ?		14.650 cal BP	Clear evidences for warming up.
	Pleniglacial	Upper	Gschnitz Stadial	2	19.100	Last advance of Alpine glaciers.
			Aare Rhone Glacier		21.1Ka	LGM
			CR5/CR6 at Nu		22.330 Cal BP	
			Ice decay in Alp region		24.000 Cal BP	
			Heinrich Event 2		24Ka ca	
			$\delta^{18}O$		27.5 Ka	
			Glacier advance in Swiss Jura		29.500 cal BP	
			Hiatus at F. *Unit 21-24* at Nu. *Units 1- 3* DV.	3 & 2	28-30Ka	Erosional lower contact, higher sedimentation rate, cryosols. Evidences for glacier advance.
		Middle	Series of locally documented stadial and interstadials (Nu, DV, W, U, F)	3	55Ka ca	Cambisols (Lohne soil) and tundra-gleys.
		Lower	*3rd Stadial . Drünten Interstadial* at F.	4	65Ka ca	Tundra like environment. Luvisols.
	Early Glacial		*2° Interstadial* at S , U. *Odderrade Interstadial , Stadial C* and *Drünten Interstadial* at F.	5a	109ka ca	Glaciers not present in The Alpine Foreland. Erosions and Landslides in U.
			2nd Stadial at S and U. *Stadial B* at F.	5b		
			1st Interstadial at at S and U. *Montaigu Event* at F.	5c		
			1st Stadial at S, U. *Stadial A* at F.	5d		Glaciers not present in The Alpine Foreland. Erosions and Landslides in U.
	Riß-Würm Interglacial		*Eemian Interglacial . Unit 1* at Nu.	5e	130Ka ca	Between Riß and Eemian Danube left the Alb. Terrae Calcis formation.
Middle Pleistocene	Riß Glacial				790Ka ca	Ice north from the Danube in the area of Sigmaringen and Balingen.

Table 1.2. Summary of the last Apline Glaciation. Abbreviations of localities mentioned in the text: ***DV*,** Dolní Věstonice; ***F***, Furamoos; ***Nu***, Nussloch; ***S***, Samerberg; ***U***, Unterangerberg; ***W*,** Willendorf. Calibrate dates and information from Müller et al. 2003, Raab and Völkel 2003, Buoncristiani and Campy 2004, Ivy-Ochs et al. 2008, Starnberger et al. 2013, Antoine et al. 2001, 2009, 2013, Heiri et al. 2014, Cupillard et al. 2015.

The beginning of the Pleniglacial is marked by the end of the second Würm interstadial at Samerberg (Bavaria) and Unterangerberg (Starnberger et al. 2013), and by the Drünten interstadial at Furamoos (Müller et al. 2003. Fig. 1.4 and Tale 1.2). This passage corresponds to the transition from MIS5 to MIS4 (Ivy-Ochs et al. 2008, Starnberger et al. 2013). Evidence from the first two sites supports a cold phase that lasted for the entire MIS4 and was dominated by a tundra-like environment (Ivy-Ochs et al. 2008, Starnberger et al. 2013 and Heiri et al. 2014). Different results have been published for the site of Nussloch (Fig. 1.4), where paleosols indicative of steppe landscape are also documented (Antoine et al. 2001 and 2009). The MIS3 was characterized by a less severe climate (Starnberger et al. 2013), and during its interstadials forests and woodlands recolonized the landscape. More in detail at Unterangeberg a birch forest has been documented around ca 57 Ka, which was replaced by a pine-spruce forest around 40.000 ^{14}C BP (radiocarbon years before calibration). At about the same time, during the Willendorf interstadial, in the Unit D of Willendorf (Austria, Fig. 1.4) a mollusk assemblage representative of a mixed forest ecosystems was documented (Heiri et al. 2014). The end of MIS3 and the entire MIS2 were dominated by tundra gley paleosols at Willendorf, Nussloch (Antoine 2001 and 2009) and Dolní Věstonice (Fig. 1.4, Antoine 2013).

Evidence of glacier advance in the Alpine Foreland during the whole Pleniglacial has been debated. In western Switzerland (Finsterhennen, Fig. 1.4) proglacial outwash underlying a residual till has been dated to ca. 70 Ka (Ivy-Ochs et al. 2008). Moreover, in the Kempten Basin (SW Bavaria, Fig. 1.4) three phases of lake formation have been interpreted as indicative of the advance of glaciers into the area (Ivy-Ochs et al. 2008). The oldest phase has been interpreted as pre-Würm, the second phase has been dated to MIS3/4, while the youngest has been correlated with the MIS2. However, data from several sites show that glaciers had nearly reached the foot of the Alps by the end of the MIS3, 28.000 ^{14}C BP (Ivy-Ochs et al. 2008). This advance of the Alpine glaciers likely resulted from further climate deterioration, which corresponds to the Last Glacial Maximum (LGM) of the Würm Glacial (Tale 1.2). Between 21.500 ^{14}C BP and 17.500 ^{14}C BP the French and Swiss Jura were covered with glaciers (Buoncristiani and Campy 2004). Likely around the same time, glaciers moved in the Alpine foreland up to ca. 50 km south from the Danube (Fiebig et al. 2011. Fig. 1.3). Meanwhile the Feldsberg glacier was active in the southern Black Forest, and a small ice cap (Groser Heuberg) might have

been present in the very west of the Swabian Jura (Hantke and Rahm 1976, Hantke 1978). Also, evidence of glaciation has been documented in the Bavarian Forest (Kleiner Arbersee, Fig. 1.4) between 32.4 ka and 12.500 ^{14}C BP (Raab and Völkel 2003). Moreover, the Bohemian Forest underwent three phases of glaciation in the area of Prášilské Lake and Stará Jímka (Fig. 1.4, Mentlík et al. 2010). In the Jura Mountains the ice decay took place between ca. 17.500 ^{14}C BP and 15.000 ^{14}C BP (Buoncristiani and Campy 2004, Cupillard et al. 2015). In this time interval a final, minor glacial advance took place in the Austrian Alps around ca. 15.500 ^{14}C BP (Gschnitz stadial, Ivy-Ochs et al. 2008). In the whole south of Central Europe, cool summer temperatures well below modern values lasted until ca. 12.500 ^{14}C BP, when a sudden warming of about 2-3 °C and an increase in precipitation marked the end of the Pleniglacial and the beginning of the Late Glacial (Heiri et al. 2014).

This warmer phase appears to display a chronology comparable with the Meiendorf interstadial of Northern Germany (Litt et al. 2007, Lotter et al. 2012, Heiri et al. 2014. Tale 1.2). The climatic reconstruction of the following two millennia in the Alpine Foreland is more tentative (Heiri et al. 2014). Nevertheless, δ^{18}O datasets appear to indicate the occurrence of two cooling episodes, which display chronology comparable with the Oldest and Older Dryas of Northern Europe (Litt et al. 2007). The correlation between climatic phases from northern and southern Germany became more consistent towards the end of the Late Glacial and the beginning of the Holocene. In particular pollen and stalagmite records support the hypothesis of a distinct and rapid cooling in summer temperature (Egen stadial), which presents a chronology comparable with the Younger Dryas (Ivy-Ochs et al. 2008, Heiri et al. 2014). The link between northern and southern Alps during the Younger Dryas was also strengthened by the Laacher See tephra deposit, which covered significant parts of Germany and continental Europe (Litt et al. 2001. For the location of Laacher See, Fig. 1.4).

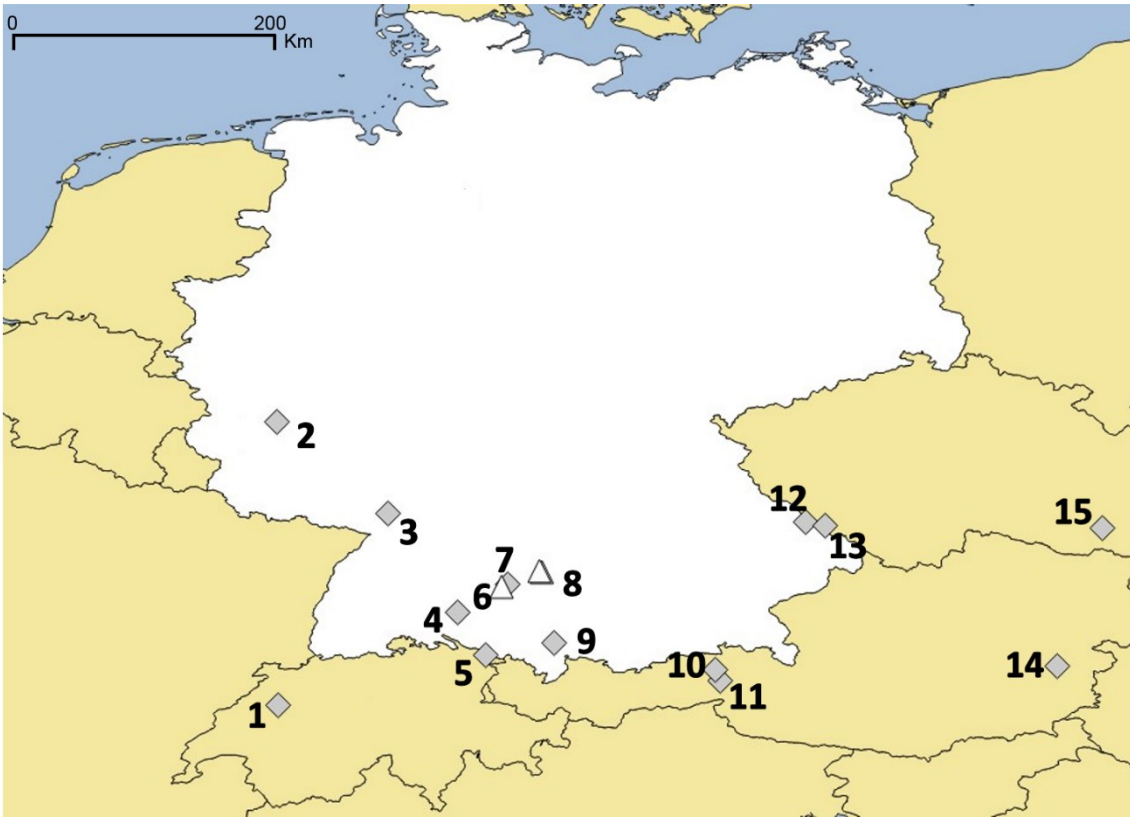

Fig. 1.4. Map of localities mentioned in the main text. ***1***, Finsterhennen; ***2***, Laacher See; ***3***, Nussloch; ***4***, Sigmaringen; ***5***, Füramoos; ***6***, Schelklingen (Hohle Fels); ***7***, Blaubeuren; ***8***, Hohlenstein and Bockstein; ***9***, Kempten; ***10***, Hopfgarten; ***11***, Unterangerberg; ***12***, Kleiner Arbersee; ***13***, Prášilské Lake; ***14***, Willendorf; ***15***, Dolní Věstonice. Triangles (7 and 8) indicate the approximate location of the areas we have investigated.

In the Swabian Jura Würm-aged sediments represent by far the most common parent material of Holocene soils and for this reason they have been studied mainly by soil scientists (Kleber 1992, Mailänder and Veit 2001, Semmel and Terhorst 2010). The AG Boden (2005) proposes to classify such sediments into a Basal, Middle and Upper Layer. The Basal Layer (*Basislage*) is described as free of loess and rich in rock fragments. The Middel Layer (*Mittellage*) is largely made from loess and appears strongly controlled by the topography, and the Upper Layer (*Hauptlage*) contains loess and has a consistent thickness of 50 cm. Although helpful for the study of Holocene soils, this approach to Würm-aged sediments does not appear useful for our research. The most recurrent Würm-aged formations described in the geological literature of the region are: Loess, *Braunlehm*, *Residualton* and *Bergkies*.

In the Swabian Jura the abundant presence of coarse and medium silt-sized particles of quartz, micas, hornblende and epidote in Pleistocene and Holocene sediments suggests

that the Alb was likely covered with loess during the Würm Glaciation. Moreover, the petrography of these components reveals that the loess source was likely the Molasse Basin and more generally the southern Danubian Basin (Gwinner 1989). Only few *in situ* loess deposits are documented north of the Danube (Sauer et al. 2016). The scarcity of these deposits has been explained by a combination of two factors. In the first place the aeolian sedimentation on the Jura would have been relatively weak during the Last Ice Age. Secondly, the thin loess coverage would have been rework by cryoturbation and solifluction shortly after deposition (Schall 2002). After this post-depositional disturbance, the mixed loess was also affected by diagenetic processes, such as calcite dissolution and translocation, which were more pronounced during the Holocene (Riek 1957). The resulting reworked loess deposits are usually densely bedded and enriched in sand- and clay-sized particles of different compositions. In particular secondary calcite is very common also as pedofeatures within buried Bk horizons. These deposits are documented in thickness of 1-2.5 m and have been called *Alblehm*, *Lößlehm* or *Quartär Lehm* (Riek 1957, Gwinner 1989, Schall 2002). In the geological literature these terms have been used largely to indicate the silty-clayey/clayey-silty fine fraction commonly present in the large part of the Quaternary sediments of Swabia.

Additionally, siliceous residues of limestone dissolution are incorporated in the periglacial sediments of Swabia. These residues are separated into two different groups, *Braunlehm* and *Residualton*. The term *Braunlehm* indicates clayey-loamy brown, yellowish or reddish brown siliceous sediments (Bullman and Heinrich 2013, Bleich 1993). Nowadays *Braunlehm* is very rarely preserved *in situ* within depressions and in areas exposed by denudation processes (Altermann and Rabitzsch 1976). More often it has been documented in secondary deposition mixed together with *Bergkies* or other debris (Bullman and Heinrich 2013). The dating of *Braunlehm* is controversial and most authors have suggested that it might have formed during the Eemian or an even older warm period. Only Bullman (2010) has suggested that it might have formed during the Würm Glaciation. According to this author, the humid or warmer Würm phases might have had enough free water to dissolve the limestone and leave insoluble components behind. On the other hand, siliceous sediments with bright brownish yellow silty clay matrix are named *Residualton*. They are usually documented at the bottom of reworked loess deposits and are generally dated to the Pleistocene (Schall 2002).

The term "*Bergkies"* has been used by the Swabian farmers (Riek 1973) to indicate sediments largely present in the Jura just below the soil, which are mainly composed of 2 to 5 cm long (1-2 cm according to Wolff 1962. Fig. 1.2, detail 1), elongated, platy, angular and fresh limestone gravel. The fine fraction represents a minor component of this sediment and it is composed of non-decalcified silty sand, which is well sorted and very rich in quartz. Wolff (1962) interpreted this silty sand as loess redeposited by solifluction. The formation of *Berkgies* has been correlated with the break-down of exposed bedrock under frost action (Riek 1957, Wolff 1962, Riek 1973, Campen 1990, 1995, Freund 1998). Along the flanks of the Swabian Jura, Bergkies can display an internal arrangement quite similar to the *Grèzes Litées* (see below), with the long axes of the gravel particles oriented parallel to the slope. Additionally, it is documented within sorted-patterned ground, as infilling of ice wedges and in solifluction lobes. Furthermore, it occurs as infilling in karst systems (see below and Fig. 1.5). In a few cases *Bergkies* is reported on top of buried, reddish soil horizons (Wolff 1962).

The use of the term "*Bergkies*" has not been consistent in the literature, and, for instance, even Riek did not use it systematically. In some publications the expression "*Feinsplitterig Kalkschutt*" replaces the term *"Bergkies*" (e. g. Wetzel and Bosinski 1969), but in others the two expressions are present together and they appear to identify sediments with slightly different characteristics (Freund 1998). In particular, the term "*Bergkies*" is preferred when the sediment is open-work or displays little fine fraction. On the contrary in cases of a higher percentage of silty-loam matrix the expression *"Feinsplitterig Kalkschutt"* appears to be preferred.

As briefly mentioned above, there are significant similarities between *Bergkies* and some of the stratified periglacial sediments largely identified in France and other parts of Europe. Among those, the *Grèzes Litées* are sandy sediments with a mode of 2.5 mm and maximum grain size for the gravel of about 12.5 mm (Bertran et al. 1992, 1994. Ozouf et al. 1995). The gravel displays a parallel orientation to the present day topography and usually their sedimentation is characterized by the alternation of matrix-supported and gravel-supported or even open-work planar beds (*Litées*). The beds range from multi-centimetric to multi-decimetric in thickness. Remarkably, similar alternating bedding has also been described in some *Bergkies* deposits. More in detail, the sequence of Fesställe is characterized by the alternation of coarse and fine *Bergkies* layers (AH IIIA and AH

IIIB), which have been interpreted as the same original archaeological horizon disturbed by post-depositional solifluction processes (Kind 1987). Interestingly, the constant reworking by solifluction and run-off are hypothesized to be also responsible for the bedding of the *Grèzes Litées* (Bertan et al. 1992, 1994). Moreover, as with *Bergkies,* for the *Grèzes Litées* the fine fraction is hypothesized to be inherited from reworked loess (Harris 1975, Karte 1983), paleosols (possibly *terra rossa*) or other sediments (Jornaux 1976, Coltorti et al. 1983, Van Steijn et al. 1984, Bertran et al. 1994, Deshaies et al. 1995). Similarities apart, there are also some substantial differences between these two classes of periglacial sediments. In particular, *Bergkies* has a coarser mean grain size and has never been described in the literature as affected by illuvial/elluvial processes. Other periglacial sediments similar to *Bergkies* are the so called *Groize Litées* and *Grèzes Terreuses*. The first are a coarser variety of *Grèzes Litées* commonly present on the East side of the Rhone, in the Mediterranean and in Morocco (Bertran et al. 1994, Ozouf et al. 1995). The second type of sediment displays less developed bedding, no evident eluvial/illuvial character, and has been associated with the sedimentary regime of solifluction lobes (Bertran 1992).

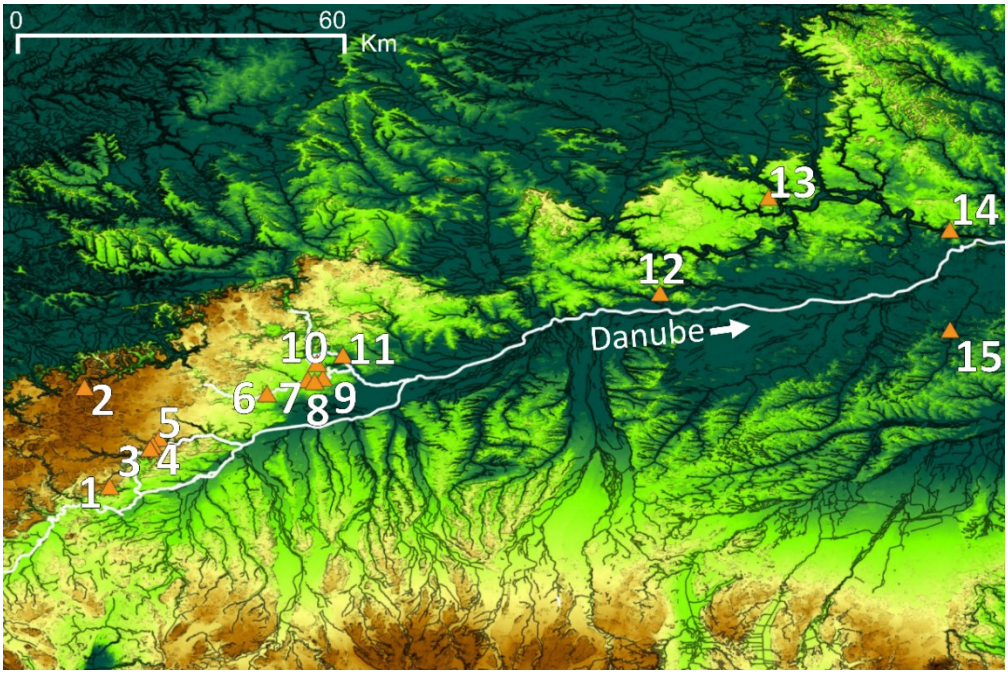

Fig. 1.5. Cave sites with *Bergkies* deposit. ***1***, Felsställe; ***2***, Burkhardtshöhle; ***3***, Helga Abri; ***4***, Hohle Fels; ***5***, Sirgenstein & Brillenhöhle; ***6***, Fohlenhausen; ***7***, Bockstein; ***8***, Hohlenstein; ***9***, Vogelherd; ***10***, Malerfels I; ***11***, Spitalhöhle & Klingenfelsschutzdach; ***12***, Mauern; ***13***, Euerwanger Beuhl; ***14***, Sesselfelsgrotte; ***15***, Speckberg. Map compiled from SRTM data and projected in WGS-84 coordinate system.

While the dating of the various *Litées* appears to fluctuate from the end of the Riß Glaciation (Torres-Giron and Recio-Espejo 1992) to the LGM (Bertran et al. 1994), detailed information about the dating of *Bergkies* deposits comes from the sequence of several Swabian and Franconian Prehistoric cave sites. Although *Bergkies* has been occasionally reported from Middle and earlier Paleolithic deposits in these caves, more commonly this type of sediment contains Magdalenian materials. This association has been reported at Felsställe (Kind 1987), Burkhardtshöhle (Riek 1935), Spitalhöhle (Riek 1957), Vogelherd (Riek 1934), Bockstein (Wetzel and Bosinski 1969), Brillenhöhle (Riek 1973) and Sirgenstein (Schmidt 1912). At Sesselfelsgrotte, Hohle Fels, Felsställe and Helga Abri, *Bergkies* is found also in deposits of potential Holocene age (Freund 1999, Kind 1987, Campen 1990, field notes from Maria Malina).

Quaternary – Holocene

After the Würm glaciation, during the Holocene, the southwards expansion of the Neckar drainage caused the subterranean deflection of some minor tributaries of the Danube (Villinger 2003). Today, thick valley infillings of gravel and the absence of permafrost facilitate the direct drainage of meteoritic water deep into the karst system of the *Alb* (German et al. 1995). At the surface, the Swabian Jura appears crossed by dry valleys and ephemeral streams which occasionally overflow after exceptionally long lasting heavy rains (Binder 1988, 1993, Thost 1986). Modern erosive processes occur mainly in the form of landslides, along the scarplands delimiting the north flank of the Jura, and colluviation, triggered by agricultural practices (Eberle et al. 2010). From a tectonic point of view, the Rhenish Massif and the Rhine Graben have been quite active with uplifting and rifting movements, respectively (Bourgeois et al. 2007). In Swabia a series of significant earthquakes have been registered since as early as 1655 (Schneider 1979) through the nineteenth century up until 1978 (Turkonovsky and Schneider 1982, Hassler et al. 1980). This tectonic activity has been correlated with the orogeny of the Italian Apennine Mountains (Schneider 1967).

1.1.2 Geological questions addressed with this dissertation

As stated in the introduction, the knowledge available for the geomorphology of the Ach and Lone valleys during the middle and late Pleistocene appears fragmentary and relies on relatively few published studies. The work of Dongus (1974), Brost (et al. 1987), and

German (1995) shows that the Lone and Ach valleys might have undergone phases of incision and flood plain aggradation during the middle and late Pleistocene. Miller (2015) has hypothesized that part of the deposits originally accumulated inside the cave of Hohle Fels might have eroded around the LGM as a consequence of major changes in the drainage system of the Ach Valley (see below). German (et al. 1995) also suggested that colluviation was the major process responsible for the filling of the Ach Valley. A similar hypothesis is advanced by Schneidermeier (1999) for the Lone Valley, where he reported the alternation of potential paleosols and colluvial deposits.

Starting from these previous investigations, the aim of this dissertation is to achieve a sound reconstruction of the geomorphological processes that shaped the landscape and the cave deposits of Ach and Lone valleys around the LGM. In particular, we intend to verify the role of colluviation and river valley incision in the accumulation and erosion of sediment inside the cave sites of Bockstein and Hohlenstein, in the Lone Valley, and Hohle Fels, in the Ach Valley.

1.2.1 Archaeological investigations in the Ach and Lone valleys

The discovery of the rich prehistoric heritage of the Ach and Lone valleys is closely related to the first scientific excavations documented in Germany and the various scholars that favored the emergence of an institute for prehistory at the University of Tübingen (location of main sites mentioned in the text is reported in Fig. 1.6).

The excavation of Oscar Fraas at Hohlenstein-Bärenhöhle in the Lone Valley is regarded as the beginning of systematic Palaeolithic research in Germany (Fraas 1862, Conard et al. 2006). According to Conard (et al. 2006), Fraas, who was a minister and curator of the department of mineralogy and paleontology at the Royal Württemberg museum of natural history in Stuttgart, helped to define the goals and methods of modern Palaeolithic archaeology. In the early years of the twentieth century R. R. Schmidt, then PhD student and later professor at the University of Tübingen, conducted excavations which focused on the cave site of Sirgenstein, in the Ach Valley. His research led to the publication of an influential monograph (Die *Diluviale Vorzeit Deutschlands*, 1912) and to the foundation of the department for prehistoric research at the University of Tübingen (1921), which represents a predecessor to the current Institute for Pre- and Protohistory and Archaology of the Middle Ages. From the 1930s to the 1970s Gustav Riek was at the

forefront of prehistoric research in the Swabian Jura. Riek was *Privatdozent* and later Professor and director of the Institute of Geology and Paleontology at the University of Tübingen. He conducted excavations at various cave sites, such as Vogelherd, in the Lone Valley (Riek 1934), Sirgenstein and Brillenhöhle in the Ach Valley (Riek 1959 and 1973), and at other cave sites in the Swabian Jura (Riek 1935, 1957). In the same years, Robert Wetzel, professor of anatomy and rector of the university for the period 1937-1940 (with interruptions), conducted new excavations at the sites of Hohlenstein (Wetzel 1961) and Bockstein (Wetzel 1958, Wetzel and Bosinski 1969). In the last decades of the twentieth century, Joachim Hahn, professor at the Institute of Prehistory, Early History and Medieval Archaeology of the University of Tübingen, led excavations at the sites of Hohlenstein (Hahn and Koenigswald, 1977), Geißenklösterle (Hahn 1988) and Hohle Fels. Additionally, his efforts led to the foundation of the *Urgeschichtliches Museum* in Blaubeuren. Since the late 1990s, under the leadership of Nicholas Conard, a multidisciplinary working group from the University of Tübingen has conducted further investigations at several sites in the Ach and Lone valleys, with a main focus on the site of Hohle Fels. The Landesamt für Denkmalpflege Baden-Württemberg has provided essential contributions to the study of the prehistory in this region. In particular, since the early 1980´s, under the direction of Joachim Kind, archaeological excavations have been carried out at numerous sites, such as Hohlenstein (Kind and Beutelspacher 2010) and Felsställe (Kind 1987). Thanks to the efforts of all these scholars, today the Ach and Lone valleys provide an excellent dataset for many research questions concerning human history (Conard et al. 2006).

1.2.2 The prehistoric record of the Ach and Lone valleys

This section provides a short chronological overview of the archaeological record documented for the Paleolithic in the Ach and Lone valleys.

Middle Paleolithic

The Middle Paleolithic is a period known for the emergence of the *Homo Neanderthalensis*. This new species evolved from groups of hominins that migrated from Africa to Europe, starting ca. 600 ka (Hublin 2009, Posth et al. 2017). Neanderthal skeletal remains are nearly absent from the Swabian Jura, with one notable exception represented by a femur specimen from Hohlenstein-Stadel. However, this specimen

displays carnivore tooth marks and fractures caused by carnivore activity (Kunter and Wahl, 1992; Kitagawa 2014; Posth et al. 2017), and since this cave was likely a hyena den during the Middle Paleolithic, it is likely that this bone was transported inside Hohlenstein-Stadel by hyenas (Kitagawa 2014).

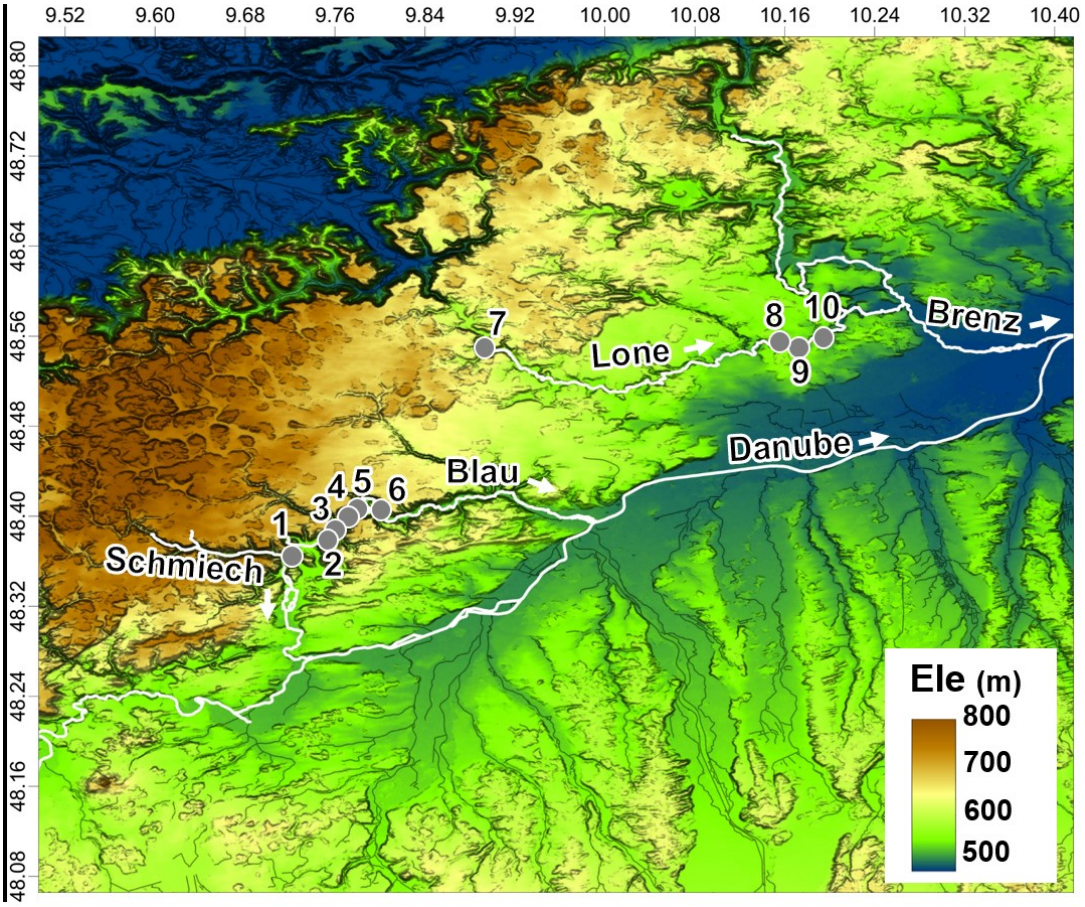

Fig. 1.6. Main cave sites in Ach and Lone valleys. ***1***, Kogelstein; ***2***, Hohle Fels; ***3***, Sirgenstein; ***4***, Geißenklösterle; ***5***, Brillenhöhle; ***6***, Große Grotte; ***7***, Haldenstein; ***8***, Bockstein; ***9***, Hohlenstein; ***10***, Vogelherd. Map compiled from SRTM data and projected in WGS-84 coordinate system. The labels along the upper and left axes indicates the coordinates of the WGS-84 coordinate system.

Given the near lack of skeletal remains, the attribution to the Middle Paleolithic of the lowermost deposits preserved in the Swabian caves largely relies on study of lithic assemblages, radiocarbon measurements, and limited ESR dating.

Throughout Europe, together with the occurrence of a new human species, the Middle Paleolithic also saw the emergence of a new technology, called Levallois, in the production of stone tools (Delagnes et al. 2007). Apart from this common trait, Middle Paleolithic industries are divided in “technocomplexes” (Gamble 1986), each of them

presenting characteristic tool type(s). Technocomplexes that occur in the Swabian Jura are the Micoquian, which is characterized by the common occurrence of bifacial tools (Rosendahl, 2011; Ruebens, 2007), the Keilmesser group, which displays bifacial backed knives (Conard and Fischer, 2000), and the Blattspitzen group, with leaf points (Bosinski 1967, Bolus 2004). These technocomplexes are, however, almost exclusively present at Bockstein (Bosinski 1967). Some leaf points have been found also in non-secure contexts, at Vogelherd, Große Grotte (Wagner 1983) and Haldenstein (Riek 1938). The technocomplex characteristic of the Middle Paleolithic in the Swabian Jura ("Swabian Mousterian", Kitagawa 2014) displays a low level of standardization with highly reduced Levallois components and is not defined by a particular tool type (Beck 1999, Conard 2011). The lithic raw material is dominated by the Jurassic grey chert, Bohnerz brown chert, and radiolarite. The first two were exploited from local sources while the latter was probably collected from the Riß- and Würm-aged terraces of the River Danube (Burkert and Floss 2005, Çep et al. 2011, Floss and Kieselbach 2004).

Results of ^{14}C and ESR dating performed on fauna remains recovered from the excavations conducted in the years 2008-2013 in the back and at the entrance of Hohlenstein-Stadel indicate that this cave was likely occupied by Neanderthals before 40.000 ^{14}C BP (Kind and Beutelspacher 2011). Similar dating has been reported also from Archaeological Horizon (from here on AH) VII at Geißenklösterle (Richter et al. 2000, Higham et al. 2012). The earliest ESR dating from these sites cluster around 50 Ka, yet the recovery of straight-tusked elephant remains from Vogelherd seems to indicate that Neanderthals might have been already present in the Swabian Jura at least by the Eemian (Hahn et al. 1985, Niven 2006).

Aurignacian

In the caves of Geißenklösterle, Hohle Fels, Sirgenstein (Ach valley), Bockstein, Hohlenstein and Vogelherd (Lone valley), Middle Paleolithic deposits are overlain by deposits displaying increased numbers of lithic artifacts, burnt bones, charcoal and organic tools (Conard 2011, Conard et al. 2012). In the lithic assemblages scrapers and burins are abundant and blades are produced by unidirectional knapping techniques (Bolus 2003, Conard et al. 2006). Organic tools result from the exploitation of a wider range of raw materials, including bone, antler and ivory (Conard et al. 2006, Liolios 2006,

Wolf 2015). One remarkable discontinuity with the Middle Paleolithic is the emergence of numerous objects of personal ornament (Kölbl and Conard 2003, Vanhaeren and d´Errico 2006), mobile art (Conard 2009, Kind et al. 2014) and musical instruments (Conard et al. 2009, Conard et al. 2006, Münzel et al. 2002). At Hohle Fels and Sirgenstein these materials are associated with human teeth that have been identified as belonging to the species *Homo sapiens* (Sala and Conard 2016, Conard et al. 2004).

The appearance of such innovations associated with early modern human remains has been linked with the emergence of the Aurignacian culture and the arrival of groups of *Homo Sapiens* in the Swabian Jura (Conard and Bolus 2006).

Among other cave sites of this region, the sequences of Hohle Fels and Geißenklösterle are regarded as a chronostratigraphic reference in the study of the transition between the Middle and Upper Paleolithic in Europe (Hahn 1988, Conard and Bolus 2003). Results from the analysis of micromorphological samples and Aurignacian materials from these sites seem to argue against the co-occurrence of Neanderthals and modern humans in the Swabian Jura. Accordingly to Miller (2015) the Middle Paleolithic deposits preserved at Geißenklösterle were covered with a sterile sediment (GH 17), which was truncated by erosive processes and later covered with fresh loess (GH 15) containing Early Aurignacian materials. Miller (2015) revealed that at Hohle Fels the Middle Paleolithic deposit (GH 9) was covered with unit GH 8, which was sterile at the bottom and contained rare Early Aurignacian materials in the upper part. The occurrence of comparable sterile layers is also reported from the sites of Sirgenstein and Vogelherd (Conard et al. 2006). Following some debate (Hahn 1988, Kozlowski and Otte 2000, Zilhão and d'Errico 1999, Zilhão 2001), Bolus (2003) and Bolus and Conard (2001) deny the occurrence of any transitional (Proto-Aurignacian) technocomplex in the caves of the Swabian Jura. All these observations appear to argue against the hypothesis of contact and possible competition between Neanderthals and modern humans in the Swabian Jura, leaving the cause for the Neanderthal disappearance still unresolved.

The data currently available for the Swabian Aurignacian cannot rigorously confirm nor refute models for the emergence of such culture (Zilhão and d'Errico 2003, Verpoorte 2005, Conard and Bolus 2008). Most of the ^{14}C ages from the Aurignacian at Hohle Fels fall in the period 39.000 – 33.000 ^{14}C BP, with a few data points in the Early Aurignacian

deposit (AH Va) stretching back to 36.000 ^{14}C BP (Conard and Bolus 2008). The Aurignacian deposits of Geißenklösterle gave ages between 30.000 and 34.000 ^{14}C BP, with the oldest age of 36.500 ^{14}C BP coming from the lower (AH III) deposit (Conard and Bolus 2008). Such results seem supported by additional TL dating, which gave an age of 40.200 ± 1.500 calendar years (Richter et al. 2000). Conversely, based on results from ultra-filtrated ^{14}C measurements, Higham (et al. 2012) proposed to date the arrival of modern humans at this site further back to 38.000 ^{14}C BP. Both non- and ultra-filtrated ^{14}C datasets from Geißenklösterle present some discrepancies. In particular, the Middle Paleolithic deposit displays younger ages than the upper Aurignacian sediment (Conard and Bolus 2003, 2008, Higham et al. 2012). Zilhão and d'Errico (2003) consider this discrepancy as evidence of significant post-depositional disturbance, which might undermine the reliability of this part of the sequence. Conversely, Conard and Bolus (2003 and 2008) interpret this anomaly as an artifact of the radiocarbon determination, which might result from fluctuation in the radiocarbon atmospheric production during the late Middle Paleolithic.

Given these chronostratigraphic data the arrival of early modern humans in the Swabian Jura might have occurred according to the "Population Vacuum", the "Danube Corridor" (Conard 2003; Conard et al. 2006; Conard and Bolus 2008) and/or the "*Kulturpumpe*" models (Conard and Bolus 2003). The "Population Vacuum" model argues that modern humans "entered Swabia when few if any Neanderthals occupied the region. This situation allowed the incoming population to quickly establish demographic dominance and to displace the indigenous Neanderthals" (Conard et al. 2006, p. 309). Cold climate conditions (possibly the terrestrial equivalent of the Heinrich 4 cold phase) might have offered suitable conditions for such an evolutionary event (Conard 2003, Conard et al. 2006). According to the "Danubian Corridor" model, early modern humans colonized the upper Danube valley and the Swabian Jura earlier than the rest of Central Europe (Conard and Bolus 2003, 2008, Conard et al. 2006). The "*Kulturpumpe* model" argues that the Aurignacian and Gravettian of Swabia originated in this region from the competition between modern humans and Neanderthals, or the successful adaptation of modern humans to sudden climate deterioration. Alternatively, the emergence of Aurignacian and Gravettian cultures in Swabia might have occurred independently from the competition

of modern humans with other groups of hominins, and their adaptation to climate change (Conard and Bolus 2003).

Any of these models could be more securely supported or exclusively refuted after the acquisition and critical evaluation of additional chronological, archaeological, botanical and geological data (Conard and Bolus 2003, Conard et al. 2006).

Gravettian

At the sites of Sirgenstein (Liolios, 2006), Brillenhöhle (Riek, 1973, Moreau 2009b), Geißenklösterle (Hahn 1988, Moreau 2009b) and Hohle Fels (Conard and Moreau 2004, Moreau 2009b, Taller and Conard 2016) the Aurignacian deposits are covered with sediments yielding a different material culture. The lithic industry preserved in these sediments is characterized by the production of standardized, straight and regular bladelets and/or small blades destined for the manufacture of projectiles (Conard and Moreau 2004, Moreau, 2009b, Taller and Conard 2016). Also burins, end scrapers, splintered pieces, flechéttes, gravette points and micro-gravette points are common in these assemblages (Floss and Kieselbach 2004, Moreau 2009b, Taller and Conard 2016). The local Jurassic chert was used less intensively in comparison with the Aurignacian, although it was still the main raw material exploited for tool production. Conversely, the tool types characteristic of these assemblages are commonly made of radiolarite, which was likely collected from the Riß- and Würm-aged river terraces located 10-20 km southwards from the Swabian Jura (Burkert and Floss 2005, Floss and Kieselbach 2004, Taller and Conard 2016). This shift in the use of raw material can be interpreted as reflecting the need to produce standardized blades and bladelets (Conard and Moreau 2004). Additionally this raw material might have been more accessible due to the occurrence of erosional phases (Hahn and Kind 1997).

In the Ach Valley the deposits overlaying the Aurigncian sediments also display a different set of organic tools (Barth et al. 2009). In the Aurignacian ivory was largely exploited for the production of everyday tools, personal ornaments, figurative art and flutes, whereas in later deposits artefacts made from ivory appear less abundant. The production of ivory beads decreases and is largely replaced by tear-drop shaped ivory pendants, perforated teeth and shells (Barth et al. 2009, Münzel et al. in press). Apart from rare notable exceptions (Conard and Malina 2004), figurines are rare. In the

production of everyday tools, ivory is largely replaced by mammoth ribs, which were employed for the fabrication of points and awls (Conard and Moreau 2004, Barth et al. 2009, Moreau 2009b, Taller and Conard 2017, Münzel et al. in press).

Due to their composition (for instance the presence of flechéttes), the assemblages from the Ach Valley find close comparison with Early Gravettian assemblages from Central Europe (Taller and Conard 2016). More precisely, Moreau (2009b) identified closer similarities between the Gravettian of the Ach Valley and the Gravettian of Weinberghöhlen at Mauern, in the Frankonian Alb, and layer 5 of Willendorf II, in Austria. The hypothesis for an early Swabian Gravettian also appears to be supported by results from radiocarbon dating. At Geißenklösterle Gravettian deposits have yielded ultra-filtrated and non-ultra-filtrated ^{14}C dates between 33.000 ^{14}C BP and 26.000 ^{14}C BP (Conard and Bolus 2008, Higham et al. 2012), with most ages falling in the interval 27.000 - 29.000 ^{14}C BP (Conard and Moreau 2004, Moreau 2009b). Similarly, the Gravettian deposits preserved at Hohle Fels gave radiocarbon ages between 26.000 ^{14}C BP to 30.000 ^{14}C BP, with most dates falling in the interval 27.000 - 30.000 ^{14}C BP (Taller and Conard 2016). Conard and Moreau (2004), and Taller and Conard (2016) have emphasized the presence of discrepancies in the Gravettian chronostratigraphy of Hohle Fels. More in detail AH II cf, the richer Gravettian deposit recovered at this site, displays ^{14}C dating between 27.000 ^{14}C BP and 28.000 ^{14}C BP, while the above laying Gravettian sediment (AH II c) yielded older dates (28.000-30.000 ^{14}C BP). These authors also reported the presence of "Magdalenian infiltrations" (artifact and raw material) in the uppermost Gravettian layer (AH II b, Taller and Conard 2016). Furthermore, some mixing might have occurred between the basal Gravettian layer and the Late Aurignacian deposits (see below). These arguments are also supported by the results of micromorphological analyses, which show that the layer AH II cf is not *in situ* but rather results from secondary dumping events (Schiegl et al. 2003, Goldberg et al. 2003, Miller 2015). In addition AH II b, II c and II cf were likely affected by gelifluction, and the uppermost AH II b was partly removed in the course of a significant erosive phase (Miller 2015). Although all these data indicate that at least some of the Gravettian deposits at Hohle Fels are not intact, the radiocarbon ages from these sediments have a good convergence, do not display significant overlap or mixing with Aurignacian nor Magdalenian, and thus can be regarded as representative (Taller and Conard 2016).

Riek (1973), Conard and Moreau (2004), and Moreau (2009b) have remarked on the existence of a technological continuity between the Swabian Aurignacian and Gravettian deposits, thus supporting the *Kulturpumpe* model formulated by Conard and Bolus (2003). Moreau (2009b) argues that the preparation of prismatic bladelet cores on small nodules and the use of backing in the production of projectiles was already present in the Aurignacian industries of this region and became more standardized in the Gravettian. Additional elements seem to support the hypothesis that, at least to some extent, the Swabian Jura represented a key region for the emergence of the Gravettian in Europe (Taller and Conard 2016). Numerous Venus figurines have been documented from various contexts assigned to the fully developed Gravettian culture, which emerged in Europe starting approximately 27.000 ^{14}C BP. These figurines likely do not make their first appearance with the Gravettian but rather represent the emergence of cultural aspects already present in the Swabian Aurignacian. In fact, the Venus figurine from the Early Aurignacian deposits of Hohle Fels is the earliest example of such representation in the world (Conard 2009). Until recently, the hypothesis of the local evolution of the Swabian Gravettian has also been based on the presence at Hohle Fels of assemblages (AH II d and AH II e) which have been regarded as evidence of a progressive transition from the Aurignacian to the Gravettian (Conard and Malina 2004). However, Taller and Conard (2016) have reassigned these two industries respectively to the Gravettian (AH II d) and the Aurignacian (AH II e) and also have hypothesized that the sediments in which these materials were buried might have suffered significant post-depositional mixing.

The post-depositional disturbance that affected at least some of the Gravettian deposits preserved in the Ach Valley (Miller 2015, Taller and Conard 2016) did not impede a sound reconstruction of the settlement strategy used by the Gravettian humans. Multiple refitting artefacts from Geißenklösterle, Brillenhöhle and Hohle Fels indicate that between 29.000 ^{14}C BP and 27.000 ^{14}C BP the Ach Valley was likely inhabited by the same group of Gravettians (Scheer 1986, 1993, Moreau 2009a, 2009b, 2010). The character of the refitting pieces indicates that Brillenhöhle served primarily as a base-camp, while Geißenklösterle was possibly a satellite site used for the production or reparation of projectiles and personal ornaments (Moreau 2009a, 2009b). At the moment, the study of the lithic industry from Hohle Fels is still undergoing to verify the presence

of additional refitting pieces and to clarify the role of this site in the above-mentioned settlement pattern (Taller and Conard 2016, Taller personal communication).

Unlike the Ach Valley, evidence of the Gravettian period in the Lone Valley is sparser and more contested. This disparity in the archaeological record is noteworthy, particularly considering the homogeneity and richness of the Aurignacian record in this region. At Vogelherd, radiocarbon dates performed on bone fragments (also displaying cut marks) from the Aurignacian layers AH IV and AH V yielded ages between 28.000 – 26.000 ^{14}C BP (Conard and Bolus 2003), which are comparable with the dates for the Gravettian of the Ach Valley (Conard and Moreau 2004, Moreau 2009b). The Aurignacian layer AH IV from Vogelherd also displays features (like backed elements) that might be regarded as anticipation of traits which are more common and standardized in the Gravettian of the Ach Valley (Moreau 2009b). Re-evaluation of the lithic assemblages from Bockstein-Törle led to a reassignment of layers BT VI – BT IV to the Gravettian culture (Borges de Magalhães 2000). This new interpretation appears supported by radiocarbon determinations performed on bone samples from layer BT VI, which yielded ages from ca. 31.000 ^{14}C BP to ca. 21.000 ^{14}C BP (Conard and Bolus 2003). At Hohlenstein excavations conducted in various areas of the cave complex did not recover any preserved Gravettian deposits (Fraas 1862, Schmidt 1912, Wetzel 1961, Kind and Beutelspacher 2010, Beutelspacher et al. 2011, Soergel-Rieth 2011). In the Upper Paleolithic deposit of this site only rare and scattered bone fragments and ^{14}C dating might be related with the Gravettian time period (Kitagawa 2014).

Magdalenian colonization in between two phases of depopulation

At Hohle Fels the top of the Gravettian deposits was shaped by erosive processes, which resulted in the formation of a large gully (Miller 2015). Comparable features were also exposed in the course of excavations conducted at the entrance (*Vorplatz*) of Hohlenstein-Stadel (Kind and Beutelspacher 2010, Beutelspacher et al. 2011, Jahnke 2013). At the two sites, these disconformities have been covered with sediments and artifacts, which have been assigned to the Magdalenian culture (Kind and Beutelspacher 2010, Beutelspacher et al. 2011, Miller 2015, Taller 2015. See below).

Results from the study of the Magdalenian materials from Hohle Fels show that this assemblage is largely composed of backed pieces, burins, perforators, conical bladelet

cores, bone needles, Cheddar points with a double-angled back, shouldered points, tanged points, backed pieces with oblique end retouch, and antler harpoons with bilateral barbs (Taller et al. 2014, Taller 2015). Based on its general composition and on the presence of diagnostic tool-types, this assemblage has been assigned to the Late Magdalenian (Schmidt 1912, Bosinski and Hahn 1973, Taller et al. 2014, Taller 2015). Depending on the needs, backed pieces were used as projectile points, knives for butchering/cutting, and perforators, thus they can be regarded as a multifunctional toolkit (Taller et al. 2012). The trend of raw material procurement continues from the Gravettian period, with a further increase in radiolarite and Bohnerzhornstein (outcropping 20 Km from The Ach Valley), as well as Keuper and Tertiary cherts (40 km northwest from Hohle Fels. Burkert and Floss 2005, Taller et al. 2014, Taller 2015). Although it represents only about 2% of the raw material of the Magdalenian assemblage of Hohle Fels, the use of tabular chert from Lower Bavaria and Jasper from the Upper Rhine marks the activation of 200 km long-distanced contacts (Taller et al. 2014, Taller 2015). Perforated (fresh and fossil) marine shells from the Atlantic, the Mediterranean, and the Mainz Basin are a further indicator of the high mobility of the Swabian Magdalenian groups (Taller et al. 2014, Taller 2015). Among the organic tools, the increased amount of harpoons and the recovery of diverse fish remains suggest a more intensive fish consumption (Conard et al. 2013, Owen 2013, Torke 1998).

Assemblages similar to those preserved inside Hohle Fels and Hohlenstein-Stadel have been reported from numerous cave sites and rockshelters located not only in the Ach and Lone valleys but across the Swabian Jura, which in this period appears as a "consistent and territory conscious Unit" (Maier 2015). 89% of these sites display faunal assemblages in which reindeer is predominant, followed by horse (Weniger 1987). The sites richer in reindeer remains were possibly visited in autumn to winter, while the sites focused on horse hunting reveal evidence of summer and spring occupations (Weniger 1987).

Recent re-evaluation of already published human remains from the caves of Hohle Fels and Brillenhöhle has brought to light new aspects concerning the mortuary behavior of the Magdalenian people that colonized the Swabian Jura (Sala and Conard 2016). In the center of Brillenhöhle, in the Magdalenian layer IV, Riek (1973) recovered one mandible, some cranial fragments and one isolated tooth associated with a hearth. According to Sala and Conard (2016) these human remains represent evidence of skinning, defleshing,

evisceration, disarticulation, and intentional breakage. The association of these anthropic traces with human tooth marks led the authors to conclude that the consumption of human corpses took place in Brillenhöhle during the Magdalenian (Sala and Conard 2016). From the Magdalenian deposit of Hohle Fels archaeological excavations uncovered two femora fragments, which present cut marks (Czarnetzki 1983, Haas 1991, Orschiedt 2000) but no human tooth marks (Sala and Conard 2016). The fact that the two caves are only a couple of kilometers apart seem to suggest that anthropophagic practices also might have taken place at Hohle Fels (Sala and Conard 2016).

The set of radiocarbon measurements available for the Magdalenian of the Swabian Jura shows that this region was occupied only for a short period of time between ca. 12.500 ^{14}C BP and 13.500 ^{14}C BP (Kind 2003, Jahnke 2013, Taller 2015). Remarkably, inside the Swabian cave sites there is nearly no sediment nor dating representative for the ca. 12.500 ^{14}C years that occurred in between the last evidence of a Gravettian occupation (ca. 26.000 ^{14}C BP) and the arrival of Magdalenian groups (ca. 13.500 ^{14}C BP - Conard and Bolus 2003, 2008, Kind 2003, Conard and Moreau 2004). Many authors regard this chronostratigraphic gap as indicative of the approaching LGM conditions which resulted in the depopulation of southwestern Germany and the whole of Central Europe (Jochim et al. 1999, Terberger and Street 2002, Kind 2003, Terberger 2003, Küßner and Terberger 2006, Maier 2015).

During this time period groups of hunter-gatherers survived only at the margins of Central Europe, in the Franco-Cantabrian region, and south of the Alps (Maier 2015). In the Southwest, the Franco-Cantabrian region experienced the emergence of the Solutrean, which was characterized by the flourishing of prehistoric art and the introduction of novelties in lithic technology (Joachim et al. 1999). Meanwhile, in southeastern Europe, the Balkan Peninsula to Greece and the Italian Peninsula was inhabited by groups assigned to the Epigravettian (Maier 2015). Around 21.000-22.000 ^{14}C BP the Solutrean was replaced by a new culture (the Badegoulian), characterized by changes in the lithic production along with a shift towards an increase in the use of bone points (Cretin 2007).

According to a more traditional model, the Magdalenian evolved from the French Soultrean/Badegoulian and spread into the rest of Europe due to the emigration of hunt-gatherers from the Franco-cantabrian region (Joachim et al. 1999). Joachim (et al. 1999)

has argued that the challenging environmental conditions of the LGM and the demographic circumscription in this *refugium* might have resulted in social friction and competition among groups of hunter-gatherers. Therefore, as soon as the environmental conditions improved, after the LGM, these groups of humans emigrated from the southwest of France towards Central Europe following the Rhine, the Danube, and the Saale valleys to the Vistula basin (Bosinski 1990, Otte 1992, Svoboda et al. 1996, Valoch 1996, Floss and Terberger 2002, Küßner 2009).

Maier (2015) proposes a different reconstruction for the recolonization of Central Europe and the emergence of the Magdalenian. This author argues that the emergence of the Badegoulian, which presents traits similar to the Epigravettian (Montet–White 1994, Terberger and Street 2002), might have originated from the early contacts between the previously isolated hunter-gatherers of Franco-Cantabria and East Europe. This hypothesis would be supported by the occurrence of some ^{14}C ages in the range 18.000-22.000 ^{14}C BP from several sites in Central Europe, such as Grub, Ságvár, Stránská Skála, Bockstein-Törle, Mittlere Klause, Kastelhöhle-Nord and Wiesbaden-Igstadt (Maier 2015). Furthermore, ^{14}C dating from sites in Austria and Poland show that the Magdalenian occupation in this region is as old as the earliest Magdalenian occurrence in the Franco-Cantabrian area. Also many ^{14}C ages from the Magdalenian sites in Poland, Moravia and Thuringia are older than the dates from the Magdalenian sites located in the Danube and Rhine valleys. Therefore, Maier (2015) suggests that the Epigravettian of Eastern Europe might have played a more relevant role in the emergence of the Magdalenian culture, which in any case seems to result from a more complex interaction between different human groups rather than one unidirectional migration.

As discussed above, the Magdalenian colonization of the Swabian Jura was probably quick and short-lived (Taller et al. 2014, Taller 2015). At the moment there is no definitive answer to questions concerning the sudden abandonment of this region, which occurred around 13.500 ^{14}C BP (Kind 2003, Taller et al. 2014, Taller 2015). Taller (et al. 2014, Taller 2015) proposes that the Magdalenian groups were highly adapted to the arid grassland steppe environment that characterized the late Pleniglacial and the early Late Glacial. Consequently, in the following stages of the Late Glacial the progressive climate improvement and thus the change in landscape, vegetation and fauna might have pushed the Magdalenian groups to leave Swabia. Remarkably, the likely emigration of

Magdalenian people is followed by a second relevant chronological gap in the cave sequences of the Swabian Jura. In fact the appearance of Mesolithic groups in this region is documented starting ca. 10.000 ^{14}C BP (Kind 2003).

1.2.3 Archaeological questions addressed with this dissertation

As discussed above, there are many hypothesis concerning the prehistory of the Ach and Lone valleys that need further verifications and additional studies. Summarized below are the most relevant archaeological questions that we address with this research.

Middle to Upper Paleolithic transition

Three main models have been proposed to explain the Middle to Upper Paleolithic transition in this region: the "Population Vacuum", the "Danube Corridor" (Conard 2003, Conard et al. 2006, Conard and Bolus 2008) and/or the "*Kulturpumpe*" models (Conard and Bolus 2003). These models, despite differences, hypothesize that the arrival of early modern humans and the extinction of Neanderthals might be related to the occurrence of a cold climate period. Previous micromoprhological investigations conducted by Miller (2015) at the caves of Hohle Fels and Geißenklösterle seem to contrast partly with these models. Miller (2015) argued that Neanderthals probably abbandoned the Ach Valley in the course of a warm period, while early modern humans arrived in the region during a subsequent colder phase.

In this dissertation we contribute to this debate thanks to the micromorphological analysis of the deposits preserved inside Hohlenstein-Stadel.

Gravettian to Magdalenian transition

The Ach and Lone valleys represent a key region in the study of the Gravettian and the recolonization of central Europe after the LGM. However, the knowledge that archaeologists have about the Gravettian and Magdalenian of the Swabian Jura might be biased due in part to some taphonomic issues. For instance, the Gravettian record for the Ach and Lone valleys is remarkably uneven. Due to the many refitting artifacts among the sites at Brillenhöhle, Hohle Fels and Sirgenstein, the Gravettian of the Ach Valley represents a unique example in Paleolithic archaeology (Scheer 1986, 1993, Moreau 2009a, 2009b, 2010). On the contrary, evidence of the Gravettian period from the Lone Valley consists exclusively of one small assemblage (Bockstein-Törle, Borges de

Magalhães 2000; Conard and Bolus 2003), some reworked ^{14}C dating and sporadic reworked faunal material (Vogelherd and Hohlenstein, Kitagawa 2014). Furthermore, the cave sequences of the Ach and Lone valleys present nearly no material nor sediment documenting the time interval that separates the last unquestionable evidence of Gravettian occupation (26.000-27.000 ^{14}C BP) from the earliest presence of Magdalenian groups (13.000-13.500 ^{14}C BP, Jahnke 2013, Taller 2015). In previous publications it has been hypothesized that the preservation of cave deposits from this region might have been considerably affected by the dramatic landscape changes that took place around the LGM (Jahnke 2013, Miller 2015).

Once again the principal aim of this dissertation is to reconstruct the landscape changes that took place in this region towards the LGM and evaluate their impact on the archaeological record of cave sites, such as Bockstein and Hohlenstein (in the Lone Valley), and Hohle Fels (in the Ach Valley).

2 Methods

In this chapter we present the various techniques we used in the course of our research.

2.1 GPR and EC-logging

Depth-to-bedrock, grainsize, structure and geometry of the deposits accumulated in the Ach and Lone valleys have been investigated by applying Ground-Penetrating Radar (GPR) and Direct Push-based logging of electrical conductivity (EC. Barbieri et al. 2018).

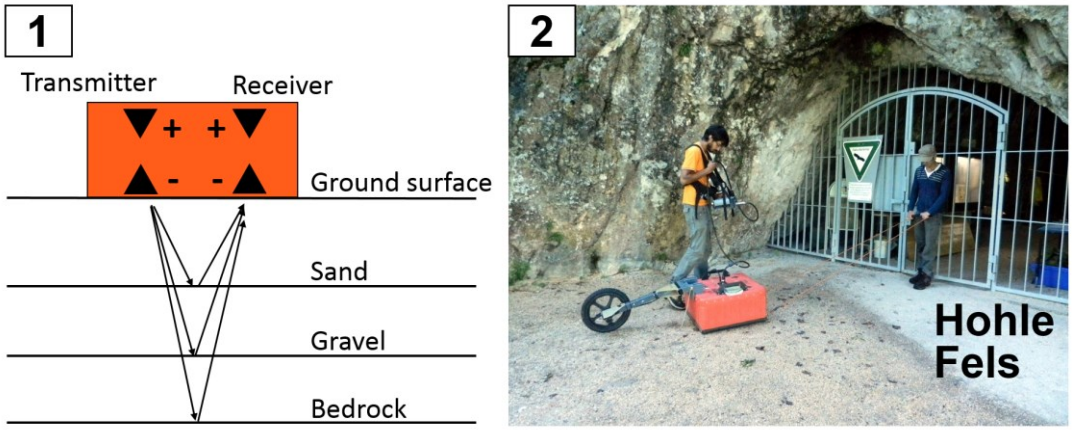

Fig. 2.1. GPR. ***1***, GPRs are designed to transmit radio waves into the ground and record the electromagnetic component reflected at the contact between two media which display different electric resistance. ***2***, GPR survey with a 200 MHz along the *Vorplatz* of Hohle Fels.

We employed GPR to investigate shallow deposits by measuring high resolution, 2D, vertical, time-profiles of electrical resistance; this method exploits the interaction between radio waves and the subsurface (Annan 2009). More in detail, when a radio wave reaches the boundary between two materials with different electrical resistance it separates into three components. A first component of the original electromagnetic wave travels further into the new medium, a second component is lost in the form of heating and a third component is reflected back, as a new electromagnetic wave. GPRs are designed to transmit radio waves into the ground and record the electromagnetic component reflected at the contact between two media which display different electric resistance (Annan 2009, Fig. 2.1, detail 1). Typically, equipment electricity is sent by a computer (called a unit) to an antenna, which often acts at the same time as a transmitter and receiver. If attached to a survey wheel, GPR can be used to perform continuous measurements along a line.

The velocity of the reflected waves can be used to deduce the material corresponding with the detected feature. For instance, higher velocities (ca. 0.06-0.09 m/ns, Davids and Annan 1989) could be indicative of sand and gravel. In contrast, the electromagnetic waves reflected back by deposits rich in silt and clay commonly present lower velocities (lower than 0.06 m/ns, Davids and Annan 1989). Since they are good electrical conductors (and thus display low electrical resistance), clay and ground water generally slow down the velocity of reflectors and might hinder the detection of deeper structures (Davids and Annan 1989).

Depth of penetration, however, does not depend exclusively on the composition and the grain size of the investigated materials, but also on the central frequency of the waves transmitted into the ground by the GPR. Depending on the geological setting, penetration down to 10-25 m has been reported for GPR antennas with a central frequency around 40-50 MHz (Møller 2006). Conversely, for antennas with central frequencies between 500-1000MHz the penetration decreases to only a couple of meters (Møller 2006).

The vertical resolution of GPR data is primarily dependent on the length of the wave transmitted into the ground. Theoretically, the distance between two reflectors should be at least ¼ of the wavelength to be resolved (Sheriff and Geldart 1995), although most commercial GPRs would not be able to distinguish two features separated at such a distance. For instance, the expected vertical resolution for a 200 MHz antenna is 12.5 cm; however, GSSI reports for its 200 MHz antenna a nominal vertical resolution of 20 cm (Jens Hornung, personal communication).

In addition to the electrical resistance of the ground materials and the central frequency of the employed antenna, horizontal resolution of GPR measurements also depends on the setup used in the field (particularly the amount of scans per meter, Neal 2004) and depth of the detected reflectors (Heinz 2001).Summing up, the choice of antenna(s) and GPR setting largely relies on the expected geology and hydrology of the underground as well as the goals of the geophysical prospection.

In the course of preliminary surveys in the Ach and Lone valleys, we tested a GSSI TerraSIRch SIR System-3000 (SIR-3000) connected to 100 MHz, 200 MHz (Fig. 1, detail 2) and 400 MHz antennas to determine its suitability for our investigation. The measurements conducted with the 200 MHz antenna revealed a good balance between

penetration and resolution, therefore we recorded the vast majority of our GPR data (1633 2D-profiles) with this antenna. Measurements were collected in continuous mode, recording 50 to 60 scans per meter. In the field we set up all the GPR grids by triangulation, using fiberglass measuring tapes. Grid corners were marked with wooden sticks or survey flags and their position was recorded using either total station or Differential-GPS (D-GPS). All the GPR data have been processed in Reflex 7.5 with the following filters/steps (for more detail see Appendix I):

- Remove Header Gain;
- Move start time to the first direct wave;
- Manual Gain;
- Band Pass Butterworth;
- Average xy;
- Subtracting the average or background removal. We have not applied this filter to the first direct wave;
- Kirchhoff Hyperbolae migration (2D or more rarely 1D), based on velocity analysis combined with the study of ec-loggings and cores. This filter has not been applied to the direct wave;
- Time-depth correction, based on the same analysis used for the migration;
- Topography correction using the trace headers.

After processing we exported the GPR data from Reflex into GOCAD2.1.6, where we produced 3D models of the subsurface.

EC-logging can be regarded as a technique complementary to GPR, in that it is employed to measure 1D-vertical profiles (logs) of electrical conductance in soils and sediments. EC-logging can be performed to 12 m of depth and can precisely located the bedrock (Leven et al. 2011).

Since the electrical conductance (EC) is the inverse quantity of the electrical resistance, the results of measurements performed with these two techniques can be easily compared. For instance, coarser-grained deposits (sand and gravel) would display reflectors with high velocities in GPR measurements and low EC values in the EC-logging data. As opposed to GPR, EC-logging provides highly resolved depth-profiles of EC, which can

be advantageous, as it does not require post-collection processing (Schulmeister et al. 2003).

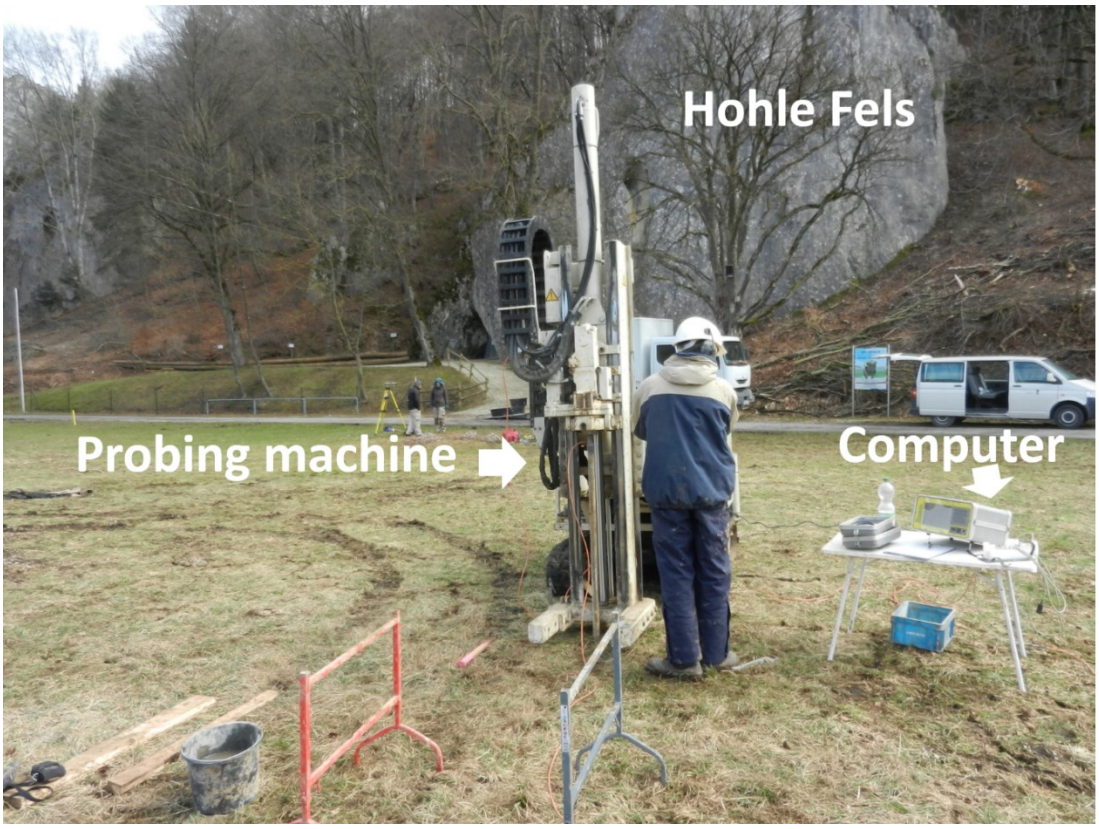

Fig. 2.2. EC-logging. Collection of EC-logging in front of Hohle Fels.

In the Lone Valley opposite from Hohlenstein and in the Ach Valley in front of Hohle Fels (Fig. 2.2), EC-logging was performed using a Geoprobe® 6610 DT probing unit combined with a Direct Image® SC-500 Soil Conductivity System. The measurement of EC-logging consists in applying direct current to a downhole probe, which is advanced in the ground. The probe is 44.4 mm in diameter and is composed of four-poles. In the course of our survey we recorded one measurement of electrical conductance each 1.5 cm. At the survey area opposite from Hohlenstein, logging was performed down to bedrock, while at Hohle Fels it was conducted down to a depth of 12 m. In the field we recoded the position of each EC-log with a D-GPS. In the lab, thanking to the software "R" we exported the EC-loggings and their position into the 3D environment of GOCAD (for more detail see Appendix I).

2.2 Augering and Grain size analysis

We studied the shallow deposits and the main geomorphological features located in the Lone Valley between the cave sites of Vogelherd and Bockstein by means of augering and grain size analysis.

Sediments were recovered with a German auger down to a maximal depth of 1 m. The locations of the cores (126) and outcrops (ca. 10) was recorded with GPS. In the field we photographed and described texture, Munsell color, and composition of the sediments we recovered below the soil. Data were inserted into a PostGis database and visualized in QGIS.

Since field descriptions alone could not provide a satisfactory lithological classification of the sediments, we selected 70 samples to undergo grain size analysis. We conducted this analysis following the protocol designed by the laboratory of Soil Science and Geoecology of the University of Tübingen (protocols and results of the surface mapping are further discussed in Appendix II).

2.3 Coring and sediment description

Basing on the results from our geophysical surveys and surface mapping, we selected key areas to investigate with deeper coring. For this step of our fieldwork we decided to employ the same probing device as used for the EC-logging (Fig. 2.3, detail 1). Apart from core 5, for all the cores we used a Dual Tube Sampling System DT325. Sediment was trapped in 1.22 m long, 50 mm wide, transparent polyethylene sample liners. In the case of core 5 (from the survey area opposite from Hohlenstein) we encountered unexpected shallow refusal, likely due to the presence of coarse limestone pebbles and boulders. Therefore, for this core we decided to use a single-rod Geoprobe® Macro Core MC5 system, which allows to achieve greater sampling depths. With this method sediment was recovered in slightly smaller liners (1.2 m long and 40 mm in diameter).

For each core, sediment was recovered until refusal and geographic coordinates were measured with a D-GPS.

After recovery, cores were transported to the Sand laboratory at the University of Tübingen for description and sampling (Fig. 2.3, detail 2). By lithological description, we distinguished over 300 different sediments, which we named as geological layers (GL).

For each GL we described depth, transition to the next lower unit (according to Fitzpatrick 1983), and amount of coarse (> 2 mm) and fine (< 2 mm) fraction by comparison with frequency charts (Chilingar et al. 1967). For the fine fraction we described the Munsell color and the texture by "feel" (Vos et al. 2016) and with the aid of a ca. 8X field lens. For the coarse fraction, we reported the composition, the sizing (accordingly to the ISO 14688-1:2002 standard), the color, the sorting (Stoops 2003, p. 48), the equidimensionality (Stoops 2003, p. 51), the roundness (Bosellini et al. 1989) and their relative frequencies (Chilingar et al. 1967. The description of GL is reported in Appendix III). Samples were collected for reference and further analyses (reaction with acids, FTIR, micromorphology, dating).

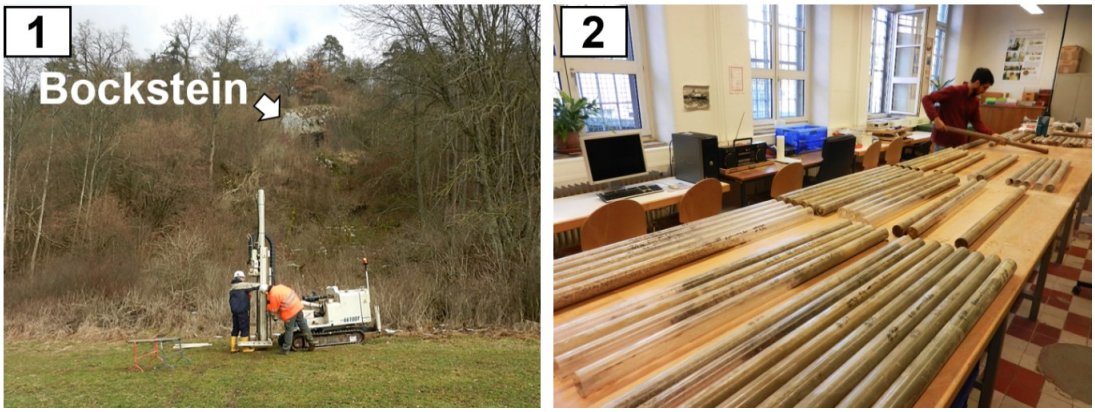

Fig. 2.3. Coring. ***1***, Core recovery at the foothill of Bockstein; ***2***, Sediment analysis at the Sand Laboratory, in Tübingen.

During the sediment description, we extensively photographed the cores with a Nikon Coolpix S9100 camera. Moving from the top down, we documented each liner with an average of ca. 40, partially overlapping images. Overview pictures were taken for all the cores, they were rectified, inserted in a GIS environment (QGIS) and used to locate the various samples we collected.

By comparing their stratigraphic position and lithology we subsequently grouped all the geological layers (GL) into 27 geological units. In the following chapters we referred to the geological units from our survey areas at Hohlenstein, Bockstein and Hohle Fels as HS-GU, BS-GU and HF-GU, respectively. Lithological information and geographic location of each core were imported into the software GOCAD.

2.4 Micromorphology

Micromorphology is generally defined as the study of soils and sediments in their undisturbed state at the microscopic level (Stoops 2003). Since the late 1970s, this technique has been successfully applied to the study of Paleolithic cave deposits (Goldberg 1979) and Pleistocene open air geogenic sequences (Bertran and Texier 1999).

With this technique we studied depositional process, sediment source, and diagenesis of cave and open-air deposits. From the cave of Hohlenstein-Stadel we collected 10 block samples, out of which we produced and studied 14 thin sections (Fig. 2.4, detail 1). From the sediments we recovered in our cores we took 62 block samples (Fig. 2.4, detail 2 and 3) and we focused our analysis on 26 of them, for a total of 30 thin sections.

All block samples were removed with plaster bandages and were subsequently prepared for thin section production at the University of Tübingen. Following our internal protocol, for about 3 days samples were dried in the oven at ca. 40 °C. Once dried, the blocks we impregnated with a mixture of styrene, resin, and hardener. After three weeks in the fume hood, the blocks were hard and ready to be cut with a rocksaw into chips, which were finally ground down to 30 μm thick and 6x9 cm large thin sections. Following Stoops (2003), we described our thin sections (45 in total) with a petrographic microscope under plane polarized (PPL), crossed polarized (XPL), and fluorescent light (FL).

2.5 FTIR

FTIR is a spectroscopic technique that examines the vibrational energy of molecular bonds, thereby facilitating the identification of minerals and the determination of the effects of heating on certain materials. For our research we used both micro-FTIR and KBr-pellet methods.

Micro-FTIR allowed us to perform infrared measurements on key features identified directly in thin section. We used an Agilent Technologies Cary 600 Series FTIR microscope, and measurements were performed in total reflectance and transmission mode (the latter only for the clays), collected between roughly 4000 and 450 cm-1. We interpreted the spectra by comparing them to published spectra (Chukanov 2014, Van der Marel and Beutelspacher 1976) and to our in-house reference spectral library.

Fig. 2.4. Micromorphology. ***1***, Sampling inside Hohlenstein-Stadel; ***2*** and ***3***, collection of micromorphological samples from the samples recovered in our cores.

From our cores we recovered few organic materials potentially suitable for radiocarbon dating (see next section). With the aim of verifying their composition and preservation we sampled these materials and analyzed them with the KBr pellet method. For each specimen, we grinded few milligrams of sample with a mortar and pestle of agate. After having wasted any material in excess, in the mortar we mixed ca 0.1 mg of the sample with ca. 0.5 mg of KBr (FT-IR grade, Sigma-Aldrich). Last, we pressed the mixture into a 7-mm pellet (PIKE Technologies). With an Agilent Technologies Cary 660 spectrometer we measured infrared spectra at 4 cm-1 resolution in 32 scans within the 4000-400 cm-1 spectral range (Barbieri et al. 2018). For each specimen we determined its composition with the software Resolutions Pro and by comparison with our in-house references and published literature (Van der Marel and Beutelspacher 1976; Lin-Vien et al. 1991).

2.6 Dating

We determined the age of our sediments with ^{14}C rather than luminescence methods considering our coring method (transparent PE sample liners) and the large radiocarbon

dataset published for the Swabian Paleolithic (Bolus and Conard 2003, 2008. Barbieri et al. 2018).

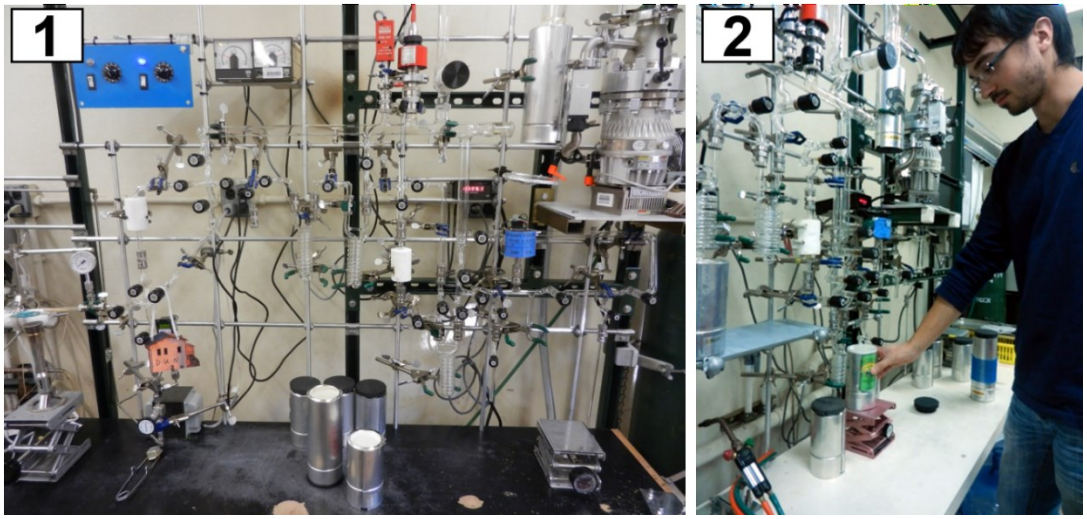

Fig. 2.5. ^{14}C dating at the AMS Laboratory at the University of Arizona in Tucson. ***1*** and ***2***, the line used for the carbon separation.

The results from our FTIR analysis showed that 7 samples were suitable for ^{14}C dating (Table 2.1). Three samples of sediment appeared to contain organic carbon sufficient for ^{14}C measurement (ID-19, ID-58 and ID-72), while gastropod shells from two mixed samples resulted to be composed of fresh aragonite (ID-69 and ID-73). Additionally, the FTIR ensured the good preservation of one sample of charcoal fragments (ID-57) and one bone fragment (ID-63).

Based on the sediment description and the results of the micromorphological analysis we pretreated these 7 samples following different protocols (Table 2.1). Macroscopically ID-19 and ID-72 were formed from medium to coarse sand-sized aggregates of silty clay, which appeared dark brown and yellowish red in color. Results from the micromorphological analysis revealed that these aggregates were slightly reworked, impregnated with iron-manganese oxides and embedded in reworked loess. Both our macroscopic and micromorphological observations denied the occurrence of preserved organic matter in these specimens. Only the results from FTIR analysis suggested the presence of organic compounds (Barbieri et al. 2018). Since these specimens were sampled from deeper than 4 m below the ground surface, we excluded the possibility that ID-19 and ID-72 contained younger carbon translocated from the Holocene soil (Barbieri

et al. 2018). Basing on all these observations, we pretreated ID-19 and ID-72 exclusively with 1 N HCl in order to remove inorganic carbon and acid soluble organic molecules.

ID	Lab num	Core	GU	Depth	Material	Pre-treat.	Sample (mg)	C (mg)
19	X29378	12	HS-GU4	-4.2	Tot. O. Carbon	A	518.48	0.47
57	X29380	37	HF-GU6	-1.2	Charcoal	A-B-A	3.79	2.52
58	X29381LT	37	HF-GU6	-1.5	Humin fraction	A	35.08	1.07
63	X29273	37	HF-GU3	-8.2	Bone	A-B-A	3.23	1.02
69	X29382	31	BS-GU3	-2.2	Aragonite shells	Etching	12.28	1.47
73	X29384	31	BS-GU3	-3.2	Aragonite shells	None	7.9	0.93
72	X29383LT	31	BS-GU2	-5.6	Tot. O. Carbon	A	649.27	1.44

Table 2.1. Samples selected for ^{14}C measurement. In this table our internal sample ***ID***, used in the text; the sample ID used by the AMS laboratory in Tucson (***Lab num*****;** the provenience of each sample (***Core***, ***GU*** and ***Depth*** in m below ground surface); the specimen type (***Material***); the process followed for pre-treatment (***Pre-treat.***); the mass of the sample used for analysis (***Sample (mg)*****;** the mass of the extracted carbon (***C (mg)***). Table from Barbieri (et al. 2018).

Our sediment description and micromoprhological analysis show that ID-58 was composed of a reworked, peat-like sediment which resulted quite rich in mineral fraction. We sampled ID-58 from the top of the second liner of core 37, less than 2 m below the ground surface. In this case we could not exclude the possibility that carbon might have been translocated from the overlying Holocene soil into ID-58. Therefore, we pretreated this specimen with the so called acid-base-acid protocol (ABA) which consists in cleaning the sample with 1 N HCl, 0.1% NaOH and again with 1 N HCl (Hatté et al. 2001, McGeehin et al. 2001, Pessenda et al. 2001, Jull et al. 2013).

The results from our micromorphological analysis showed that ID-19, ID-58 and ID-72 had been possibly affected by reworking. For none of these specimens we could determine the source of the organic carbon preserved in them. Therefore, in attempt to extract exclusively the organic carbon that they might have incorporated at the time of their final deposition, we burnt ID-19, ID-58 and ID-72 at 400 °C (McGeehin et al. 2001, Wang et al. 2013, Barbieri et al. 2018).

Following the protocol commonly used for these specimen types at the AMS Laboratory of the University of Arizona, we pretreated charcoal and bone samples with ABA flow

and burnt them at 900 – 1100 °C. We sonicated the two mixed shell samples (ID-69 and ID-73) to remove any remaining sediment. Shell fragments are usually etched with pure H_3PO_4 until 50-85% of the carbonate is removed (Burr et. al. 1992). This step aims at removing the external layers of the shell which might have been contaminated with younger carbon. We pretreated with H_3PO_4 only ID-69, while the amount of shell fragments we collected for ID-73 was not large enough to be etched (Barbieri et al. 2018).

After pretreatment, we measured the $\delta^{13}C$ of the samples, we graphitized them and we measured their ^{14}C content with the AMS. The dating results and their calibration are presented in the following chapters (3, 4 and 5).

All the radiocarbon dates mentioned in this dissertation are ^{14}C ages before calibration (^{14}C BP). By doing so we attempted to be homogeneous with most of the previously published dates from the Swabian Jura (Conard and Bolus 2003, 2008, Moreau and Conard 2004, Moreau 2009). Furthermore, we prefer to mention our results as radiocarbon ages before calibration due to the nature of our samples. As previously argued we actually ignore the source of the carbon we extracted from ID-19, ID-58 and ID-72. ID-69, 73 and 57 are made from fragments of shells and vegetal material which originated from the death of different and separate gastropods and plants. Therefore the ages we determined for ID-19, ID-58, ID-69, ID-72 and ID-73 must be regarded as range of ages. Only the age of the bone fragment ID-63 determines the time of one precise event (death of one animal). Therefore, although we calibrated all our ^{14}C dating (OxCal 4.3, curve IntCal 13), from a formal point of view only the calibrated age of ID-63 is worth to be considered (Greg Hodgins, personal communication).

3 Results from the Lone Valley opposite from Hohlenstein

3.1 Previous research at the site

The site of Hohlenstein is situated roughly 3 km to the northwest from the village of Asselfingen, in the Lone Valley (Fig. 3.1, detail 1). Here, a limestone outcrop located approximately 3 m above the floodplain hosts 2 larger phreatic tubes (Hohlenstein-Stadel and Hohlenstein-Bärenhöhle) and two small rockshelters (Hohlenstein-Ostloch and Kleine Scheuer. Fig. 3.2).

Oscar Fraas was the first to conduct systematic excavations at this site (Hohlenstein-Bärenhöhle, Fraas 1862). After this early investigation, for over a century numerous scholars such as Schmidt (1912), Soergel and Soergel-Rieth (2011), Wetzel (1961) and Hahn and Koenigswald (1977) have conducted intensive excavations, which led to the recovery of rich archaeological and faunal assemblages. Nevertheless, poor documentation techniques and occasionally imprecise publication of the finds have caused some confusion regarding the exact location of these old excavations and their stratigraphy (Kitagawa 2014).

Among the numerous finds recovered in over a century of archaeological investigations, particularly the Lion-man (*Löwenmensch*) from Hohlenstein-Stadel has gained much attention, being one of the earliest examples of figurative art in Europe (Conard and Bolus 2003, Kind et al. 2014). It was in 1968-69 when for the first time Hahn pieced together this figurine from over 200 ivory fragments previously discovered by Völzing in 1939 (Wetzel 1961). With the intent to clarify the extent and stratigraphy of previous excavations and locate the original context of this spectacular find, from 2008 to 2013 Claus-Joachim Kind and Thomas Beutelspacher led new excavations in the back and at the entrance (*Vorplatz*) of Hohlenstein-Stadel. Remarkably, in the back of the cave the excavators discovered new ivory fragments fitting some missing parts of the Lion-man (Kind et al. 2014).

In the past 20 years previous researchers have investigated the surrounding of the Hohlenstein cave complex. In the late 1990s Schneidermeier (1999) investigated various areas of the Lone Valley between Hohlenstein and Bockstein and reported the occurrence of bone fragments and artifacts exclusively in the cores he recovered in front of Hohlenstein.

With the intent of verifying the presence of intact, open-air archaeological deposits, a team of archaeologists led by Michael Bolus excavated three test pits along the slope in front of the site (Bolus et al. 1999. Fig. 3.2). Based on the gravel content of the sediments, Bolus distinguished two main units (GE1 and GE2) in these test pits. From the upper part of the exposed stratigraphy he reported GE1, which he described as a fine deposit rich in Pleistocene/Holocene faunal remains and artifacts including stone tools, one glass pearl and pottery fragments dated back to Mesolithic, Neolithic, Hallstatt and Roman time (Bolus et al. 1999). Given the composition of such an assemblage, Bolus (et al. 1999) and Geiling (et al. 2015) interpreted GE1 as a mixed Holocene-aged, colluvial deposit.

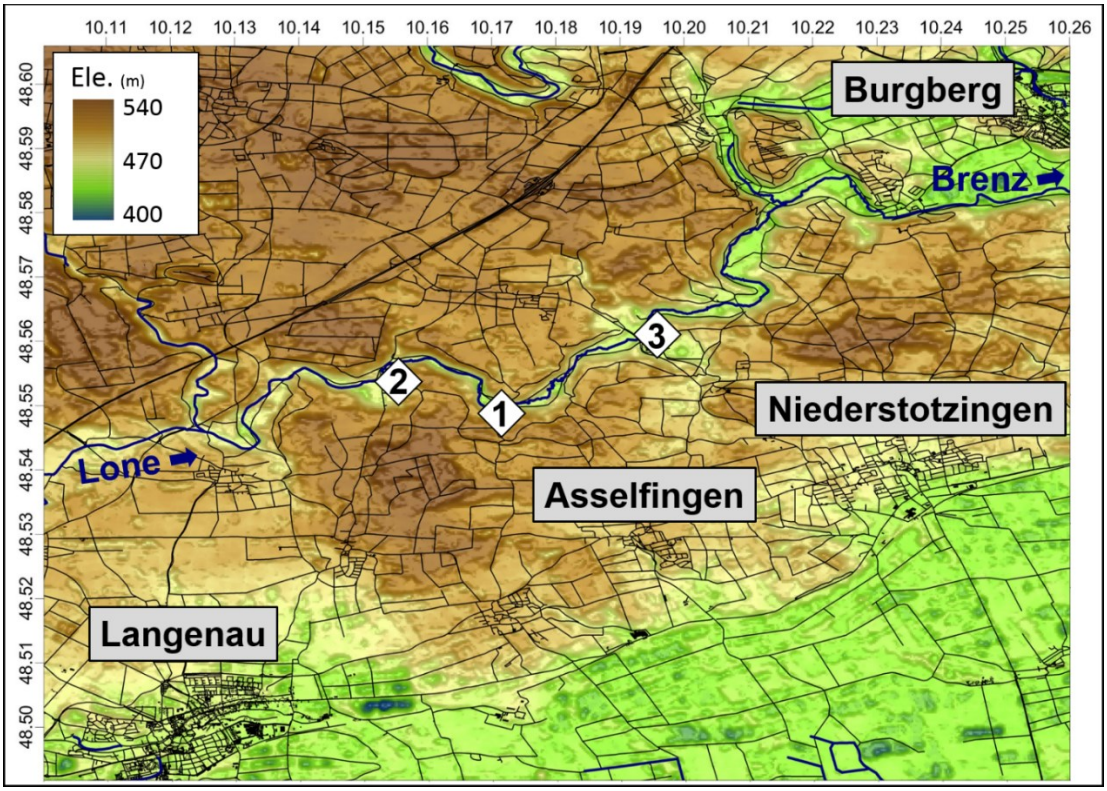

Fig. 3.1. Cave sites in The Lone Valley. ***1***, location of Hohlenstein; ***2***, location of Bockstein; ***3***, location of Vogelherd. The map is compiled from SRTM 90m Digital Elevation Data and it is projected in the WGS 84 coordinate system. The labels along the upper and left axes indicate the WGS 84 coordinates.

From the deeper portion of the three tests pits Bolus (et al. 1999) exposed gravelly and blocky sediments (GE2), which contained numerous Pleistocene faunal remains and 25 Middle Paleolithic stone tools. Accordingly to profile drawings published by Geiling (et al. 2015) GE2 displayed also one ice wedge, in test pit C, and one involution, in test pit A. Based on the study of faunal (Geiling et al. 2015) and lithic materials (Bolus et al.

1999), GE2 has been regarded as a less disturbed deposit. Nevertheless, given the abundance of unmodified cave bear remains, Kitagawa (2014) has argued that GE2 might correspond, at least in part, to material removed from the uphill cave deposits.

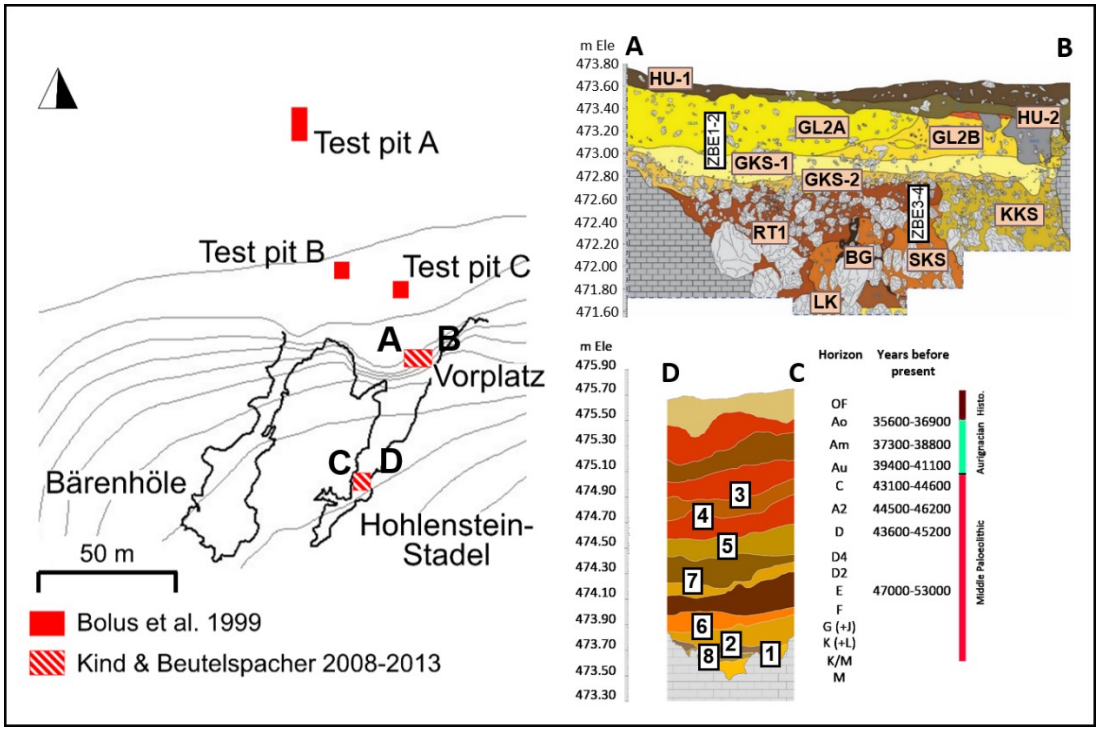

Fig. 3.2. Hohlenstein-Stadel. ***On the left***, location of the most recent archaeological excavations conducted inside and outside Hohelnstein-Stadel. Squares filled with red, diagonal dashes locate the excavations conducted by Kind and Beutelspacher in the years 2008-2013. Completely filled, red squares mark the excavations conducted by Bolus et al. 1999. ***On the right***, profiles investigated with micromorphology. ***AB***, profile exposed at the Vorplatz. Archaeological units are labelled in pink. Micromorphological blocks are numbered on white background. ***CD***, profile exposed in the back of the cave. Micromorphological blocks are numbered on white background. Drawings of both profiles have been modified from original graphics realized from the Landesamt für Denkmalpflege Baden-Württemberg.

3.2 Results

3.2.1 Micromorphological results from Holenstein-Stadel

We sampled and described the profiles exposed at Hohlenstein during the 2008-13 excavations for micromorphological analysis (Fig. 3.2, AB and CD). Our aim was to study the processes that led to the formation of the archaeological sequence preserved at this site. The results of this analysis are presented extensively in a dedicated publication (Barbieri and Miller, in press), and in this section we have summarized the findings.

Unit M

Unit M is the lowermost, sterile unit that has been exposed at the back of Hohlenstein-Stadel. This deposit represents a very different sediment in comparison with the rest of the investigated sequence. It is mainly composed of clay and sand-sized grains of quartz, chalcedony, glauconite and rare micas. These components are organized in graded laminations which exhibit a subangular blocky microstructure. This unit is completely free of calcite, bone, tooth and charcoal fragments. Furthermore, the groundmass has not been phosphatized and phosphate grains are only rarely present (Fig. 3.3, detail 1).

Unit K/M to Unit Au

Unit M is covered with the Middle Paleolithic sediments from Unit K/M through Unit C (Fig. 3.2, profile CD). These deposits are largely composed of coprolites, aggregates of clay and silt (quartz and micas), as well as bone and tooth fragments. All these components are embedded in a clayey silty groundmass which results phosphatized, poor in calcite and rich in quartz and micas (reworked loess). Despite similarities, these units display various degrees of phosphatization, different morphology of the phosphatic crusts, and various size, frequency and weathering of the components.

Unit K/M is made of abundant, large bones (up to 2cm), coprolites (Fig. 3.3, detail 2) and clayey silt aggregates (Fig. 3.4). Furthermore we observed rare sand-sized fragments of charcoal and frequent, reworked phosphatic crusts, which originally formed along the cave walls.

In Unit K we identified thin phosphatic crusts preserved on top of buried surfaces associated with bone fragments that were probably burnt at around 600°C (based on FTIR comparison with our internal collection. Fig. 3.3, detail 3). This unit also displays extensive iron-manganese staining of bones and matrix groundmass.

Unit G displays a phosphatization of the fine fraction comparable to the lower units (Fig. 3.3, detail 4); however, it is characterized by a diminished number of aggregates of clay and silt together with generally greater roundness of the sand fraction. Furthermore we observed clear evidence of bioturbation at the contact between Unit G and Unit F, which has resulted in the translocation of bone fragments – also burnt ones – from the upper Unit F.

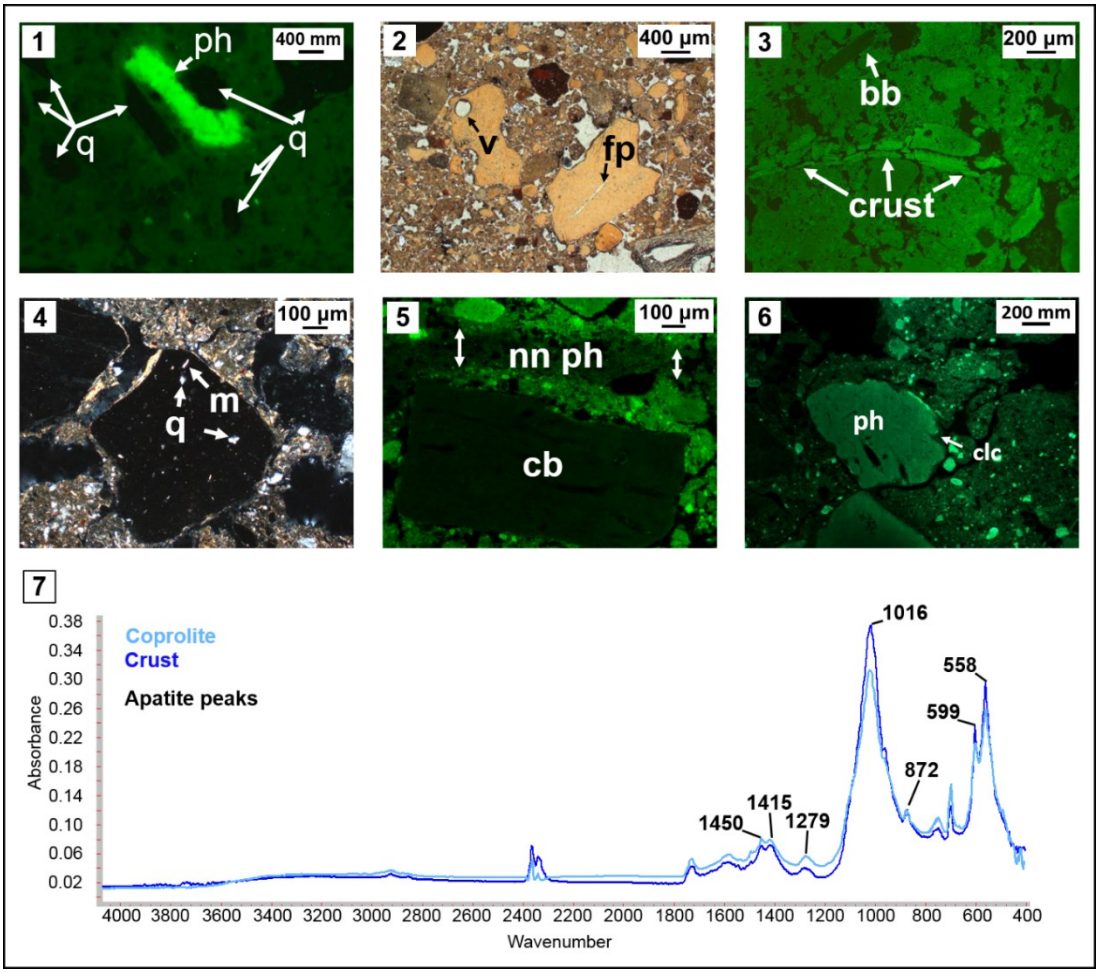

Fig. 3.3. Phosphate features from Hohlenstein-Stadel and *Vorplatz*. ***1***, photomicrograph in fluorescent light (FL) depicting one isolated phosphatic grain (**ph**) and quartz sand (**q**) embedded in the non-phosphatic groundmass of Unit M. ***2***, photomicrograph in plane polarized light (PPL) from Unit K/M showing phosphatized grains, which display vesicles (**v**) and fur pseudomorphic voids (**fp**). These voids are considered diagnostic for carnivore coprolites (Horwitz and Goldberg 1989). ***3***, photomicrograph in FL from Unit K capturing a surface defined by a phosphate crust (**ph**), which was later covered with sediment containing one burnt bone fragment (**bb**). ***4***, photomicrograph in crossed polarized light (XPL) from Unit G portraying one grain composed of silt-sized micas (**m**) and quartz (**q**), embedded in a phosphatic groundmass. Due to its composition we interpreted this type of phosphate feature as phosphatized loess. ***5***, photomicrograph in FL from Unit D4 showing a fragment of calcined bone (**cb**) embedded in phosphatic groundmass and covered with a thin lamination of less phosphatic sediment (**nn ph**). ***6***, photomicrograph in FL from Unit RT1 displaying one fragment of coprolite (**ph**) coated with clay (**clc**). We interpreted this coating as the result of rolling. ***7***, unprocessed µFTIR spectra representative of coprolite and crust fragments. Both types of phosphate features display peaks comparable with apatite minerals.

Our micromorphological observations from Unit D2 suggest that the components of this sediment might have only suffered minor diagenesis, and in particular bone fragments

appear generally fresh or well preserved. In this deposit we also noted a consistent drop in aggregates of silt and clay.

Within the overlaying Unit D4 we identified one of the rarely preserved sedimentary structures we documented in the whole Hohlenstein-Stadel sequence. This sedimentary feature is composed of a calcined bone fragment underlying a 200 µm thick lamination of decalcified and non-phosphatic reworked loess (Fig. 3.3, detail 5).

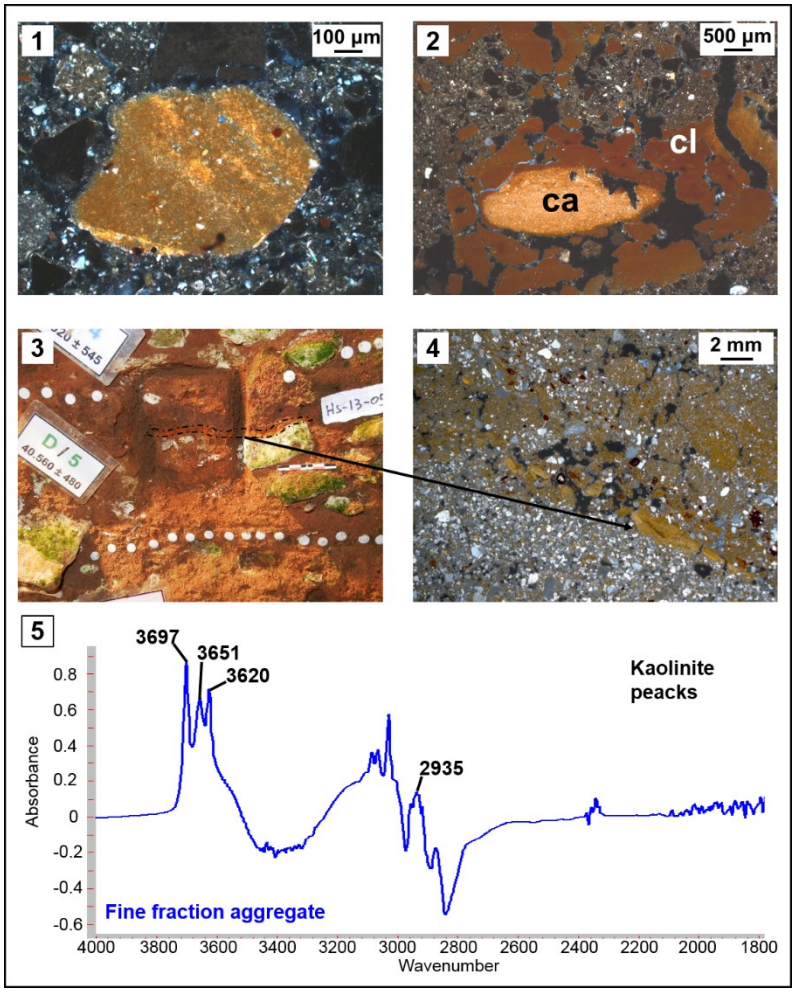

Fig. 3.4. Fine fraction aggregates from Hohlenstein-Stadel. ***1***, photomicrograph in XPL from Unit K/M depicting one aggregate of laminated clay and quartz silt, which displays striated b-fabric. ***2***, photomicrograph in XPL from Unit K showing one concentric aggregate of secondary, iron stained calcite (**ca**) and iron stained clay (**cl**) from Unit K. ***3***, large, platy aggregates of stained clay exposed in the CD profile at the back of the cave (see Fig. 3.2). ***4***, photomicrograph in XPL from Unit D of the aggregate depicted in ***detail 3***. ***5***, unprocessed µFTIR spectra representative for the fine fraction aggregates we observed at the site. The spectra presents peaks diagnostic for kaolinite minerals. Figure from Barbieri and Miller in press.

Our micromorphological results from Unit D reveal a more complex stratigraphy for this deposit. The lower portion of the thin section collected from this unit exhibits laminations of clay and sand-sized quartz, feldspar, glauconite, aggregates of silt and clay (Fig. 3.4, details 3 and 4) and very rare phosphatic grains. After the deposition, these laminations have been disturbed by a large burrow and have not been phosphatized.

Below Unit D, Unit A2 is composed of a phosphatic silty clay and displays a locally vermicular and granular microstructure. The contact with the upper Unit C appears interdigitated and with a clear transition.

Unit C presents a slight but significant increase in sand- and silt-sized calcite grains together with a decrease in coprolites, phosphatic crusts, as well as altered bone and tooth fragments. This unit is finer at the bottom and more gravelly closer to the contact with Unit Au. In Unit C we observed phosphatic crusts still associated with the limestone fragments along which they had formed. Angular elongated bone fragments display sub-horizontal orientation.

Unit Au corresponds to the lowermost Aurignacian deposit identified in the back of the Stadel cave. In comparison with the Middle Paleolithic sequence the phosphatic components of this unit are fewer in number, display a rougher, diffuse border and greater roundness. In Unit Au we have also documented a further increase in calcite content.

Unit SKS to Unit GL2A

Unit SKS corresponds to the lowermost unit we analyzed from the Middle Paleolithic sequence of the *Vorplatz*. This sediment is composed of phosphatized grains of loess, coprolite and bone fragments in a non-phosphatic reworked loess (Fig. 3.5, detail 1). Most of these components are coated with limpid clay. Unit SKS displays a platy microstructure possibly indicative of post-depositional formation of ice lenses (Fig. 3.5, detail 1). Surprisingly this represents the sole example of a frost-related features in all our samples.

Similar to Unit SKS, the overlying Unit RT1 is rich in fresh limestone gravel, coprolites, bone fragments and phosphatic grains of loess embedded in a reworked, non-phosphatic loess (Fig. 3.5, detail 6). GKS-1 represents a break in the sequence, it is composed of only rare limestone gravel and it is free of bones, coprolite, phosphatic grains and artifacts

(Jahnke 2013). In this unit we have also observed calcite hypocoatings around root voids, and fresh root remains from the modern soil are present.

Based on a few stone tools GL2A has been dated to the end of the Upper Paleolithic (Jahnke 2013) and thus it represents the youngest sediment we have covered in our analysis. In thin section it exhibits fine (largely <1cm), sorted, angular limestone gravel (*Bergkies*) in a non-decalcified reworked loess (Fig. 3.5, detail 2). As with GKS-1, in GL2A we have also found calcite hypocoatings around root voids.

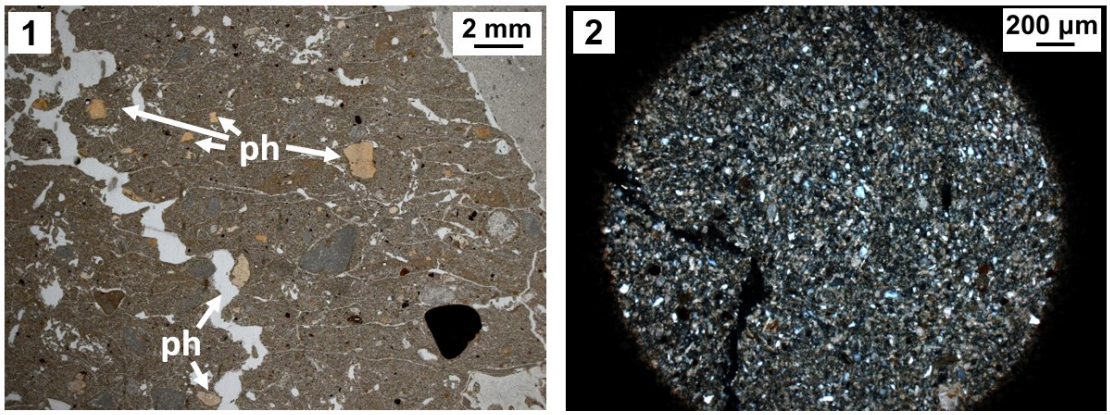

Fig. 3.5. Shift in sediment source at the *Vorplatz*. *1*, photomicrograph in PPL depicting a representative area of SKS. This unit contains reworked phosphatic grains (**ph**) and displays platy microstructure possibly indicative of post-depositional formation of ice lenses. ***2***, photomicrograph in XPL depicting a representative area of the fine fraction of GL2A, which is composed of *Bergkies* embedded in fresh, reworked loess (in the photomicrograph).

3.2.2 Results from the Lone Valley in front of Hohlenstein

In order to better understand the processes that led to the accumulation and removal of sediment from Hohlenstein-Stadel we have investigated the open-air areas surrounding this cave.

During a preliminary GPR survey and geomorphological mapping, we identified buried river channels, river bar deposits and a potential river terrace along the hillside opposite from Hohlenstein. Since this hillside appeared to be a key area for the study of the geomorphological history of the Lone Valley, we decide to investigate it with 11 GPR grids, measuring 30 x 40 m each. We collected GPR profiles with a spacing of 1 to 3 m along *x* and *y* grid axes. Thanks to this systematic survey we identified key areas that we further investigated with coring (7 in total) and EC-loggings (22. Fig. 3.6).

Part of the data we collected from the surveys we conducted in this part of the Lone Valley has been published and summarized in a dedicated article (Barbieri et al. 2018). In this section we present in more details the results of our geophysical and coring investigations (the complete description of all the geological layers is provided in Appendix III).

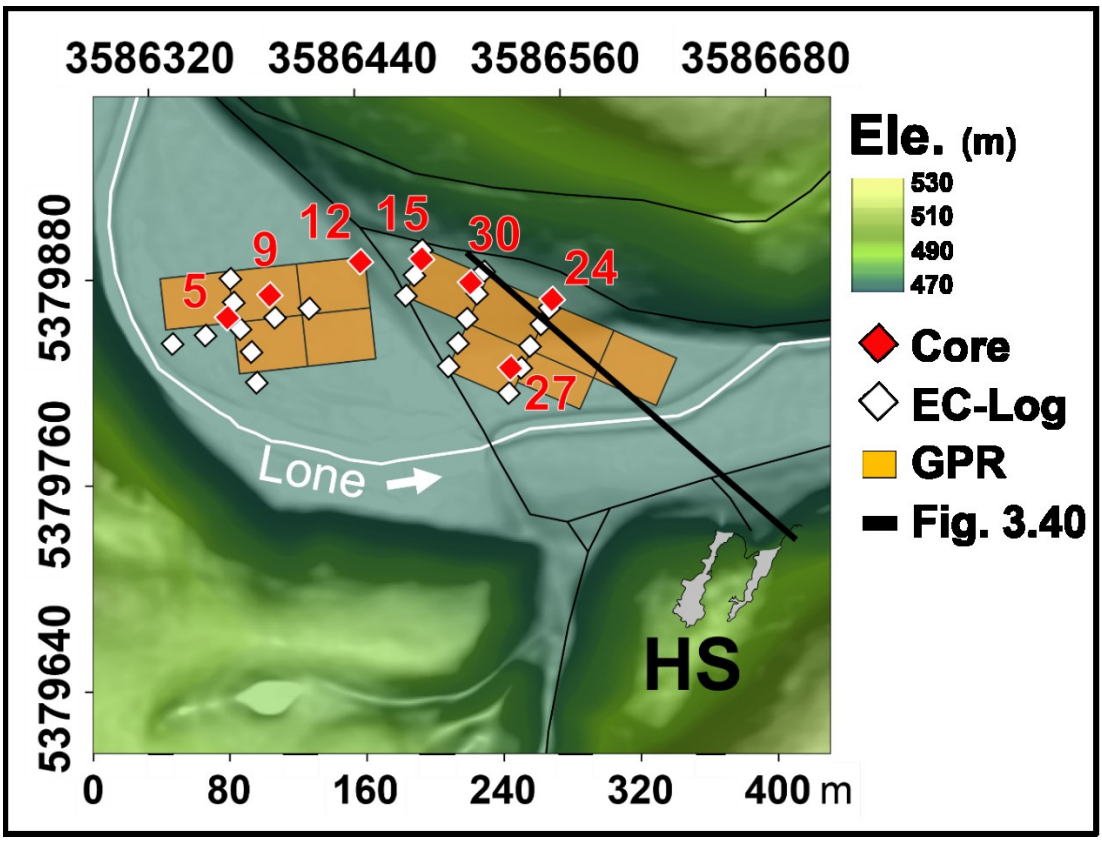

Fig. 3.6. Survey area opposite from Hohlenstein. ***HS***, Hohlenstein-Stadel; numbers and diamonds in red mark the location of the cores presented in the text; white diamonds locate the EC-loggings. GPR grids are depicted in transparent orange. The position of Fig. 3.40 is marked by the black line that crosses from North to South the valley. The map is compiled from Lidar data with 1 m resolution and it is projected in the DHDN Gauss-Krüger coordinate system (coordinates are reported along the upper and left axes). The lower axis displays distance in meters (Figure modified from Barbieri et al. 2018).

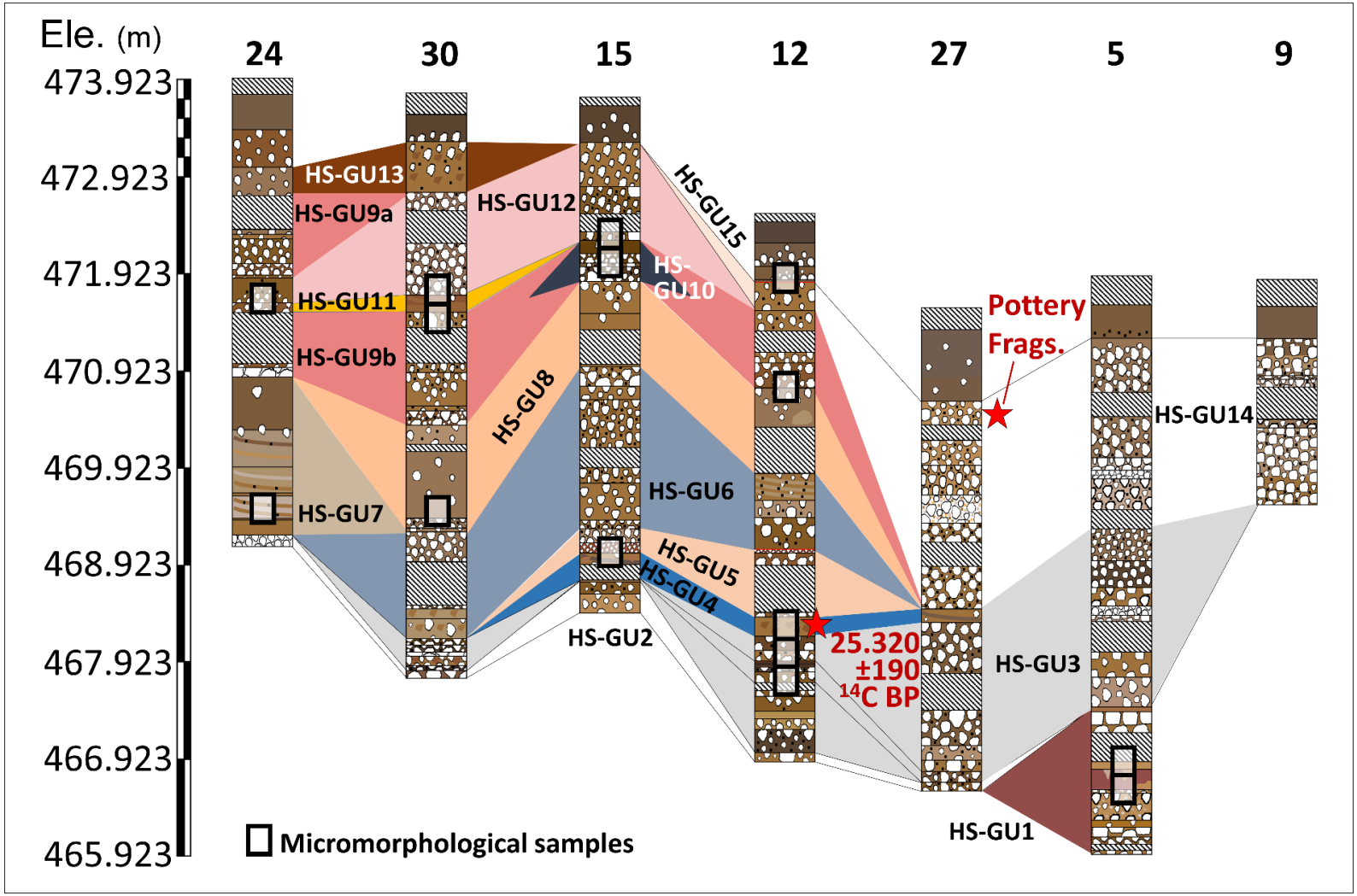

Fig. 3.7 Cross correlation of the cores collected from the area opposite from Hohlenstein. Explanation in the text. (Figure from Barbieri et al. 2018).

Depth to Bedrock

Based on the maximum depth we reached with our EC-loggings (Leven et al. 2011), we estimated that in our survey area the bedrock lies between 9.9 m to 2.8 m below the ground surface (Table 3.1). Our assessment is consistent with the results from the previous seismic survey conducted by Schneidermeier (1999) from the Hohlenstein caves down to the Lone Valley (Barbieri et al. 2018).

EC-logging	Depth (m)
1	4.7
2	2.8
3	6.6
4	6.8
6	3.6
7	4.5
8	6.2
10	6.9
11	8.5
13	9.5
14	9.9
16	6.7
17	7.9
18	8.7
19	7
20	7.5
21	7.6
22	8.1
23	7.3
25	5.6
28	7
29	7.4
31	8.2

Table 3.1. Depth to bedrock based on EC-logging data. In the left column (**EC-logging**) we have listed the name of our EC-loggings from the survey area opposite from Hohlenstein. Their location is mapped in Fig. 3.8. In the right column (**Depth**) we have listed the maximum depth reached with each EC-logging.

By converting EC-logging depth values into elevation above sea level we modelled the topography of the bedrock. The resulting surface appears asymmetric across the valley. Along the western flank the bedrock displays elevation values between 465 m to 464.5 m, while the opposite hillside appears 2 m to 3 m lower (462-461 m). In the center of the valley the bedrock displays a 100m-large depression (ca. 460 m of elevation) crossing our survey area from the northwest to the southeast (Fig 3.8).

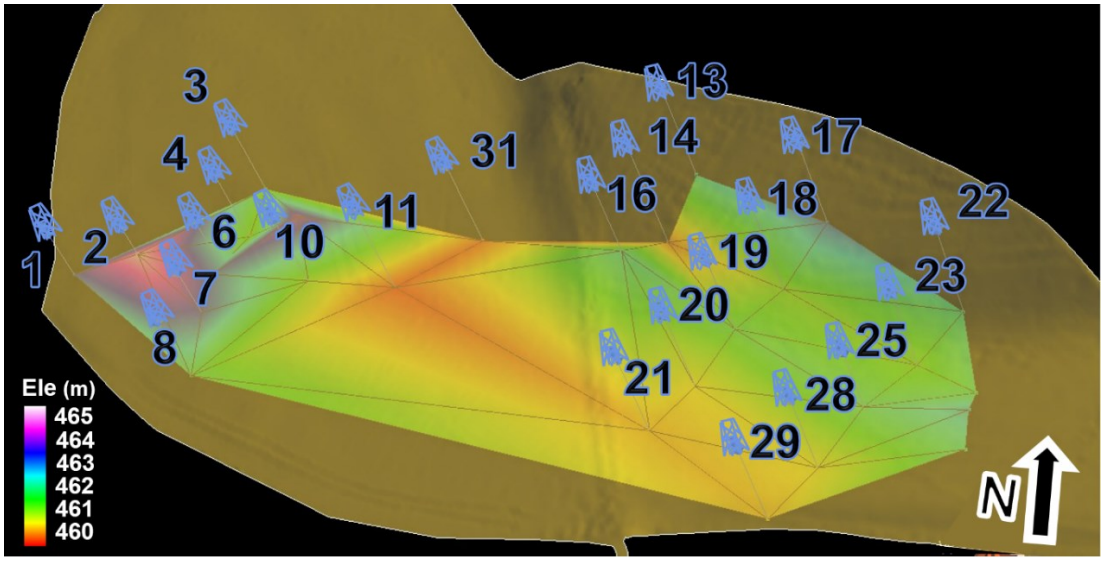

Fig. 3.8. Bedrock topography. We have reconstructed the bedrock topography based on the maximum depth reached with our EC-loggings (depicted and numbered in blue). The bedrock topography is displayed in absolute elevation values. For the depth below ground surface see Table 3.1. The modern topography is displayed in transparent orange.

HS-GU1

In HS-GU1 we grouped GL 312 through GL 322, which we recovered in the lower half of liner 4 and whole liners 5 and 6 from core 5 (Fig. 3.7). These layers are made of silty clay alternating with fine to coarse, subangular, limestone gravel. These bed types are separated by sharp contacts. GL 312 is the uppermost layer of this unit and rests at about 4.5 m below the ground surface. This layer is composed of rare, sand-sized iron-manganese nodules and rare, fine, limestone gravel embedded in a well-sorted, brown (7.5YR 5/6) silty clay matrix. Below GL 312, GL 313 is made from dry gravels and boulders. This coarse deposit covers subangular to angular, medium and fine gravel of limestone embedded in a moderately sorted silty clay (GL 314). The matrix of GL 314 appears yellowish brown (10 YR 5/6) with rare, red (7.5 R 4/6) sand-sized aggregates of silty clay. The transition to the underlying GL 315 is marked by a very sharp change in

color and composition - indeed GL 315 is mainly composed of nearly pure silty clay that is red in color (7.5R 4/6). GL 315 covers fine, medium, subrounded, limestone gravel that appears black in color, likely due to the extensive impregnation with iron-manganese oxides (GL 316). Below this layer we recovered graded, rounded to subangular, medium and fine gravel in a brownish yellow (10YR 6/6), silty clayey matrix (GL 317). The matrix of GL 317 is composed of coarse sand-sized aggregates of fine fraction which are white (10YR 8/1) and pale brown (2.5Y 7/3) in color. At the bottom of core 5, GL 318 is composed of moderately sorted yellowish brown (10 YR 5/8), silty clay with subrounded to rounded medium and fine limestone gravel (Barbieri et al. 2018).

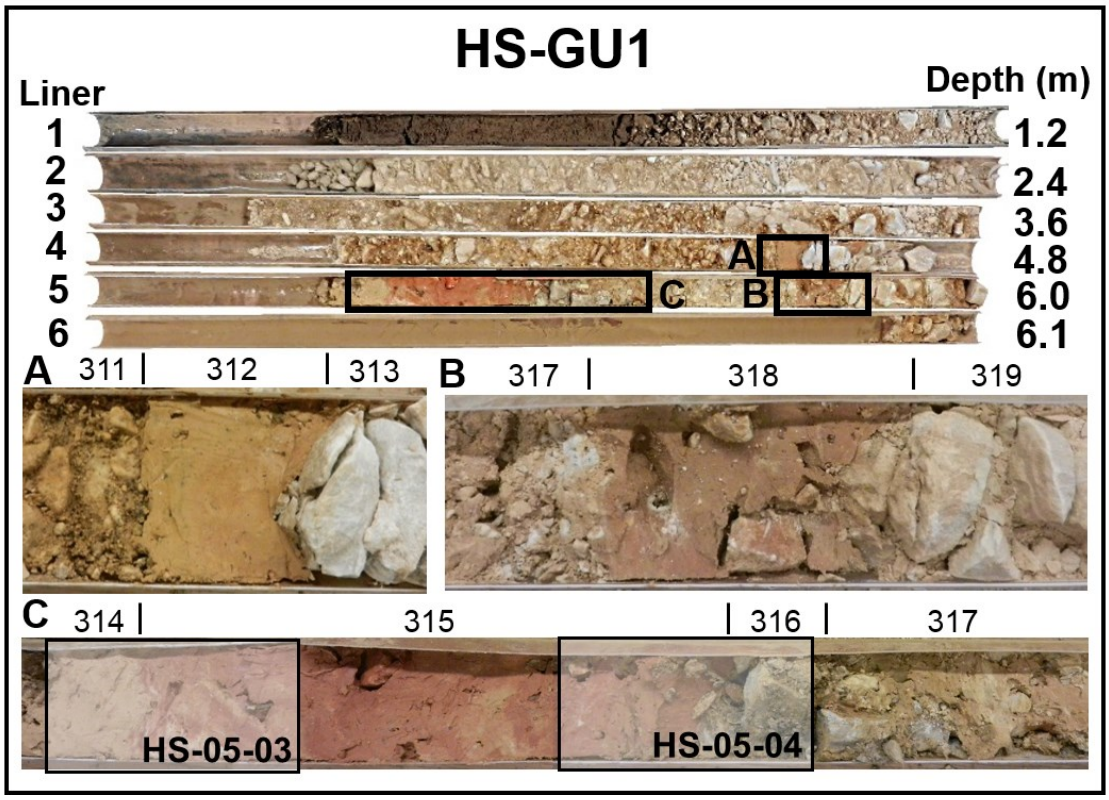

Fig. 3.9. HS-GU1. ***In the upper part***, the liners of core 5. ***In the lower part***, details from the main GL (numbered in the figure) which are discussed in the text. ***HS-05-03*** and ***HS-05-04***, indicate the location of the micromorphological samples displayed in Fig. 3.10.

Our EC-logging revealed the presence of high EC values (min 35 mS/m, max 150 mS/m) from above the bedrock. Such values are comparable with depth, thickness and grain size of GL 315 (or similar deposit) and are detectable over a surface of approximately 720 m^2. This highly conductive deposit is up to 3.5 m thick along the valley flanks, while it does not appear to be present (or preserved) in the central part of the survey area (Fig. 3.10).

Based on this evidence we hypothesize that at least part of HS-GU1 might be laterally continuous in the Lone Valley and likely lies deeper than the maximum depth we reached in most of our cores (Barbieri et al. 2018. see HS-GU2). Interestingly, the area over which we did not recover high EC values corresponds with the previously mentioned depression of the limestone bedrock (see previous section, Fig. 3.8).

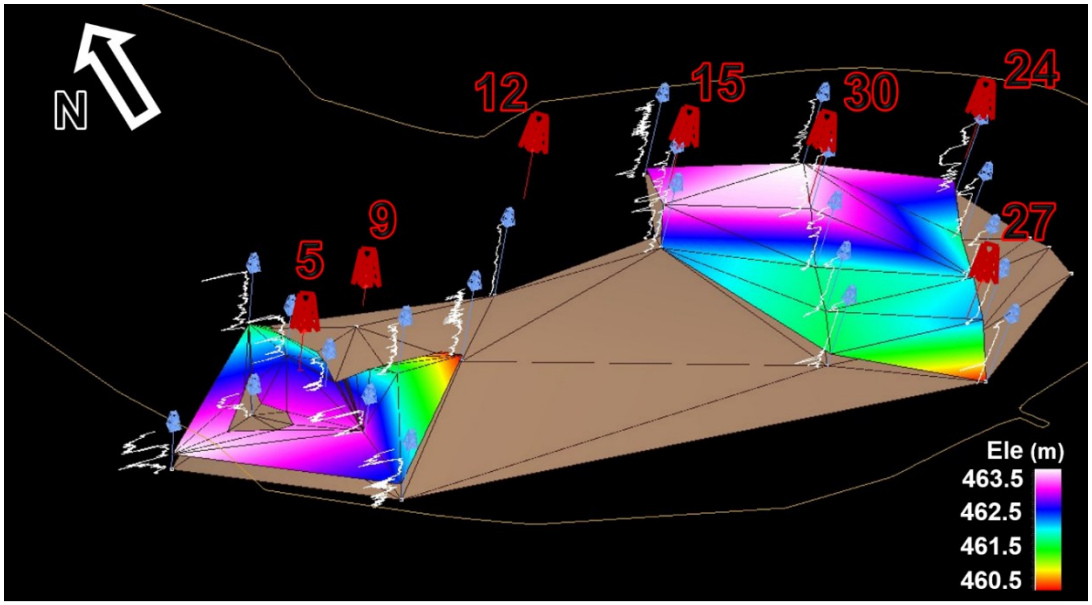

Fig. 3.10. Tentative reconstruction of HS-GU1 topography. We have reconstructed the topography of HS-GU1 basing on peaks of high electrical conductivity detected in our EC-loggings, at a depth comparable with the depth of HS-GU1 in core 5. The HS-GU1 topography is displayed in absolute elevation values. The ground surface of the survey area is marked with an orange contour line. The surface we reconstructed for the bedrock (see Fig. 3.8) is depicted in light brown. Basing on this reconstruction, HS-GU1 appears to dip towards the center of the valley, where we have also detected a depression in the bedrock (see Fig. 3.8). Cores are depicted and numbered in red, EC-logging in blue.

From HS-GU1 we have collected six block samples for micromorphological analysis, two of these samples were processed and analyzed. Specifically, we studied samples HS-05-03 and HS-05-04, which cover GL 314, 315 and 316. As presented above, GL 315 and 316 display very distinct and contrasting colors, suggesting that these deposits might have suffered intensive diagenesis.

Due to its very fine clay matrix, a large portion of GL 314 has been lost during the preparation of thin section HS-05-03 (Fig. 3.11). In comparison with the lower GL 315, GL 314 displays a less intensive staining of the clay minerals, fewer fragmented clay coatings and a higher percentage of silt-sized quartz and calcite grains. The most

significant element of continuity between GL 314 and GL 315 is represented by the calcite capping on top of gravel-sized limestone fragments (Fig. 3.11, detail 1 and 2).

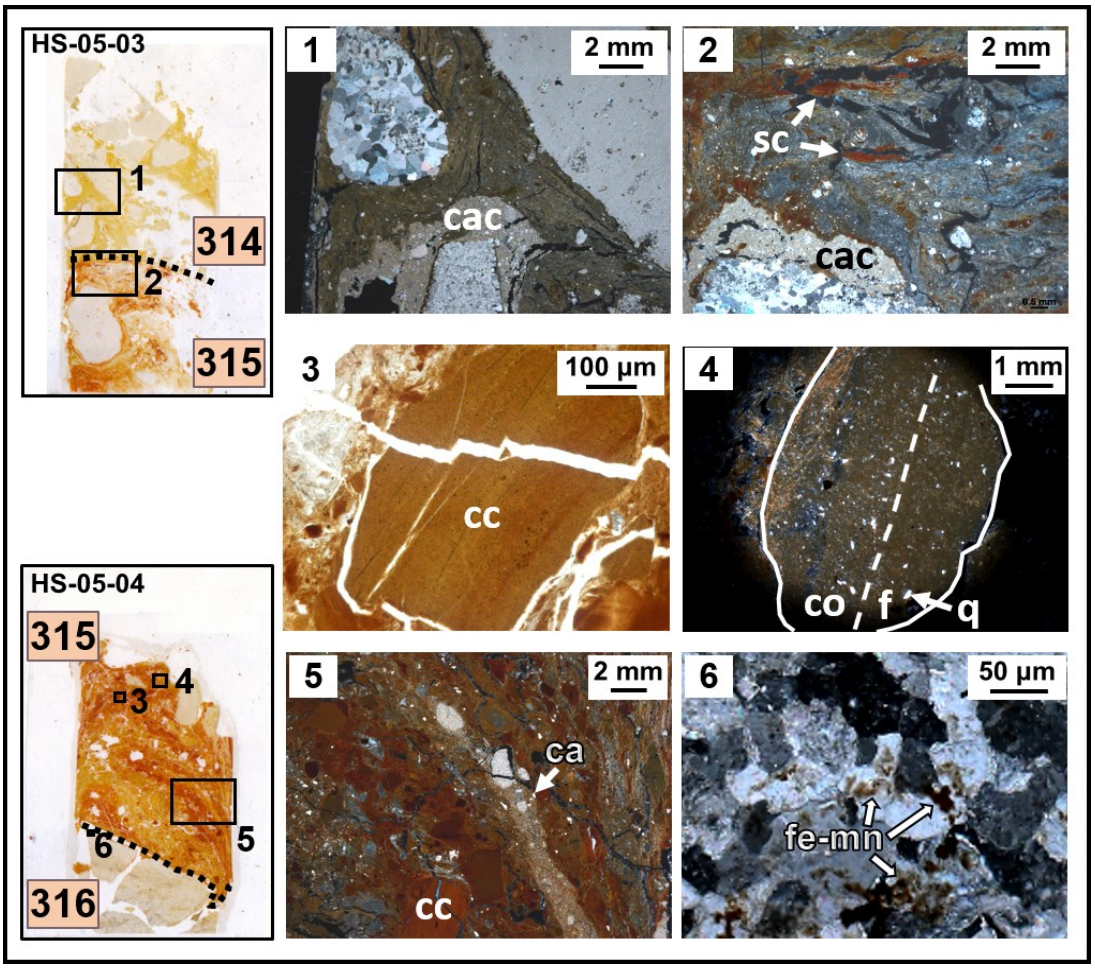

Fig. 3.11. Micromorphological features from HS-GU1. ***On the left***, thin section scans of samples HS-05-03 and HS-05-04. GL numbers are labelled in pink. ***1***, photomicrograph in XPL from GL 314 displaying coating of sand and silt-sized grains of calcite (**cac**) around weather limestone fragment. ***2***, photomicrograph in XPL from the contact area between GL 314 and GL 315. The photomicrograph depicts alternating laminations of gleyed and iron stained clay (**sc**). This photomicrographs displays also one calcite coating (**cac**) comparable to the one captured in the previous detail. ***3***, photomicrograph in PPL from GL 315 displaying a fragmented, iron stained, dusty, and laminated clay coating (**cc**). ***4***, photomicrograph in XPL from GL 315 presenting one fine fraction aggregate. Within it, clay and silt-sized grains of quartz (**q**) are organized in coarse (**co**) and fine (**f**) laminations. ***5***, photomicrograph in XPL from GL 315 displaying alternated laminations of iron stained clay coatings (**cc**) and calcite sand (**ca**). 6, photomicrograph in XPL from the limestone gravel of GL 316 portraying recrystallized calcite crystals, which contain iron and manganese oxides (**fe-mn**).

Micromorphological results from GL 315 show that this layer is largely made of clay (kaolinite accordingly to FTIR measurements) and rare silt-sized grains of calcite and quartz (Fig. 3.11, detail 3, 4 and 5). These components are often arranged in angular to

subangular, sand- to silt- sized aggregates that display speckled and granostriated b-fabric, partially hidden by the iron-manganese impregnation of the groundmass. Moreover they appear limpid and laminated, even though boundaries separating the laminae are diffuse (Fig. 3.11, detail 3). Based on these characteristics we propose interpreting these aggregates as fragments of clay coatings (Barbieri et al. 2018). Although GL 315 appears extensively oxidized, we have observed few possibly iron-depleted laminations in the contact area with GL 314 (Fig. 3.11, detail 2).

Our micromorphological study revealed that the black, carbonatic gravel from GL 316 is composed of calcite crystals displaying iron-manganese impregantions (Fig. 3.11, detail 6). Furthermore the irregular shape of the crystals and the lack of microfossils sugget that this calcite fragment may have dissolved and later recrystallized.

HS-GU2

We were able to obtain data below 6 m in our EC-logging and only in core 5; all the other cores reached refusal at this depth (Barbieri et al accepted. Fig. 3.7 and Fig. 3.12). We argue that this results from a methodological bias. As illustrated in chapter 2, we acquired EC-logging data by advancing into the ground an EC probe, which is 44.4 mm in diameter. We recovered all our cores by means of a Dual Tube Sampling System DT325, which requires the use of probe rods with an external diameter of 88.9 mm. During a preliminary attempt to recover core 5, with the 88.9 mm probe rods we encountered refusal at ca. 2.4 m below the ground (after two liners). Shallow refusal appeared unexpectedly in core 5 considering that we drilled the nearby EC-logging (number 4) down to a depth of 6.8 m (Table 3.1 and Fig. 3.8). Therefore, we decided to continue drilling core 5 with a different method (Macro Core MC5 system) which cannot exclude the possibility of sample mixing but takes advantage of much thinner probe rods (57.1 mm). With this method we succeeded in drilling core 5 down to a depth of 6.2 m, which is consistent with the depth of the nearby EC-logging number 4.

We conclude that the diameter of the rods employed for the drilling impacted the maximum depth we could reach with our probing machine.

Based on this evidence and our EC-logging data, we hypothesize that we could not reach HS-GU1 in most of our cores because it is covered with sediments rich in coarser rock fragments (cobbles and boulders). We designate this hypothetical unit as HS-GU2. We

assigned the lowermost layers we recovered from core 27, 12, 15, 24 and 30 to this unit since they are quite rich (30% to 90%) in coarse fraction.

The sediments that rest on top of HS-GU1 in core 5, and above HS-GU2, in cores 12 and 30, display a gradually darker matrix color and increasing Bohnerz content. Based on these characteristics we have interpreted these layers (GL 13-14, GL 43-46) as a diffuse transition towards the overlying HS-GU3 deposits.

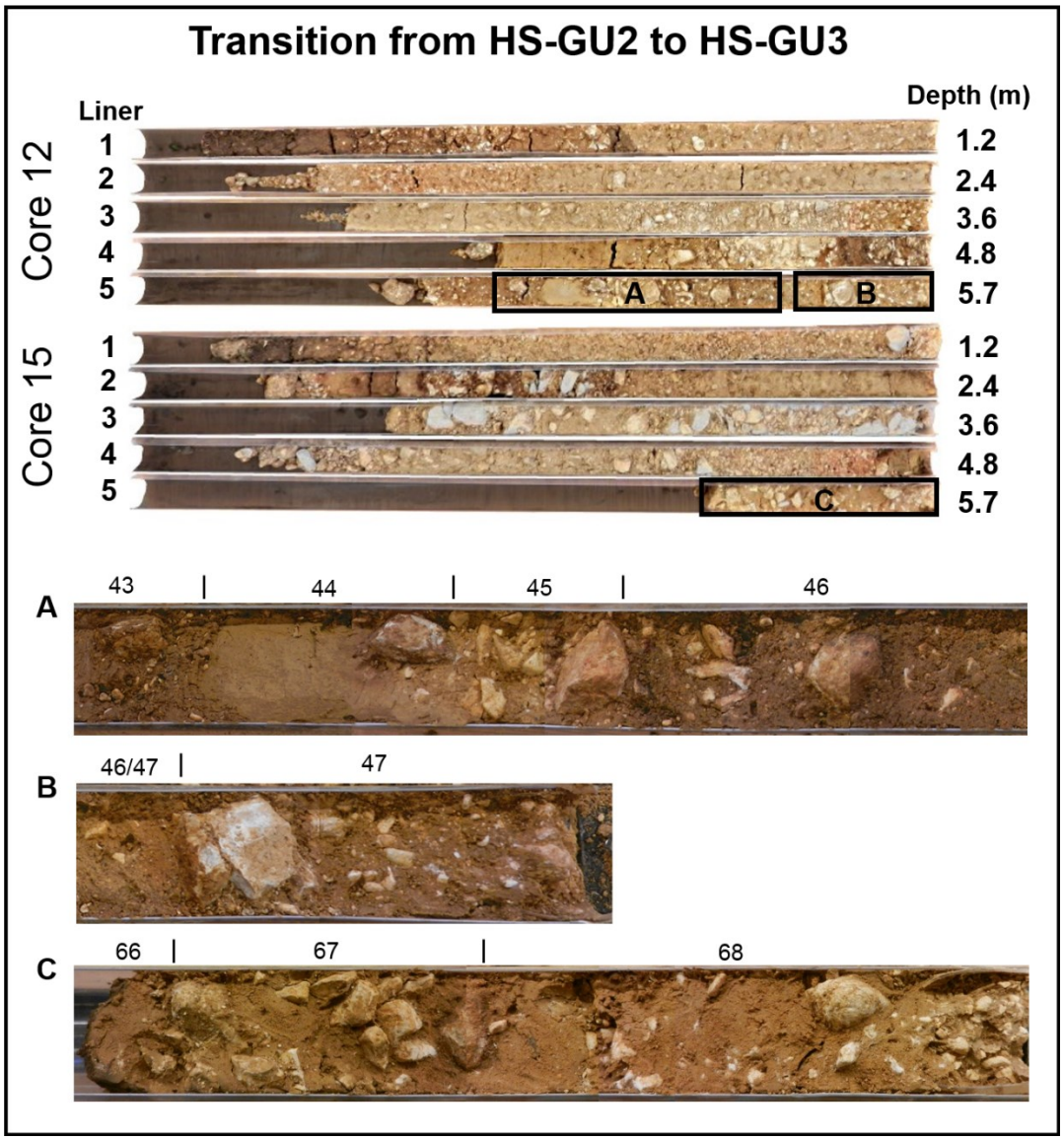

Fig. 3.12. Transition from HS-GU2 to HS-GU3. ***In the upper part***, the liners of cores 12 and 15. ***In the lower part***, details from the main GL (numbered in the figure) which are discussed in the text.

HS-GU3

The sediments we recovered from the bottom of cores 12, 27, 30, and possibly 5 display a very distinctive dark brown matrix color and are composed of quartz, calcite, limestone and Bohnerz fragments (Fig. 3.7 and Fig. 3.13. Barbieri et al. 2018).

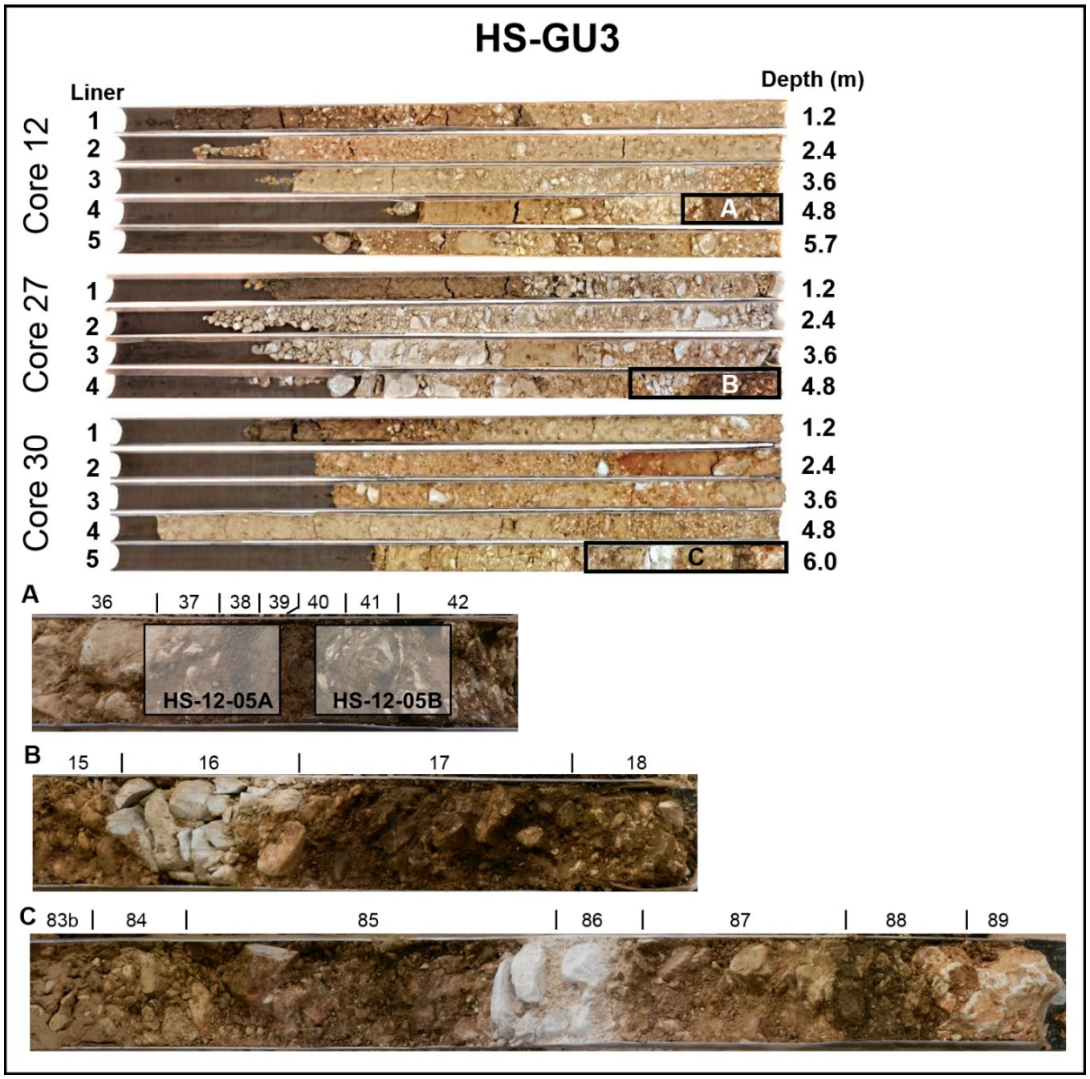

Fig. 3.13. HS-GU3. ***In the upper part***, the liners of cores 12, 27 and 30. ***In the lower part***, details from the main GL (numbered in the figure) which are discussed in the text. ***HS-12-05A*** and ***HS-12-05B***, indicate the location of the micromorphological samples displayed in Fig. 3.15.

In core 12, between 5.17 m and 5.60 m below the ground surface, we recovered the sequence of GL 37-42 (Fig. 3.7 and Fig. 3.13). GL 35-36 are mainly composed of fine to medium, angular limestone gravel in a silty, clay matrix. GL 37 and GL 41-42 are laminated and composed of subrounded fine- to medium-gravel-sized fragments of

limestone, Bohnerz and quartz that are embedded in dark brown sand and silt. These deposits alternate with the layers GL 38-40, which display similar composition but are gravel-free (Barbieri et al. 2018).

GL 85-88 are found in core 30, between 5.7 m and 6 m below the ground surface (Fig. 3.7 and Fig. 3.13). GL 85, 87 and 88 are made from subangular to subrounded limestone gravel and Bohnerz embedded in a dark brown (10 YR 3/3) to very dark brown (10YR 2/2), silty sandy matrix. GL 86 is nearly free from fine fraction and rich in coarse gravel-sized and possibly pebble-sized limestone fragments.

In core 27, between 3 m and 4.79 m below the ground surface, we recovered the sequence of GL 14-17 (Fig. 3.7). These layers are made from medium and fine, rounded to angular limestone gravel embedded in a dark brown silty, sandy matrix.

The deposit contained in the third and fourth liner of core 5 (GL 305-311) also display darker brown colors and could be regarded as part of this unit.

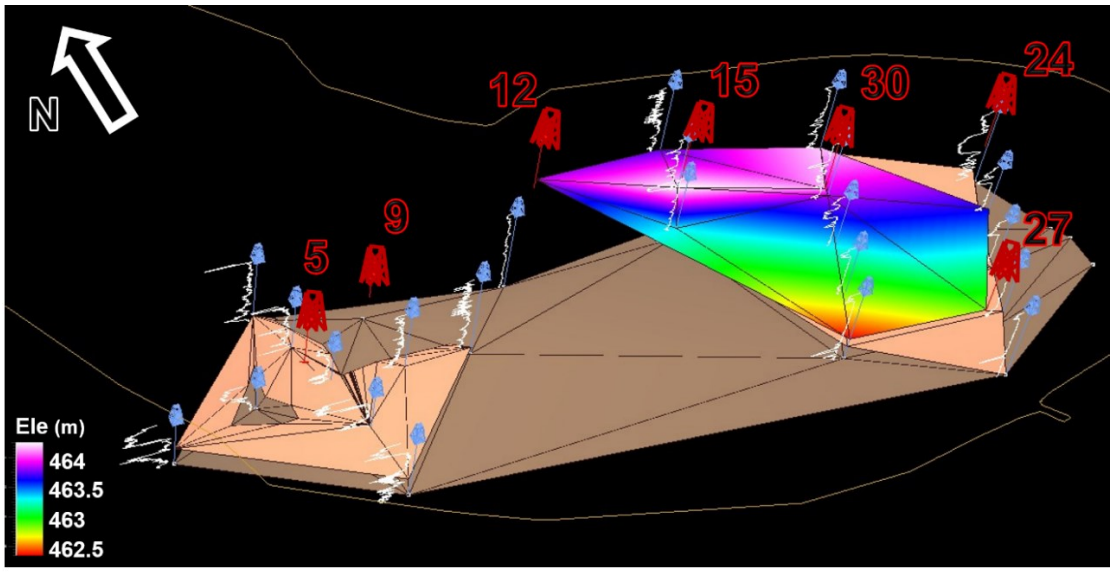

Fig. 3.14. Tentative reconstruction of HS-GU3 topography. We have reconstructed the topography of HS-GU1 basing on our data from core 12, 27 and 30. In order to produce a surface with slightly higher resolution we have insert few points basing on EC-logging data comparable with depth and lithology of HS-GU3. The HS-GU3 topography is displayed in absolute elevation values. The ground surface of the survey area is marked with an orange contour line. The surface we reconstructed for the bedrock (see Fig. 3.8) and HS-GU1 (see Fig. 3.10) are respectively depicted in light brown and pink. Cores are depicted and numbered in red, EC-logging in blue.

By combining coring and EC-logging data we could reconstruct a coarse topography for HS-GU3, which appears to dip gently (ca. 1.2°) from the north hillside towards the center of the floodplain (Fig. 3.14).

From the HS-GU3 deposits of cores 5, 12, 15, 27 we collected block samples for micromorphological analysis. We processed the sample HS-12-04 and HS-15-05 from core 12, since they were richer in fine fraction and thus more suitable for micromorphological study.

From sample HS-15-05 we produced two thin sections, HS-15-05A and HS-15-05B. Our micromorphological results from these thin sections show that GL 37-42 are largely composed of silt- and sand-sized grains of quartz, Bohnerz, iron nodules, calcite, chalcedony and chert. Furthermore we have observed fragments of laminated, limpid clay coatings impregnated with iron-manganese oxides. In comparison with HS-GU1, these fragmented coatings present more distinct laminae. Weathered limestone gravels are also present in HS-GU3. Based on the grain-size distribution, the GL 37-42 sequence can be further divided into a number of subunits (Fig. 3. 15), which are briefly summarized in the following paragraphs.

The uppermost GL 36 is composed of unsorted and rounded to subrounded limestone gravel embedded in a silty clay matrix. This layer is quite rich in secondary calcite. Number and sizing of gravel decrease from GL 37 down to GL 38. Both these units present a comparable composition, with numerous coarse sand-sized grains of quartz, Bohnerz, chert, anorthic iron-manganese nodules, fragmented clay coatings and very rare silt and sand-sized calcite crystals. In these sediments we observed rare orthic iron-manganese nodules (Fig. 3.15, detail 1). GL 39 displays better grading, more intensive staining of the clays, frequent glauconite grains and a more pronounced granostriated b-fabric (Fig. 3.15, detail 1). From a granulometric point of view in GL 40 we have distinguished a coarser (GL 40b) and a finer subunit (GL 40a), neither of them presenting remarkable compositional differences in comparison with the lower GL 41.

We have divided GL 41 into GL 41a, 41b and 41c. The first and the second present a composition comparable respectively with to GL 37 and 38, while GL 41c is represented by a 2 to 5 mm thick layer of sand- and silt-sized grains of weathered calcite impregnated with iron-manganese oxides. Sediment similar to GL 41c is discontinuously present on

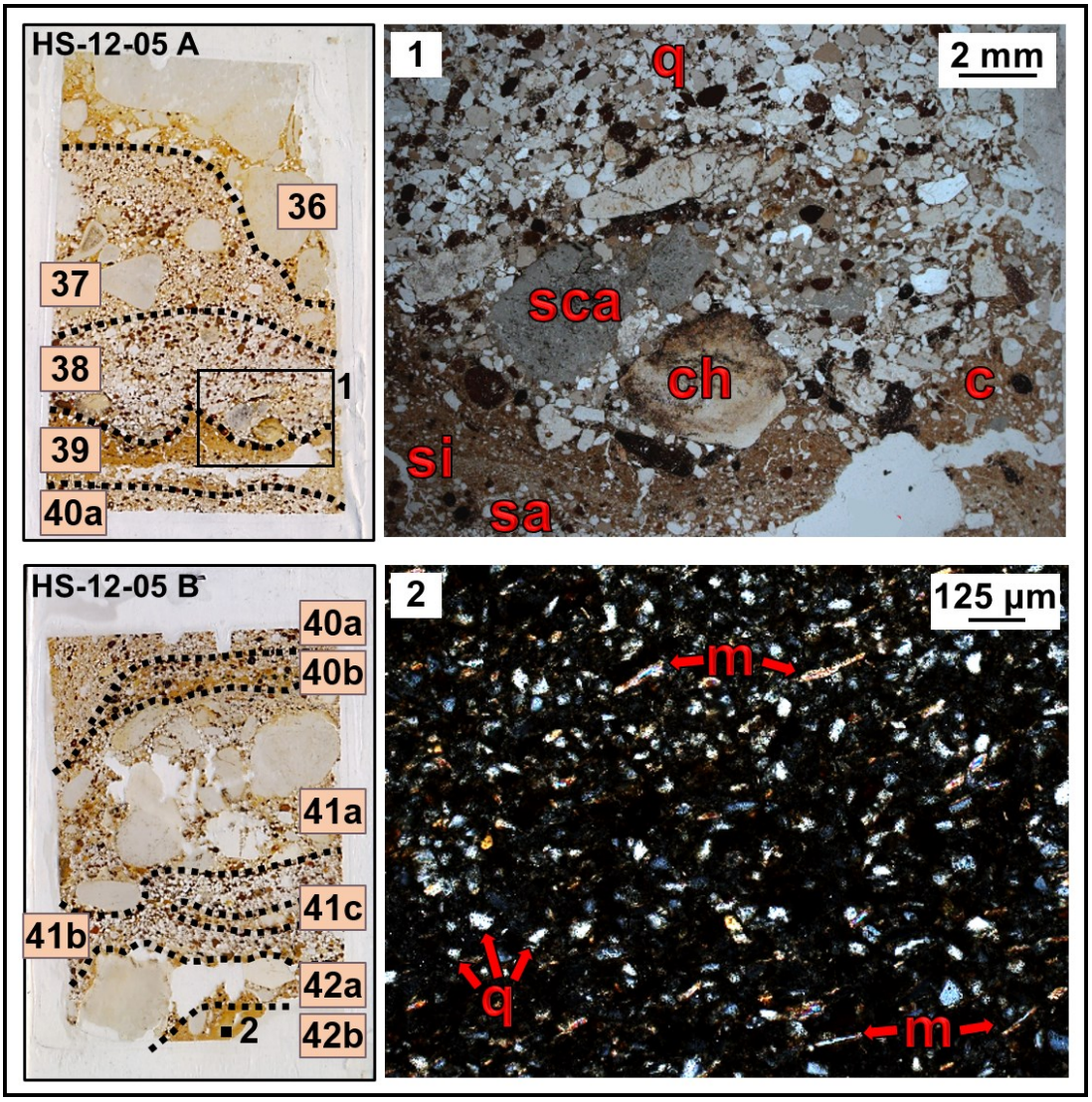

Fig. 3.15. The laminated bedding of HS-GU3 in core 12. ***On the left***, thin section scans of samples HS-12-05 A and HS-12-05 B. GL numbers are labelled in pink. ***1***, photomicrograph in PPL from the contact between GL 38 and GL 39 within HS-GU3. In the upper part GL 38 is largely composed of well sorted, subrounded to subangular medium sand of quartz (**q**) and gravel of chert (**ch**). In this unit there are also concentration of secondary calcite (**sca**). GL 39 is captured in the lower part of this photomicrograph. This sediment appears finer than GL 38 and is formed from laminations of clay (**c**), silt (**si**), and sand (**sa**). ***2***, photomicrograph in XPL from GL 42b, which is mainly composed of silt-sized grains of quartz (**q**) and micas (**m**).

top of GL 41a. The underlying GL 42a is unsorted, coarser, richer in orthic iron-manganese nodules and largely composed of weathered limestone gravel. The fine fraction is composed of quartz, Bohnerz, chalcedony and chert sand. The lowermost GL 42b is made of well sorted, silt-sized grains of quartz, micas and rare calcite with only a few sand-sized grains of quartz (Fig. 3.15, detail 2). The finer fraction is composed of

clay that is locally impregnated with iron-manganese oxides. This sediment appears massive with mica fragments occasionally horizontally oriented.

We collected HS-12-04 from the contact between HS-GU3 and HS-GU4. The lower portion of the thin section is occupied by GL 35, which is part of HS-GU3 (Fig. 3.17). This layer presents the typical composition of this unit, being quite rich in sand and gravel from chert, chalcedony, Bohnerz, fragmented limpid clay coatings and very weathered limestone fragments. The passage to GL 34 (HS-GU4) is quite sharp and presents an unusual shape, which is probably an artefact resulting from the coring.

HS-GU4

In core 12, 15 and 27 the coarser HS-GU3 is covered with GL 34, GL 65, and GL 13 (Fig. 3.7 and Fig. 3.16). These sediments are mostly composed of fine fraction (90-95%), which is made from yellowish brown (10 YR 5/6) silty clay and medium to coarse-sand-sized red silty aggregates (5YR 5/6. Barbieri et al. 2018). The remaining 5-10% of these layers is composed of subangular to rounded fine and medium limestone gravel.

Radiocarbon measurements performed on a mixed sample of these aggregates from GL 34 have yielded an age of 25.320 ± 190 ^{14}C BP (ID 19 in table 2.1 and Table 3.2).

ID	δ^{13}C (± 0.1‰)	^{14}C age		Calibrate age 95%	
		(^{14}C BP)	±	(BC/AD)	(BP)
19	-25.7	25320	190	27991 – 26918 BC	29940 – 28867

Table 3.2 Radiocarbon determination of ID 19 (HS-GU4). In this table we present the results of the radiocarbon determination performed on ID 19 (the ID used by the laboratory in Tucson is reported in Table 2.1). The table includes ***δ^{13}C (± 0.1‰)***, the estimated radiocarbon age (***^{14}C age***, ***^{14}C BP***) and its uncertainty (±). We also present the corresponding calendar years Before/After Christ (***BC/AD***) and Before Present (***BP***), which we obtained performing a 2σ calibration with the program OxCal 4.3 (curve IntCal 13).

We have studied with micromorphology two of the three blocks collected from HS-GU4, namely the samples HS-12-04 from core 12 and HS-15-06B from core 15. With this analysis we aimed at verifying the correlation we proposed between these two cores, investigating the lower and upper contacts of HS-GU4, and studying the material we have used for ^{14}C dating.

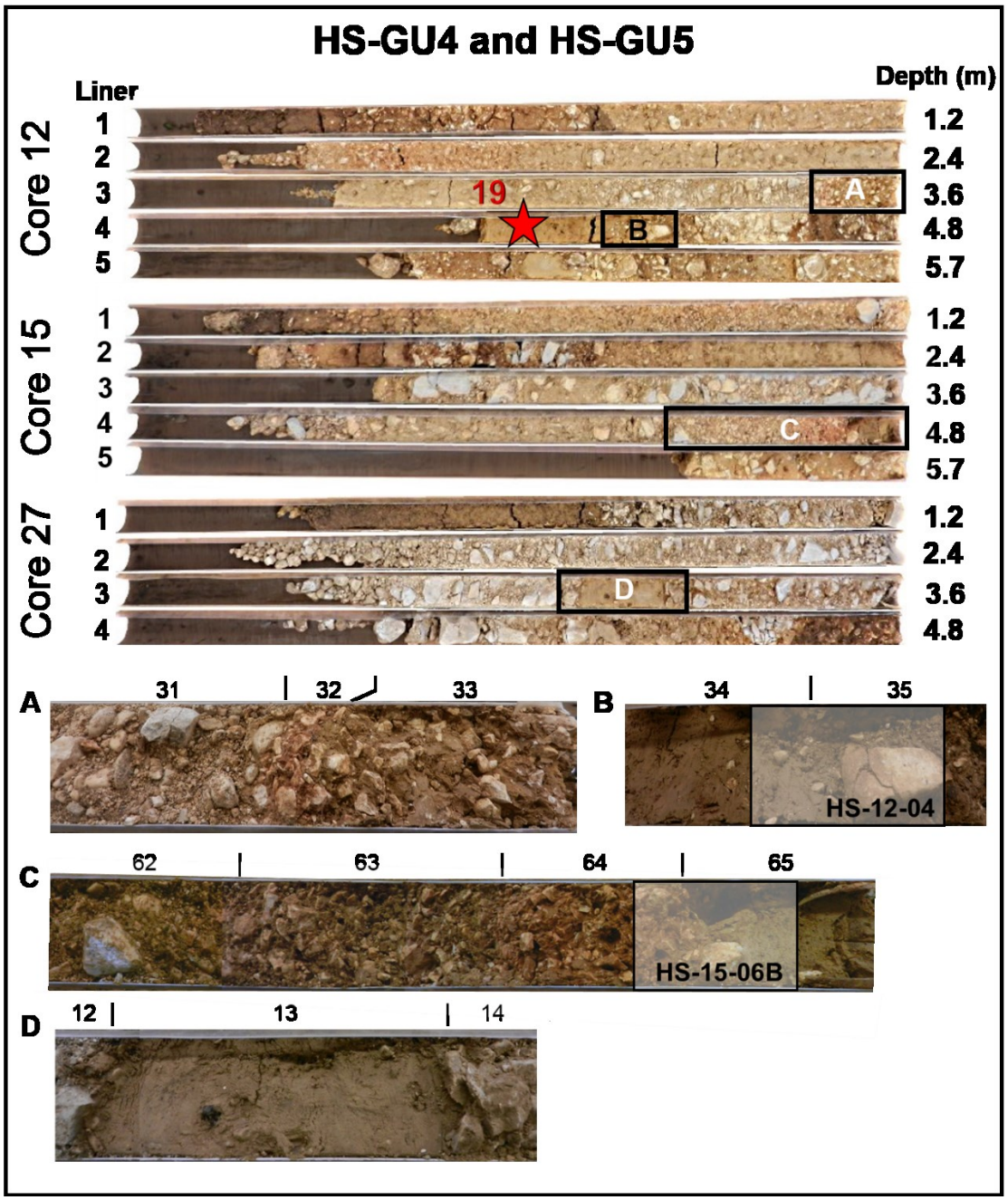

Fig. 3.16. HS-GU4 and HS-GU5. ***In the upper part***, the liners of cores 12, 15 and 27. ***In the lower part***, details from the main GL (numbered in the figure) which are discussed in the text. ***HS-12-04*** and ***HS-15-06B***, indicate the location of the thin sections displayed in Fig. 3.17 and 3.18. The red star locate the dating sample (ID **19**) discussed in the main text.

HS-GU4 deposits are contained in the upper part of sample HS-12-04 (GL 34) and the lower portion of HS-15-06B (GL 65). The fine fraction (<200 μm) of both layers is largely made from loess-like components (silt of calcite, quartz and micas) and rare secondary calcite. The coarser fraction is made of well-rounded quartz sand, sand-sized grains of calcite, typic disorthic iron-manganese nodules, fragmented limpid and laminated clay

coatings (smaller than 300µm) and limestone gravel. Additionally we observed a significant amount of medium to coarse-sand-sized aggregates which display composition (reworked loess) and texture (silt – clay) comparable with the groundmass in which they are embedded. These aggregates are made of smaller angular peds separated by star-shaped vughs which have been infilled with iron-manganese oxides (Fig. 3.17, detail 2). Occasionally these smaller peds present also pressure faces (Kühn et al. 2010). We suggest that these impregnated aggregates correspond to the material we have dated with ^{14}C.

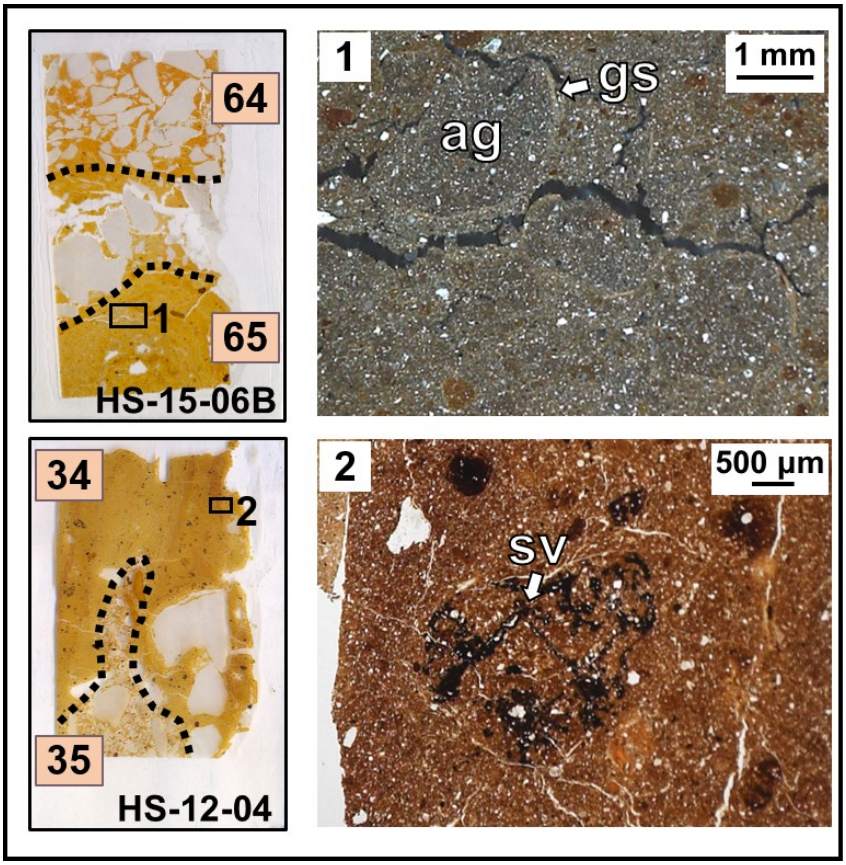

Fig. 3.17. Reworked aggregates from HS-GU4. ***On the left***, thin section scans of samples HS-15-06 B and HS-12-04. GL numbers are labelled in pink. ***1***, photomicrograph in XPL from GL 65 displaying sorted, coarse sand-sized, rounded fine fraction aggregates (**ag**) displaying granostriated b-fabric (**gs**). Such aggregates are comparable with the cryogenic microfabrics described by Huijzer (1993) and Van Vliet-Lanoë (2010). ***2***, photomicrograph in PPL from GL 34 showing fine fraction aggregates, which are composed of smaller angular peds separated by star-shaped vughs (**sv**) which have been infilled with iron-manganese oxides

The components of GL 34 and GL 65 often appear organized in numerous sorted, coarse sand-sized, rounded aggregates displaying granostriated b-fabric (Fig. 3.17, detail1). Additionally, close to the upper contact with HS-GU5, the HS-GU4 sediments are

organized in laminations displaying graded bedding and variable degree of groundmass oxidation. In thin section HS-15-06B the passage to the higher HS-GU5 is more gradual and marked by an increase in gravel content. In this contact area composition, fine fraction laminations and granostriated b-fabric are still very similar to those we have described for HS-GU4.

HS-GU5

In HS-GU5 we grouped GL 32-33 from core 12 and GL 63-64 from core 15 (Fig. 3.7 and Fig. 3.16). GL 33 is made from angular to rounded, well-sorted, fine (<1cm), limestone gravel. In GL 32 we distinguished three 1 cm-thick laminations, which alternate in a "sandwich-like" structure. The upper and lower laminations are composed of a yellowish brown silty clay matrix with rounded medium gravel, up to 2 cm in size. The central lamination differs in regards to the matrix color, which is strong brown (7.5YR 4/6), the smaller sizing (<1cm) and higher angularity of the limestone gravel (Barbieri et al. 2018).

In core 15 GL 64 occupies the lower portion of HS-GU5. This layer presents matrix color, angularity and size of the limestone gravel comparable to GL 32. The upper GL 63 is very rich (95%) in fine to medium, angular limestone gravel embedded in Bohnerz sand and little clay, which appears yellowish brown in the lower part (10 YR 5/4) and more reddish in the upper part (7.5 YR 5/4. Barbieri et al. 2018).

We analyzed HS-GU5 with thin section HS-15-06B, collected at the contact between GL 64 and GL 65 in core 15. In the previous section we have presented the data concerning GL 65, and in the following paragraphs we have summarized the main result for GL 64.

Our micromorphological analysis shows that GL 64 is largely composed of weathered limestone fragments that display irregular and diffuse border and are coated with secondary calcite. More occasionally we observed fresh (Fig. 3.18, detail 2) limestone fragment in which microfossils are still recognizable. The fine fraction of this layer is formed of loess-like components, sand-sized grains of quartz, sand-sized grains of calcite, typic disorthic iron-manganese nodules and fragments of limpid and laminated clay coatings. Furthermore we observed well-rounded aggregates composed of sand-sized calcite fragments coated with alternating iron stained clay and silt (Fig. 3.18, detail 1 and 2). Similar features have been reported from Pleniglacial deposit in England ("snowball",

Rose et al. 2000) and in various solifluction/gelifluction deposits across Europe (Huijzer 1993, Bertran and Texier 1999, Van Vliet-Lanoë 2010).

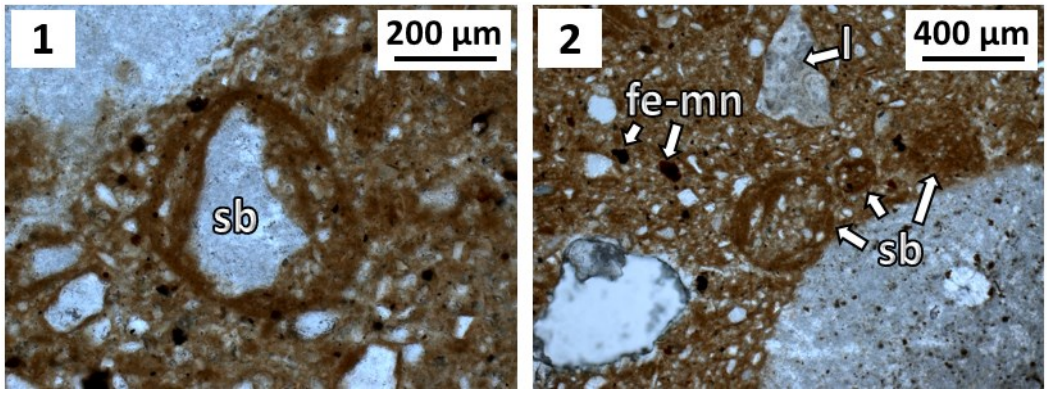

Fig. 3.18. Examples of "snowballs" from GL 64 (HS-GU5). ***1***, photomicrograph in PPL showing one sand-sized grain of calcite coated with alternating iron stained clay and silt. This feature is comparable with the snowball features (**sb**) described by Rose (et al. 2000) and additional micromorphological features reported from various solifluction/gelifluction deposits (Huijzer 1993, Bertran and Texier 1999, Van Vliet-Lanoë 2010). ***2***, photomicrograph in PPL displaying further examples of the same feature (**sb**), fresh limestone fragments (**l**) and typic disorthic iron-manganese nodules (**fe-mn**).

HS-GU6

HS-GU6 is composed of layers coming from cores 12, 15 and 30 that are present at comparable depth and are rich in fine to coarse, well-rounded, polished limestone gravel (Fig. 3.7 and Fig. 3.19). Despite these similarities these layers differ in sizing and roundness of the limestone gravel. GL 58-62 from core 15 are composed of unsorted gravel, with the finer-sized fragments displaying higher roundness. GL 29-31 from core 12 reveal an opposing trend in roundness, with the fine-sized gravel more angular than the medium-sized one. Additionally GL 29-31 are free from coarse gravel. The matrix of GL 58-62 and GL 29-31 is silty sandy and yellowish brown (10 YR 5/6 to 4/6. Barbieri et al. 2018).

Although we assigned this layer to HS-GU6, GL 83 from core 30 displays quite different characteristics. This layer is much richer in fine fraction, which is composed of yellow (2.5Y 6/4) silt and clay. In the matrix of this layer we have also observed yellowish red (5YR 5/6) mottles. Based on its gravel content, within this layer we distinguished an upper GL 83a, which is nearly free of gravel, and a lower GL 83b, which is composed of rare (20%), subrounded and angular limestone gravel (Barbieri et al. 2018).

Given the general high content of gravel we decided not to analyze the micromorphological blocks collected from this unit.

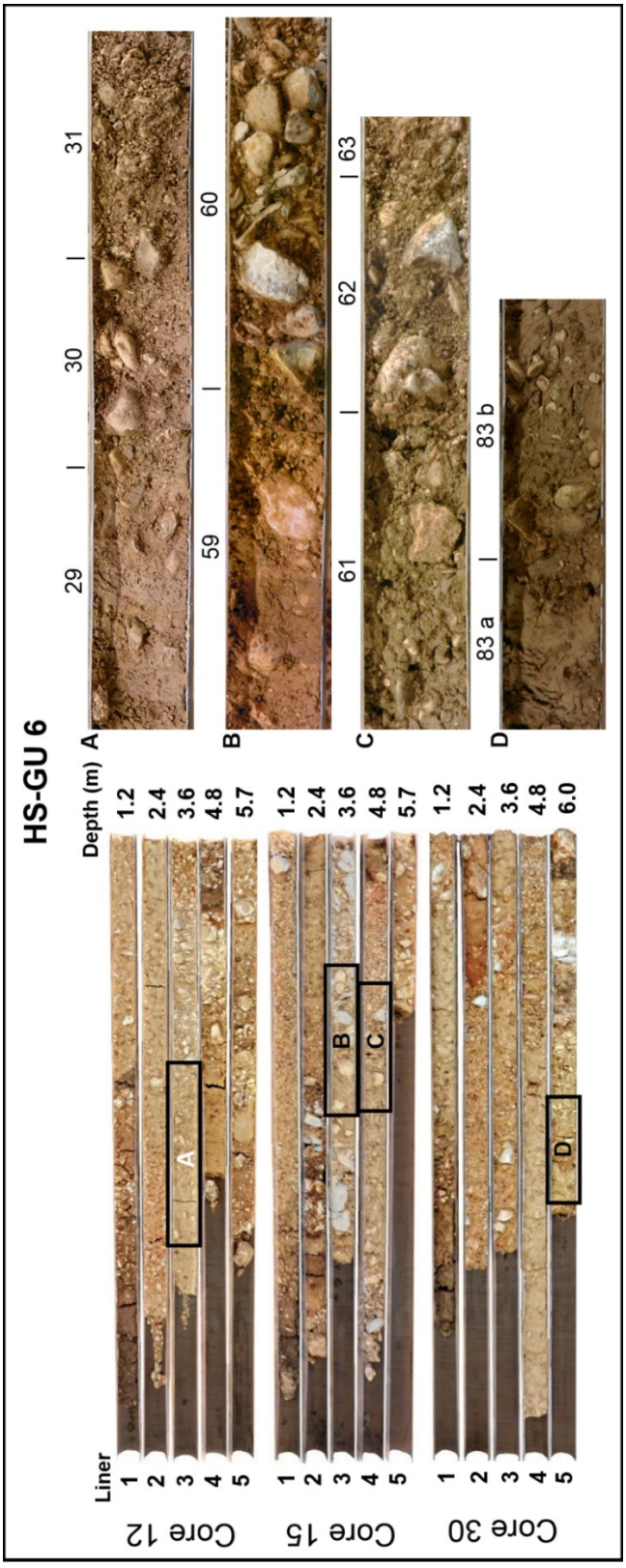

Fig. 3.19. HS-GU6. ***On the left***, the liners of cores 12, 15 and 30. ***On the right***, details from the main GL (numbered in the figure) which are discussed in the text.

HS-GU7

HS-GU7 corresponds to the sediments (GL 100-107) we recovered in the last two liners of Core 24, which are composed of laminated silts and sands (the latter comprising calcite and Bohnerz) with a variable clay and gravel content. GL 100 and the upper part of GL 101 are dark yellowish brown (10YR 4/4) and light yellowish brown (2.5Y 6/4 and 6/3) silt. These sediments display some reddish laminations, which do not display evident grading. The lower portion of GL 101 and all of GL 102 are composed of yellowish brown (2.5Y 6/3) and light gray (2.5Y 7/2) silt alternating with brown (7.5YR 4/4) or brownish yellow (10YR 6/6) clayey silt laminations. Meanwhile the layers below GL 103-107 are mainly composed of yellowish brown (10 YR 5/6) clayey silt and display a variable amount of dark mottles, likely resulting from the presence of iron-manganese oxides (Barbieri et al. 2018).

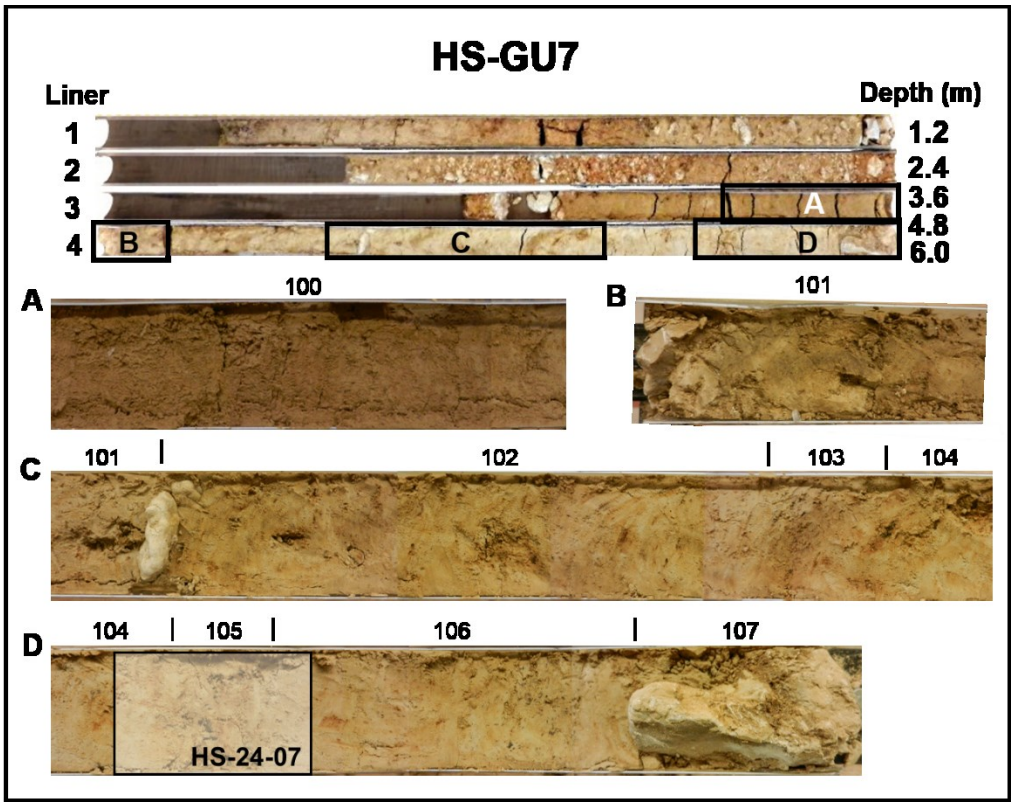

Fig. 3.20. HS-GU7. ***In the upper part***, the liners of core 24. ***In the lower part***, details from the main GL (numbered in the figure) which are discussed in the text. ***HS-24-07*** indicates the location of the thin section displayed in Fig. 3. 22.

With the EC-logging 22 that we collected nearby core 24 we measured very high conductivity values (50-80 mS/m) between 2.5 and 4.5 m below the ground surface. Such depth and conductivity values are comparable with the grain size and depth of HS-GU7. Interestingly none of the other EC-loggings we collected in the surveyed area present similar values, suggesting that HS-GU7 probably has been accumulated or preserved only in a localized "trap" such as a depression or a channel (Fig. 3.21).

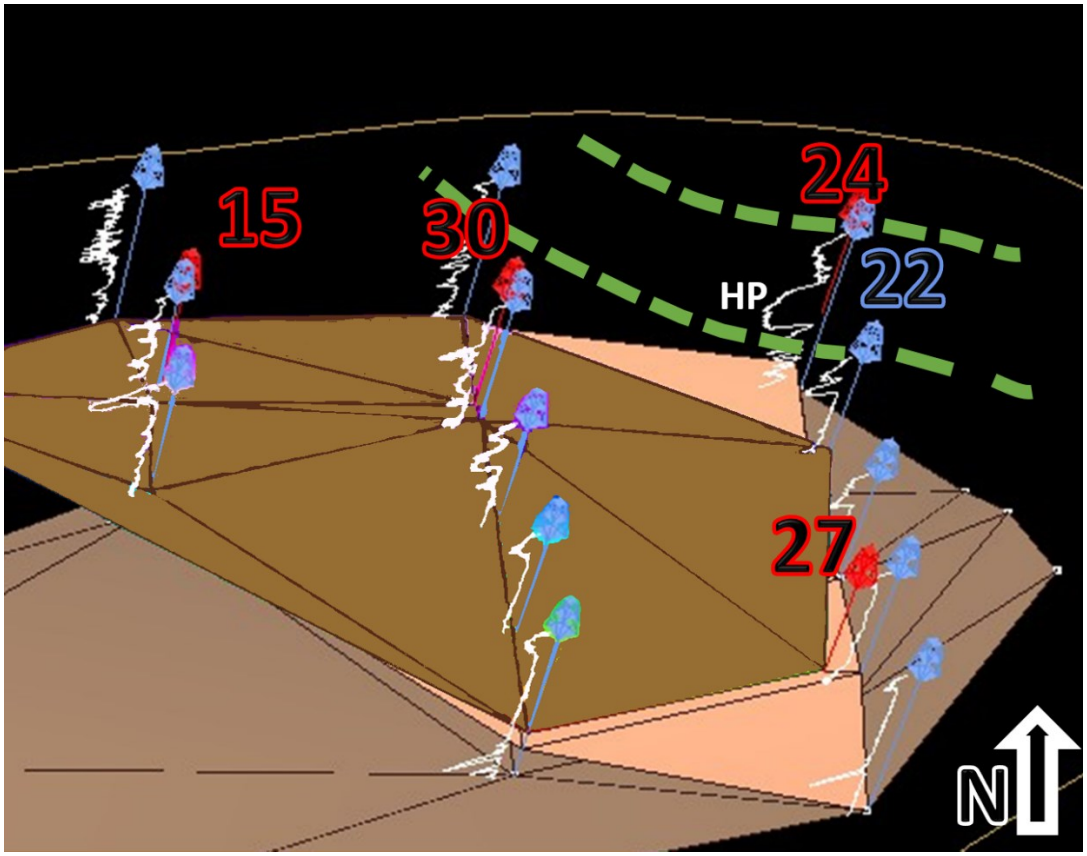

Fig. 3.21. Lateral extension of HS-GU7. We recovered HS-GU7 from core 24 and we measured electrical conductivity values comparable with such deposit exclusively in EC-22. Thus, we hypothesize that HS-GU7 is trapped in a localized depression (marked with a green dashed line in figure), either a river channel or a gully. The surface we reconstructed for the bedrock (see Fig. 3.8), HS-GU1 (see Fig. 3.10) and HS-GU3 (see Fig. 3.14) are respectively depicted in light brown, pink and dark brown. Cores are depicted and numbered in red, EC-logging in blue.

Of the three blocks we collected from HS-GU7 we processed one, HS-24-07. We collected this sample at the contact between GL 104 and GL 105. Our goals with this micromorphological study were to investigate the composition of these layers and verify whether this loess-like deposit had been preserved *in situ* or reworked by surface water.

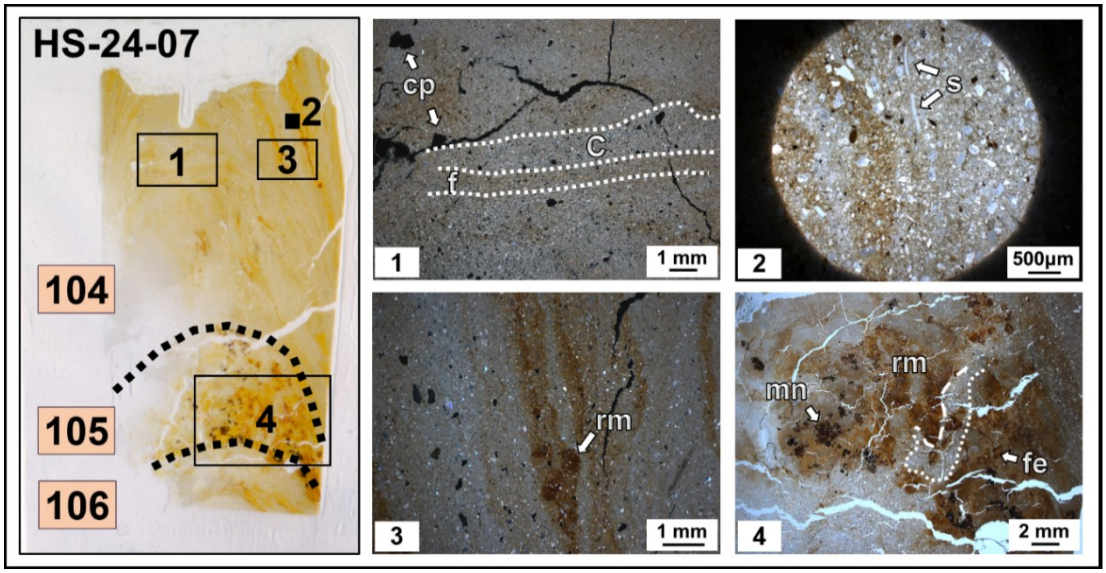

Fig. 3. 22. Micromorphological results from HS-GU7. ***On the left***, thin section scan of sample HS-24-07. GL numbers are labelled in pink. ***1***, photomicrograph in XPL from GL 104 showing the sandy silt (**c**) and clay silt (**f**) laminations characteristic for this unit. In this photomicrograph calcite pseudomorphic voids (**cp**) are also visible. ***2***, photomicrograph in XPL from GL 104 displaying rare shell fragments (**s**). ***3***, photomicrograph in XPL from GL 104 depicting redoximorphic masses (Vepraskas et al. 1993. **rm**) within iron stained laminations. ***4***, photomicrograph in PPL from GL 105 presenting one redoximorphic mass (**rm**) containing manganese (**mn**) and iron (**fe**) oxides. Within this mass we observed a non-redoximorphic zone of coarser silt and sand. The boundary between this area and the surrounding redoximorphic mass is diffuse (dotted white line) to sharp (dashed white line). The fact that the border between this two zones is partially sharp might indicate some form of disturbance after the formation of the mass. Since the remaining border between these two zones is diffuse, the redoximorphic process might have restarted after the disturbance.

Our micromorphological results reveal that sample HS-24-07 is largely composed of silt and medium to fine sand composed of calcite, quartz, and micas embedded in a clayey groundmass. The calcite sand appears weathered and calcite pseudomorphic voids are quite common in the matrix (Fig. 3.22, detail 1). Other components such as chert, chalcedony and snail shell fragments (Fig. 3.22, detail 2) are very rare. Small fragmented, limpid clay coatings are exceptionally present. All of these components are organized in laminations with graded bedding (Fig. 3.22, detail 1) that display various degrees of iron-manganese staining (Fig. 3.22, on the left). In these laminations redoximorphic masses (Vepraskas et al. 1993) are very common; these features display diffuse borders and are composed of iron and manganese (Fig. 3.22, detail 3 and 4). In Unit 105 one of these large masses contains a non-redoximorphic zone of coarser silt and sand. The boundary between this area and the surrounding redoximorphic mass is diffuse to sharp (Fig. 3.22, detail 4). The occurrence of a sharp contact between these two zones within the

redoximorphic mass suggest that the latter, after its formation, might have been affected by some disturbance (of possible biological origin).

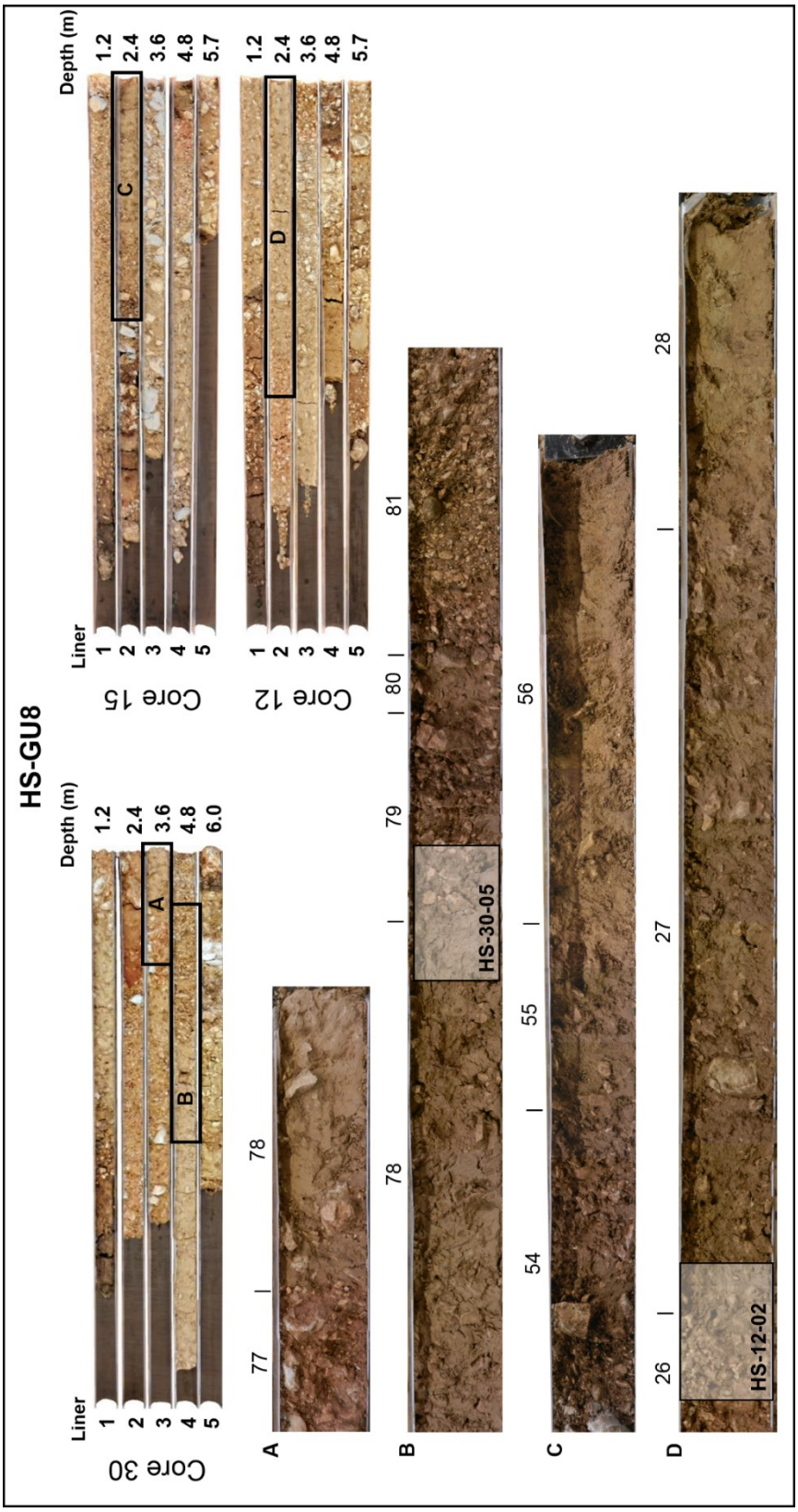

Fig. 3. 23. HS-GU8. ***In the upper part***, the liners of core 12, 15 and 30. ***In the lower part***, details from the main GL (numbered in the figure) which are discussed in the text. ***HS-30-05*** and ***HS-12-02*** indicate the location of the thin section displayed in Fig. 3.24.

HS-GU8

We assigned GL 27-28 from core 12, GL 55-57 from core 15 and GL 78-80 from core 30 to HS-GU8 (Fig. 3.7 and Fig. 3.23. Barbieri et al. 2018). All of these layers are composed of angular (exceptionally subrounded), fine to medium limestone gravel embedded in a yellowish brown matrix (10YR 5/4 or 5/6). Among these sediments, GL 79 has the highest content of coarse fraction (90%), while gravel-sized fragments are rarer in the other layers (generally not more than 30%). The texture of these layers varies from silty clay/ clayey silty (GL 28, 57, 78, 79, 80) to silty (GL 27, 55, 56).

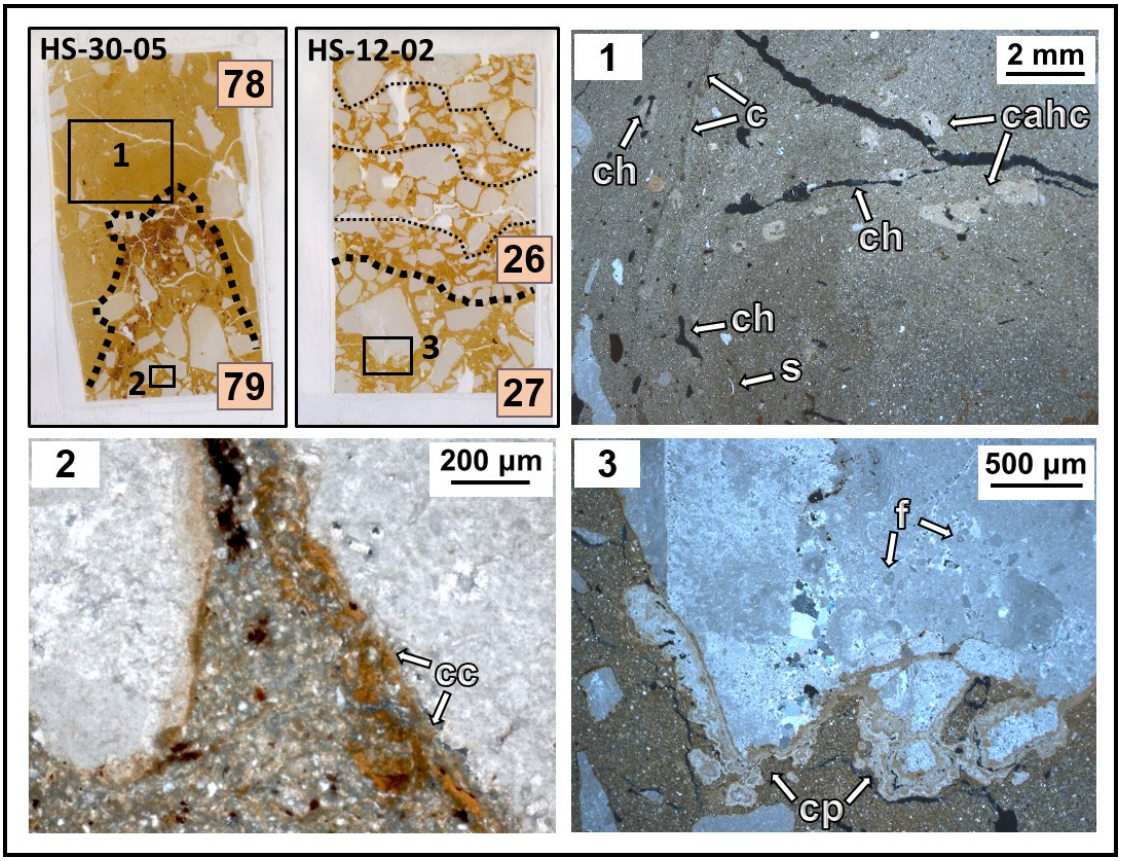

Fig. 3.24. Clay and calcite pedofeatures from HS-GU8. ***Upper left***, thin section scans of samples HS-30-05 and HS-12-02. GL numbers are labelled in pink. To be noted the weak graded bedding of GL 26 (HS-GU9). ***1***, photomicrograph in XPL from GL 78 displaying channel voids (**ch**), calcite hypocoatings around voids (**cahc**), iron stained clay laminations (**c**), and rare shell fragments (**s**). ***2***, photomicrograph in XPL from GL 79 showing laminated, limpid clay coating (**cc**) partly displaced from the limestone gravel on which it originally formed. ***3***, photomicrograph in XPL from GL 27 presenting calcite pendants (**cp**) formed on one fresh limestone fragment, in which microfossils (**f**) are still in part recognizable.

We analyzed two of the three micromorphological samples collected from this unit, sample HS-30-05 from the contact between GL 78 and GL 79 and thin section HS-12-02 from the passage between GL 27 and GL 28. The fine fraction of these layers is made of clay, loess-like minerals (quartz, micas and calcite), snail shells (Fig. 3.24, detail 1) and fragments of disorthic manganese nodules. Furthermore we observed fragments of limpid, laminated clay coatings and compound-layered coatings composed of clay and silt partly displaced from the limestone gravel on which they had originally formed (Fig. 3.24, detail 2). In GL 78 clay coatings are much rarer, in this layer clay is largely present in few, graded, iron stained laminations (Fig. 3.24, detail 1). Calcite hypocoatings around voids (Fig. 3.24, detail 1) and cappings/pendants on limestone (Fig. 3.24, detail 3) are also very common in GL 78 and GL 27.

HS-GU9

We grouped GL 24-26 from core 12, GL 92-96 and 99 from core 24, as well as GL 73-77 from core 30 in HS-GU9 (Barbieri et al. 2018). These layers are mainly composed of fine to coarse, angular gravel of limestone and Bohnerz. Fine gravel is also present but with a lower percentage. In HS-GU9 the composition of the matrix varies from silt to clay. Similarly to HS-GU5, the sequence of HS-GU9 displays alternating colors (yellowish brown and strong brown) and alternating grain sizes (fine and medium gravel).

As mentioned above we decided to include in HS-GU9 GL 99 from core 24, since this layer displayed characteristics comparable with the rest of HS-GU9. GL 99, however, does not lie directly on top of the other layers from core 24 that we assigned to HS-GU9. In fact GL 92-96 and GL 99 are separated by GL 96, which we assigned to HS-GU12, and GL 97, which we assigned to HS-GU11 (Fig. 3.7). Therefore in core 24 we distinguished a lower HS-GU9a, which includes GL 92-96, and an upper HS-GU9b, which includes GL 99 (Fig. 3.7 and Fig. 3.25).

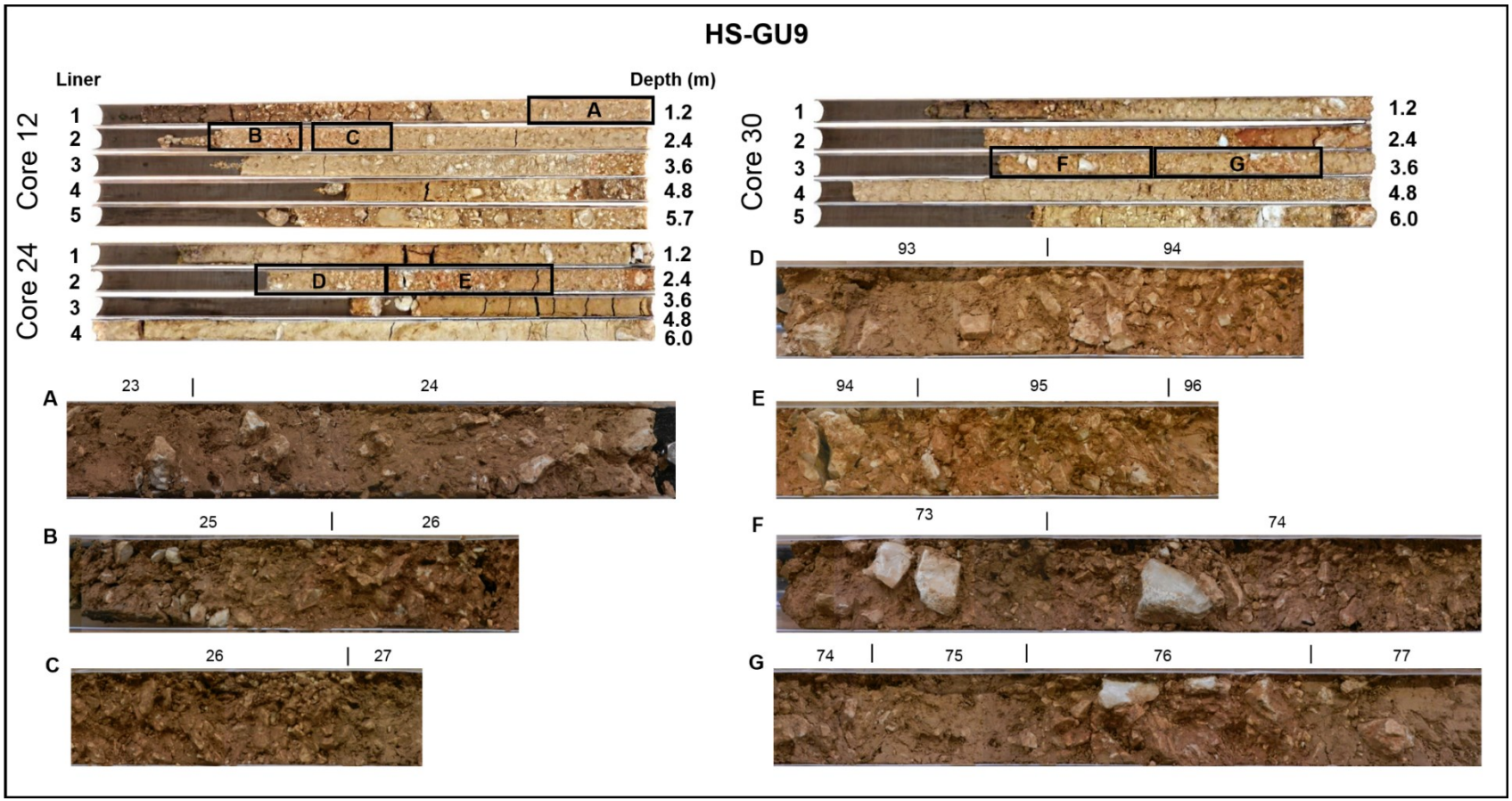

Fig 3.25. HS-GU9. ***In the upper part***, the liners of core 12, 24 and 30. ***In the lower part***, details from the main GL (numbered in the figure) which are discussed in the text.

For HS-GU9 we analyzed thin section HS-12-02, partially presented in the previous section. Here we present the results from GL 26, which is located in the upper portion of this micromorphological sample and represents the lowermost layer of HS-GU9 in core 12. Our micromorphological analysis revealed that GL 26 is formed of ca 2 cm-thick, graded laminations of fine and medium, angular, limestone gravel (Fig. 3.24, upper left) and occasional 1 mm-thick lamination of sand (Fig. 3.26, detail 1). The fine fraction is composed of clay, loess-like components, Bohnerz, snail shell fragments and disorthic to orthic, typic to dendritic, iron-manganese nodules. We also observed potential tail-like features (Bertran and Texier 1999) connected to limestone fragments (Fig. 3.26, detail 2). Moreover we identified fragments of calcite coatings (capping/pendants) scattered throughout the matrix. Larger components present limpid, laminated clay coatings and compound-layered coatings composed of clay and silt (Fig. 3.26, detail 3). Fragmented, limpid clay coatings are common in the matrix (Fig. 3.26, detail 3), while slightly disrupted clay coatings are occasionally incorporated within calcite pendants (Fig. 3.26, detail 4).

HS-GU10

We recovered GL 51-54 in core 15 between 1.2 m and 1.8 m below the ground surface, based on their composition we assigned these layers to HS-GU10 (Fig. 3.7 and Fig. 3.27. Barbieri et al. 2018). This deposit is composed of rounded to angular fragments of limestone, chert and Bohnerz embedded in dark yellowish brown silt (10 YR 4/6, 3/6, 4/4 and 3/6). In GL 51 secondary calcite features up to 5 mm in size were recognizable without the use of magnification lenses. GL 51-54 differ in terms of grain size, in GL 51 and GL 53 the fine fraction is predominant (90% and 60%, respectively) while in GL 52 and GL 54 the coarse fraction is more abundant (95% in both layers).

From HS-GU10 we analyzed sample HS-15-02, which we collected at the contact between GL 51 and GL 52. The goal of this analysis was to define the composition of these sediments and collect useful data to reconstruct their formation processes.

The upper GL 51 is made of a well-sorted sandy silt composed of reworked loess (silt-sized quartz and micas) almost depleted of calcite. Secondary calcite is exclusively present as calcite hypocoatings, coatings, and calcified root cells (Fig. 3.28, detail 1). In this layer iron-manganese nodules are present (Fig. 3.28, detail 2). Up to 1 mm-large

fragments of clay coatings and compound-layered coatings formed of silt and clay (Fig. 3.28, detail 3) are present within laminations rich in iron-manganese oxides.

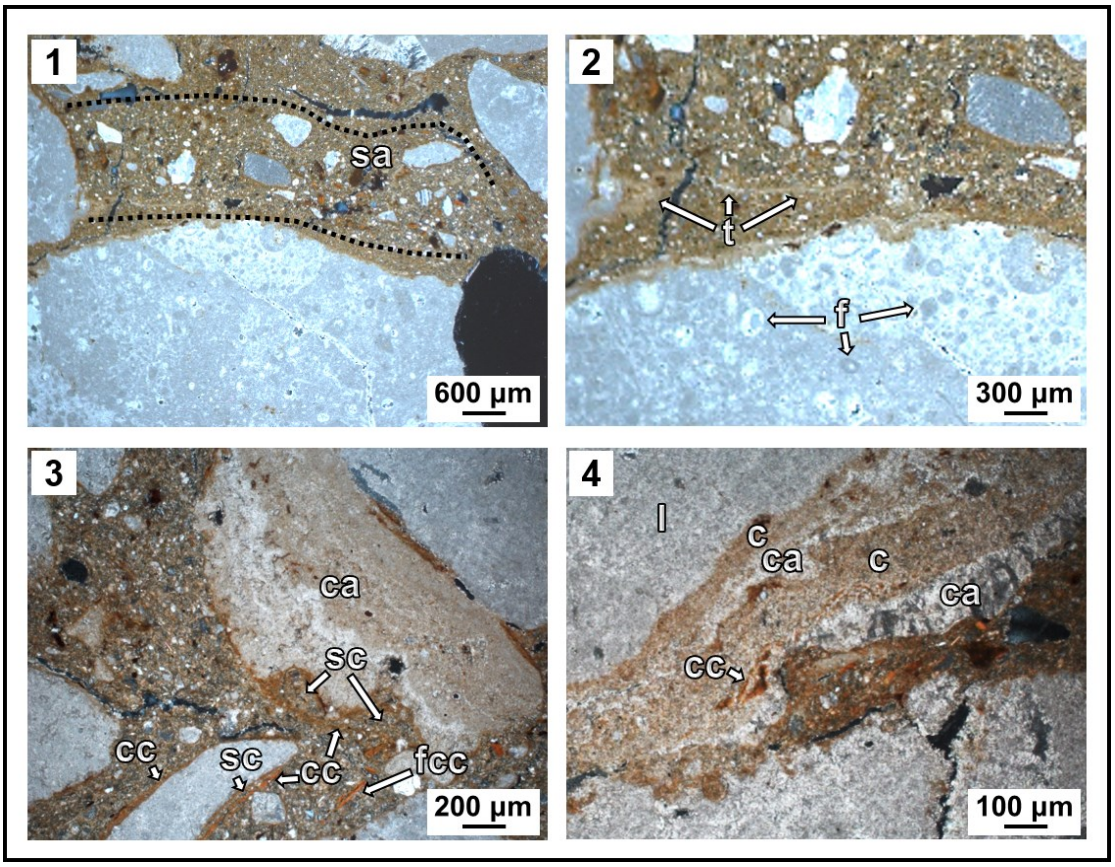

Fig. 3.26. Sedimentary and pedogenic features from HS-GU9. ***1***, photomicrograph in XPL from GL 26 displaying a lamination richer in medium, angular to subrounded sand (**sa**). ***2***, close up from previous photomicrograph focusing on a potential tail-like feature (Bertran and Texier 1999) formed from secondary calcite (**t**) associated with a fragment of limestone gravel. In GL 26 limestone fragments appear quite fresh, as evident from the present of recognizable microfossils (**f**) within them. ***3***, photomicrograph in XPL from GL 26 showing a displaced fragment of calcite capping/pendant (**ca**) presenting compound-layer coating composed of silt (**sc**) and clay (**cc**). Similar coatings are present also around limestone fragment, below from the reworked calcite capping/coating. Fragmented, limpid, clay coatings (**fcc**) are scattered in the matrix. ***4***, photomicrograph in XPL from GL 26 displaying a limestone fragment coated with alternating laminations of calcite and clay (**c**) and purer calcite (**ca**). The first type of lamination occasional present fragments of slightly displaced clay coating (**cc**).

Micromorphological analysis confirmed that GL 52 is an unsorted sediment composed mainly of gravel and sand-sized grains of limestone, chert, chalcedony and Bohnerz. The limestone fragments range from subangular to rounded, from fresh to weathered, and occasionally present silt coatings. The fine fraction of this layer is largely composed of loess-like minerals (quartz, micas and rare calcite), typic orthic and disorthic iron-manganese nodules, fragments of limpid, laminated clay coatings and compound-layered

coatings composed of clay and silt. Locally GL 52 displays weakly-developed granular microstructure with graonstriated b-fabric (Fig. 3.28, detail 4). The groundmass is extensively impregnated with iron-manganese oxides.

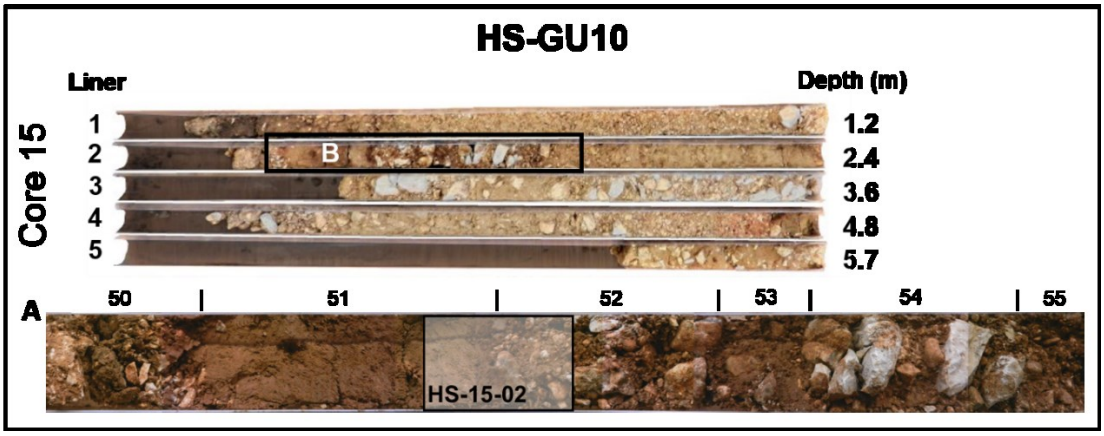

Fig. 3.27. HS-GU10. ***In the upper part***, the liners of core 15. ***In the lower part***, details from the main GL (numbered in the figure) which are discussed in the text ***HS-15-02*** indicates the location of the thin section presented in Fig. 3.28.

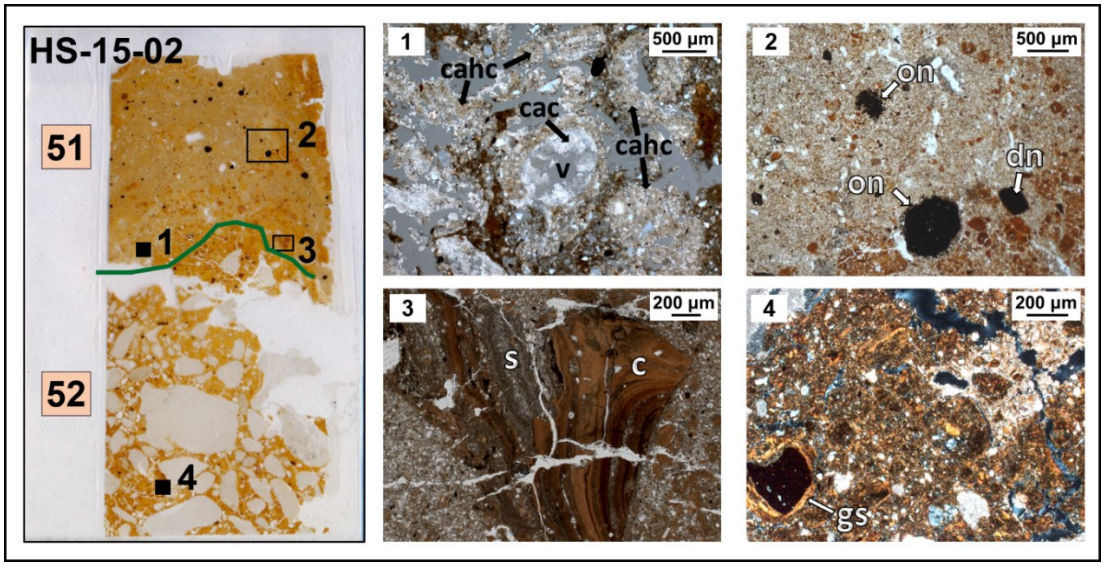

Fig. 3.28. Micromorphological results from HS-GU10. ***On the left***, thin section scan of the sample HS-15-02. GL are labelled in pink. ***1***, photomicrograph in PPL from GL 51 displaying calcite hypocotaings (**cahc**) and calcite coatings (**cac**) around root voids (**v**). ***2***, photomicrograph in PPL from GL 51 showing orthic (**on**) and disorthic (**dn**) iron-manganese nodules. ***3***, photomicrograph in PPL from GL 51 presenting a fragment of compound-layered coating formed of silt (**s**) and clay (**c**). ***4***, photomicrograph in XPL from GL 52 showing the granostriated b-fabric of the groundmass.

HS-GU11

In cores 24 and 30, from roughly 2.4 m below the ground, we recovered GL 98 and GL 72 (Fig. 3.7 and Fig. 3.29). These layers are composed of rare angular, fine and medium limestone gravel embedded in a well sorted, strong brown (7.5YR 4/6) to reddish brown (5YR 4/4), laminated silty clay matrix (Barbieri et al. 2018).

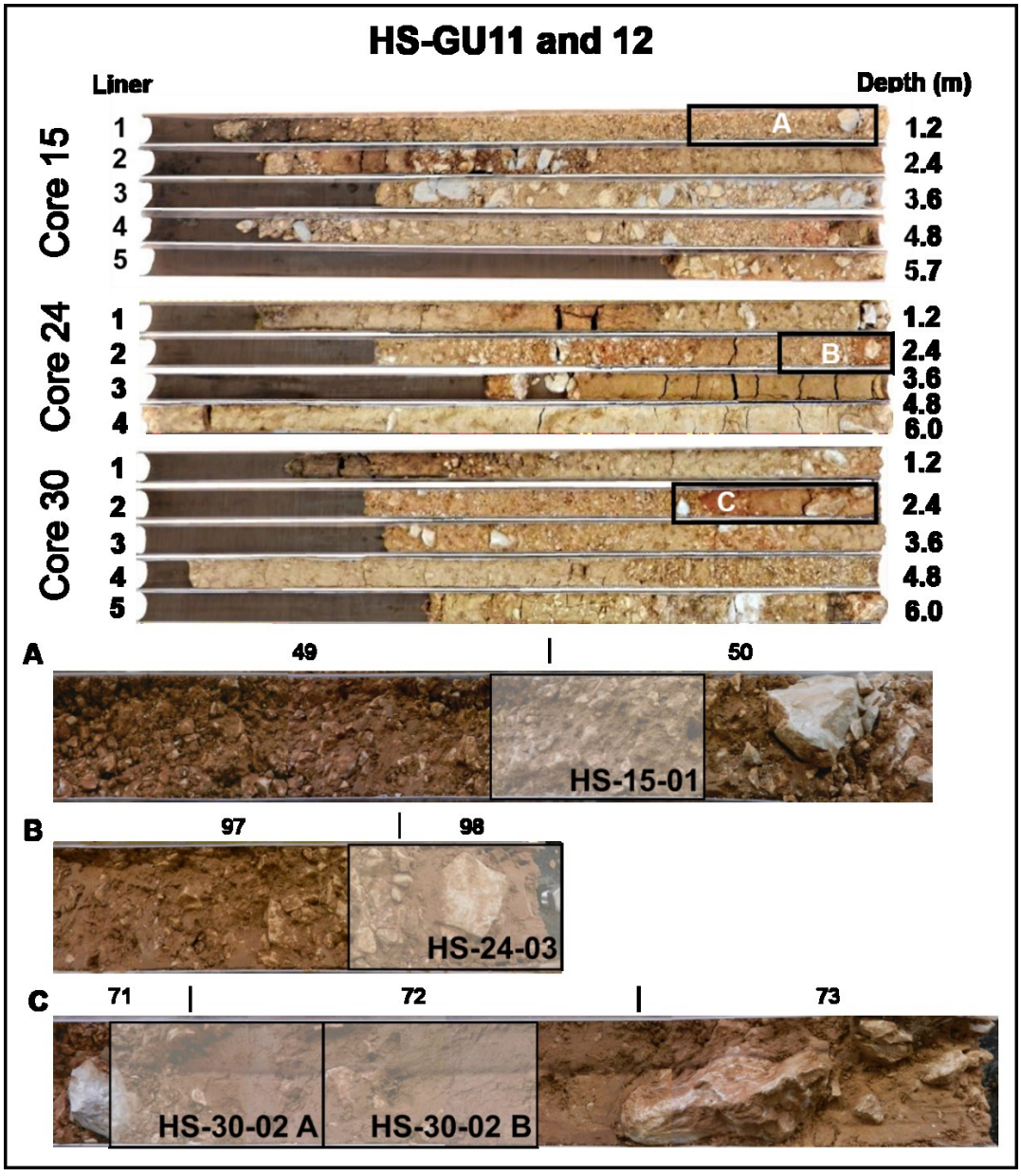

Fig. 3.29. HS-GU11 and 12. ***In the upper part***, the liners of core 15, 24 and 30. ***In the lower part***, details from the main GL (numbered in the figure) which are discussed in the text. ***HS-15-01***, ***HS-24-03***, ***HS-30-02A*** and ***HS-30-02B*** indicate the location of the thin sections we analyzed from these deposits.

Although we recovered HS-GU11 only in cores 24 and 30, the strong attenuation of our GPR measurement starting from a depth of circa 2.5 m suggests that silty clay-rich deposits might be more extensive in the surveyed area. However, since in nearby core 15 we documented other fine sediments (see HS-GU10), this "attenuation zone" might correspond only partially with HS-GU11.

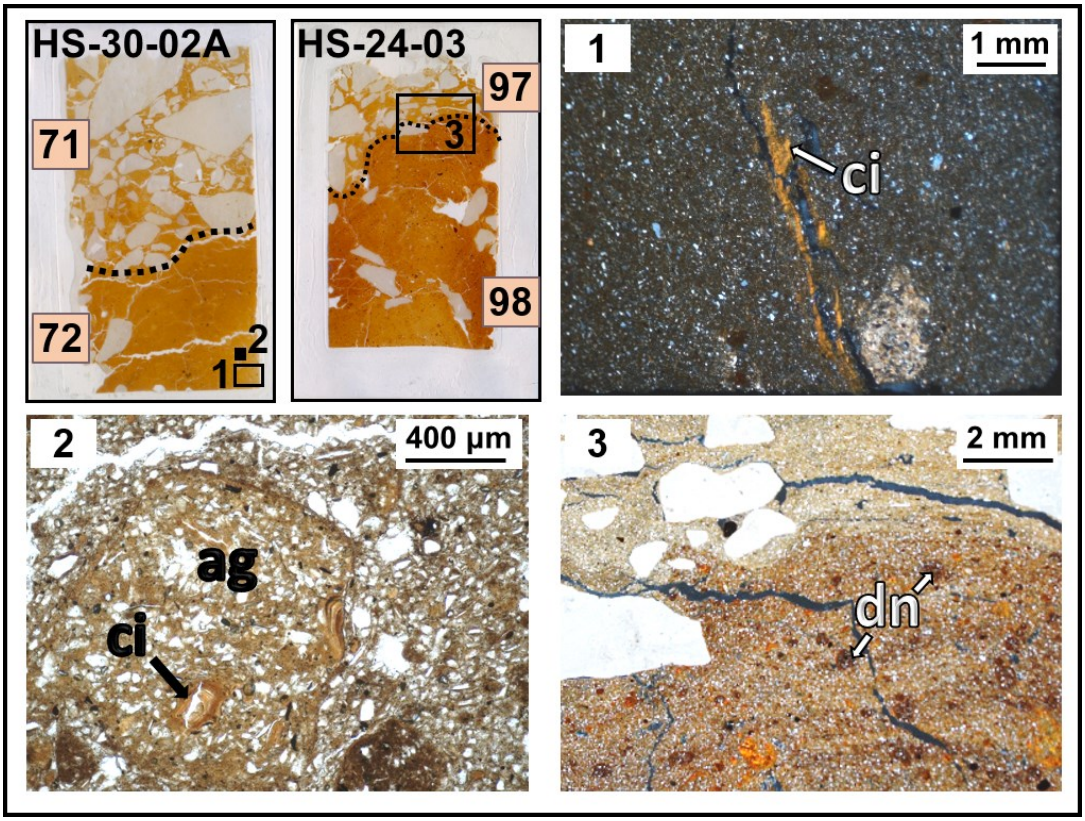

Fig. 3.30. Pedofeatures from HS-GU11. ***In the upper left***, thin section scans of the samples HS-30-02A and HS-24-03. GL are labelled in pink. ***1***, photomicrograph in XPL from GL 72 showing slightly displaced clay infilling (**ci**) along potential channel. ***2***, photomicrograph in PPL from GL 72 displaying reworked aggregate (**ag**) with clay infillings (**ci**). ***3***, photomicrograph in PPL from GL 98 portraying laminations with weak graded bedding below the contact with GL 97. These laminations are largely composed from clay aggregates and reworked, iron stained nodules (**dn**).

We investigated this unit with two block samples for micromorphological analysis, HS-24-03 at the passage from GL 97 to GL 98 and HS-30-02 at the contact between GL 71 and GL 72. From these two samples we produced three thin sections: HS-24-03, HS-30-02A and HS-30-02B. Our micromorphological results show that GL 72 and GL 98 are composed of rare, weathered, angular gravel-sized limestone fragments embedded in reworked, decalcified loess (silt-sized quartz and calcite) and clay. Furthermore in both layers we observed reworked limpid clay coatings, fragmented compound-layered

coatings composed of clay and silt, clay aggregates (Fig. 3.30, detail 2) and *in situ* to reworked, dense, incomplete to complete clay infillings (Fig. 3.30, detail 1). Fragmented clay coatings are coarser and more intensively impregnated with iron-manganese in a lamination located at the bottom of sample HS-30-02B. In both layers we also observed numerous well rounded aggregates impregnated with iron-manganese oxides (Fig. 3.30, detail 3). These nodule-like features have the same composition as the surrounding matrix and usually display a granostriated b-fabric. Calcite hypocoatings, quasicoatings and calcified root cells are exclusively present in the upper part of HS-GU11 and increase in number at the contact with HS-GU12. Just below this contact in sample HS-30-02B we documented laminations with weak graded bedding (Fig. 3.30, detail 3).

HS-GU12

We recovered GL 49 in core 15, GL 97 in core 24 and GL 71 in core 30 from shallow depths (0.5 m to 2 m below the ground surface). These layers are composed of subangular to angular, fine and medium gravel of limestone embedded in yellowish brown (10YR 5/6) to dark yellowish brown (10YR 4/6) sandy, silty clay (Fig. 3.7 and Fig. 3.27). This unit appears to be organized in coarser- and finer-grained beds (Barbieri et al. 2018).

The penetration of our GPR measurements along the hillside was limited by the presence of shallow units richer in silty clay (such as HS-GU7, HS-GU11 and HS-GU13). Only in the area between cores 15 and 30 we could detect clear structures with our geophysical data. In this part of the slope at a depth comparable with HS-GU12 our GPR measurements revealed 10 x5 m large reflectors densely stacked in an imbricated fashion (Blikra and Nemec 1998, Fig. 3.31). At the passage between hillside and valley floor the sedimentary structure corresponding to HS-GU12 and 11 appear truncated by reflectors dipping towards the center of the plain with an angle of ca. 11° (Fig. 3.35. Barbieri et al. 2018).

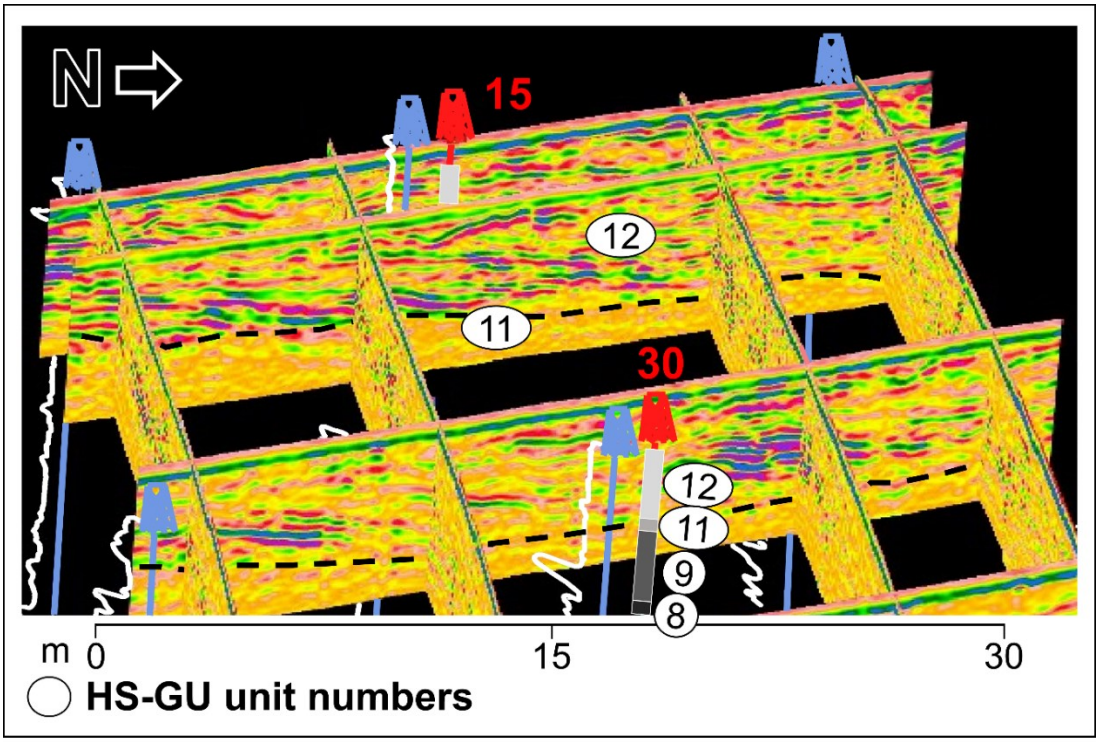

Fig. 3.31. Bedding of HS-GU12 in the geophysical data. In the figure geological units are labelled with numbers on white background, cores are depicted and numbered in red, ec-logs are depicted in blue (Figure from Barbieri et al. 2018). In between cores 15 and 30 our GPR data revealed reflectors that appear laterally continuous, densely stacked in an imbricated fashion (Blikra and Nemec 1998) and rest at depths comparable with HS-GU12 (***12***). Interestingly this unit displays a comparable bedding also in thin section (Fig. 3.32).

We sampled this unit with three blocks for micromorphological analysis, namely HS-15-01, HS-24-03, HS-30-02. Our results from this study confirm the bedded structure observed at the macroscopic level, with laminations richer in fine fraction alternating with laminations richer in limestone gravel. The gravel fragments appear fresh, angular, well-sorted (commonly < 1 cm) and present preferred sub-horizontal orientation, only in part affected by the coring. Chert, disorthic iron-manganese nodules and Bohnerz are minor components of the coarse fraction. The fine fraction of this unit is composed of loess-like minerals, shell fragments and clay. Reworked, limpid clay coatings are rare. Although fresh calcite is more common in this deposit, most of the calcite we identified is present as calcite hypocoatings, coatings, calcified root cells and infillings of medium-sand sized grains of calcite (Durand et al. 2010).

Fig. 3.32. Bedding of HS-GU12 in thin section. Scan of thin section HS-15-01 showing the alternation of coarser and finer laminations. The main component of this sample (and of the entire HS-GU12) is angular, fresh, limestone gravel (*Bergkies*).

HS-GU13

GL 70 and GL 91 are the uppermost sediments recovered directly below the modern soil from core 30 and core 24, respectively (Fig. 3.7 and Fig. 3.33). They are composed of rare, angular, fine to medium limestone gravel in a yellowish brown (10YR 5/6 – 10YR 5/4) clayey, silty matrix. In the matrix we observed also strong brown (7.5YR 4/6) mottles. Given the likely more intensive bioturbation caused by modern roots, which are commonly present, we decided not to analysis the block sample we collected from this unit.

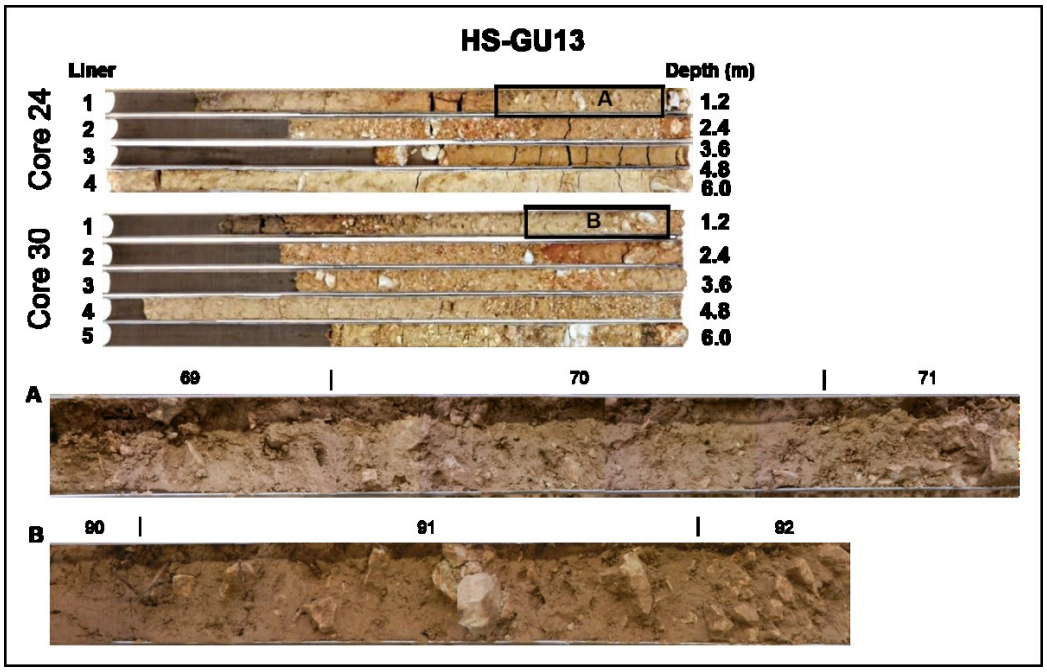

Fig. 3.33. HS-GU13. ***In the upper part***, the liners of core 24 and 30. ***In the lower part***, details from the main GL (numbered in the figure) which are discussed in the text.

HS-GU14

On top of HS-GU4 we documented two different sequences: along the north flank of the valley we recovered HS-GU5 through HS-GU13 while from the center of the flood plain we recovered HS-GU14 (Fig. 3.7. Barbieri et al. 2018). The latter is composed of the shallowest deposits (3.13 m max depth) we recovered from the Lone floodplain, namely GL 9-12 from core 27, GL 300-304 from core 5 and the entire core 9 (Fig. 3.34). These GL range from clast-supported to open-work and are made of well-rounded to angular, coarse, medium and fine gravel of limestone, quartz, Bohnerz and chert. From GL 9, which we recovered from the first liner of core 27, we reported the occurrence of rare fine gravel-sized fragments of pottery (Barbieri et al. 2018).

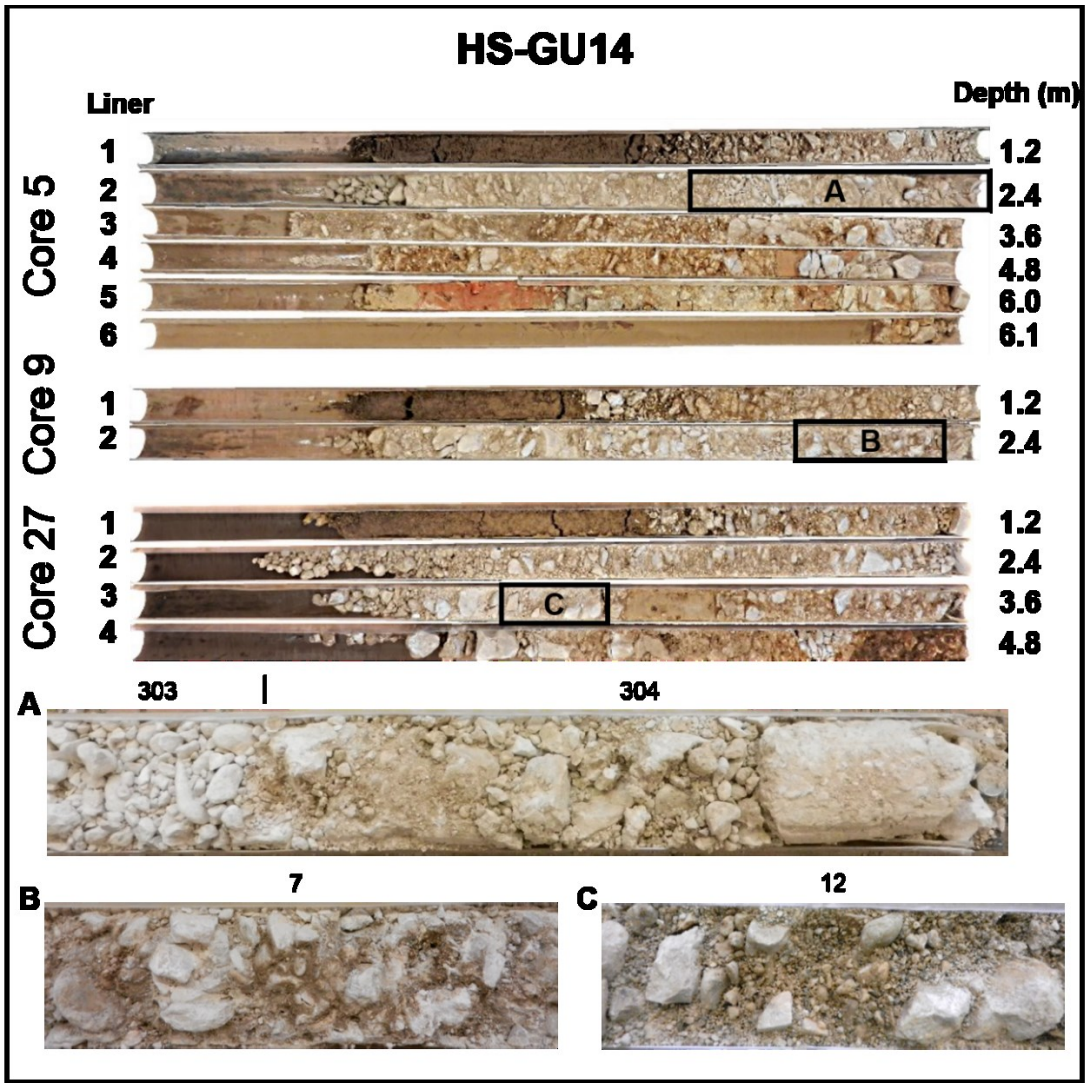

Fig.3.34. HS-GU14. ***In the upper part***, the liners of core 5, 9 and 27. ***In the lower part***, details from the main GL (numbered in the figure) which are discussed in the text.

In the Lone floodplain with the GPR we detected laterally continuous reflectors (2x2 m to 5x5 m) that are located between 1 m to 3 m below the ground surface and dip northwards with an angle of 3° - 5°(Fig. 3.35, detail A). In the passage between the hillside and floodplain we detected a depression, which appears 1 m deep, ca. 10 m wide and 80 m long (Fig. 3.35, detail B). Our results from the surface mapping (Appendix II) and the velocity analysis of the GPR measurements (Davids and Annan 1989) show that this potential depression is filled with silty clay sediments. On the southernmost edge of our survey area, close to the Lone River, our geophysical measurements revealed 10x30 m large, laterally continuous reflectors that dip southwards with an angle of 3° (Fig. 3.35, detail C. Barbieri et al. 2018).

We decided not to sample this unit for micromorphology, given the unsuitable grain size for such analysis.

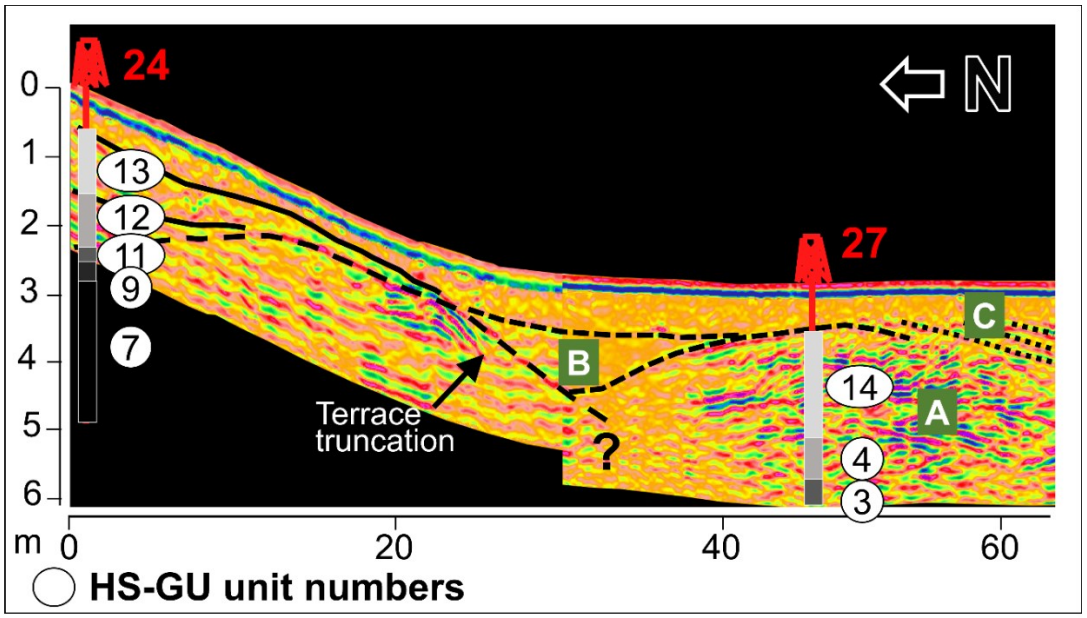

Fig. 3.35. Terrace truncation. Two merged GPR profiles from core 24 to core 27 (numbered in red) which display reflectors likely indicative for an incision of the HS-GU5-11 sequence accumulated along the hillside (***Terrace truncation***). ***A***, gravelly deposits resulting from northwards migrations of the Lone. ***B***, potential channel filled with silty clay sediments. ***C***, sedimentary structures suggesting a final southwards migration of a paleo-channel. Figure from Barbieri et al. 2018.

HS-GU15

We recovered GL 20-23 from below the modern soil, in the first liner of core 12 (Fig. 3.7 and Fig. 3.36). GL 20, 21 and 23 are composed of abundant coarse fraction (at least 60%) embedded in a clayey, silty matrix. The coarse fraction is composed of fine to medium gravel of limestone and Bohnerz, medium gravel is more abundant in the lower part of GL 20 and 21. In contrast, GL 22 is composed of a very well-sorted silty clay completely free from gravel (Barbieri et al. 2018).

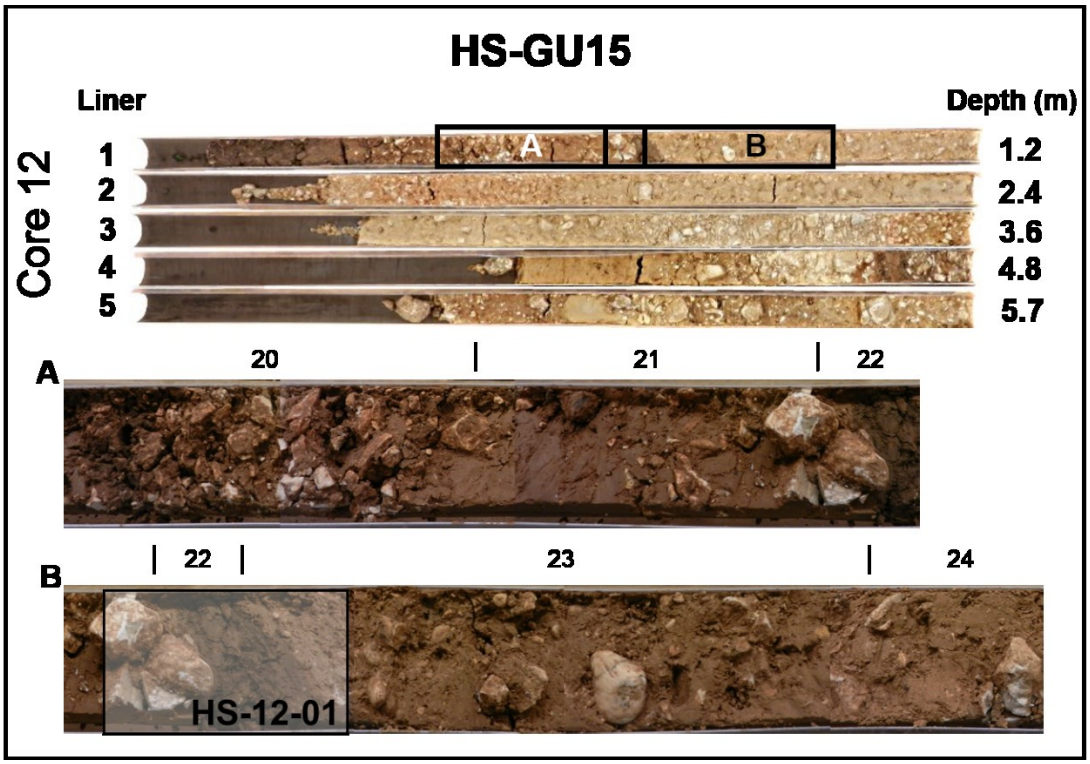

Fig. 3.36. HS-GU15. ***In the upper part***, the liners of core 12. ***In the lower part***, details from the main GL (numbered in the figure) which are discussed in the text. ***HS-12-01*** indicates the location the thin section displayed in Fig. 3.38.

The GPR measurements we collected in the surroundings of core 12 show sub-horizontal reflectors at 0.80 m to 1.5 m below the ground surface (Fig. 3.37). Such depth is comparable with GL 25, 24 (HS-GU9) and probably GL 23 (the lowermost from HS-GU15). This structure appears truncated by a reflected phase that dips towards the center of the valley and is covered with the gravel of HS-GH14, which we recovered from nearby core 9. Closer to the hillside, on top of the mentioned truncation, we have detected reflectors dipping from the hillside towards the floodplain at a depth comparable with the upper part of HS-GU15, probably GL 20-22.

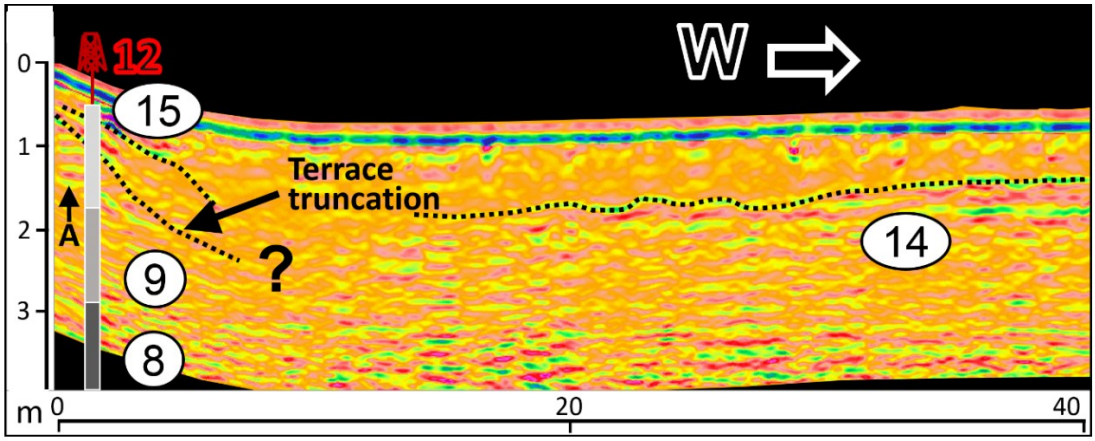

Fig. 3.37. The stratigraphic position of HS-GU15. GPR profile collected from core 12 (numbered in red) towards West. ***A*** indicates sub-horizontal reflectors that seem truncated by a steeper reflected phase, which dips towards west. This shift in orientation of the reflectors resembles the one we describe for the area between cores 24 and 27 in Fig. 3.35. HS-GU unit numbers are labelled on white background.

We studied HS-GU15 with micromorphological sample HS-12-01. Our results show that the two gravelly layers GL 21 and GL 23 are quite similar in terms of composition. Their coarse fraction is composed of medium and fine gravel of limestone, quartz, Bohnerz, anorthic, typic iron nodules and chert fragments. The same components are also present in the sand and silt fraction together with loess-like minerals, fragmented limpid and laminated clay coatings and shell fragments. Needle-fibre calcite and infilling of sand-sized grains of calcite are also present together with coalescent, calcite hypocoatings around root voids. In the lower GL 23 the gravel is more rounded, imbricated and organized in laminations (Fig. 3.38, detail 3).

The contact between these two layers and GL 22 is very sharp, deformed, and interdigitated (Fig. 3.38, detail 2). GL 22 is formed of a well-sorted, extensively decalcified loess together with a considerable amount of clay impregnated with iron-manganese. Calcite is occasionally present in intercalations and along root voids where it partially replaced vegetal material. This layer is also characterized by potential platy microstructure (Fig. 3.38, detail 1).

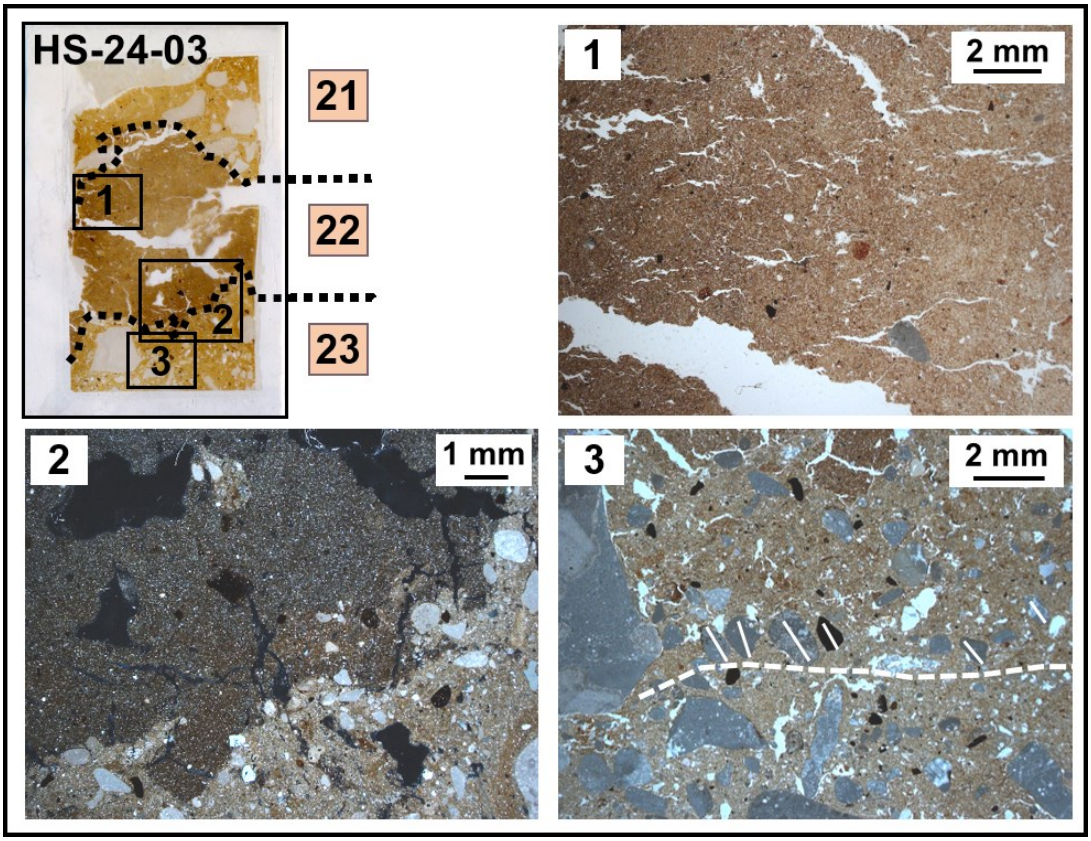

Fig. 3.38. Micromorphological result from HS-GU15. ***In the upper left***, thin section scan of sample HS-24-03. GL are labelled in pink. ***1***, photomicrograph in PPL showing potential platy microstructure from GL 22. ***2***, photomicrograph in XPL displaying the sharp contact between the decalcified GL 22 (top) and the calcite rich GL 23 (bottom). ***3***, photomicrograph in PPL from GL 23 presenting potential imbricated bedding. The major axis of the (rounded) sand fragments is marked with white lines.

3.3 Data interpretation

3.3.1 Site formation processes at Hohlenstein-Stadel

Our reconstruction of the processes that led to the formation of the deposits accumulated inside the cave of Hohlenstein-Stadel and at its *Vorplatz* has been published in Barbieri and Miller (in press). In this section we summarize that site formation model.

Silt-sized grains of quartz and micas are very common in the two sections we studied at this site (Barbieri and Miller in press). As discussed in chapter 1.1.1 (pp. 15-16), silt-sized particles of quartz and micas are commonly reported from Pleistocene and Holocene sediments in the Swabian Jura. Based on their petrography and sizing, Gwinner (1989) and Schall (2002) argued that these mineral grains were deposited in this region by winds coming from the Danubian basin during the stadials of the Pleistocene. Possibly shortly

after their deposition, colluviation processes moved these aeolian deposits (loess) from the plateau down into the valleys and inside the karst system of the Swabian Jura (Schall 2002, Sauer et al. 2016). Similarly to what Goldberg (et al. 2003) and Miller (2015) described at Hohle Fels, we hypothesized that reworked loess entered Hohlenstein-Stadel from cracks and openings located in the back of this cave (Barbieri and Miller in press. Fig. 3.39, detail 1).

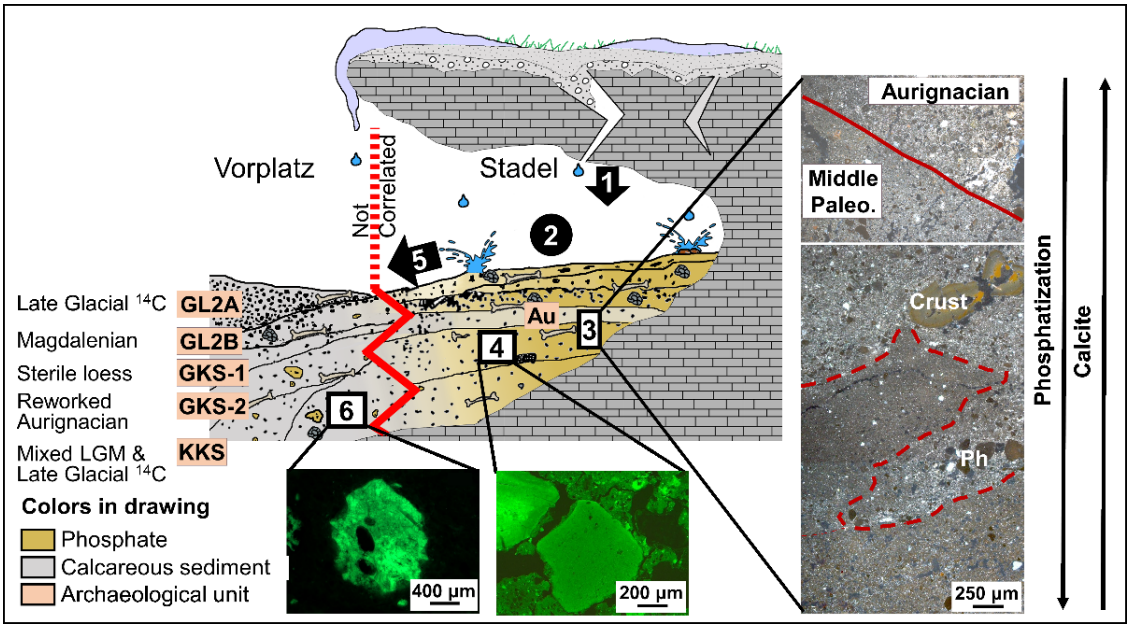

Fig. 3.39. Site formation processes at Hohlenstein-Stadel. Idealized drawing of the sequence that Kind and Beutelspacher exposed at the *Vorplatz* and inside Hohlenstein-Stadel. In the drawing, light brown depicts phosphatized sediment, gray indicates calcareous sediment. Pink labels indicate the archaeological units mentioned in the text. Numbers on black background indicate the processes discussed in the text: ***1***, sediment entering the cave through cracks, ***2***, sediment becoming phosphatized inside the cave, ***5***, sediment moving from the back of the cave towards the Vorplatz. The location of photomicrographs in the figure is marked with connecting lines and numbers on white background: ***3***, photomicrographs collected in PPL from the contact between Early Aurignacian (**Au**) and Middle Paleolithic (**Middle Paleo.**) deposits preserved inside Hohlenstein-Stadel. The Early Aurignacian deposit exhibits a better preservation of calcite (white speckles) and less intensive phosphatization in comparison with the Middle Paleolithic. ***4***, photomicrograph collected under FL displaying phosphatized loess in the Middle Paleolithic deposits accumulated in the back of the cave. ***6***, photomicrograph collected under FL showing one isolated grain of phosphatized loess in non-phosphatic sediment from the Middle Paleolithic deposits accumulated at the *Vorplatz*. Figure from Barbieri et al. 2018.

Particularly in the deposits preserved in the back of Hohlenstein-Stadel clay (kaolinite, Fig. 3.4, detail 5) is present as aggregates and groundmass (Barbieri and Miller in press). It is possible that such clay originated from the intense weathering of the Jurassic limestone before the Quaternary Period (Schall 2002, Ufrecht 2008a, Strasser et al. 2009).

Alternatively it might have formed in the course of phases of soil formation that took place in the surroundings of the cave during the Pleistocene (see next section 3.2.2. Barbieri et al. 2018). Similarly to the reworked loess, clay might have entered Hohlenstein-Stadel through openings located in the back of the cave (Fig. 3.39, detail 1). Inside the karst system, both these components underwent multiple phases of deposition and erosion, as documented by numerous aggregates made from clay and reworked loess (Barbieri and Miller in press. Fig. 3.4, detail 1, 2 and 4. See below).

Faunal remains and coprolites are the most abundant components in the deposits accumulated in the back of Hohlenstein-Stadel (Barbieri and Miller in press). Faunal remains (bones and teeth) are largely weathered, stained with iron-manganese oxides, more rarely burnt and occasionally calcined (Barbieri and Miller in press. Fig. 3.3, detail 5). Coprolites are composed of apatite minerals, they display vesicles, vughs, pseudomorphic fur voids, rare bone fragments, silt and sand-sized grains of quartz and micas (Barbieri and Miller in press). Based on their composition we interpret these components as carnivore (Horwitz and Goldberg 1989), possibly hyena (Barbieri and Miller in press), coprolites. Our data and interpretation are consistent with previous faunal analysis conducted by Kitagawa (2014), who suggested that Hohlenstein-Stadel might have been a hyena den during the Middle Paleolithic. Such hypothesis is also supported by the low counts for charcoals and calcined bones in the Middle Paleolithic deposits, which suggest that at that time humans visited the site occasionally (Barbieri and Miller in press). The claim for a more intensive human presence at Hohlenstein-Stadel during the Aurignacian (Kitagawa 2014) is supported by the lower amount of coprolites in the Au deposit (Barbieri and Miller in press. Table 3.3). However the nearly lack of charcoals and calcined bones in this unit suggests that during the early Aurignacian either human occupation in the back of the cave was occasional or that it did not involve frequent use of fire (Barbieri and Miller in press).

The numerous coprolites and animal carcasses accumulated by hyenas inside Hohlenstein-Stadel released phosphoric acid that caused the apatite replacement of the calcite originally present in the reworked loess accumulated inside the cave (Braillard et al. 2004, Sanz et al. 2016, Sanz et al. in press, Barbieri and Miller in press. Fig. 3.39, detail 4). Goldberg (et al. 2003) and Miller (2015) reported evidence of phosphatization from the sites of Hohle Fels and Geißenklösterle, in the Ach Valley. At these sites

Chrono	Unit	Ca	Ph	A	BT	Ch	BB	Interpretation
After LGM	GL2A	XXXXX	/	/	/	/	/	End of erosion of cave sediment. Fresh loess and gravel moving from the hillside into the cave entrance.
	GKS-1	XXXXX	/	/	X	/	/	
Aurig.	Au	XXX	XX	XX	XX	/	/	Better preservation of calcite and less intensive erosion. Change in environment or use of the cave.
Midd. Paleo.	SKS	XXXX	X	X	X	$	$	Sediment eroded from back of the cave and redeposited at the Vorplatz.
	RT1	XXXX	X	X	X	/	/	
	C	X	XXX	XXXX	XXX	/	/	Cave occupied by humans and animals. Phases of erosion and redeposition. Dissolution of calcite and apatite neoformation.
	A2	X	XXXX	XX	XX	/	/	
	D	/	XX	XXXXX	/	/	/	
	D4	/	XXXXX	XX	XX	/	$	
	D2	XX	XXXXX	X	X	/	/	
	F	X	XXX	XX	XXX	$	$	
	G	/	XXXX	XX	XX	$	/	
	K	/	XXXX	XXXXX	XXX	/	$	
	K/M	/	XXXXX	XXXX	XX	$	/	
Sterile	M	/	X	XX	/	/	/	Natural sedimentation. Cave occasionally occupied.

Table 3.3. Frequency of the main components and its relevance for the site formation model. ***Chrono***, chronology of the Units; ***Unit*****,** archaeological Unit; ***Ca***, presevation of calcite,; ***Ph***, amount of phosphatic sediment; ***A***, fine fraction aggregates; ***BT***, bone and tooth fragments; ***Ch***, charcoal; ***BB***, burnt bones; ***Interpretation***, interpretation of our micromorphological oservations. Data are presented in a semiquantitative way. Legend: ***/***, absent; ***X***, rare; ***XX***, common; ***XXX***, abbundant; ***XXXX***, frequent; ***XXXXX*** dominant. For trace components such as charcoals and burnt bones we have marked their presence with the symbole ***$***. Modified from Barbieri and Miller in press.

phosphatization seem to have been triggered by the accumulation of bat or bird guano inside the caves (Goldberg et al. 2003 and Miller 2015). The lack of gizzard stones (Karkanas et al. 2000), and limited occurrence of bat fossil remnants (only in units SKS

and BG, Jahnke 2013) seem to deny the hypothesis that guano might have represented a major source for phosphoric acid at Hohlenstein-Stadel.

Inside this cave phosphate neoformation has not been continuous over time (Barbieri and Miller in press). For instance, in the Middle Paleolithic sequence units F and D2 exhibit a better preservation of calcite, while Unit D4 displays a non-phosphatized lamination (Barbieri and Miller in press. Fig. 3.3, detail 5). Particularly the transition from the Middle to Upper Paleolithic (Unit C/AU) displays an increasing calcite content (Barbieri and Miller in press. Fig. 3.39, detail 3. Table 3.3), which might be related to the decreasing animal use of the cave.

The hypothesis of regular redeposition of the Middle Paleolithic and partly Upper Paleolithic sediment is supported by lack of preserved occupational surfaces and mixing of bones with different degrees of alteration (Barbieri and Miller in press). More in detail we hypothesize that reworked loess and clay entered Hohlenstein-Stadel through cracks located in the back of the cave. Once deposited inside the cave these materials got phosphatized and underwent cycles of erosion and redeposition, which moved the sediment accumulated in the back of the cave towards the Vorplatz (Fig. 3.39, detail 5). The presence of isolated grains of phosphatized loess in the non-phosphatized Middle Paleolithic deposits of the *Vorplatz* (SKS and RT1) supports this reconstruction (Barbieri and Miller in press. Fig. 3.39, detail 6). Together with isolated grains of phosphatized loess Unit SKS exhibits platy microstructure, supporting the hypothesis of gelifluction (Barbieri and Miller in press. Fig. 3.5, detail 1). None of the deposits we investigated in the back of the cave displays micromorphological features diagnostic for ground freezing, probably because the profile we analyzed is located approximately 50 m from the cave entrance leaving it less exposed to the external environment. We conclude that other colluviation processes also originated from the back of the cave (Barbieri and Miller in press). During the LGM the erosion of cave sediment probably became more intensive causing the removal of Gravettian-aged deposits and some Aurignacian artifacts, which partly redeposited at the *Vorplatz* (Units KKS and GKS-2, Jahnke 2013). During the Late Glacial the Magdalenian deposit GL2B and the underlaying sterile GKS-1 might have also suffered some erosion (Jahnke 2013). Our data from the contact area between GL2A and GKS-1 cannot confirm or refute the erosive nature of this contact. The transition between these two deposits appears relatively diffuse in thin section, however this might

be resulting from some bioturbation which was caused by the numerous root voids we observed in this portion of the stratigraphy (Barbieri and Miller in press). This potential disconformity was covered with the late Upper Paleolithic deposit of GL2A, which is free of phosphatic components and thus marks the end of cave erosion at this site. The deposition of GL2A represents also a shift in sedimentation source, with fresh loess and gravel moving from the hillside towards the entrance of Hohlenstein-Stadel (Fig. 3.5, detail 2. Table 3.3. Barbieri and Miller in press).

3.2.2 Interpretation of the data from the Lone Valley

In this last section (3.2.2) we discuss our data from the survey area in the Lone Valley opposite from Hohlenstein. Part of this section has been summarized and published in Barbieri (et al. 2018).

I. Phases of soil formation, soil erosion and possibly river incision (pre-Quaternary and Pleistocene?)

At the survey area opposite from Hohlenstein-Stadel, GL 315 (within HS-GU1) corresponds to the deepest deposit (ca. 5 m below the ground) we investigated with micromorphology. Our results show that this layer is rich in redeposited aggregates of clay and fragments of limpid, laminated clay coatings (Fig. 3.11). We conclude that GL 315 represents the earliest evidence for soil erosion we recovered from this part of the Lone Valley (Barbieri et al. 2018).

Micromorphological and FTIR analyses revealed that this deposit is extremely rich in clay (kaolinite) and is nearly free from calcite. Such composition supports the hypothesis that the abundant clay redeposited in GL 315 originated from the complete dissolution of calcium carbonate, followed by clay neoformation, and subsequent clay illuviation (Barbieri et al. 2018). In GL 315 clay coatings and clay aggregates appear fragmented and are organized in graded laminations. Such bedding is indicative for water deposition (Blikra and Nemec 1998) and thus supports the hypothesis that the clay pedofeatures we observed in GL 315 have been eroded from the soil in which they formed.

Outcrops of deposits comparable with GL 315 are documented in a few areas of the Swabian Jura, such as Hörvelsingen, Allmendingen and Schelklingen (Kösel 2016, Velliky personal communication). Ufrecht (2008a) and Kösel (2016) argued that such

deposits are possibly relict soils that formed before the Pleistocene, during phases of intensive weathering, and were exposed to erosional processes during the Quaternary. Considering that in some localities (Allmendingen and Schelklingen) these relict soils/deposits are preserved on top of the Swabian plateau, we argue that GL 315 was deposited at the bottom of the Lone Valley during a major phase of landscape erosion.

Thanks to our geophysical measurements, in the survey area opposite from Hohlenstein we detected the presence of fine deposits comparable with GL 315 over a surface of ca. 720 m^2. These deposits do not appear to be preserved in the central part of the Lone Valley, where we also documented a depression of the limestone bedrock (Fig. 3.8). We argue that the absence of fine deposits and the bedrock depression in the center of the Lone Valley resulted from a phase of river incision (Barbieri et al. 2018). Measuring the difference between the maximum elevation of the EC values comparable with GL 315 along the hillsides and the minimum elevation of the bedrock in the center of the Lone Valley, we propose that during this erosive phase the Lone may have lowered the valley floor by up to 3.5 m (Barbieri et al. 2018).

II. Phases of soil formation, soil and sediment erosion, river deposition (around 25.000 ^{14}C BP)

Based on our EC-logging and coring data we hypothesized that the alternating fine and coarse layers of HS-GU1 (among which GL 315) were likely buried by a unit composed of pebbles and boulders (HS-GU2). This coarse deposit was later covered with the dark brown sediments of HS-GU3. We studied with micromorphology the HS-GU3 layers we recovered in core 12, namely GL 36-42 (Fig. 3.15). Our results show that the dark color of these sediments likely results from the extensive impregnation of the sand- and gravel-sized components with iron-manganese oxides. Apart from a few exceptions in GL 42a, our data show that such oxidation processes took place before the deposition of HS-GU3.

Our micromorphological results revealed also the presence of fragmented, limpid clay coatings that display more distinct laminations in comparison with the clay coatings we reported from GL 315. Based on this difference in their internal organization, we hypothesized that the fragmented clay pedofeatures redeposited in HS-GU3 and HS-GU1 originated from two separate phases of soil erosion (Kühn et al. 2006. Barbieri et al. 2018).

Our macroscopic and micromorphological descriptions show that HS-GU3 is rich in gravel of Bohnerz, quartz and chert. In the Swabian Jura such components are commonly described in pre-Quaternary relict deposits (Bohnerz and quartz), local bedrock (chert) and pre-Quaternary to Pleistocene-aged karst infillings (se sections 3.2.1). We argue that these are the potential sources for most of the components accumulated in BS-GU3. Nevertheless, we tend to exclude that BS-GU3 might have originated from the erosion of cave deposits, due to the absence of components diagnostic for cave environments, such as speleothem fragments or grains of phosphatized loess.

Our micromorphological study of GL 36-42 revealed that these layers correspond to graded laminations, which display good sorting and mostly rounded components. We conclude that these layers were deposited by flowing water (Blikra and Nemec 1998). Remarkably, GL 42b, which is rich in loess-like components (silt-sized grains of quartz, micas and rare calcite), represents the earliest reworked loess deposit we have documented in this survey area. Water deposition might not been have the sole process responsible for the accumulation of the entire HS-GU3. Given their coarser gain size, lower roundness and poorer sorting, the remaining HS-GU3 deposits we recovered in core 27 and 30 might have been deposited by colluviation processes.

HS-GU3 was covered with HS-GU4. Our micromorphological results from this unit show that it is composed of reworked loess and fragmented limpid, laminated clay coatings. We detected also numerous displaced aggregates composed of smaller angular peds of silt separated by star-shaped vughs, which have been infilled with iron-manganese oxides and occasionally display pressure faces (Fig. 3.17, detail 2. Kühn et al. 2010). Towards the contact with the upper HS-GU5, the components of HS-GU4 appear to be organized into numerous sorted, coarse sand-sized, rounded aggregates which display granostriated b-fabric (Fig. 3.17, detail1).

We argue that the impregnated aggregates with star-shaped vughs and the rounded aggregates with granostriated b-fabric are comparable with frost-induced microstructures described by Van Vliet-Lanoë for silty clay deposits (Van Vliet-Lanoë 2010 p.84 and 90). The impregnated aggregates display no petrographic difference in comparison with the surrounding sediment. Furthermore the iron-managanese oxides that formed inside the star-shaped vughs occasionally expanded in the surrounding matrix (reworked. Fig. 3.17,

detail2). We conclude that these aggregates likely suffered minor displacement. Experiments conducted by Van Vliet-Lanoë (1990) and Huijzer (1993) have showed that repeated cycles of cryoturbation might lead to the disruption of clay coatings. However our data cannot deny the hypothesis that other processes might have led to the disruption of the coatings we observed in HS-GU4. Indeed they display internal organization comparable with the pedofeatures we discussed as eroded and redeposited in HS-GU3 (Kühn et al. 2010).

Apart from the specific process that might have led to their disruption, the fragmented clay coatings deposited in HS-GU3 and HS-GU4 indicate that, after the deposition and incision of HS-GU1, the Lone Valley in the Hohlenstein area experienced further phases of landscape instability. Radiocarbon measurements performed on a mixed sample of the impregnated aggregates with star-shaped vughs from HS-GU4 have yielded an age of 25.320 ± 190 ^{14}C BP (ID 19 in Table 2.1 and Table 3.2). Since this ^{14}C dating falls in the range of the Gravettian as published for the Ach Valley by Conard and Bolus (2008), we hypothesize that in the course of this phase of landscape instability Gravettian-aged deposits might have been eroded from Hohlenstein and other cave sites in the Lone Valley (Barbieri et al. 2018).

HS-GU4 was subsequently buried by HS-GU5, which is composed of well-sorted, fine, fresh to weathered, angular limestone gravel. *Bergkies* (Riek 1973, Wolff 1962, Campen 1990) and *Grèzes Litées* deposits (Bertran et al. 1992, 1994; Ozouf et al. 1995) display lithological characteristics and grain-size distribution comparable with HS-GU5 (Barbieri et al. 2018). Such sediments are regarded as debris resulting from the breakdown of bedrock exposed to repeated frost cycles. Results from the micromorphological analysis of HS-GU5 show that this unit also contains well-rounded aggregates composed of medium and coarse calcite sand coated with alternating laminations of iron-stained clay and silt (Fig. 3.18). Rose (et al. 2000) has reported similar features ("snowball") from poorly-drained sheet wash deposits of Pleniglacial age. Huijzer (1993), Bertran and Texier (1999) and Van Vliet-Lanoë (2010) have described concentric aggregates similar to those we have identified in HS-GU5 in deposits influenced by solifluction and gelifluction. We conclude that the deposition of HS-GU5 resulted from the combined action of repeated frost cycles and mass-wasting of the hillside.

HS-GU5 was later covered with HS-GU6, which is composed of polished, generally well-rounded fine to coarse limestone gravel. Comparable sizing and roundness have been observed in gravel subject to river transport of 2 to 10 km from its original source (Pearce 1971, Attal and Lavé 2009). In HS-GU6 we have also recovered more angular limestone fragments. Such fragments were deposited in HS-GU6 likely after a shorter-distance of fluvial or colluvial transport. Angular gravel and poor sorting have been commonly reported for periglacial alluvial deposits (Martini et al. 1993). The high frequency of medium- to coarse-sized limestone gravel indicates that HS-GU6 was accumulated during a phase of increased sediment supply from the hillside. Nevertheless, the fact that most of the medium and coarse gravel is well rounded and polished suggest that the Lone River was strong enough to mobilize such limestone fragments for a few kilometers (Attal and Lavé 2009).

III. Increasing deposition of loess (LGM?)

Hillside denudation and floodplain aggradation were later followed by the deposition of HS-GU7. According to our macroscopic and micromorphological descriptions, this unit is composed of reworked loess organized in laminations with graded bedding that display various degrees of iron-manganese staining (Fig. 3.22). This deposit is comparable with sheet flow deposits found across Europe (Van Steijn et al. 1995, Bertran et al. 1997, Blikra and Nemec 1998, Hétu and Gray 2000, Pawelec 2006 and Mucher et al. 2010). However, our coring and geophysical data show that HS-GU7 is localized, probably in an erosive depression, such as a narrow channel or a gully. The hypothesis that HS-GU7 might correspond to a gully/channel fill appears to be supported by the presence of rare, polished and rounded limestone gravel at the contact between GL 101 and 102.

All the redoximorphic features we observed in this unit are associated with sedimentary structures, therefore they likely not associated to phases of soil formation.

HS-GU7 appears almost free from limestone gravel and fragmented clay coatings and thus it represents a break in the sequence that we reconstructed for this part of the Lone Valley. We hypothesize that HS-GU7 resulted from increasing loess deposition which did not alternate with *Bergkies* production, significant soil formation or soil erosion. Such processes may indicate that HS-GU7 accumulated in a period dominated by colder and drier climate (Barbieri et al. 2018).

IV. Alternating phases of soil formation, soil erosion and hillside mass-wasting (Late Glacial to Holocene?)

HS-GU7 was covered with a thick sequence composed of sediments rich in angular, fresh, coarse to fine, limestone gravel embedded in reworked loess. The lower part of this sequence is occupied by HS-GU8 and HS-GU9. In HS-GU8 we did not observe sedimentary structures diagnostic for a specific depositional process. Based on the angularity of the components, the high fine to coarse fraction ratio and the moderate to poor sorting we hypothesize that HS-GU8 has been deposited by debris flows or mud flows (Blikra and Nemec 1998). HS-GU9 appears poorly laminated with graded bedding and contains few tail-like features. According to Bertran and Texier (1999) such characteristics are indicative for earth slide and earth flow deposits.

Our micromorphological results revealed that HS-GU8 and HS-GU9 contain fragmented limpid, laminated clay coatings and compound-layered coatings of clay and silt that are only in part displaced from the limestone gravel on which they had originally formed (Fig. 3.24, detail 2). In both deposits we observed numerous *in situ* and redeposited secondary calcite pedofeatures, such as hypocoatings around voids (Fig. 3.24, detail 1), cappings and pendants around limestone fragments (Fig. 3.24, detail 3 and Fig. 3.25, detail 2). Some of these pendants display alternating *laminae* of calcite and clay (occasionally even laminated clay coatings. Fig. 3.25, detail 4). Following Courty (et al. 1994), we argue that these compound coatings of calcite and clay might have formed during alternating drier and wetter periods.

HS-GU8 and HS-GU9 were covered with HS-GU10. This unit is composed of beds of reworked loess nearly depleted from calcite alternated with beds rich in gravel of limestone, chert, chalcedony and Bohnerz. Our micromorphological results revealed that both bed types contain *in situ* calcite pedofeatures, fragmented clay coatings and compound-layered coatings of silt and clay (Fig. 3.27, detail 1 and 3). In comparison with the HS-GU8 and HS-GU9, the clay pedofeatures we observed in HS-GU10 appear highly reworked. The abundant fragments of chert, chalcedony and Bohnerz deposited in the gravel beds were likely eroded from a sediment source comparable to the one of HS-GU3. Sequences similar to HS-GU10 are commonly reported from the terminal part of slopes. In some cases the alternation of finer and coarser beds has been correlated with the

periodic alternation of higher and lower energy mass-wasting triggered by snow melting (Van Steijn et al. 1995, Blikra and Nemec 1998, Hétu and Gray 2000).

HS-GU10 was followed by further deposition of well sorted, reworked, decalcified loess (HS-GU11). This deposit appears extremely rich in redeposited soil materials, such as fragmented clay coatings, compound-layered coatings of clay and silt, clay aggregates displaying clay infillings (Fig. 3.30, detail 2) and well-rounded aggregates impregnated with iron-manganese oxides (Fig. 3.30, detail 3). These components are mostly organized in graded laminations, indicating that they have been largely redeposited by flowing (possibly surface) water. Nevertheless, this unit displays very rare *in situ* to reworked, dense, incomplete to complete clay infillings (Fig. 3.30, detail 1). The occurrence of *in situ* clay pedofeatures indicate that after deposition HS-GU11 was affected by clay illuviation. In this unit secondary calcite features associated with root voids are very rare and mainly located at the contact with the upper HS-GU12, possibly indicating a relatively quick deposition of HS-GU11.

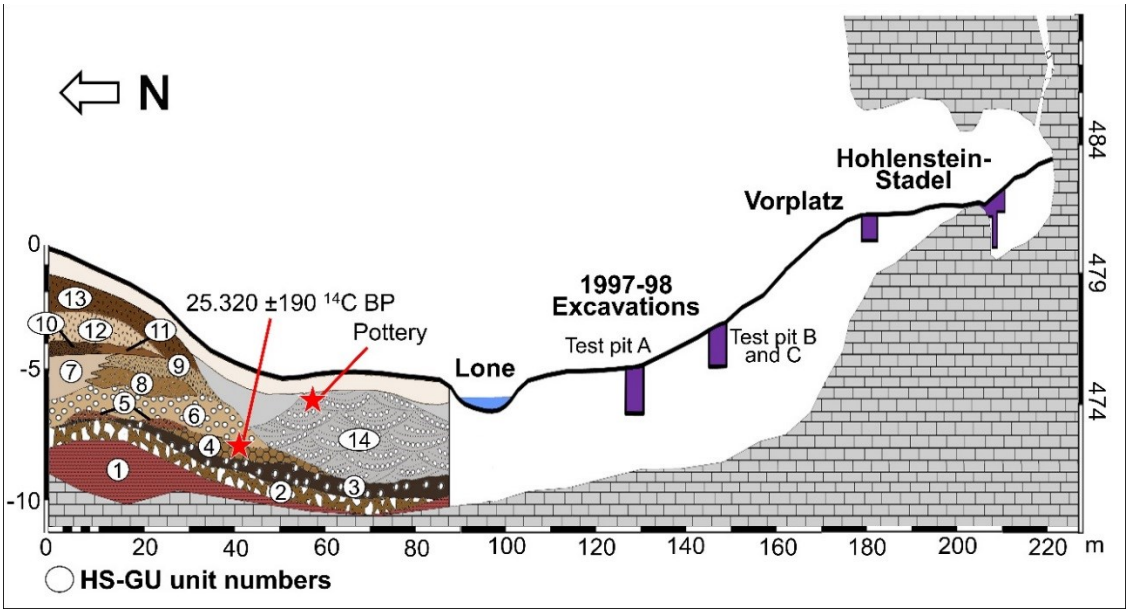

Fig. 3.40. The Lone Valley at Hohlenstein. Idealized profile crossing the valley from the cave complex of Hohlenstein to our survey area, on the opposite side of the river. Figure compiled basing on our geophysical and coring data. The location of excavations is based on Bolus et al. 1999 and Jahnke 2013 (From Barbieri et al. 2018).

V. River incision and floodplain aggradation (Late Glacial to Holocene?)

Our coring, and GPR data seem to support the hypothesis that HS-GU11, the underlying HS-GU10, 9, 8, 7, 6, 5 and possibly 4 have been removed from the center of the Lone Valley in the course of a phase of river valley incision (Fig. 3.7, Fig. 3.35 and Fig. 3.40. Barbieri et al. 2018).

Due to limits in assessing with precision of the depths of our GPR and coring data, we cannot clarify the position of HS-GU15 in relation to this disconformity (Fig. 3.37). As a working hypothesis we propose that the upper layers of this unit (GL 20-22) have been deposited after this incision. Our micromorphological results from the deposit GL 21-23 revealed that these layers are separated by interdigitated contacts. Furthermore, our micromorphological data indicate that the uppermost GL 21 and the lowermost GL 23 appear nearly identical (Fig. 3.38). Based on this observations, we hypothesize that this part of the sequence might have been affected by folding/overturning. Similar involutions have been reported from various solifluction/gelifluction deposits (Bertran and Francou 1995, Bertran et al. 1997, Bertran and Texier 1999). The hypothesis that HS-GU15 might have been deposited by gelifluction might be confirmed by the possibly platy microstructure of GL 22 (Fig. 3.38, detail 1).

We hypothesize that a phase of hillside instability followed this river valley incision, determining the emergence of a phase of flood plain aggradation (Barbieri et al. 2018). In the course of the latter, according to our reconstruction, HS-GU12 and HS-GU13 accumulated along the hillside. Our coring, GPR and micromorphological data show that HS-GU12 is composed of alternating coarser and finer beds of subangular to angular, fine to medium gravel of limestone (*Bergkies*) embedded in reworked loess. Our GPR data revealed that the beds of HS-GU12 are densely stacked in an imbricated fashion, similarly to low-viscosity debris flow relict deposits from Norway (Blikra and Nemec 1998; Barbieri et al. 2018). Our micromorphological results from this unit show that reworked, limpid clay coatings are rare, while calcite hypocoatings, calcite coatings and calcified root cells are more common. Interestingly, the composition, grain-size and pedofeatures of HS-GU12 are comparable with the late glacial deposit GL2A from the *Vorplatz* of Hohlesntein-Stadel.

While HS-GU12, HS-GU13 and possibly GL2A accumulated along the hillside, the Lone River deposited well-rounded to angular, coarse, medium and fine gravel (HS-GU14) in the floodplain (Barbieri et al. 2018. Fig.3.40 and Fig. 3.35). Based on our GPR data, we argue that after the valley incision the Lone River migrated progressively northwards (Fig. 3.35 detail A. Aspiron and Aigner 1999, Bridge et al. 1995 and 2009). During this lateral migration the river filled the previous valley incision. Once closer to the northern flank of the valley, the Lone probably caused the lateral erosion of HS-GU12 (Fig. 3.35 detail B). Basing on the presence of fragments of pottery in the upper part of HS-GU14 we hypothesize that such erosion occurred during the Holocene (Barbieri et al. 2018). Finally, the Lone migrated towards south, leading to the formation of its current course (Fig. 3.35 detail C).

4 Results from The Lone Valley downhill from Bockstein

4.1 Previous research at Bockstein

Bockstein is a cave complex which is situated about 2 km to the West from Hohlenstein, in the Lone Valley (Fig. 4.1). This site is located circa 20 m above the valley floor and is composed of 4 small cavities, which are named Bocksteinhöhle, Bockstein-Westloch, Bocksteingrotte and Bocksteinloch (Fig. 4.2).

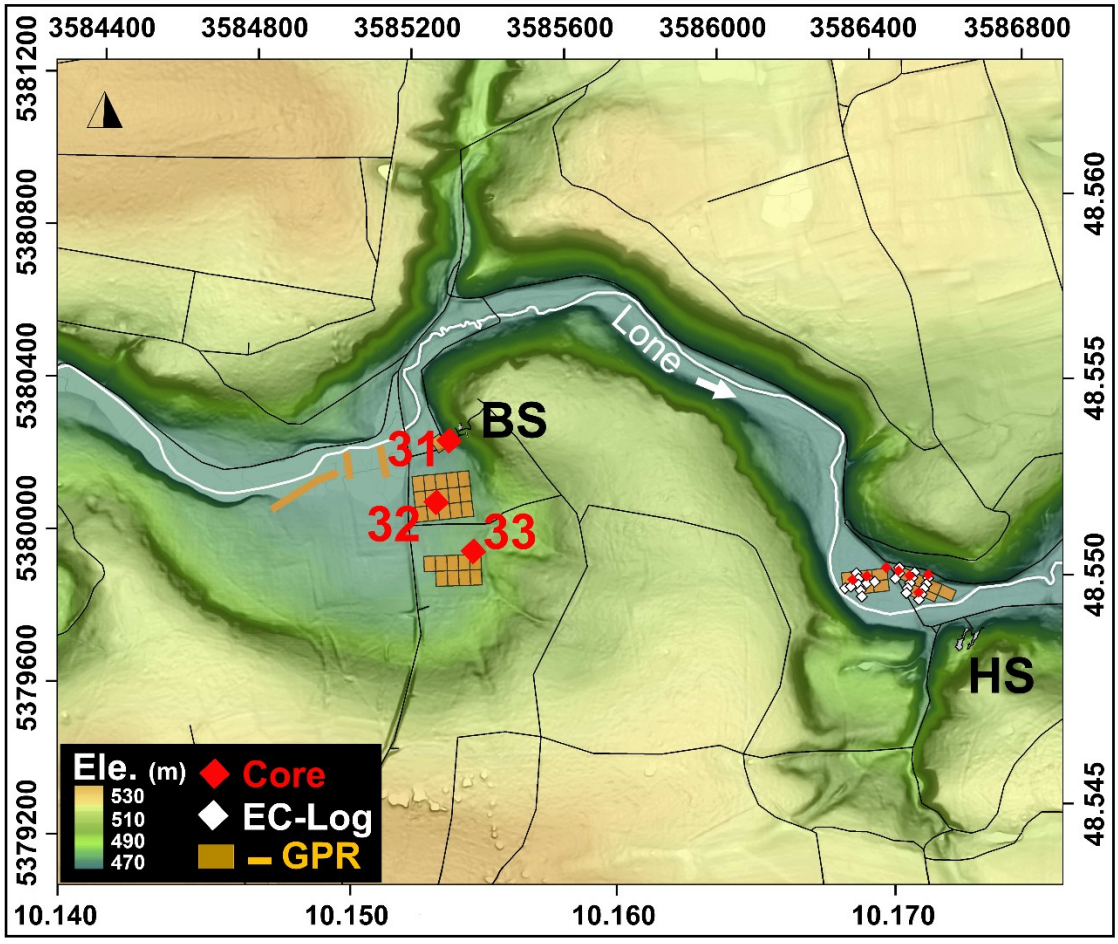

Fig. 4.1. Bockstein in the Lone Valley. Geographic map showing the areas we surveyed in front of the cave complex of Bockstein (**BK**) and Hohlenstein (**HS**). The map is compiled from Lidar data with 1 m resolution and it is projected in the DHDN Gauss-Krüger coordinate system. The labels along the upper and left axes indicate the DHDN Gauss-Krüger coordinates. The labels along the lower and right axes indicate the corresponding WGS 84 coordinates. (Figure modified from Barbieri et al. 2018).

Since the late XIX century numerous archaeological investigations lead to the extensive removal of archaeological materials and sediments from the caves of Bockstein and the surrounding hillside (Wetzel and Bosinski 1969, Krönneck 2012). In front of the cave of

Bocksteinloch, in the so called *Brandplatte* area, Wetzel exposed a sequence which is of some interest for our study. From this area he documented a deposit with mixed Upper and Middle Paleolithic stone tools, which Bosinski argued as possibly resulting from the erosion of archaeological deposits (Wetzel and Bosinski 1969). In apparent contrast with this hypothesis, Schneidermeier (1999) did not report the occurrence of archaeological materials in the cores he recovered from the Lone Valley downhill from Bockstein.

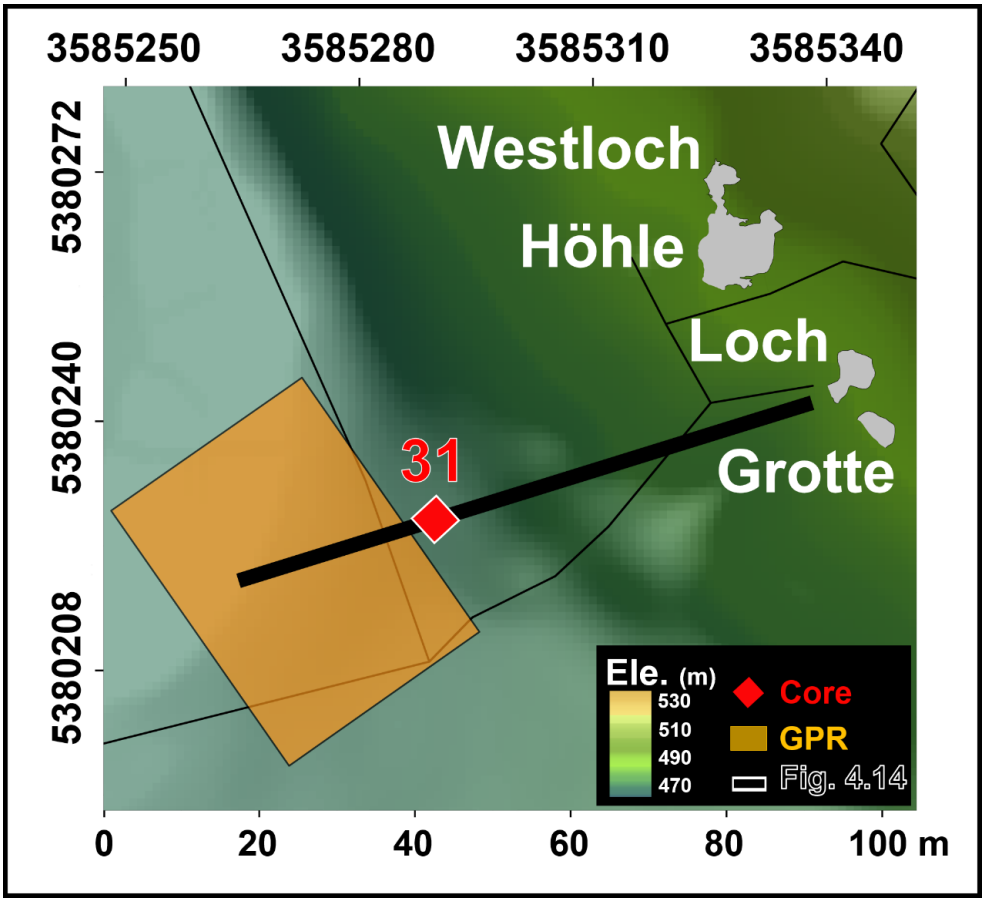

Fig. 4.2. Bockstein cave complex. Detail from the previous figure showing the various cavities that form the Bockstein cave complex, namely Bocksteinhöhle (**Höhle**), Bockstein-Westloch (**Westloch**), Bocksteingrotte (**Grotte**) and Bocksteinloch (**Loch**). Figure modified from Barbieri (et al. 2018). The map is compiled from Lidar data with 1 m resolution and it is projected in the DHDN Gauss-Krüger coordinate system. The labels along the upper and left axes indicate the DHDN Gauss-Krüger coordinates. The labels along the lower axis corresponds to a scale bar.

In the last decades, archaeological investigations at this cave complex have focused on the study of the materials recovered from the excavation conducted in the previous century. Of particular relevance for this dissertation are the radiocarbon measurements and the re-evaluation of the lithic industries published, in the early 2000s, for the cave of

Bockstein-Törle (Borges de Magalhães 2000, Conard and Bolus 2003). These analyses show that Gravettian humans occupied this cave between ca. 31.500 ^{14}C BP and 21.000 ^{14}C BP (Borges de Magalhães 2000, Conard and Bolus 2003). By far, this represents the most convincing evidence for the presence of Gravettian groups in the Lone Valley (see chapter 1.2.1).

4.2 Results

With the aim of verifying the hypothesis that cave erosion might have occurred at this site, we investigated this part of the Lone Valley with several survey campaigns. Since the slope closer to the Bockstein caves has been significantly disturbed by archaeological excavations we focused our prospections in the floodplain downslope from this cave complex. Here we collected several freely-oriented lines and 20 GPR grids, each measuring 30x40 m (Fig. 4.1). The grids were set up with a spacing of 1 to 2 m along both *x* and *y* axes. Unlike at the survey areas of Hohlenstein and Hohle Fels, at Bockstein our GPR prospection was less successful, due to the presence of thick, shallow silty deposits, which caused significant attenuation of the radar signal. We detected relevant sedimentary structures only in Grids 1-4 and 20, where the sediments buried below the soil appear richer in gravel content. From these "gravel rich" areas we collected two cores, core 33 and 31, respectively. We recovered the remaining core 32 roughly from the center of our survey area, where the penetration of the GPR signal appeared more attenuated (Fig. 4.1 and Fig. 4.3).

As for the data we collected from the Hohlenstein area, part of the data we collected from the Bockstein area is published in a dedicated article (Barbieri et al. 2018). In the following section we take the opportunity to provide more details regarding our data and their interpretation (the entire description of the GL is in Appendix III).

Depth to Bedrock

In Grid 1 of our GPR survey we detected a 4m-deep sequence of potential sedimentary structures (Fig. 4.3). The lowermost reflected phase we measured in this grid is located between 2 and 4 m below the ground surface, has a "cliff-like" appearance and displays velocities between 0.08 and 0.09 m/ns, comparable to those published for limestone bedrock (Davis and Annan 1989. Fig. 4.3, *bedrock*). On top of this feature we detected a sequence of densely stacked reflectors displaying velocities around 0.08 – 0.06 m/ns,

comparable with gravel and silty clay (Davis and Annan 1989. Fig. 4.3, *gravel* and *silty-clay*). This deposit is truncated by an upper reflected phase that lies at about 1-2 m below the ground surface and describes a 10 to 30 m wide, East-West oriented depression.

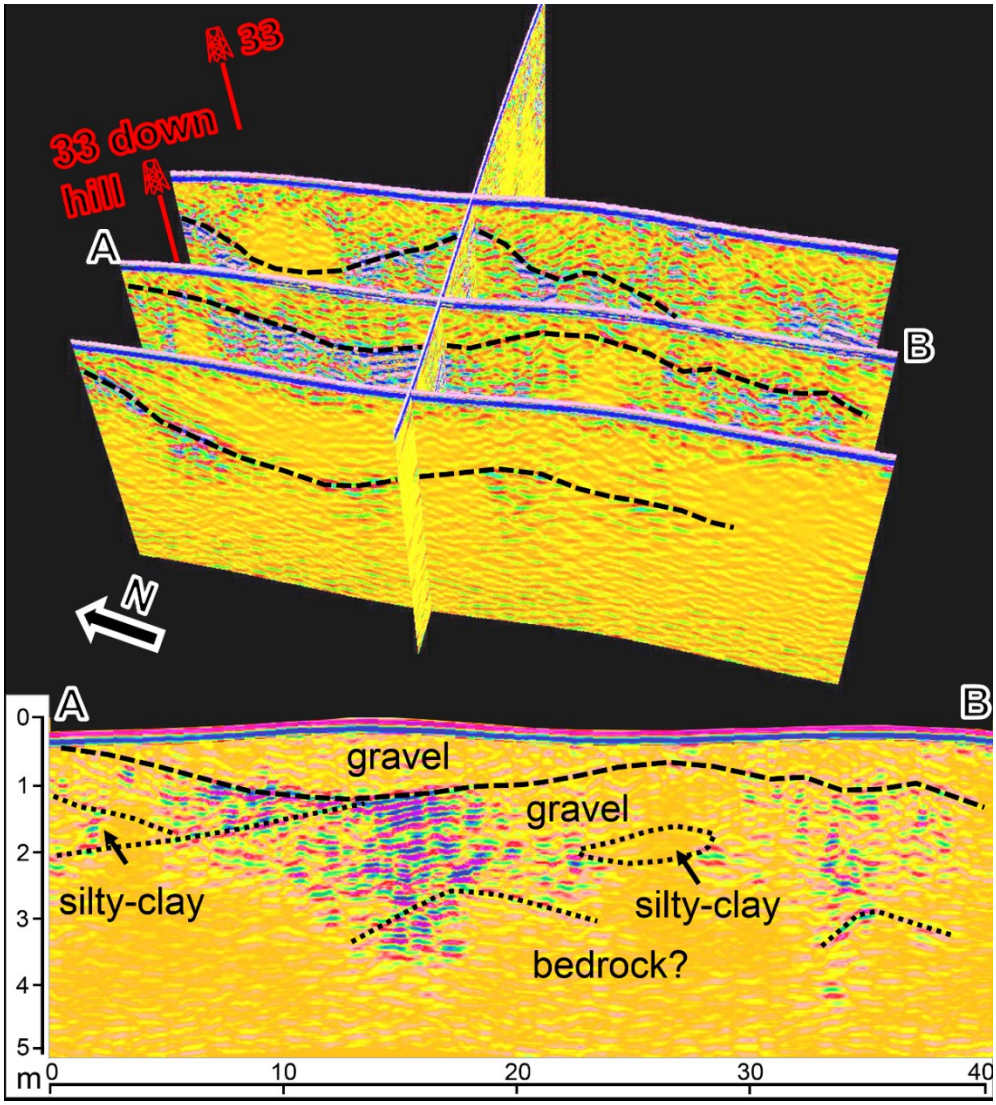

Fig. 4.3. GPR data from Grid 1, nearby core 33. ***In the upper part***, 3D plot of selected GPR profiles measured in Grid 1. In these profiles it is possible to trace a large disconformity (**black dashed line**) located around 1 m below the ground surface. ***In the lower part***, detail of GPR profile from the upper 3D plot (**AB**). Explanation of the figure is in the text.

We attempted to recover core 33 from Grid 1; however, during the drilling of this borehole the Geoprobe started to slide downslope because of a sudden increase in temperature and consequent melting of the ground ice. Thus, we decided to terminate the drilling of this core and recovered a new core (33 uphill) from upslope Grid 1, in a flatter area (Fig. 4.3). The depth we reached with this core (1.3 m) might be indicative of shallow bedrock, which would agree with our GPR measurements. On the contrary, the greater

depth reached with core 32 and 31 (> 4 m) would suggest that northwards of core 33 the bedrock is much deeper. Unfortunately our coring and geophysical data are not sufficient to further reconstruct the depth and geometry of bedrock nor the deepest deposits buried in front of Bockstein.

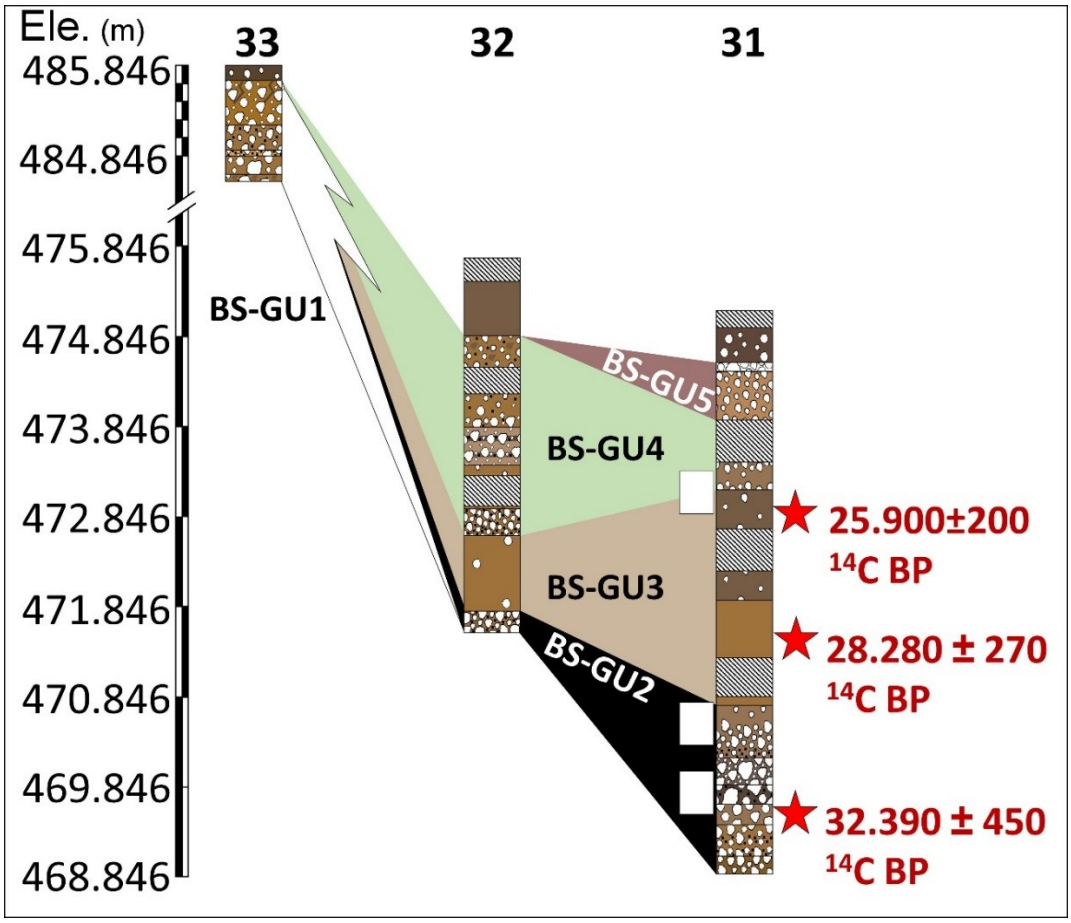

Fig. 4.4. Cross-correlation of the cores collected in front of Bockstein. White rectangles indicate the analyzed micromorphological samples, red stars mark the location of dating material. Figure from Barbieri (et al. 2018).

BS-GU1

In BS-GU1 we grouped all the sediments we recovered from core 33 (Fig. 4.4 and Fig. 4.5). This unit is composed of sediments very rich in medium and coarse angular limestone gravel, embedded in a yellowish brown silty clay (10YR 5/6 and 5/8). In the lower GL (246 to 248), together with fresh limestone fragments, we observed very common yellowish, fragile, weathered fine limestone gravel. GL 248, at the bottom of this unit, presents a composition and matrix color comparable with the lowermost GL 318 from HS-GU1.

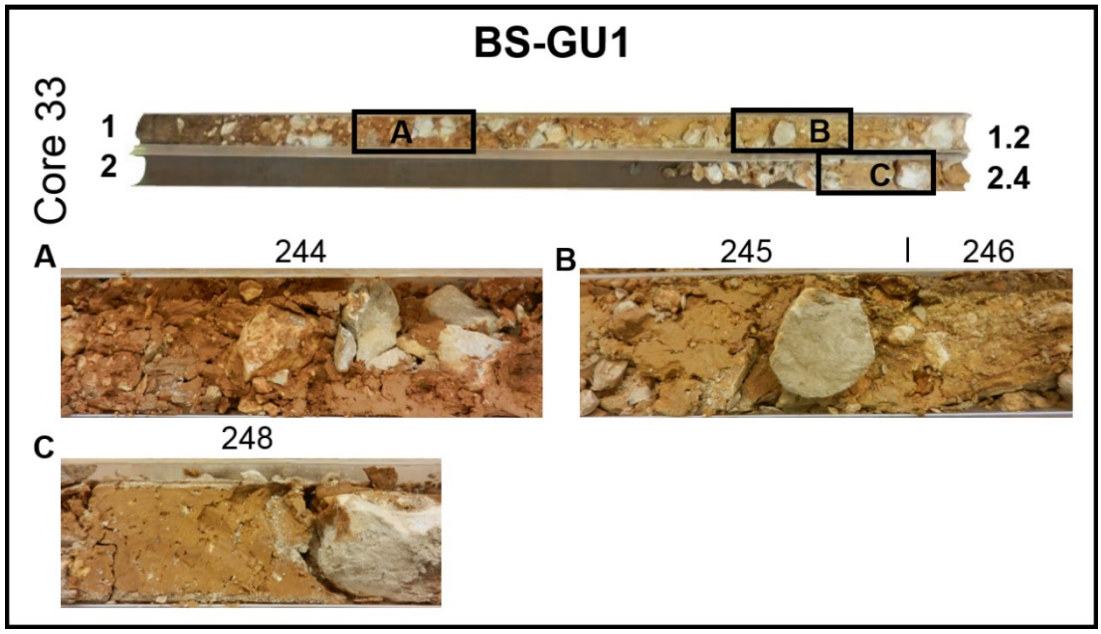

Fig. 4.5. BS-GU1. ***In the upper part***, the liners of core 33. ***In the lower part***, details from the main GL (numbered in the figure) which are discussed in the text.

BS-GU2

The last two liners of core 31 and the very bottom of core 32 are occupied by fine to coarse gravel of limestone, chert and Bohnerz embedded in silty sand (Fig. 4.4 and Fig. 4.6). These components are organized in two distinct bed types. On one hand, well-rounded, clast supported gravel occasionally alternating with sandy layers (GL 263, 264 and 269 in core 31 and 256 in core 32). On the other hand, matrix supported beds, with little angular gravel (GL 265, 266, 267 and 268 in core 31).

Within the latter bed type, GL 266 exhibits a distinctive dark color of the matrix (10YR 3/2), which is probably resulting from the extensive impregnation of the matrix with iron-manganese oxides. In this layer we also recovered chert fragments up to coarse gravel-sized, some of which have been considerably broken during the core drilling (Barbieri et al. 2018).

The lower GL 267 is composed of subangular to subrounded medium gravel of limestone and Bohnerz embedded in a yellowish brown matrix (10 YR 5/4). In the matrix we identified also sand-sized aggregates of silt, which appeared dark brown to reddish brown in color. We collected a sample of these aggregates and, after a positive check with FTIR, we dated their total organic carbon to 32.390±450 ^{14}C BP (Table 2.1 and Table 4.1, ID 72).

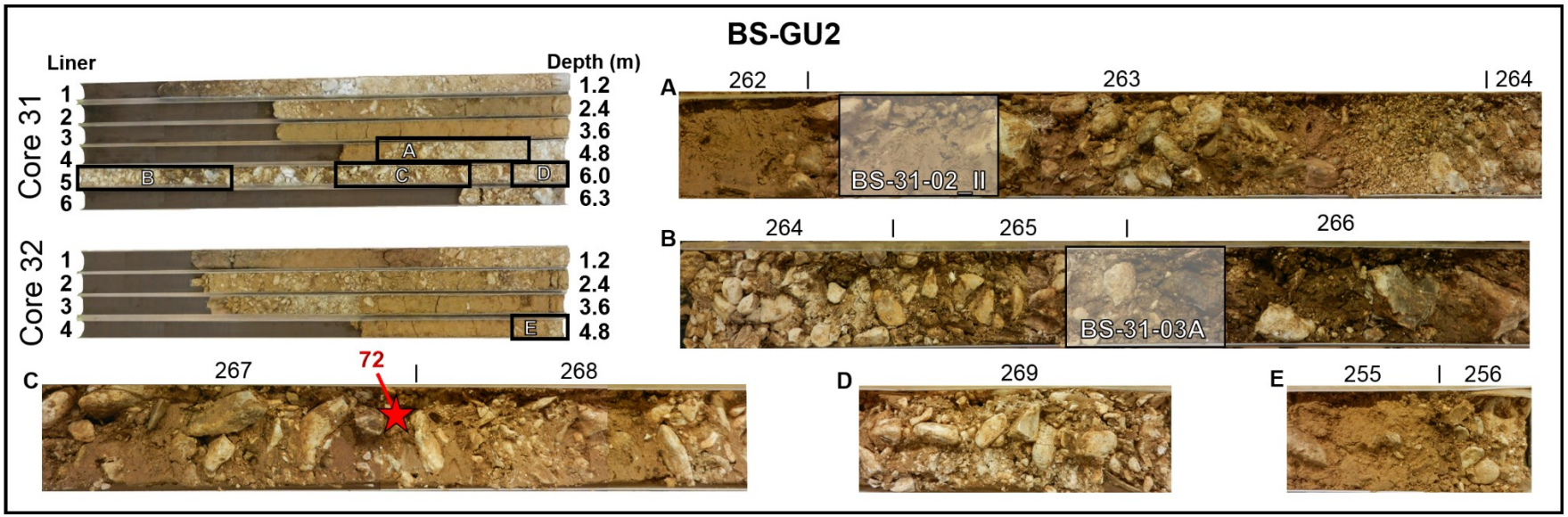

Fig. 4.6 BS-GU2. ***In the upper left***, the liners of cores 31 and 32. ***A***, ***B***, ***C***, ***D***, ***E***, details from the main GL (numbered in the figure) which are discussed in the text. ***BS-31-02_II*** and ***BS-31-03A***, indicate the location of the micromorphological samples displayed in Fig. 4.7. The red star marks the location of the dating sample (ID ***72***) discussed in the main text

We covered the contacts GL 262-263 and GL 265-266 with three block samples for micromorphological analysis. We processed two of these samples, from which we produced and analyzed two thin sections (BS-31-2-II and BS-31-03A). The uppermost layer we analyzed in thin section BS-31-2-II is GL 263. This layer, as noted in the sediment description, is almost free from redoximorphic features, which are occasionally present in rare, graded, sandy and silty laminations (Fig. 4.7, detail 1). The matrix of GL 263 is composed of reworked loess (silt-sized grains of quartz and micas), snail shell fragments and clay, which is much less abundant than in the lower GL. Fragmented, limpid clay coatings and weathered, fine gravel-sized fragments of chert are rare. Limestone fragments are subrounded, with smoother borders and are coated with secondary calcite, which also occurs as hypocoatings around root voids.

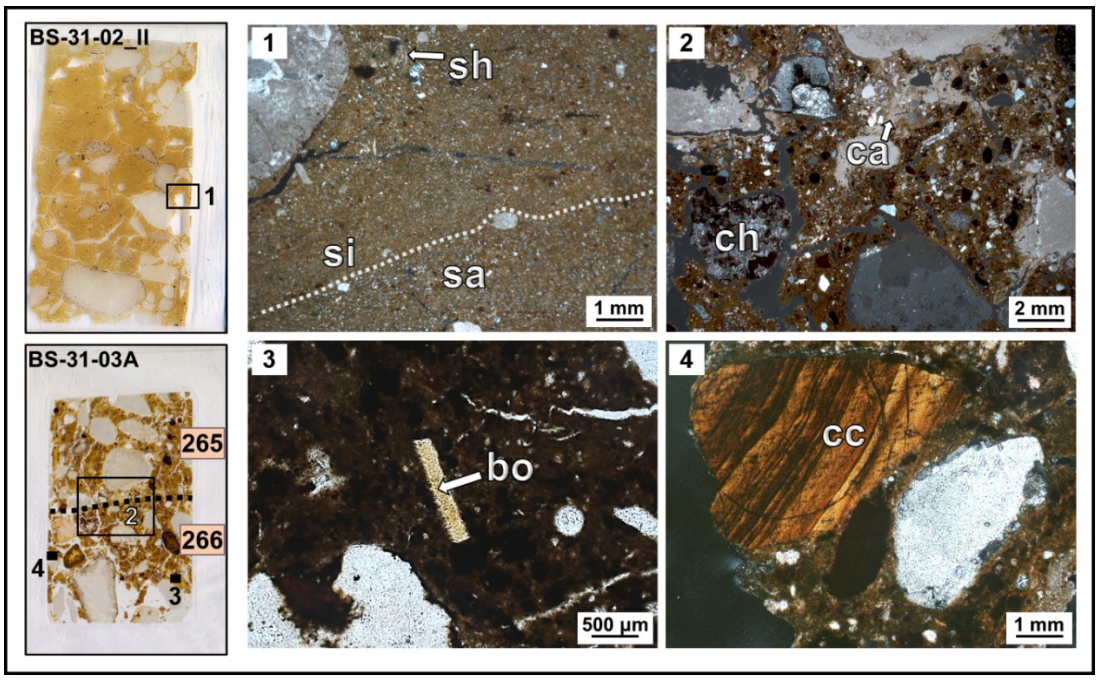

Fig. 4.7. Micromorphological results from BS-GU2. ***On the left***, thin section scans of the samples ***BS-31-02_II*** and ***BS-31-03A***. GL are labelled in pink. ***1***, photomicrograph in XPL from GL 263 showing graded laminations of silt (**si**) and sand (**sa**), containing also shell fragments (**sh**). ***2***, photomicrograph from the contact between GL 265 and 266. In the upper part, abundant secondary calcite (**ca**) coming from the weathering limestone gravel. ***3***, photomicrograph in PPL from GL 266 showing one bone fragment (**bo**). ***4***, photomicrograph in XPL from GL 266 showing one fragment of limpid, laminated clay coating (**cc**).

The upper sediment sampled in thin section BS-31-03A is GL 265. In comparison with GL 263, this layer is richer in secondary calcite, which appears to come from the weathering of the more abundant limestone gravel (Fig. 4.7, detail 2). In GL 265 silt-

sized grains of quartz and micas are more abundant. The contact with the lower GL 266 appears diffuse and marked by a decrease in secondary calcite, silt-sized grains of quartz and micas (Fig. 4.7, detail 2). Gravel fragments are more angular and are composed of chert, chalcedony, Bohnerz, limestone, which, together with the groundmass, appear extensively impregnated with iron-manganese oxides. We have also observed disorthic and orthic iron-manganese nodules, redeposited soil aggregates, very rare fragments of bone (the largest measuring 500 μm, Fig. 4.7, detail 3) and fragmented laminated, limpid clay coatings (Fig. 4.7, detail 4). The groundmass displays striated to granostriated b-fabric.

BS-GU3

We recovered GL 261 and 262 in the third liner of core 31 and GL 255 in the third liner of core 32. We grouped these layers in BS-GU3. This deposit is composed of laminated, yellowish brown (10YR 5/6) and dark grayish brown (10YR 4/3), silt and clayey silt alternated with beds of rare, fine to medium, subangular to subrounded limestone gravel (Fig. 4.4 and 4.8). From all of these layers we report the occurrence of snail shell fragments up to 1 cm in size (Barbieri et al. 2018).

ID	$\delta^{13}C$ (± 0.1‰)	^{14}C age		Calibrate age 95%	
		(^{14}C BP)	±	(BC/AD)	(BP)
69	-9.7	25900	200	28741 – 27622 BC	30690 - 29571
73	-7.3	28280	270	31029 – 29497 BC	32978 - 31446
72	-24.6	32390	450	35912 – 33396 BC	37861 - 35345

Table 4.1. Radiocarbon determinations from core 31. In this table we present the results of the radiocarbon determination performed on ID 69, ID 73 (from BS-GU3) and ID 72 (from BS-GU2. The ID used by the laboratory in Tucson is reported in Table 2.1). The table includes ***$\delta^{13}C$ (± 0.1‰)***, the estimated radiocarbon age (***^{14}C age***, ***^{14}C BP***) and its uncertainty (±). We also present the corresponding calendar years Before/After Christ (***BC/AD***) and Before Present (***BP***), which we obtained performing a 2σ calibration with the program OxCal 4.3 (curve IntCal 13).

In order to assess their suitability for ^{14}C dating, we collected two samples of shell fragments at 4 ± 0.05 m and 2 ± 0.05 m below the ground surface. The results from FTIR analysis show that both shell specimens exhibit absorption bands of aragonite at 1475, 1083, 858, 712 and 700 cm^{-1} (in Fig. 4.9 we have displayed the spectra of the most representative shell sample, ID 7. Barbieri et al. 2018). The absence of calcite indicates good preservation of the mineral fraction, suggesting that the gastropods have been buried shortly after their death. Radiocarbon measurement performed on the ID 73 gave a date

of 28.280±270 ^{14}C BP (Table 4.1), while ID 69 yielded an age of 25.900±200 ^{14}C BP (Table 4.1).

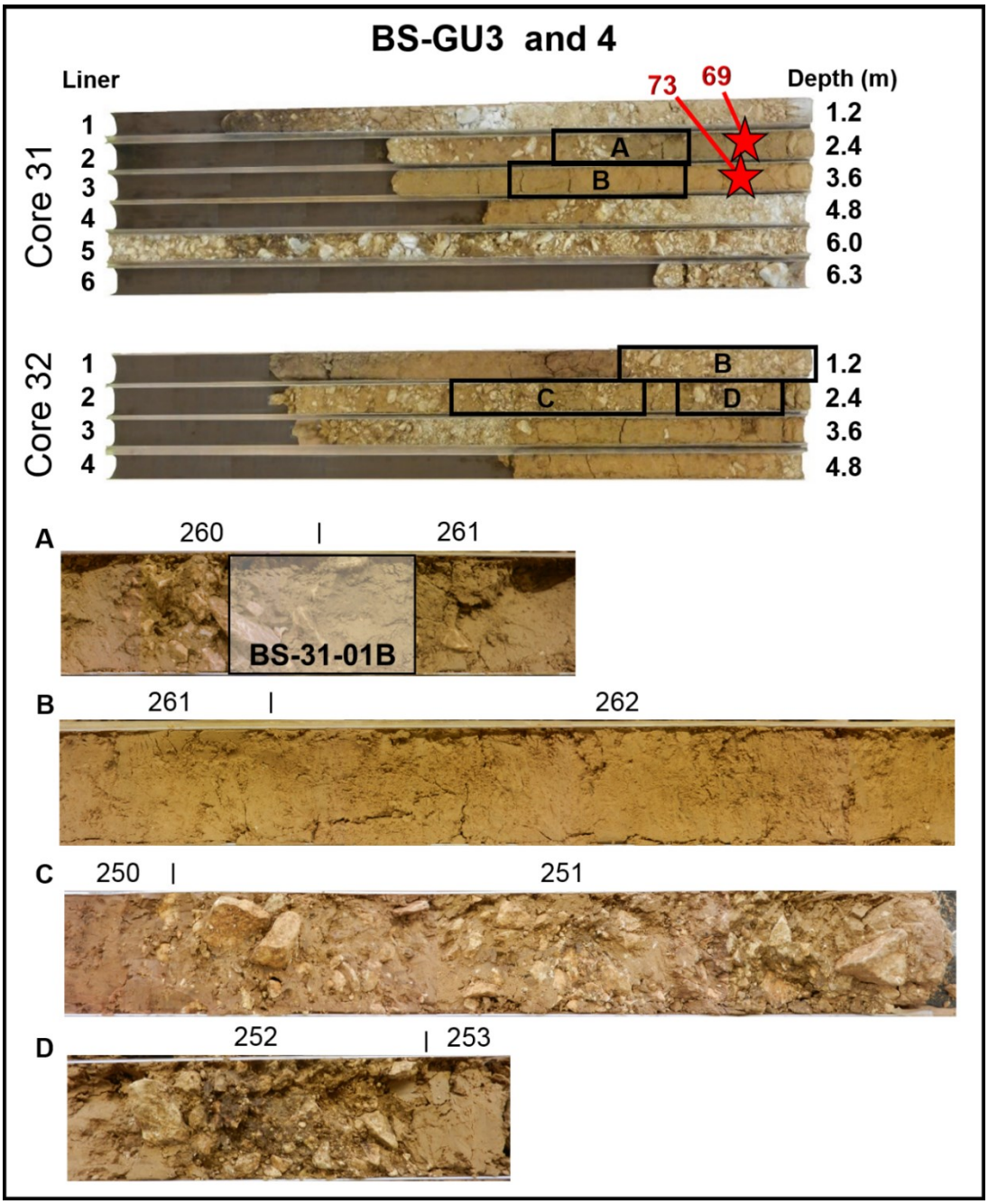

Fig. 4.8. BS-GU3 and 4. ***In the upper left***, the liners of cores 31 and 32. ***A***, ***B***, ***C***, ***D*** details from the main GL (numbered in the figure) which are discussed in the text. ***BS-31-01B***, indicates the location of the micromorphological sample displayed in Fig. 4.10. Red stars indicate the dating samples (ID ***73*** and ***69***) discussed in the main text.

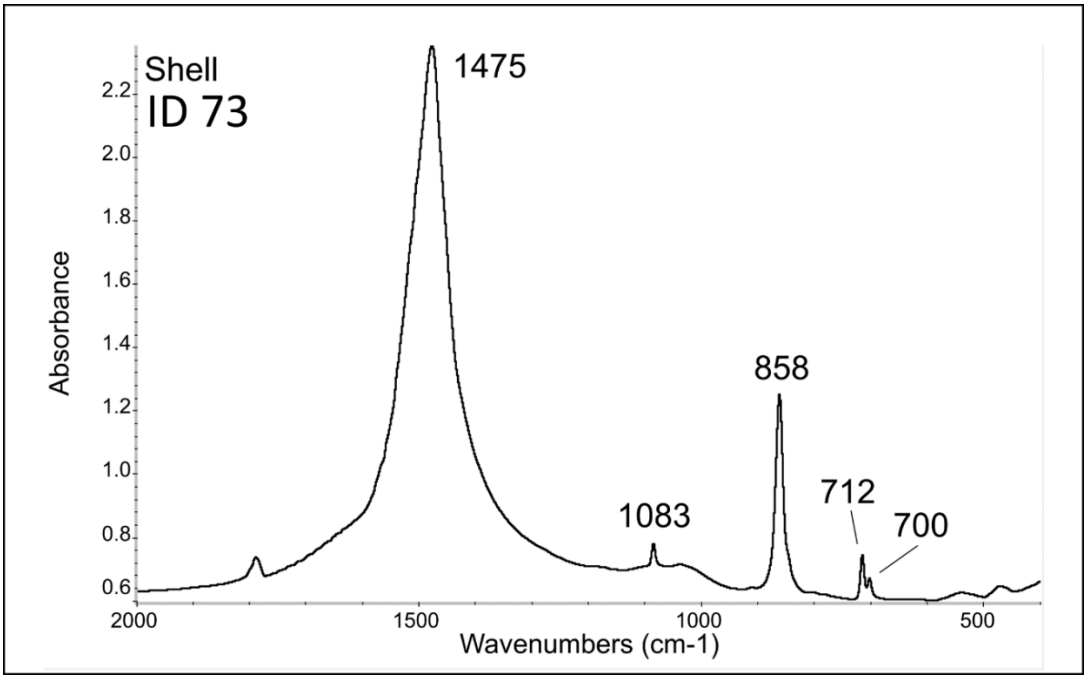

Fig. 4.9. FTIR spectra representative for shell specimens from BS-GU3. This specimen exhibits absorption bands of aragonite at 1475, 1083, 858, 712 and 700 cm^{-1}. Figure modified from Barbieri (et al. 2018).

We sampled the passage from BS-GU3 to BS-GU4 with one block sample for micromorphological analysis, producing one thin section: BS-31-01B, which covers GL 260 (from BS-GU3) and GL 261 (from BS-GU4). The results show that GL 261 is largely composed of reworked loess and fragments of snail shells, bone and very rare, 100 µm-large fragments of limpid, laminated clay coatings. Furthermore we documented medium sand-sized aggregates formed of rare quartz grains and micas embedded in a phosphatic groundmass (Fig. 4.10, detail 1 and 2). From a structural point of view, GL 261 presents very weak laminations displaying different amounts of clay and iron-manganese staining (Fig. 4.10, detail 1). We also observed weakly-developed, dusty clay coatings around coarser components, well-developed calcite hypocoatings around root voids, and secondary calcite replacement of root remains (Fig. 4.11, detail 1).

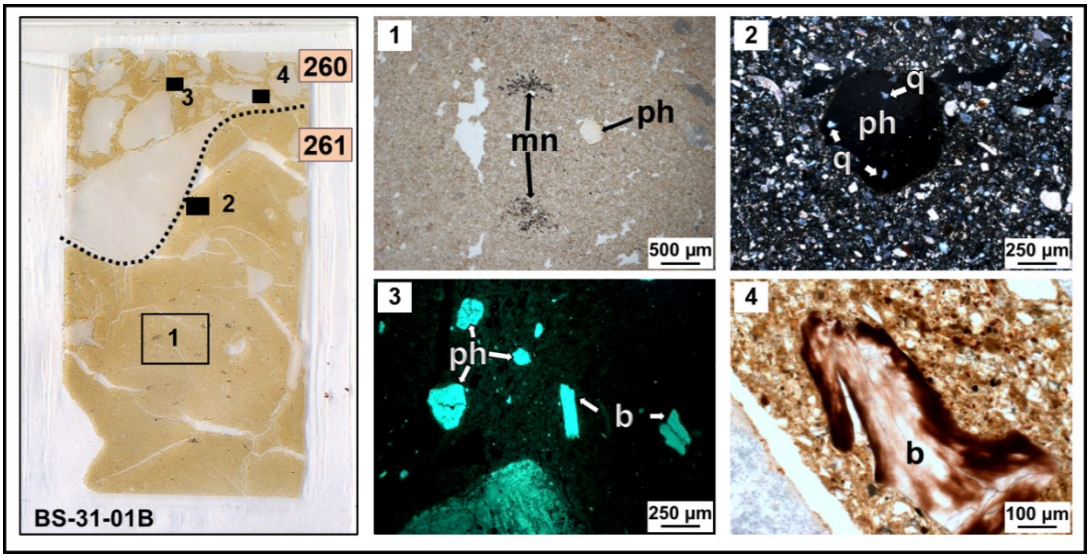

Fig. 4.10 Micromorphological evidence for cave erosion in BS-GU3. ***On the left***, thin section scan of sample BS-31-01B. GL are lebelled in pink. ***1***, photomicrograph in PPL from GL 261 displaying sand-sized grains of phosphatized loess (**ph**) and dendritic manganese staining of the groundmass with iron-manganese (**mn**). ***2***, photomicrograph in XPL from GL 261 displaying sand-sized grains made from silt-sized grains of quartz (**q**) embedded in a phosphatized groundmass (**ph**). Basing on this compositional characteristics we interpret this type of grains as phosphatized loess. ***3***, photomicrograph in FL from GL 260 displaying more abundant fragments of grains of phosphatized loess (**ph**) and bone (**b**). ***4***, photomicrograph in PPL from GL 260 showing a possibly burnt bone fragment (**b**).

BS-GU4

From the upper part of liner 2 in core 31 (GL 260) and from the central part of core 32 (GL 250-254) we recovered yellowish brown (10YR 5/6 and 5/4) silty clay-rich sediments alternating with angular limestone gravel (Fig. 4.4 and Fig. 4.8). The gravel laminations of GL 252 present very dark grayish brown lenses (10YR 3/2), likely resulting from iron-manganese oxides. In GL 260 we documented numerous fragments of snail shells, but these were too small to be sampled for radiocarbon dating. In core 32 BS-GU3 lies directly below the Holocene soil (Barbieri et al. 2018).

The upper part of thin section BS-31-01B covers a gravel lamination corresponding to the lowermost part of GL 261 in core 31. In terms of composition, GL 261 presents substantial similarities with the underlying GL 260. The main difference is represented by the increase in mean grain size and gravel content, which is composed of unsorted, fresh, angular to rounded limestone fragments. In GL 261 fragments of bone and phosphatized grains of loess are even more abundant than below and appear larger in size (500 µm maximum length. Fig. 4.10, detail 3 and 4). In this layer also calcite pedofeatures

are more abundant with calcite hypocoatings, calcified root cells and infillings of fine sand-sized crystals of calcite (Durand et al. 2010. Fig. 4.11, detail 2).

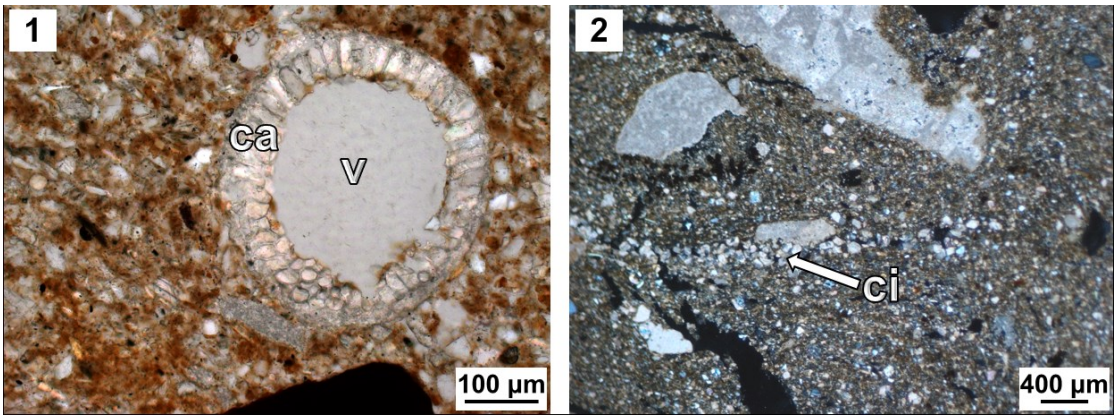

Fig. 4.11. Calcite pedofeatures from BS-GU3 and BS-GU4. ***1***, photomicrograph in PPL from BS-GU3 depicting calcite replacement of root cells (**ca**) around root void (**v**). ***2***, photomicrograph in XPL from BS-GU4 showing one calcite infilling (**ci**, Durand N. et al. 2010).

BS-GU5

Below the Holocene soil, in core 31 we recovered GL 257-259, which are composed of fine, medium to coarse, loose, angular, openwork limestone gravel (Fig. 4.4 and Fig. 4.12). Given the loose nature of this deposit we decided not to investigate it with micromorphological analysis.

The presence of shallow units richer in silt (such as BS-GU3 and BS-GU4) limited the penetration of our GPR measurements along the hillside in the Bockstein area. Only in Grid 1 (see above) and Grid 20 could our geophysical data reveal clear structures (Fig. 4.13). Grid 20 is located a couple of meters downslope from core 31, in this grid our GPR measurements detected 8x4 m-large reflectors located 20 cm below the ground surface and densely stacked in an imbricated fashion (Blikra and Nemec 1998. Fig. 4.13, *gravel*). Such imbricated bedding is comparable with the one we reconstructed for HS-GU12 (Fig. 3.31, p. 86).

The feature we detected by GPR in Grid 20 displays depth, thickness and possible grainsize (Davis and Annan 1989) comparable with the limestone beds of BS-GU5. Furthermore, the GPR data suggests that this unit is not laterally continuous and possibly covers a silty deposit that was not recovered within core 31 (Fig. 4.13, *silty clay*).

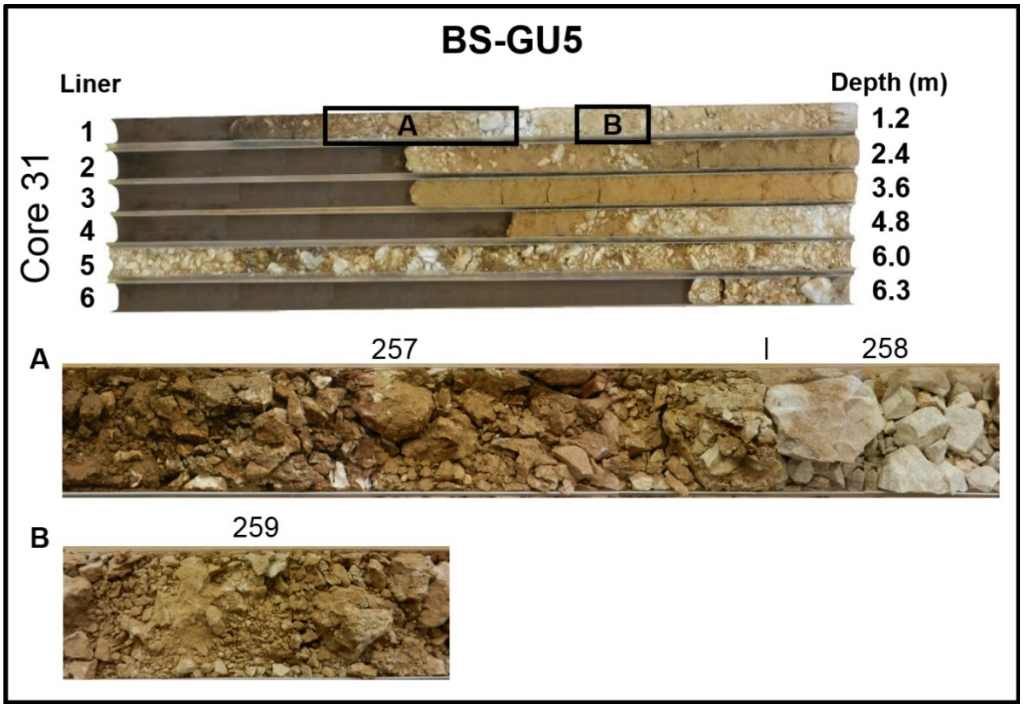

Fig. 4.12. BS-GU5. ***In the upper part***, the liners of cores 31. ***A***, ***B*** details from the main GL (numbered in the figure) which are discussed in the text.

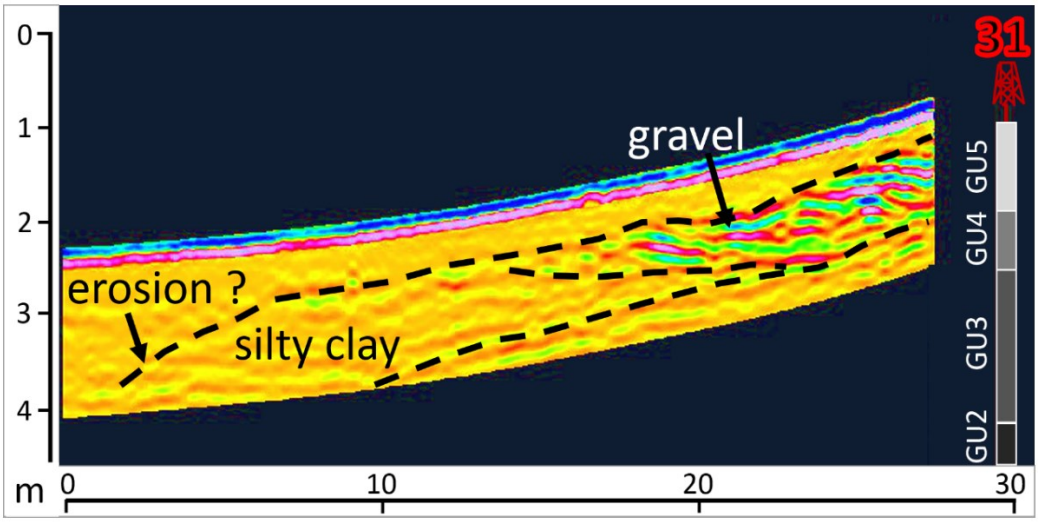

Fig. 4.13. Bedding of BS-GU5 in the geophysical data. GPR profile from Grid 20, collected along the slope downhill from core 30 (numbered and depicted in red). BS-GUs are numbered in the figure and depicted in grayscale. The GPR profile clarifies the structure of BS-GU5, which appear to be formed from gravel beds (**gravel**), densely stacked in an imbricated fashion (Blikra and Nemec 1998). Interestingly BS-GU2 displays bedding comparable to HS-GU12 (see Fig. 3.31 in Chapter 3).

4.3 Data interpretation

In this section we provide our interpretation of the data we collected from the Lone Valley in front of Bockstein, which have also been summarized elsewhere (Barbieri et al. 2018). We also propose potential correlation between the sequence we recovered from this part of the Lone Valley and the survey area opposite from Hohlenstein. These aspects are further discussed in the last chapter of this dissertation.

I. Bedrock weathering, possible colluviation, river deposition (before 32.000 ^{14}C BP)

Our coring and GPR data show that BS-GU1 lies directly on the bedrock in the South-East corner of our survey area. BS-GU1 is mostly unsorted and composed of angular, fresh and weathered limestone gravel (Fig. 4.5). The deepest GL 248 from BS-GU1 displays composition and matrix color similar to the lowermost GL 318 from HS-GU1. Based on these data we hypothesize that BS-GU1 was formed by the combined action of colluviation and bedrock alteration. Due to its similarities with HS-GU1 we propose that at least part of BS-GU1 is probably present also in the rest of the survey area, where it might rest deeper than 6.3 m (the maximum depth we reached in core 31).

The lowermost layers we recovered from cores 31 and 32 (respectively GL 269 and 256) are composed of nearly dry, well-rounded, polished fine to medium limestone gravel (Fig. 4.6, detail E and D). These layers display grain size, roundness and sorting comparable with HS-GU6, which we interpreted as being deposited in a fluvial system (Pearce 1971, Attal and Lavé 2009). Our findings from GL 269 and 256 are comparable with potential river deposits which Wetzel (1958) reported from test pits excavated further downhill from our core 31.

In core 32, GL 256 appears truncated, as indicated by the clear to sharp contact marking the transition with the upper GL 255 (BS-GU3). In core 31 the transition from GL 269 to GL 268 and GL 267 appears more gradual and it is marked by the progressive increase in fine fraction content and angularity of the coarse components.

II. Soil formation and soil erosion (before 32.000 ^{14}C BP-26.000 ^{14}C BP)

The micromorphological results from GL 266 revealed the presence of fragmented, laminated clay coatings, reworked soil aggregates and *in situ* (orthic) to displaced (disorthic) manganese nodules (Fig. 4.7). Due to the presence of redeposited clay

coatings, we interpret GL 266 as the earliest, consistent evidence for soil erosion in the Bockstein survey area. Based on our dating from GL 267 (32.390±450 ^{14}C BP), we argue that before 32.000 ^{14}C BP the surrounding of the Bockstein cave complex experienced a phase of soil formation in which clay illuviation had taken place (Barbieri et al. 2018). The hypothesis that before 32.000 ^{14}C BP the Lone Valley in front of Bockstein was a stable landscape is also supported by faunal analysis from the Aurignacian deposit of Bockstein-Törle (Krönneck 2012), which revealed the occurrence of mammal species indicative of steppe and forest environments.

This phase of soil formation was later followed by a period of landscape instability during which the soil was eroded and redeposited in GL 266 (Barbieri et al. 2018). The redoximorphic features we observed in this layer display only minor reworking (orthic to disorthic) and thus they might have formed during or after the accumulation of GL 266.

GL 266 exhibits composition, matrix color and stratigraphic position comparable with HS-GU2 (see Chapter 3). Since the area we investigated in front of Bockstein is located only 2 km away from Hohlenstein, we conclude that GL 266 and HS-GU2 are likely the result of the same, or similar, geomorphological, regional processes.

III. Potential minor cave erosion (before 32.000 ^{14}C BP-26.000 ^{14}C BP)

Along the slope uphill from our core 31, Wetzel exposed sediments that display composition, matrix color, and depth comparable with our GL 266. Embedded in this sediment, in front of the Bocksteinloch cave (*Brandplatte* area Fig. 4.14), Wetzel recovered mixed Upper and Middle Paleolithic artefacts. As previously mentioned (section 4.1), Bosinski argued that these archaeological materials might have been deposited during a phase of cave erosion (Wetzel and Bosinski 1969).

Although our stratigraphic correlation seems correct, our data cannot fully support the hypothesis that GL 266 might have been deposited by colluvial processes originating from the Bockstein caves (Barbieri et al. 2018). In fact, from this layer we reported very rare sand-sized fragments of bone (500 μm max size) but we did not recover isolated grains of phosphatized loess, speleothem fragments, or other sedimentary components that specifically originate from a cave system.

Further downhill from our cores, Schneidermeier (1999) reported sediments comparable with the sequence we presented in this chapter and did not mention the recovery of artifacts nor bones in his cores.

IV. Potential river deposition (32.000-26.000 ^{14}C BP)

The uppermost layer from BS-GU2 (GL 264) is composed of nearly dry, fine to coarse subrounded gravel of limestone and bohnerz (Fig.4.6, detail B). This layer displays composition, grainsize and fine:coarse ratio indicative for river deposition (Pearce 1971, Attal and Lavé 2009). The higher angularity of the gravel in GL 264 (subrounded) does not contrast with our interpretation, since gravel with such roundness has been commonly reported from periglacial alluvial deposits (Martini et al. 1993). Furthermore, higher angularity can also be related to shorter-distance transport.

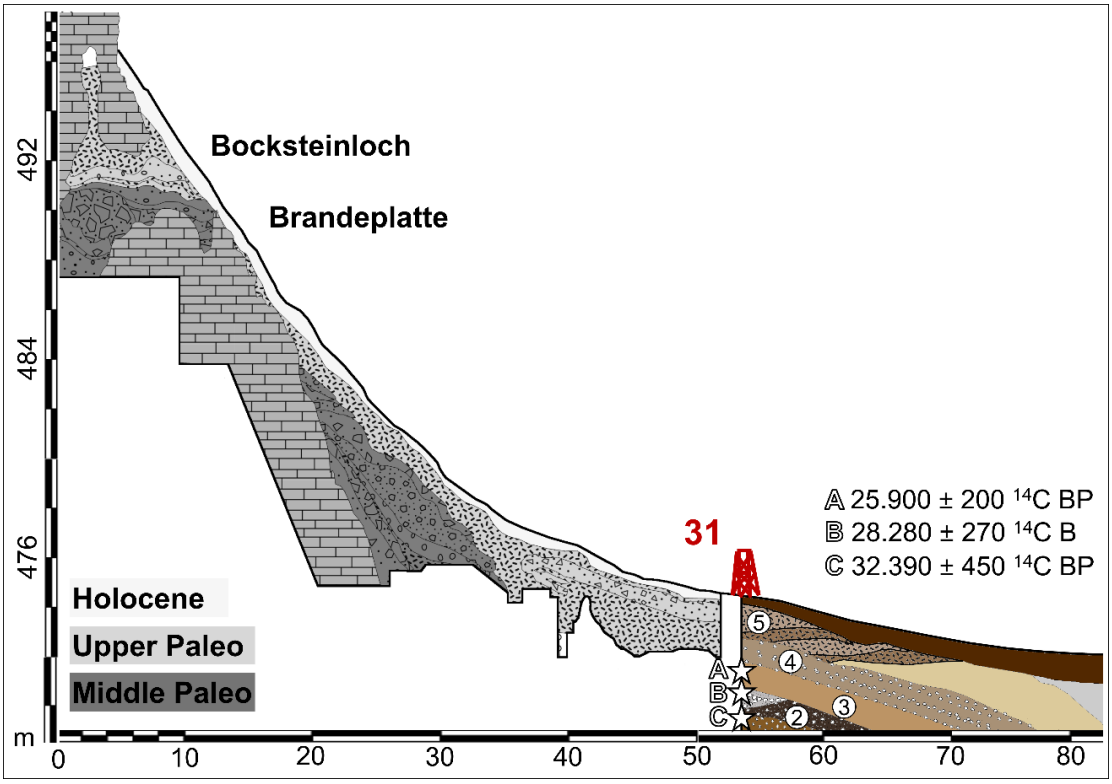

Fig. 4.14. The Lone Valley at Bockstein. This figure is based on data presented in this dissertation and profile drawings from the excavations conducted by Wetzel along the hillside (Wetzel 1958). Location of this section is indicated in Fig. 4.2. BS-GU unit numbers are labelled in the figure (***2***, ***3***, ***4***, ***5***). The position of radiocarbon dating is indicated with white stars and letters (***A***, ***B***, ***C***). Figure modified from Barbieri (et al. 2018).

V. Landscape instability, cave erosion, increasing loess deposition, soil formation (26.000 ^{14}C BP-20.000 ^{14}C BP)

GL 264 is covered with alternating beds of laminated, reworked loess and medium-to-fine, subrounded limestone gravel. We grouped these beds in two separate units, BS-GU3 and BS-GU4. Given their composition, grainsize and bedding we interpreted BS-GU3 and BS-GU4 as deposited by alternating sheet and snow-flows (Blikra and Nemec 1998, Pawelec 2006). Furthermore we argued that the upwards increasing in gravel content from BS-GU4 to BS-GU3 might be indicative for increasing energy in the mass-wasting processes (Barbieri et al. 2018).

Our micromorphological results from the contact between these two units show that both BS-GU3 and BS-GU4 display rare bone fragments and rare grains of phosphatized loess. As previously mentioned, archaeological deposits have been completely removed from the caves of Bockstein (see section 4.1) and no micromorphological study has been conducted at this site. However, micromorphological results from other cave sites of the Ach Valleys (Goldberg et al. 2003, Miller 2015) show that the Pleistocene-aged sediments accumulated inside these caves are composed of phosphatized loess and numerous, sand-sized fragments of bone. These results are in agreement with our data from Hohlenstein-Stadel, which is located only 2 km to the East from Bockstein (Barbieri and Miller, in press. Chapter 3.2.1 and 3.3.1). Therefore we hypothesize that during the Pleistocene the caves of Bockstein were also likely filled with phosphatized loess. We conclude that the bone fragments and the grains of phosphatized loess we observed at the contact between BS-GU3 and 4 were likely eroded from the Bockstein caves (Barbieri et al. 2018).

From ca. 30 cm below the contact between BS-GU3 and BS-GU4 we collected a sample of mixed shell fragments (ID 69), which display good aragonite preservation. These shells were probably buried shortly after the death of the gastropods and did not undergo significant diagenesis. The result of the radiocarbon measurement performed on this sample gave an age of 25.900 ± 200 ^{14}C BP. This age has to be considered carefully. In the first place, we sampled these shell fragments from different depths (2 ± 0.05 m below the ground surface), thus the resulting age of 25.900 ± 200 ^{14}C BP has to be considered as a range of ages. In the second place, the correct radiocarbon determination of gastropod

shells might be problematic. During their life cycle gastropods can incorporate fossil carbon from the limestone bedrock, which can lead to an age overestimation of 1.500 (Yates et al. 2002) to 3.120 radiocarbon years (Goodfriend and Stipp 1983). Therefore our age of ca. 26.000 ^{14}C BP might be up to 3.000 radiocarbon years younger (23.000 ^{14}C BP).

Nevertheless, despite these uncertainties, our age determination for the sample ID 69 appears to substantially overlap the range of 21.000-31.000 ^{14}C BP published for the Gravettian occupation at Bockstein-Törle (Conard and Bolus 2003). Therefore we hypothesize that the Gravettian deposits originally accumulated inside the caves of Bockstein underwent a phase of erosion which led to the accumulation of bone fragments and grains of phosphatized loess in BS-GU3 and BS-GU4. This erosive phase occurred shortly after the time range 26.000-23.000 ^{14}C BP and was likely triggered by the lack of arboreal vegetation along the slope. Our vegetation reconstructions fits well with the results of the faunal analysis from the Gravettian deposits of Bockstein-Törle (BT VI-IV; Krönneck 2012).

Similarly to HS-GU7 from the Hohlenstein survey area, BS-GU3 and BS-GU4 are largely composed of reworked loess and are nearly free from fragments of clay coatings. Such increasing loess sedimentation at both sites represents a second major phase of landscape change at the regional scale.

After their deposition BS-GU3 and BS-GU4 underwent a phase of soil formation, which is documented by calcified root cells, calcite hypocoatings and calcite infillings (Durand et al. 2010. Fig. 4.11).

VI. Hillside instability and river erosion (Late Glacial to Holocene)

BS-GU5 is the uppermost unit we recovered from core 31. Our coring and geophysical data revealed that BS-GU5 is composed of fine, medium to coarse, loose, angular, openwork limestone gravel which is organized in densely stacked, imbricated beds (Blikra and Nemec 1998. Fig. 4.13). Based on its structure, we interpreted BS-GU5 as a low-viscosity debris flow (Blikra and Nemec 1998). Additionally BS-GU5 appears laterally eroded, potentially by the Lone River (Fig. 4.13).

Uphill from our core 31 Wetzel recovered a deposit comparable in grainsize and bedding to BS-GU5 (Wetzel 1958). Furthermore, BS-GU5 exhibits an internal structure nearly

identical to HS-GU12, from the Hohlenstein survey area. We conclude that the HS-GU12 and BS-GU5 deposits document the last major phase of landscape change in the Lone Valley.

5 Results from The Ach Valley in front Hohle Fels

5.1 Previous research at Hohle Fels and in the Ach Valley

Hohle Fels is situated a few kilometers to the east from the source of the Ach River, in the town of Schelklingen, with the entrance to the cave approximately 3.5 m above the Ach floodplain (Fig. 5.1, detail 1). Oscar Fraas and Theodor Hartmann were the first to conduct archaeological excavations at this site in the late XIX century (Hahn 1978). Over the last two decades, The University of Tübingen under the direction of Nicholas Conard and Maria Malina has carried out seasonal excavation campaigns at this site.

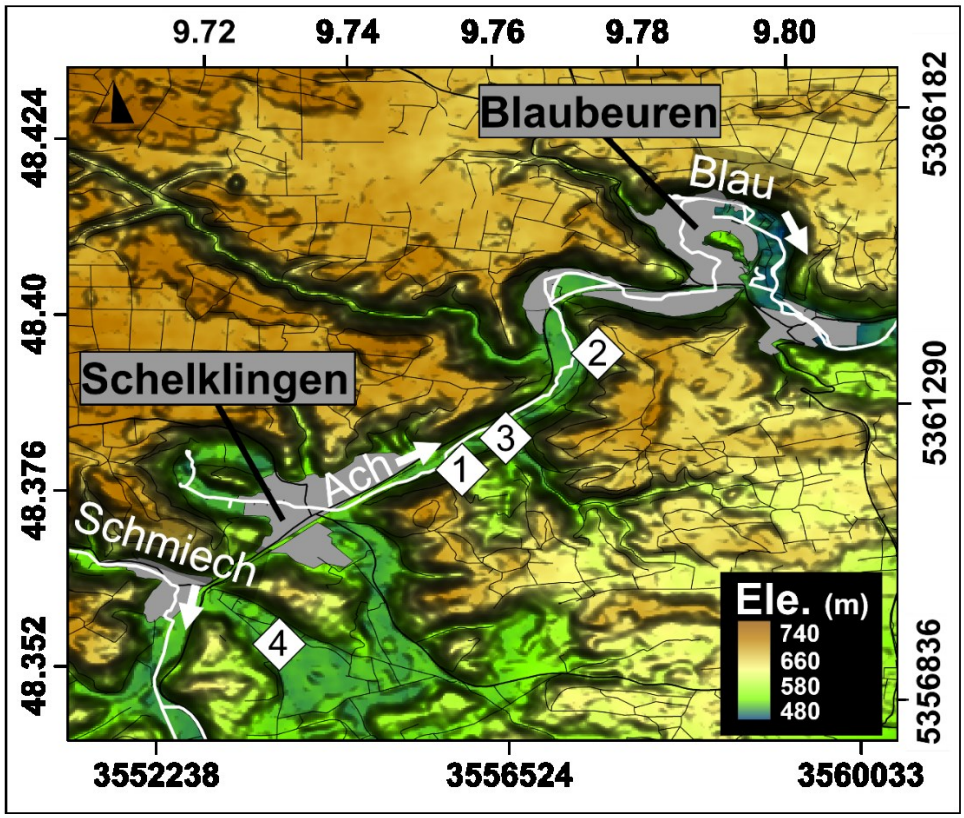

Fig. 5.1. Site location in the Ach Valley. Geographic map displaying the location of Hohle Fels (***1***), Geißenklösterle (***2***), core 7624/45 from Groschopf 1973 (***3***), and "Core Schmiecher See 1" from German et al. 1995 (***4***). The towns of Schelklingen and Blaubeuren are depicted in gray, Schmiech, Ach and Blau rivers are in white. The map is realized from SRTM 90m Digital Elevation Data and it is projected in the WGS 84 coordinate system. The WGS 84 coordinates are labelled along the upper and left axes. The corresponding DHDN Gauss-Krüger coordinates are labelled along the lower and right axes (Figure from Barbieri et al. 2018).

Previous micromorphological studies conducted on the sediments preserved inside this cave revealed that the Middle Paleolithic to Gravettian deposits are largely composed of loess and soil material that entered from the external hillside through a large chimney

located in the back of the cave (Goldberg et al. 2003, Schiegl et al. 2003, Miller 2015). Once deposited inside Hohle Fels, sediments underwent diagenesis and moved towards the entrance of the cave. Micromorphological data published by Miller (2015) and Goldberg (et al. 2003) show that the main diagenetic processes at Hohle Fels consisted of calcite dissolution and phosphate neoformation, which was triggered by the accumulation of bird or bat guano inside the cave. As observed at Hohlenstein-Stadel (chapter 3.2.1 and 3.31. Barbieri and Miller in press) and at the nearby site of Geißenklösterle (Miller 2015. Fig. 5.1, detail 2), Hohle Fels phosphate neoformation was discontinuous during the Pleistocene. In particular, the transition from the Middle Paleolithic to the Early Aurignacian deposits (GH7 in Fig. 5.2) is characterized by a less intensive replacement of calcite with apatite. Conversely, from the Late Aurignacian deposits (GH6, 5, 3db in Fig. 5.2) Miller (2015) reported more intensive phosphatization, increased clay content, and numerous clay infillings, which he argued as being indicative for wetter and warmer conditions. On top of these sediments, his results from the Gravettian-aged deposits show evidence for gelifluction, erosion, and less intensive phosphatization (GH 3c and 3b in Fig. 5.2. Miller 2015, Goldberg et al. 2003). More recently, Riehl (et al. 2015) published archeobotanical data from Hohle Fels that largely support the climatic fluctuations hypothesized by Miller.

In the Ach, Schmiech and Blau valleys, numerous cores (Groschopf 1973, Fig. 5.1, detail 3. German et al. 1995), geoelectric, and seismic measurements (Brost et al. 1987) have been collected throughout the XXth century. Particularly, the sequence recovered within "Core Schmiecher See 1" (here on CSS1. Fig. 5.1., detail 4 and Fig. 5.3) is very significant for our research. In CSS1 the bedrock was encountered at 43 m below the ground surface. On top of it lies the *Untere Kies* unit, composed of gravel transported by the Danube from the Alps (Brost et al. 1987, German et al. 1995). According to German (et al. 1995), this deposit displays a pollen spectrum potentially compatible with the Eemian. This phase of landscape stability was followed by a phase of river incision, which partially eroded the *Untere Kies* deposits. Subsequently this disconformity was covered with organic silt (*Untere Mergel* and *Obere Mergel*) alternated with limestone gravel (*Mittlerer Kies*, Brost et al. 1987). The organic silt deposit (*Untere Mergel*) shows pollen spectra indicative of tundra vegetation and probably represents the earliest Würm deposit in the Schmiech Valley (German et al. 1995). The absence of Alpine components in these

sediments indicates that the Danube had abandoned the Swabian Alb and was replaced by smaller, local drainages (Brost et al. 1987, German et al. 1995).

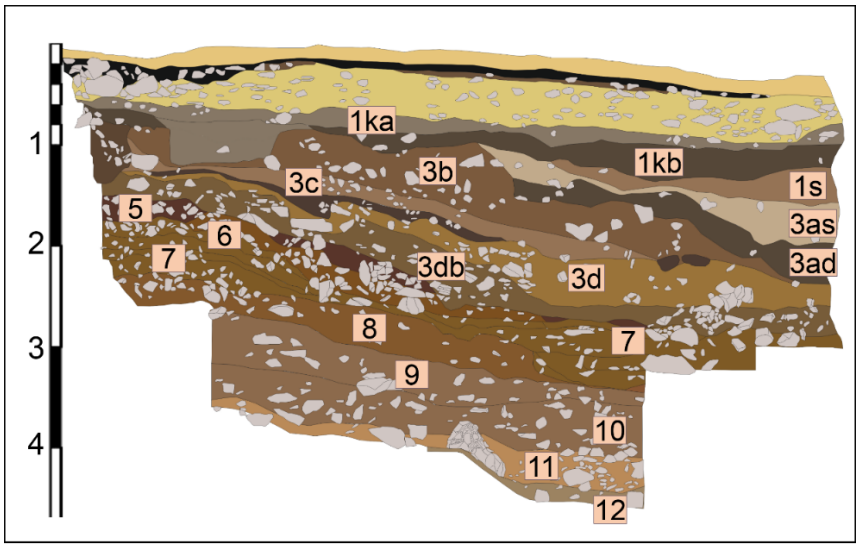

Fig. 5.2. Profile 2 from Hohle Fels. GH unit numbers are labeled in pink. Modified from Maria Malina.

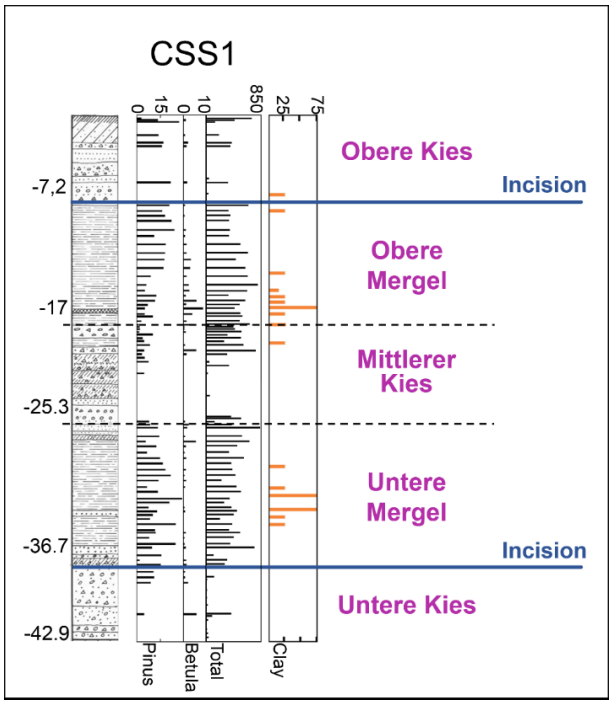

Fig. 5.3. Core CSS1. Figure compiled from German et al. 1995. From the right, lithological representation of core CSS1, palinological data (percentage of ***Pinus***, ***Betula*** and ***Total*** counts), and amount of ***Clay*** in the sediment. The main lithological units are labelled in violet.

Additional geophysical measurements (Brost et al. 1987) and cores (Groschopf 1973) show that the sequence recovered within CSS1 is largely present in both the Schmiech and Ach valleys.

5.2 Results

In the course of preliminary geophysical surveys we conducted in the Ach Valley, the GPR revealed potentially preserved sedimentary structures in the flat area located at the entrance of Hohle Fels (*Vorplatz*). Along the floodplain the radio signal appeared significantly attenuated and no clear sedimentary structures were detected. Based on these preliminary results, we covered nearly the entire surface of the *Vorplatz* with two grids measuring 9x12 m and 6x8 m, respectively. In each grid GPR profiles were collected along the *x* and *y* axes with a spacing of 1 m. Additionally, we collected several freely oriented lines along the hillside surrounding Hohle Fels and from the *Vorplatz* into the floodplain. Based on our GPR results we selected key areas which we further investigated with EC-loggings (2 in total) and coring (cores 37, 38 and 39. Fig. 5.4).

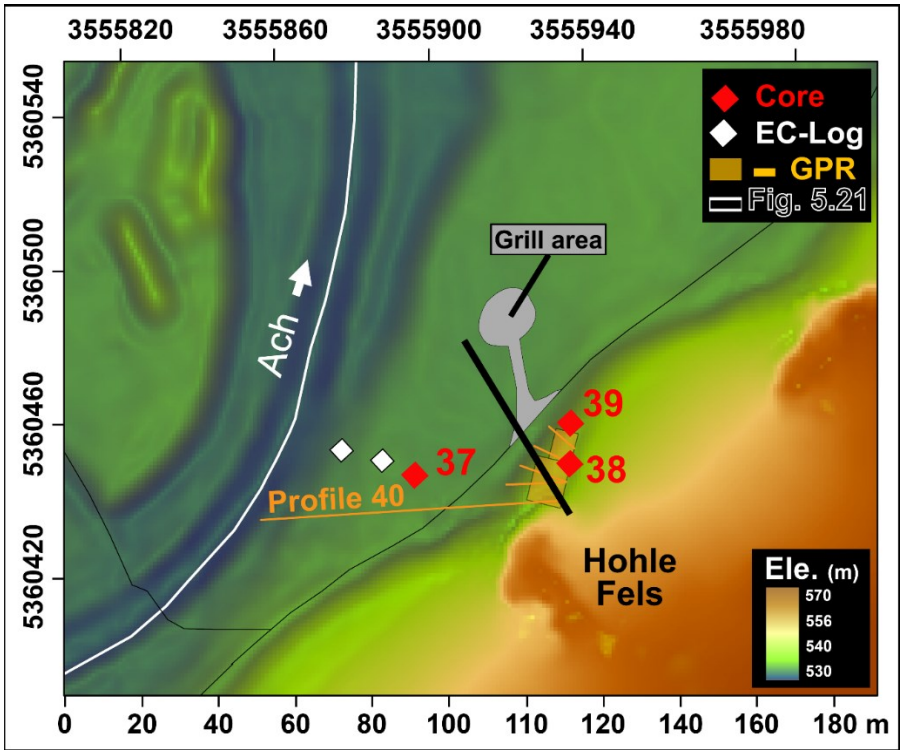

Fig. 5.4. Survey area in front of Hohle Fels. Red diamonds indicate the location of the cores mentioned in the text, white diamonds show the location of EC-logging. GPR grids and GPR freely oriented lines are depicted in orange. Among the freely oriented lines ***Profile 40*** is presented in the text. The black line from Hohle Fels to the Ach Valley indicates the position of Fig. 5.21 (Modified from Barbieri et al. 2018).

We summarized our main findings from the survey area in front of Hohle Fels in a previous publication (Barbieri et al. 2018). In this section we present and discuss our data in greater detail (the complete description for each GL is presented in Appendix III).

Depth to bedrock

Due to an aquifer that caused the loss of a significant part of the sediment recovered from 4.8 m to 6 m below the ground surface, we decided to interrupt the drilling of core 38 at 6 m depth (Fig. 5.5). In core 39 we reached refusal at 4.8 m below the ground surface (Fig. 5.5). However, based on our results from the survey area opposite from Hohlenstein, coring refusal cannot be regarded as a secure indicator of depth to bedrock. From the *Vorplatz* area in between the entrance to Hohle Fels and core 38 the radio signal was attenuated at depth greater than ca. 4 m (Fig. 5.5). Moving from core 38 to core 39 the radio signal appears attenuated even at shallower depths (Fig. 5.7). Such attenuation might be due to the higher silty clay content of the sediments recovered in core 39, which probably led to a more intensive upward capillary movement of ground water from the aquifer in this part of the *Vorplatz* (Lu and Sato 2007, Barbieri et al. 2018). In the floodplain we drilled the two EC-loggings and core 37 down to the maximum depth that these methods can safely reach, which corresponds to 12 m and 9.6 m respectively (Fig. 5.6, 5.8). These depths were not enough to reach the bedrock, which in the center of the valley is located at 40 m below the ground surface (Groschopf 1973, Brost et al. 1987).

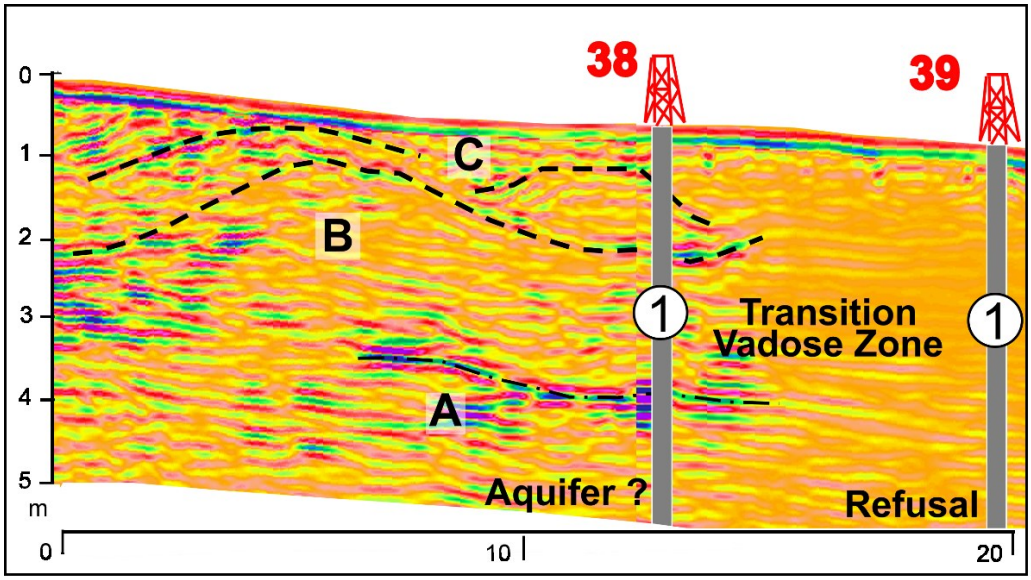

Fig. 5.5. Sedimentary structures within HF-GU1, in the geophysical data. GPR profile from the entrance to Hohle Fels to core 39. **A**, **B** and **C** indicate the main reflected phases which are discussed in the text (Figure modified from Barbieri et al. 2018).

We conclude that our data are not helpful to clarify the depth and geometry of the bedrock along the flanks and in the floodplain of the Ach Valley.

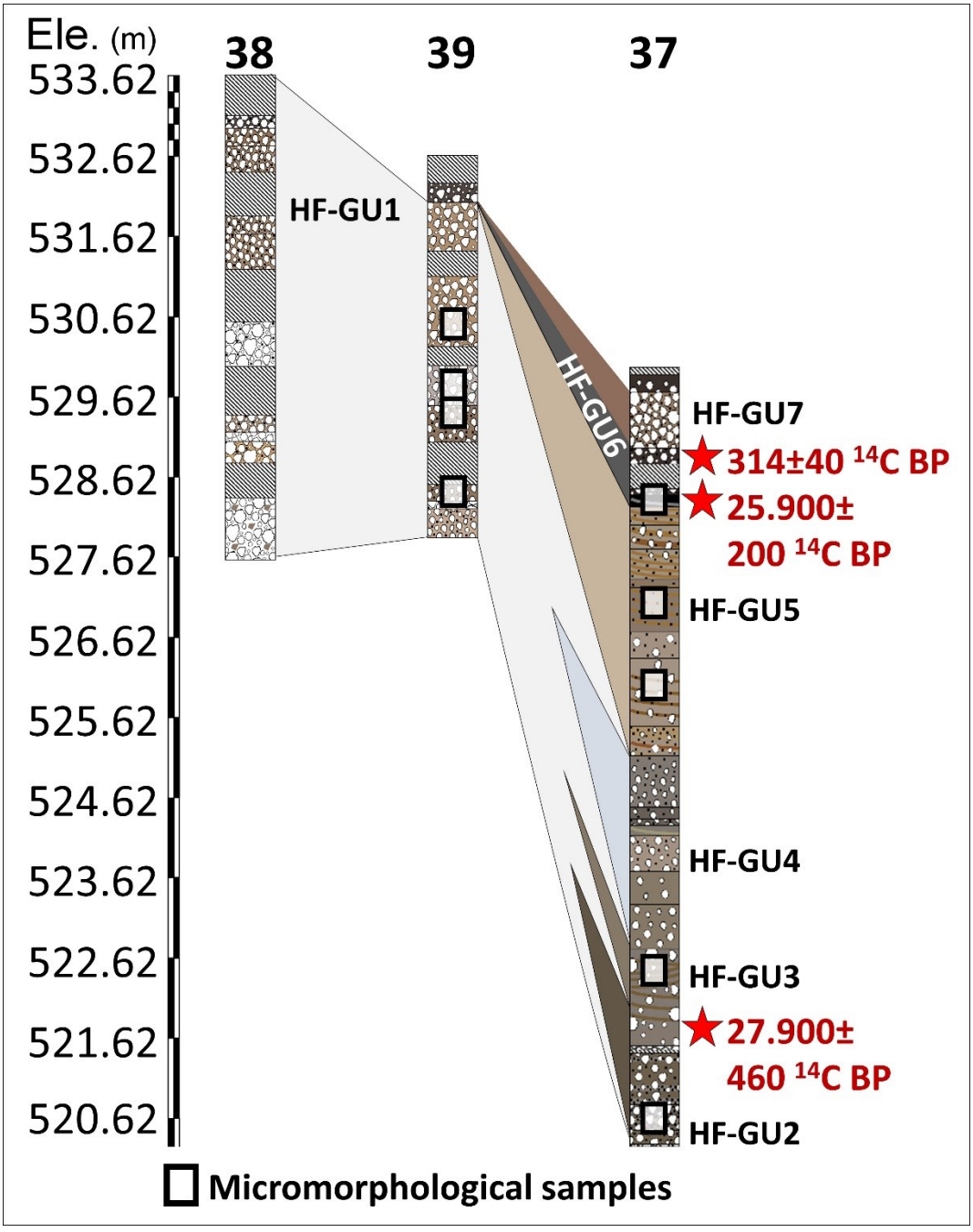

Fig. 5.6. Cross-correlation of the cores collected in front of Hohle Fels. The analyzed micromorphological are depicted with white rectangles, the location of the samples dated with ^{14}C is marked with red stars (figure from Barbieri et al. 2018).

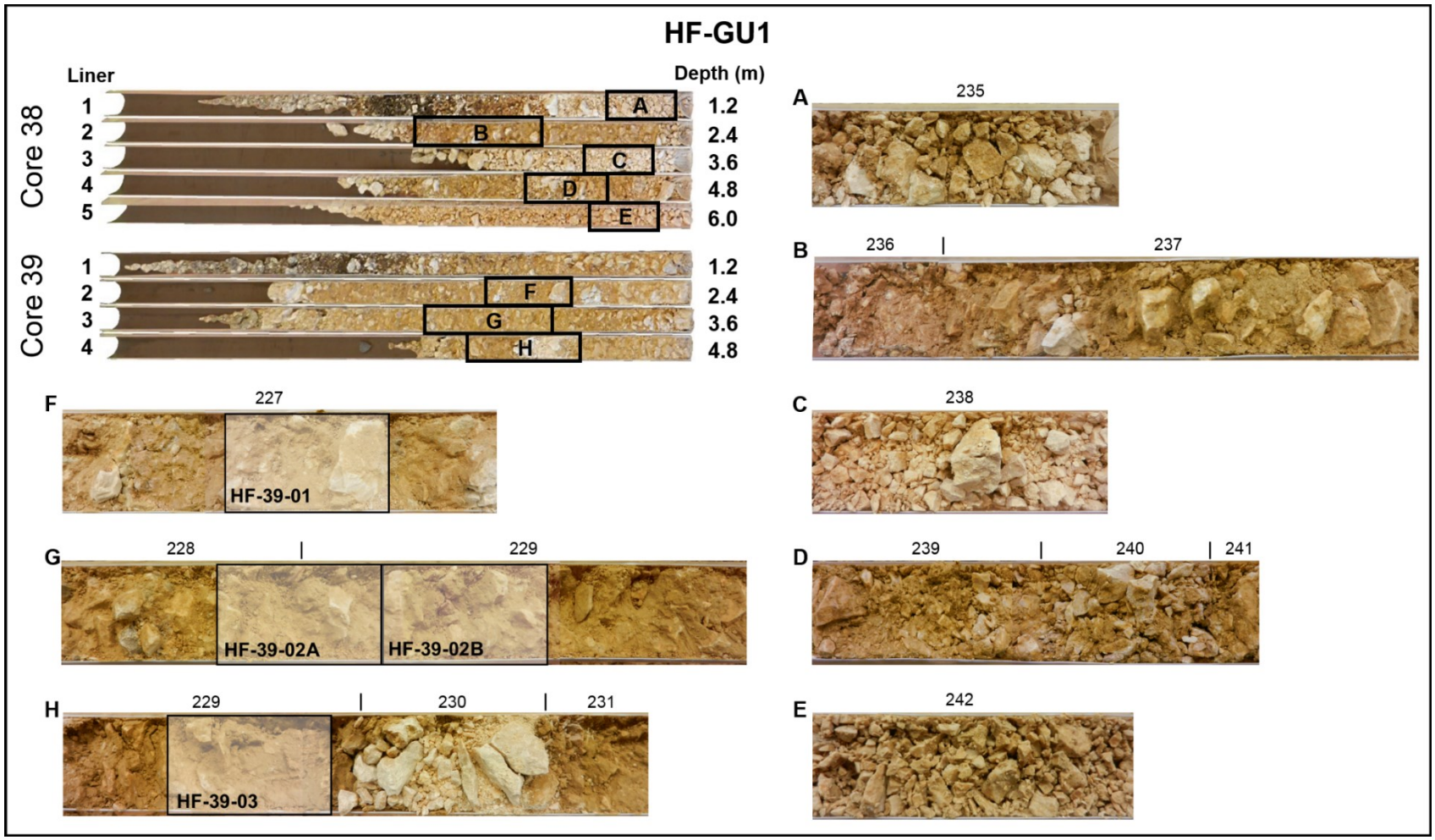

Fig. 5.7. HF-GU1. ***On the upper left***, the liners of cores 38 and 39. ***A***, ***B***, ***C***, ***D***, ***E***, ***F***, ***G***, ***H*** details from the GL (numbered in the figure) which are discussed in the main text. ***HF-39-01***, ***HF-39-02A***, ***HF-39-02B*** and ***HF-39-03*** indicate the location of the miciromorphological samples displayed in Fig. 5.9.

HF-GU1

From core 38 (GL 232-242) and core 39 (GL 226-231) we recovered loose, dry, angular, limestone gravel, alternating with rare layers composed of yellowish brown to brownish yellow (10 YR 5/4, 6/4, 6/3, 7/6) sandy silt (Barbieri et al. 2018. Fig. 5.6 and 5.7).

Our GPR data from the *Vorplatz* revealed the presence of two main reflectors (Barbieri et al. 2018). The deeper reflector is located approximately 4 m below the surface and slopes gently from the cave entrance towards the center of the Ach Valley (Fig. 5.5, detail A). Interestingly, in core 39, from a depth comparable to this reflector, we reported the occurrence of sand-sized fragments of speleothems (see Fig. 5.9, detail 6). The shallower reflector detected with our GPR is located around 1-2 m below the ground and it defines an irregular 14x5 m large surface (Fig. 5.5, detail B). Above the latter we detected densely stacked reflectors which dip towards the cave entrance and the Ach Valley (Fig. 5.5, detail C). The modern topography seems to truncate these densely stacked reflectors (Barbieri et al. 2018).

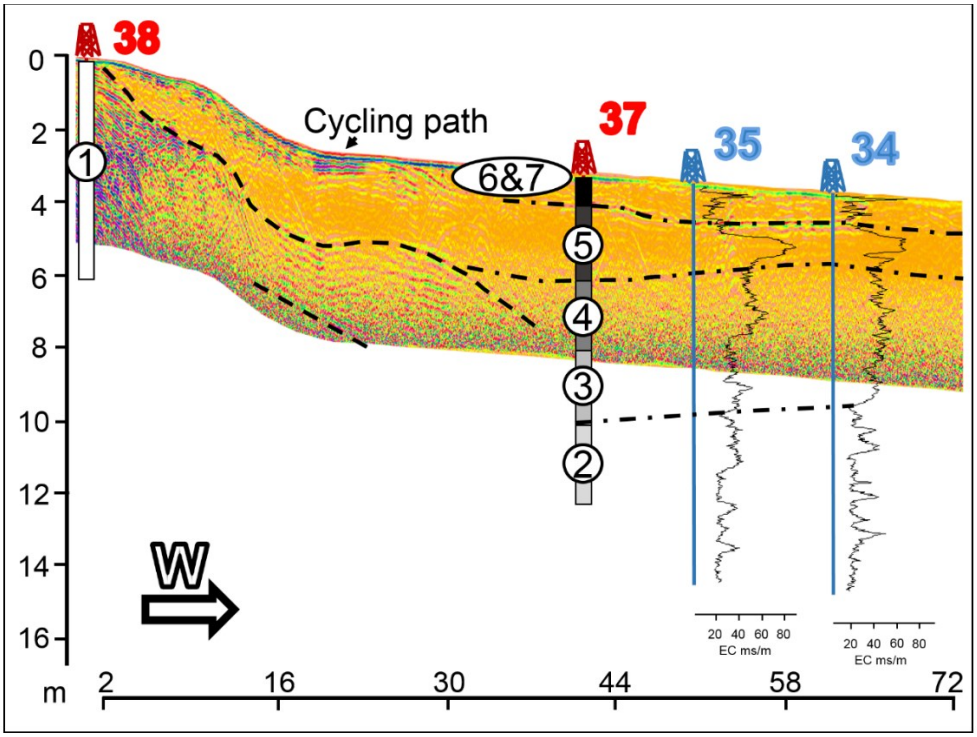

Fig. 5.8. ***Vorplatz*** **and floodplain deposits in the geophysical data**. Cores and EC-loggings are depicted rispectively in red and blue. HF-GU unit numbers are labelled in figure as numbers on white background. Due to limits in the penetration of the GPR signal we cannot clarify the stratigraphic reletionship between HF-GU1 and HF-GU2-4. HF-GU5-7 seem to cover HF-GU1. EC-logging data seem to indicate that the units recovered from core 37 are laterally continuous in towards the center of the Ach Valley.

With the intent of clarifying the physical correlation between HS-GU1 and the six units we recovered in core 37, we collected GPR Profile 40 from the Hole Fels cave entrance towards the west, down to the Ach River. More in detail, this GPR profile shows that the sedimentary sequence we identified at the *Vorplatz* appear to dip towards the center of the Ach Valley at an angle of ca. 10° (Fig. 5.8). At 20 m from the *Vorplatz* these reflectors are no longer recognizable due to the high background noise and attenuation of the GPR signal. Furthermore, noise and attenuation in the GPR measurements become even shallower moving towards the Ach River, impeding our attempts to clarify the correlation between the deeper units we recovered in core 37 and HF-GU1. By comparing core 37 with the data from EC-loggings 34 and 35 we argue that the sequence of HF-GU2-7 is laterally continuous in the center of the Ach Valley.

We collected 3 block samples for micromorphological analysis from core 39, which exhibits sediments with a higher silty clay content, thus more suitable for such analysis in comparison with the loose gravel we recovered in core 38. From the three blocks we produced 4 thin sections: HF-39-01, HF-39-02A, HF-39-02B and HF-39-03 (Fig. 5.9). Having samples from different depths (at nearly regular intervals of about 1 m) provided us the opportunity to study possible variations in terms of composition throughout unit HF-GU1.

Our results from the micromorphological analysis show that the matrix of all the four thin sections corresponds to a calcareous, loess-like sediment with only some variations in terms of grain size. For example, samples HF-39-02-A and B are richer in coarse calcite sand (Fig. 5.9, detail 4). Large parts of the gravel we observed is composed of very fresh limestone fragments in which fossils are still clearly recognizable (Fig. 5.9, detail 3 and 5). Secondary calcite and calcite-capped fragments are present throughout HS-GU1. In HF-39-03 we observed a significant percentage of large speleothem fragments (Fig. 5.9, detail 6). In samples HF-39-02-A and B some weathered limestone fragments present weakly developed, dusty, clay coatings (Fig. 5.9, detail 4). Moving upwards from HF-39-02-A to HF-39-01 we have also documented fresh root remains likely coming from modern plants (Fig. 5.9, detail 1). With regards to the organization of the components, only HF-39-01 presents graded laminations composed of silt and sand (Fig. 5.9, detail 1).

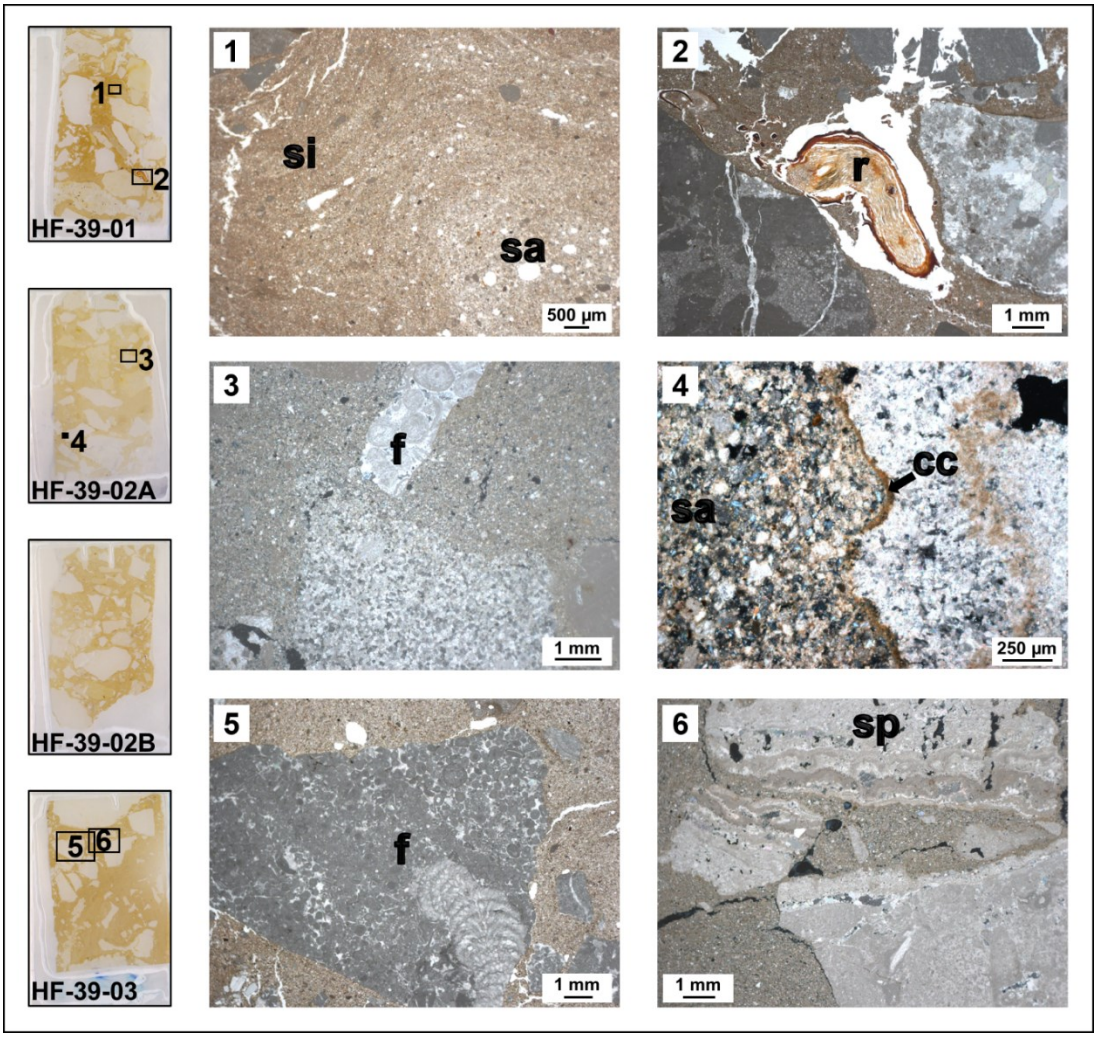

Fig. 5.9. Micromorphological results from HF-GU1. ***On the left***, thin section scans of samples HF-39-01, HF-39-02 A and B, and HF-39-03. ***1***, photomicrograph in PPL displaying graded laminations of silt (**si**) and sand (**sa**). ***2***, photomicrograph in PPL showing a fresh root fragment (**r**). ***3***, fragment of fresh limestone fragment with microfossils (**f**) embedded in fresh reworked loess and sand. ***4***, photomicrograph in XPL displaying weathered limestone fragment with dusty, clay coating (**cc**) embedded in calcite sand (**sa**). ***5***, photomicrograph in PPL capturing one fresh, angular limestone fragment with microfossils (**f**). ***6***, photomicrograph in XPL displaying speleothem fragments (**sp**).

HF-GU2

Unit HF-GU2 is composed of alternating matrix-rich and gravel-rich sediments located in the lowermost liner of core 37, from 8.4 m to 9.6 m below the ground surface (Fig. 5.6 and Fig. 5.10). Layers rich in gravel (GL 221, 222 and 223) consist of medium to fine, subangular to angular limestone gravel embedded in a gray (5Y 5/1), sandy matrix. Layers (GL 224) and laminations (GL 222 and 223) richer in fine fraction are more silty, display

an higher amount of quartz sand, and appear dark gray in color (5Y 4/1. Barbieri et al. 2018).

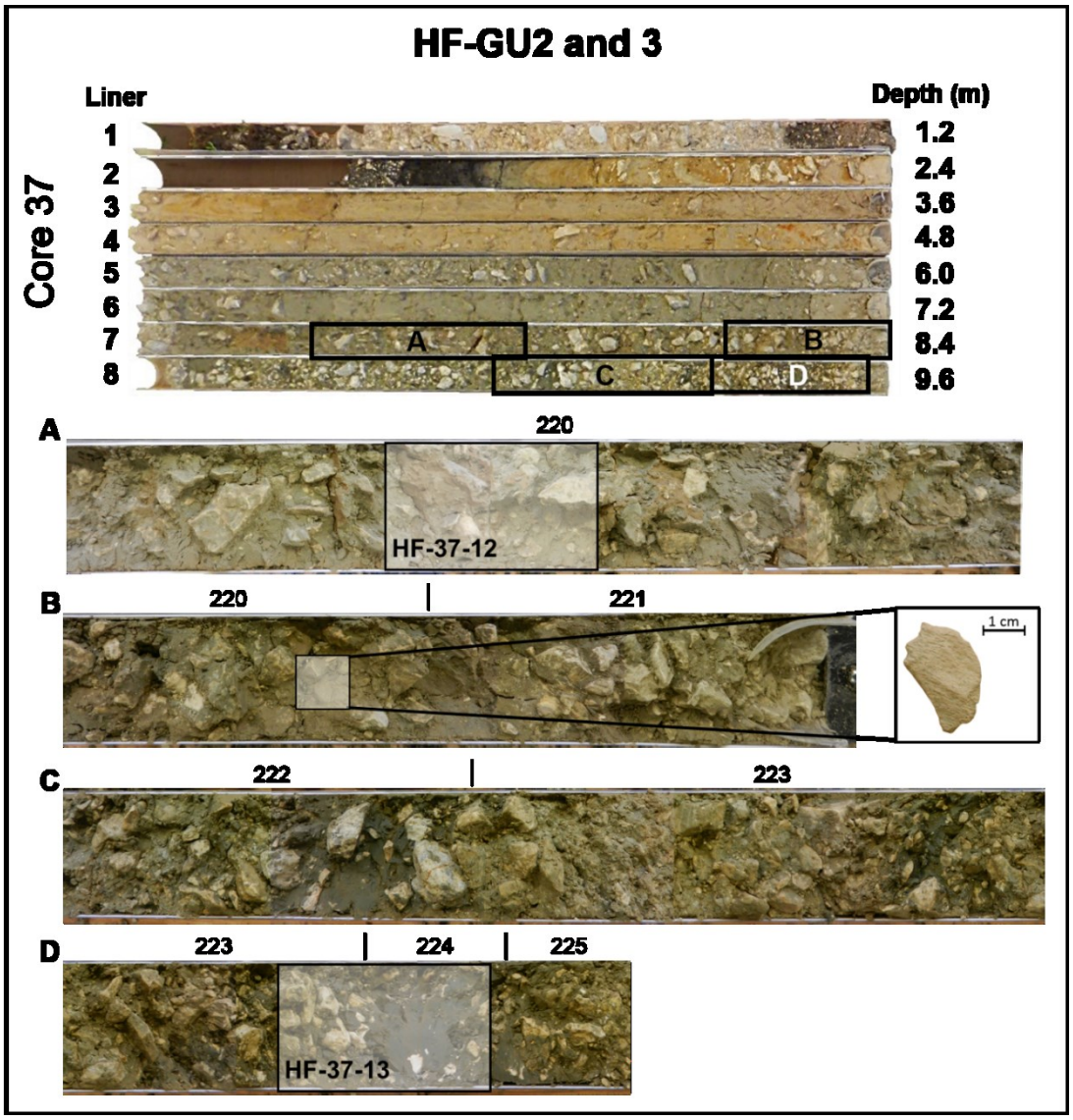

Fig. 5.10. HF-GU2 and HF-GU3. ***In the upper part***, the liners of core 37. ***A***, ***B***, ***C***, ***D*** details from the GL (numbered in the figure) which are discussed in the main text. ***HF-37-13*** and ***HF-37-12*** indicate the location of the thin sections presented in Fig. 5.11. The bone fragment from GL 220 has been dated with ^{14}C.

Our results from EC-loggings 34 and 35 show the presence of low electrical conductivity values (around 20 mS/m) alternated with isolated higher peaks (up to 40 mS/m) from 7 m to 12 m below the ground surface (Fig. 5.8). This alternation in electrical conductivity values resembles the alternating gravel- and matrix-rich layers we recovered in HF-GU2. Therefore, we hypothesized that HF-GU2 is probably laterally continuous and dips towards the hillside with an angle of ca. 2° (Fig. 5.8).

HF-37-13 is the lowermost micromorphological sample we collected from core 37. The thin section we produced out of this sample covers the contact between the gravel-rich GL 223 and the matrix-rich GL 224. The main goal of analyzing this sample was to define the composition of these two layers.

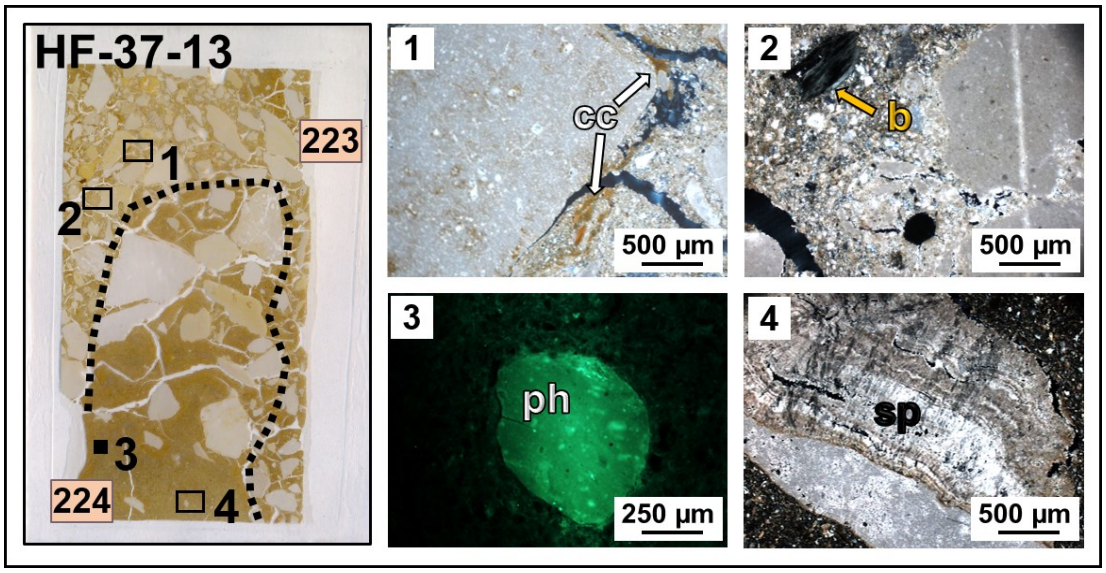

Fig.5.11. Micromorphological results from HF-GU2. ***On the left***, thin section scan of sample HF-37-13. ***1***, photomicrograph in XPL from GL 223 displaying limestone fragment with slightly displaced clay coating (**cc**). ***2***, photomicrograph in XPL from GL 223 showing bone fragment (**b**) embedded in a matrix rich in calcite sand. ***3***, photomicrograph in FL from GL 224 capturing one grain of phosphatized loess (**ph**). ***4***, photomicrograph in PPL from GL 224 showing one fragment of speleothem (**sp**).

The fine fraction of GL 224 appears like a decalcified, reworked loess, rich in quartz and micas and poor in calcite. We observed bones, sand-sized grains of phosphatized loess (Fig. 5.11, detail 3), and speleothem fragments (Fig. 5.11, detail 4). The groundmass appears locally iron stained. GL 223 is largely composed of well-sorted, subangular to subrounded, fine limestone gravel. These fragments are moderately fresh and occasionally present calcite and limpid, slightly displaced clay coatings (Fig. 5.11, detail 1). Additionally, limpid, laminated clay intercalations are present in the matrix. In comparison with GL 224, the matrix of GL 223 is richer in calcite and locally cemented. Furthermore, well-preserved shell fragments are abundant, bone and phosphatized loess grains are less frequent, but slightly larger in size (Fig. 5.11, detail 2).

HF-GU3

HF-GU3 is composed solely of GL 220, which we recovered in core 37 from 7.2 m to 8.4 m below the ground surface (Fig. 5.6 and Fig. 5.10). This layer is composed of fine, medium, coarse, rounded to angular limestone gravel (70%) in a silty matrix (30%). In the course of the sediment description we reported rare millimeter-thick olive brown (2.5 Y 4/4) laminations, which displayed apparent cross bedding (Barbieri et al. 2018).

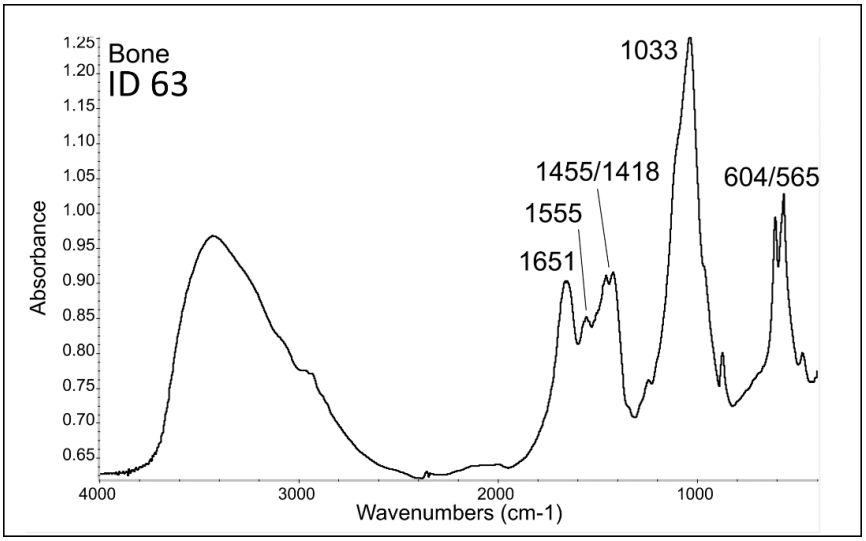

Fig. 5.12. FTIR spectra from the dated bone fragment from HF-GU3. The results of the FTIR analysis revealed absorption bands of carbonate hydroxylapatite (1455, 1418, 1033, 604 and 565 cm^{-1}) and collagen (amide I at 1651 and amide II at 1555 cm^{-1}. Weiner and Bar-Yosef 1990. Figure modified from Barbieri et al. 2018).

ID	$\delta^{13}C$ (± 0.1‰)	^{14}C age		Calibrate age 95%	
		(^{14}C BP)	±	(BC/AD)	(BP)
57	-26.9	314	40	1471 – 1651 AD	479 - 299
58	-28.5	4933	28	3771 – 3652 BC	5720 – 5601
63	-21.6	27900	460	31102 – 29107 BC	33051 – 31056

Table 5.1. Radiocarbon determinations from core 37. In this table we present the results of the radiocarbon determination performed on ID 57, ID 58 (from HF-GU6) and ID 63 (from HF-GU2. The ID used by the laboratory in Tucson is reported in Table 2.1). The table includes ***$\delta^{13}C$ (± 0.1‰)***, the estimated radiocarbon age (***^{14}C age***, ***^{14}C BP***) and its uncertainty (±). We also present the corresponding calendar years Before/After Christ (***BC/AD***) and Before Present (***BP***), which we obtained performing a 2σ calibration with the program OxCal 4.3 (curve IntCal 13).

At the very bottom of this unit we recovered a fragment of compact bone, which displayed a platy shape, subrounded edges and a surface of about $2cm^2$ (Fig. 5.10). Since FTIR analysis performed on this bone fragment revealed good preservation of the collagen (Fig.

5.12), we decided to measure its ^{14}C content, obtaining a radiocarbon age of 27.900 ± 460 ^{14}C BP (ID 63 in Table 5.1).

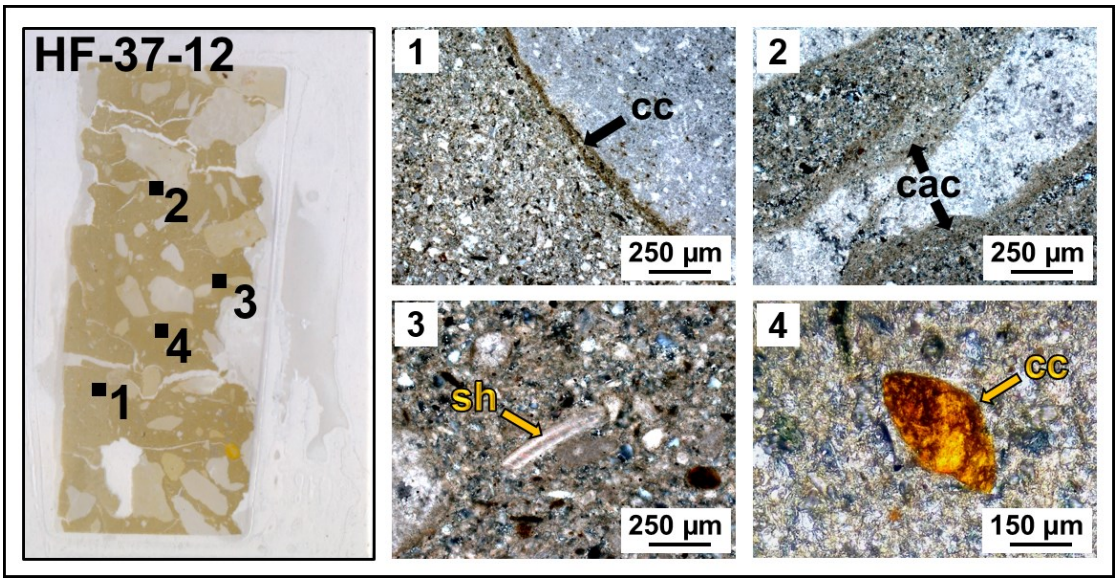

Fig. 5.13. Micromorphological results from HF-GU3. ***On the left***, thin section scan of sample HF-37-12. ***1***, photomicrograph in PPL displaying dusty, weakly developed clay coating (**cc**) on limestone fragment. ***2***, photomicrograph in PPL showing calcite coating (**cac**) on weathered limestone fragment. ***3***, photomicrograph in XPL capturing shell fragment (**sh**). ***4***, photomicrograph in XPL showing one fragment of limpid, clay coating (**cc**).

With the aim of investigating the red cross-bedded laminations we observed macroscopically, we collected the block sample HF-37-12 35 cm from the top of GL 220. The result of our micromorphological study shows that the fine fraction of this layer is composed of sand and silt of quartz, micas, calcite (reworked loess), glauconite, snail shells (Fig. 5.13, detail 3), and very rare fragments of limpid and laminated clay coatings that display reoriented clays (Fig. 5.13, detail 4). Angular limestone gravel are occasionally coated with dusty clay (Fig. 5.13, detail 1) and often appear weathered. The most weathered limestone fragments are surrounded by secondary calcite coatings (Fig. 5.13, detail 2). Surprisingly, during our micromorphological analysis we did not identify any lamination.

HF-GU4

In core 37 from depths between 4.8 m and 7.2 m we recovered GL 212 to GL 219, which we grouped in HF-GU4 (Fig. 5.6 and Fig. 5.14). In comparison with the underlying unit, HF-GU4 is more silty, it appears generally richer in light brownish gray (2.5Y 6/2) and gray (2.5Y 5/1) iron stained intercalations, and it displays graded, alternating beds and

laminations. In HF-GU4 we distinguished two bed types: GL 212, 214, 216, 218, 219 contain at least 30% of angular medium and fine limestone gravel; GL 213, 215 and 217 alternate with these layers and do not contain more than the 10% of gravel (Barbieri et al. 2018).

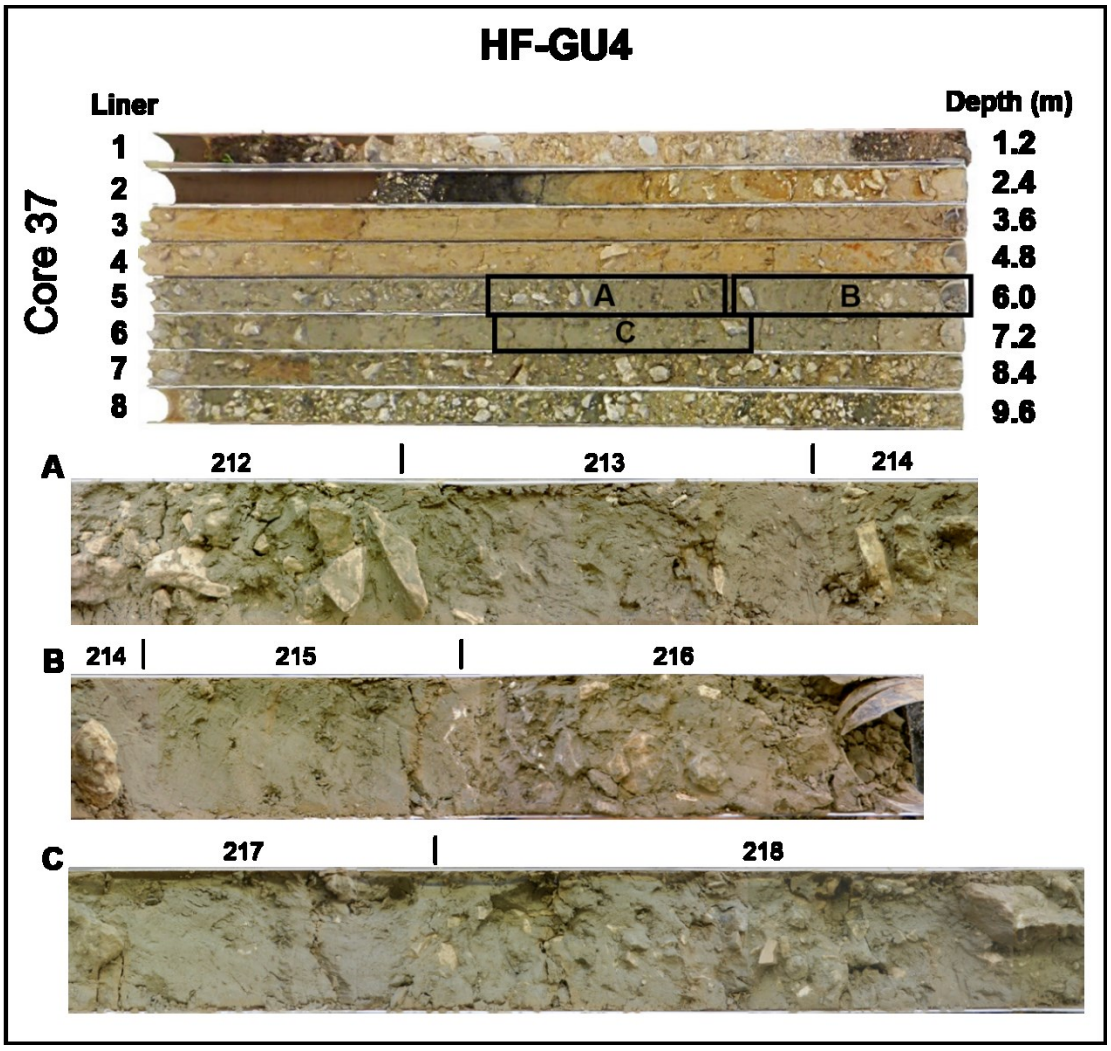

Fig. 5.14. HF-GU4. ***In the upper part***, the liners of core 37. ***A***, ***B***, ***C*** details from the GL (numbered in the figure) which are discussed in the main text.

The values of electrical conductivity measured in EC-loggings 34 and 35 between 3 m and 7 m below the ground surface are generally low (30-20 mS/m) and might correspond to the silty-sandy gravel of HF-GU3 and HF-GU4 (Fig. 5.8). Acquisition of good quality data with the GPR was impeded by attenuation and heavy background noise at depth comparable with these two units (Fig. 5.8). Based on our EC-logging, we conclude that HF-GU3 and HF-GU4 are most likely laterally continuous, and, similarly to HF-GU2, appear to dip towards the hillside of Hohle Fels at an angle of about 2°.

HF-GU5

In HF-GU5 we grouped GL 204 to GL 211, which we recovered in core 37 from the second down to the fourth liners (Fig. 5.6 and Fig. 5.15). In this unit gray and olive gray are replaced by yellow and brown as the predominant colors of the sedimentary matrix. GL 204-211 appear rich in intercalations, lenses, and grains which are strong brown (7.5YR 4/6), brown (10YR 5/3), yellowish brown (10YR 5/6), dark yellowish brown (10YR 4/6) and more rarely yellowish red (5YR 4/6) in color. Such colors possibly result from a higher content of iron oxides. With the sole exception of a clay-rich zone located at the bottom of GL 207, our sediment descriptions show that HF-GU5 is a sandy loess unit in which two main bed types alternate. GL 204, 206, 207, 208 and 211 are free of gravel or have less than 10% gravel. These layers alternate with GL 205, 209 and 210, which contain more than 10% gravel. In both bed types gravel is made of fine and medium, angular fragments of limestone.

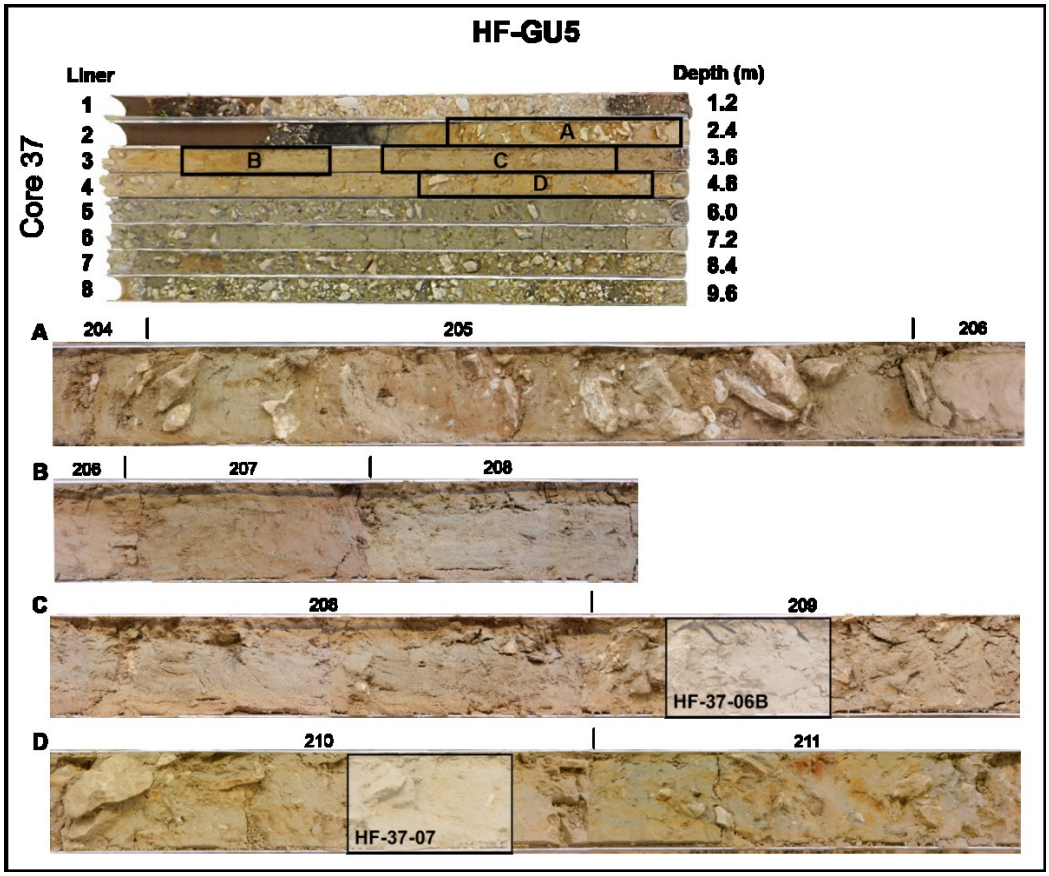

Fig. 5.15. HF-GU5. ***In the upper part***, the liners of core 37. ***A***, ***B***, ***C***, ***D*** details from the GL (numbered in the figure) which are discussed in the main text. ***HF-37-06B*** and ***HF-37-07*** indicate the position of the micromorphological samples presented in Fig. 5.16.

Our results from EC-logging 34 and 35 show high electrical conductivity values (40-90 mS/m) at depths between ca. 1 m and 3 m below the ground surface (Fig. 5.8). Such electrical values and depths are consistent with the deposits of HF-GU5. Furthermore, our GPR data also display strong attenuation of the radio signal starting from ca. 1 m below the ground (Fig. 5.8), supporting the hypothesis that silty sediments similar to HF-GU5 (and HF-GU6) might be laterally continuous in front of Hohle Fels.

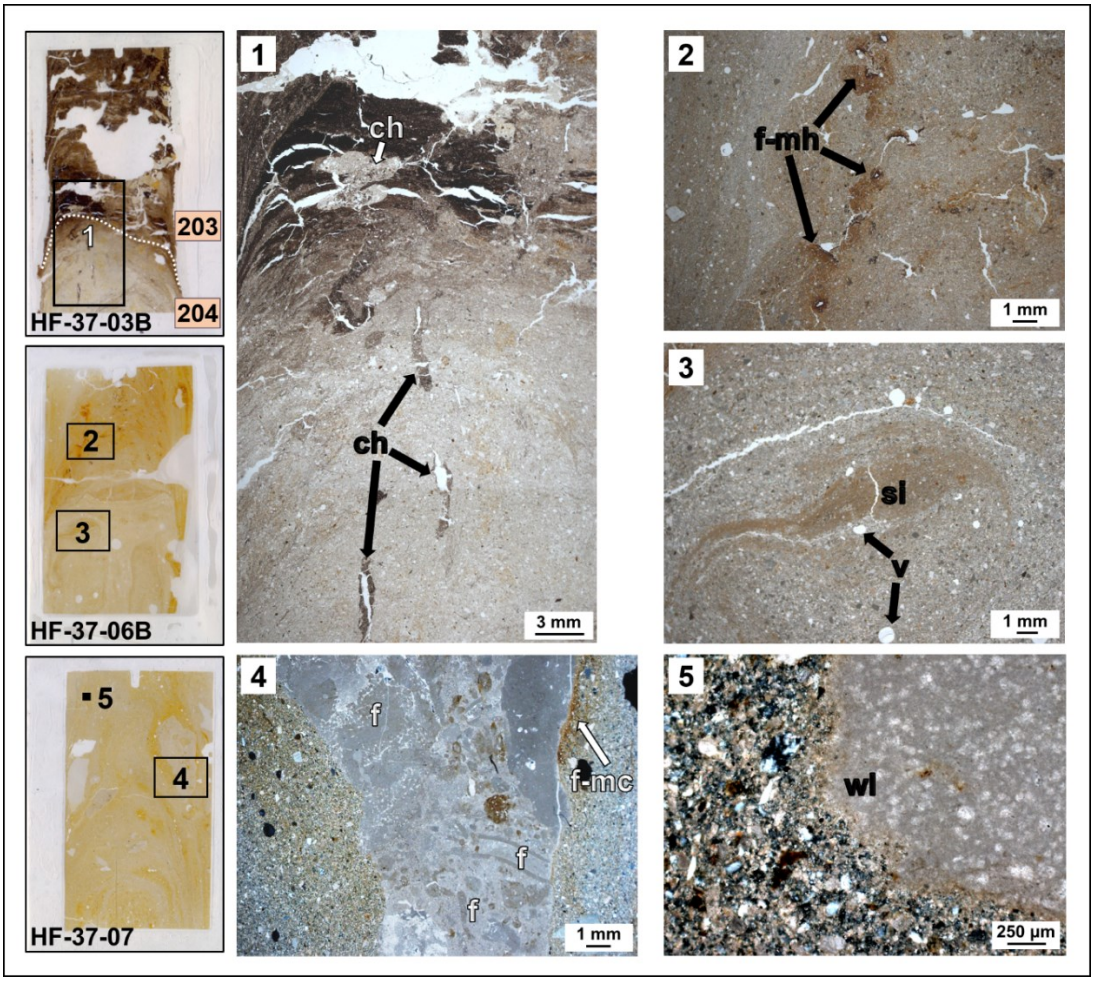

Fig. 5.16. Micromorphological results from HF-GU5. ***On the left***, thin section scans of the samples HF-37-03B, HF-37-06B and HF-37-07. ***1***, photomicrograph in PPL from the contact between GL 203 and GL 204 displaying channels (**ch**) and evidence for bioturbation between the two sediments. ***2***, photomicrograph in PPL from GL 209 showing iron-manganese hypocoatings (**f-mh**) around voids. ***3***, photomicrograph in PPL from GL 209 showing lens of silt (**si**) and vesicle-shaped vughs (**v**). ***4***, photomicrograph in PPL from GL 210 showing fresh limestone fragment with microfossils (**f**) and iron-manganese coating (**f-mc**). ***5***, photomicrograph in XPL from GL 210 capturing a fragment of weathered limestone (**wt**).

Of the five block samples we collected from HF-GU5, we produced and analyzed three micromorphological thin sections: HF-37-07 from GL 210, HF-37-06 from GL 209 and HF-37-03B from GL 204 (Fig. 5.16).

Our micromorphological results show that all three layers are largely composed of well-sorted, calcareous, coarse, reworked loess and calcite sand that is organized in graded laminations and lenses (Fig. 5.16, detail 1 and 3). Only GL 210 presents limestone fragments displaying recognizable microfossils (Fig. 5.16, detail 4). However, in this sediment limestone fragments are also weathered and exhibit rough external borders (Fig. 5.16, detail 5). We documented clear examples of iron hypocoatings around voids and iron coatings around limestone fragments in GL 209 and GL 210 (Fig. 5.16, details 2 and 4). In the lower part of sample HF-37-07, we observed several vesicle-shaped vughs (Fig. 5.16, detail 3). We did not observe fragmented clay coatings in any of the HF-GU5 layers. The topmost contact of HF-GU5 displays channels and bio-galleries in which we documented sediment that has moved from HF-GU6 (GL 203) downwards into HF-GU5 (GL 204) as result of bioturbation (Fig. 5.16, detail 1).

HF-GU6

We recovered GL 202 and GL 203 in core 37 from the bottom of the first and the top of the second liner (Fig. 5. 5 and Fig. 5.17). These layers display a distinctive black color of the matrix (10YR 2/1), appear rich in organic matter and contain up to fine-gravel-sized charcoal fragments. In GL 202 we documented sand-sized fragments of pottery and a higher content of limestone gravel. In contrast, GL 203 corresponds to a gravel-free, well-sorted, clayey silt, displaying iron-depleted (5Y 6/2) laminations (Barbieri et al. 2018).

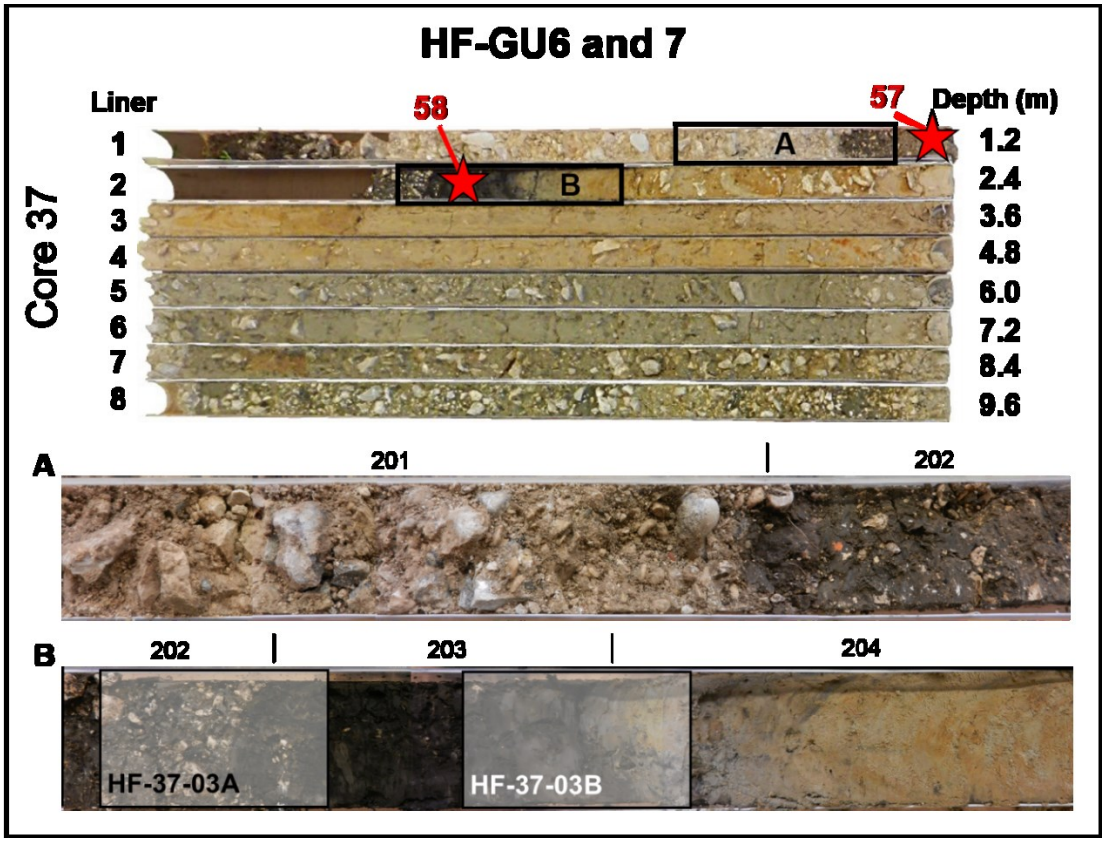

Fig. 5.17. HF-GU6 and 7. ***In the upper part***, the liners of core 37. ***A***, ***B***, details from the GL (numbered in the figure) which are discussed in the main text. ***HF-37-03A*** and ***HF-37-03B*** indicate the position of the micromorphological samples presented in Fig. 5.16 and Fig. 5.18. Red stars mark the location of the dating samples (ID ***57*** and ***58***) discussed in the main text.

FTIR analysis performed on a mixed charcoal sample from the upper part of GL 202 revealed absorption bands of carboxylate groups at 1587 and 1394 cm^{-1}, consistent with fossil charcoal (ID 57, Fig. 5.18. Barbieri et al. 2018). The FTIR spectrum of a sediment sample from the lower part of GL 203 (ID 58 Fig. 5.18) exhibits absorption bands indicative for kaolinites and smectites (at 3697, 3619, 1032, 526 and 466 cm^{-1}), and quartz (at 797 and 779 cm^{-1} Van der Marel and Beutelspacher 1976). The presence of humic acids, presumably from peat, is suggested by absorption bands at 2920, 2852, 1630 and 1425 cm^{-1} (Lin-Vien et al. 1991). Using the radiocarbon method, we dated the mixed charcoal sample to 314 ± 40 ^{14}C BP and the sediment sample to 4933 ± 28 ^{14}C BP (ID 57 and ID 58 in Table 5.1).

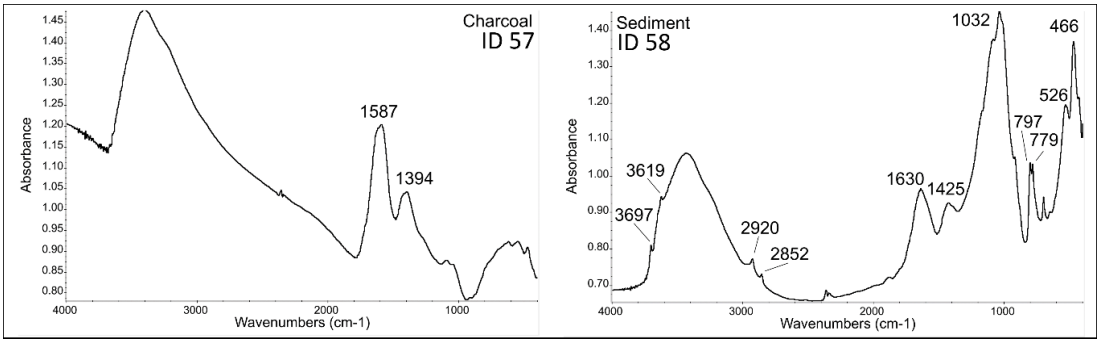

Fig. 5.18. FTIR spectra of the dated charcoal and sediment samples from HF-GU6. Details in the text (figure modified from Barbieri et al. 2018).

We covered the contacts between GL 202, 203 and 204 with the thin sections HF-37-03A and HF-37-03B (Fig. 5.19). The results of our micromorphological analysis revealed that GL 202 largely consists of rounded limestone gravel in a silty sand composed of calcite, quartz, snail shell, bone (Fig. 5.19, detail 1), and charcoal fragments (Fig. 5.19, detail 2). Particularly in the lower part of this layer, we observed cracks and bio-galleries that have been filled with sediment and components reworked from the lower GL 203 (Fig. 5.19, detail 3). Although potentially affected by bioturbation, the contact between GL 202 and GL 203 appears quite sharp and is marked by a change in grain size and composition. GL 203 is free of gravel-sized fragments and it is made of decalcified reworked loess, comminuted organic matter, sand-sized fragments of chalcedony, feldspar, and rare charcoals. Components are organized in poorly graded laminations displaying different content of organic matter (Fig. 5.19, detail 4 and 5). In thin section the content of organic matter appears much lower than expected from the macroscopic description and it is confirmed by the low carbon yield of the ^{14}C measurements (Table 2.1 p. 44). As previously discussed for HF-GU5, the lower contact of GL 203 displays channels and bio-galleries in which we documented very rare fragments of laminated, limpid clay coatings (Fig. 5.19, detail 6).

HF-GU7

We recovered GL 201 in core 37 from below the modern soil (Fig. 5.6 and Fig. 5.17). This layer is composed of limestone gravel displaying different degrees of roundness (from subangular to rounded) and size (from coarse to fine). We also observed rare fragments of glazed pottery and Bohnerz. Based on matrix color and grainsize we divided GL 201 into two alternating beds, GL 201a displaying brown color (10YR 5/3) and more

abundant coarser sand, and GL 201b, brownish yellow in color (10YR 6/6) and richer in finer sand (Barbieri et al. 2018).

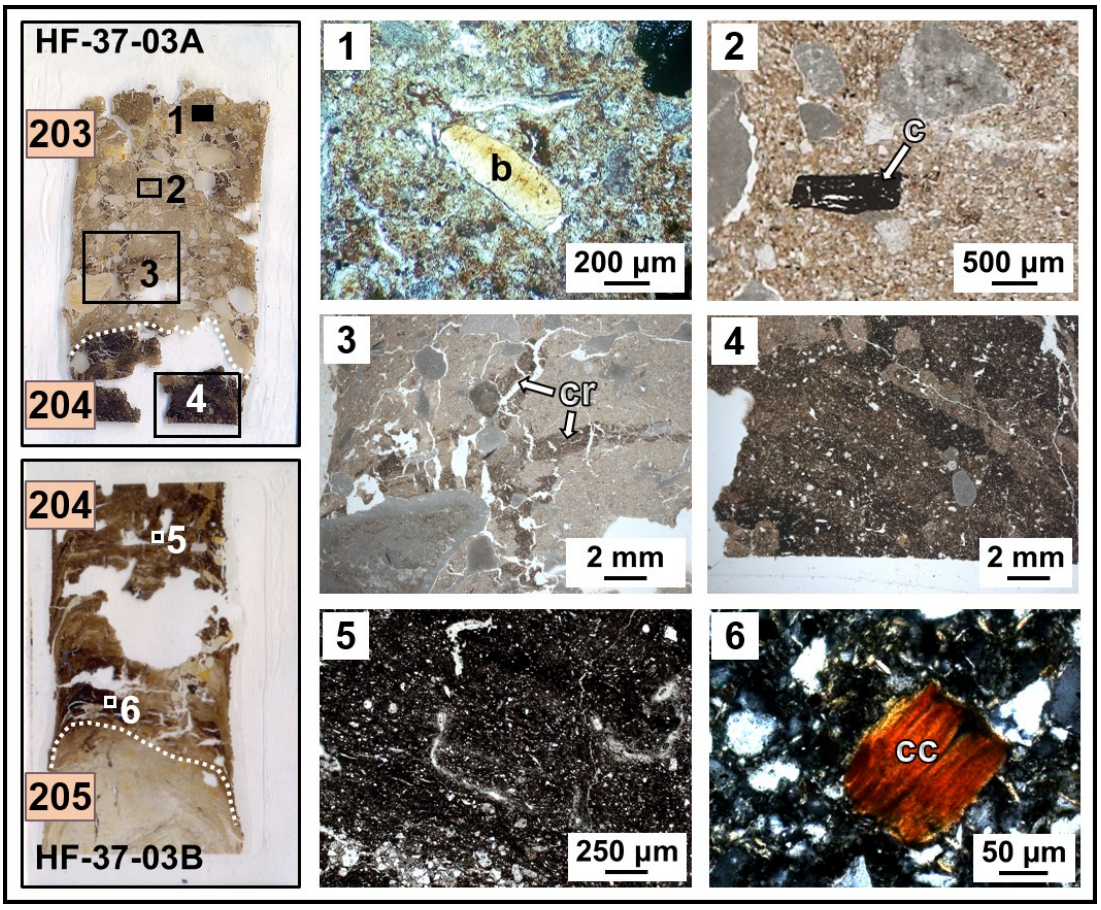

Fig. 5.19. Micromorphological results from HF-GU6. ***On the right***, thin section scans of the samples HF-37-03A and HF-37-03B. ***1***, photomicrograph in PPL from GL 203 showing bone fragment (**b**). ***2***, photomicrograph in PPL from GL 203 displaying fragment of charcoal (**c**). ***3***, photomicrograph in PPL from GL 203 displaying cracks (**cr**) filled with sediment from the under laying GL 204. ***4***, photomicrograph in XPL from GL 204 capturing laminations with varying amount of organic matter. ***5***, photomicrograph in XPL from GL 204 depicting graded laminations. ***6***, photomicrograph in XPL from bioturbated contact with GL 205 showing fragmented, limpid, laminated clay coating (**cc**).

Our GPR data from Profile 40 show that the fine deposits of HF-GU5-6 are truncated by a reflector that defines a 30 m-wide and 1.5 m-deep depression (Fig. 5.8). On top of it we detected reflection hyperbolas with a velocity between 0.06 and 0.08 m/ns, comparable with the gravel and cobbles of HF-GU7 (Davids and Annan 1989). Also, the low electrical conductivity values (<30 mS/m) we measured in EC-logging 34 and 35 suggest that gravelly deposits comparable with HF-GU7 are laterally continuous in front of Hohle Fels.

5.3 Data interpretation

In this section we discuss our results from the Ach Valley and their potential similarities with previous studies conducted inside the cave of Hohle Fels and in the Ach Valley. Some of the interpretations presented in this section have been summarized in a previous publication (Barbieri et al. 2018).

I. River incision, soil and cave erosion (after 28.000 ^{14}C BP)

HF-GU2 is the deepest deposit we recovered from the Ach floodplain. Our data show that this unit is rich in limestone gravel, reworked loess and fragmented, limpid clay coatings (Fig. 5.11). We argue that these components eroded from bedrock, sediments and soils that were located along the flanks and on top of the plateau of the Ach Valley. Our micromorphological analysis from HF-GU2 revealed that this unit is also composed of rare sand-sized grains of phosphatized loess, fragments of bone and speleothems (Fig. 5.11). As mentioned in the first part of this chapter, Miller (2015) studied with micromorphology the Middle Paleolithic to Gravettian deposits accumulated inside Hohle Fels. The results from his study show that phosphatization of loess and formation of speleothems occurred inside this cave (Miller 2015). Furthermore he reported numerous sand-sized bone fragments throughout the sequence (Miller 2015). We conclude that grains of phosphatized loess, speleothems and bone fragments in HF-GU2 eroded from Hohle Fels (Barbieri et al. 2018). In HF-GU2 the components are organized in alternating fine gravel-rich and matrix-rich beds. The contact between these bed types is usually clear and marked by medium gravel-sized fragments of limestone (Fig. 5.10 and Fig. 5.11). Based on such bedding, we argue that HF-GU2 was deposited by debris flow that originated from inside the cave of Hohle Fels and from the external hillside (Blikra and Nemec 1998).

The deposition of limestone gravel (rounded to angular), reworked loess and rare fragmented clay coatings lasted during the accumulation of HF-GU3. In comparison with the lower HF-GU2, HF-GU3 does not display alternating fine-rich and gravel-rich beds. This difference in the sedimentary structure possibly indicates a change in the processes responsible for the mass-wasting of the hillside. From the contact area between HF-GU2 and HF-GU3 we recovered one bone fragment displaying subrounded edges and sizing (2cm^2) comparable with the medium limestone gravel with which it was deposited. We

conclude that this bone fragment was not buried *in situ* and thus its radiocarbon determination of 27.900 ± 460 ^{14}C BP has to be regarded as a *terminus post quem* for the deposition of HF-GU3. This date falls in the interval of 30.000 - 26.000 ^{14}C BP published for the Gravettian occupation at Hohle Fels (Taller and Conard 2016). Therefore, a likely source for this bone fragment might be identified in the Gravettian-aged deposits accumulated inside the nearby cave (Barbieri et al. 2018). Although we lack micromorphological data from the lower part of HF-GU3, this hypothesis seems plausible given the abundant presence of bone fragments associated with grains of phosphatized loess and speleothems in HF-GU2.

By integrating our data with field (Conard and Malina 2010) and micromorphological (Miller 2015) observations from Hohle Fels, we conclude that part of the Gravettian-aged deposits accumulated inside this cave was removed by debris flow or similar processes. Consequently, sediment, faunal remains and possibly artifacts moved from the cave into the Ach Valley, resulting in a large disconformity at the top of the Gravettian sequence in Hohle Fels (Barbieri et al. 2018. Fig. 5.20).

Some hundred meters northwards from core 37 (Fig. 5.1, detail 4), Groschopf (1973) recovered sediments comparable with the sequence we recovered in core 37 (Barbieri et al. 2018). For example, Groschopf reported a peat exhibiting color, composition and depth-below-surface comparable with our HF-GU6. Below this, to a depth of -5.2 m, he described a yellow-brown silty-sand, which is similar to what we described for HF-GU5. Additionally, to a depth of -14 m, Groschopf recovered gravelly sediments characterized by a gray matrix color, which could be equivalent to our HF-GU2-4 deposits. Below -14 m, Groschopf encountered a thick marl which likely covered pre-Würm Alpine gravel.

Numerous coring and geophysical data collected throughout Ach and Schmiech valleys largely confirm the sequence recovered by Groschopf (1973). For instance German (et al. 1995) correlates the thick marl deposit recovered by Groschopf (1973) with the *Obere Mergel* deposits from core CSS1 (OM in Fig. 5.21). Seismic and geoelectric measurements collected across the Ach and Schmiech valleys revealed that these marl deposits have been eroded in a phase of river valley incision (Brost et al. 1987). Based on our correlation of HF-GU2 with the sequence described by Groschopf (1973) and German

(et al. 1995), we argue that HF-GU2 might have been deposited after a phase of river valley incision (Fig. 5.21. Barbieri et al. 2018).

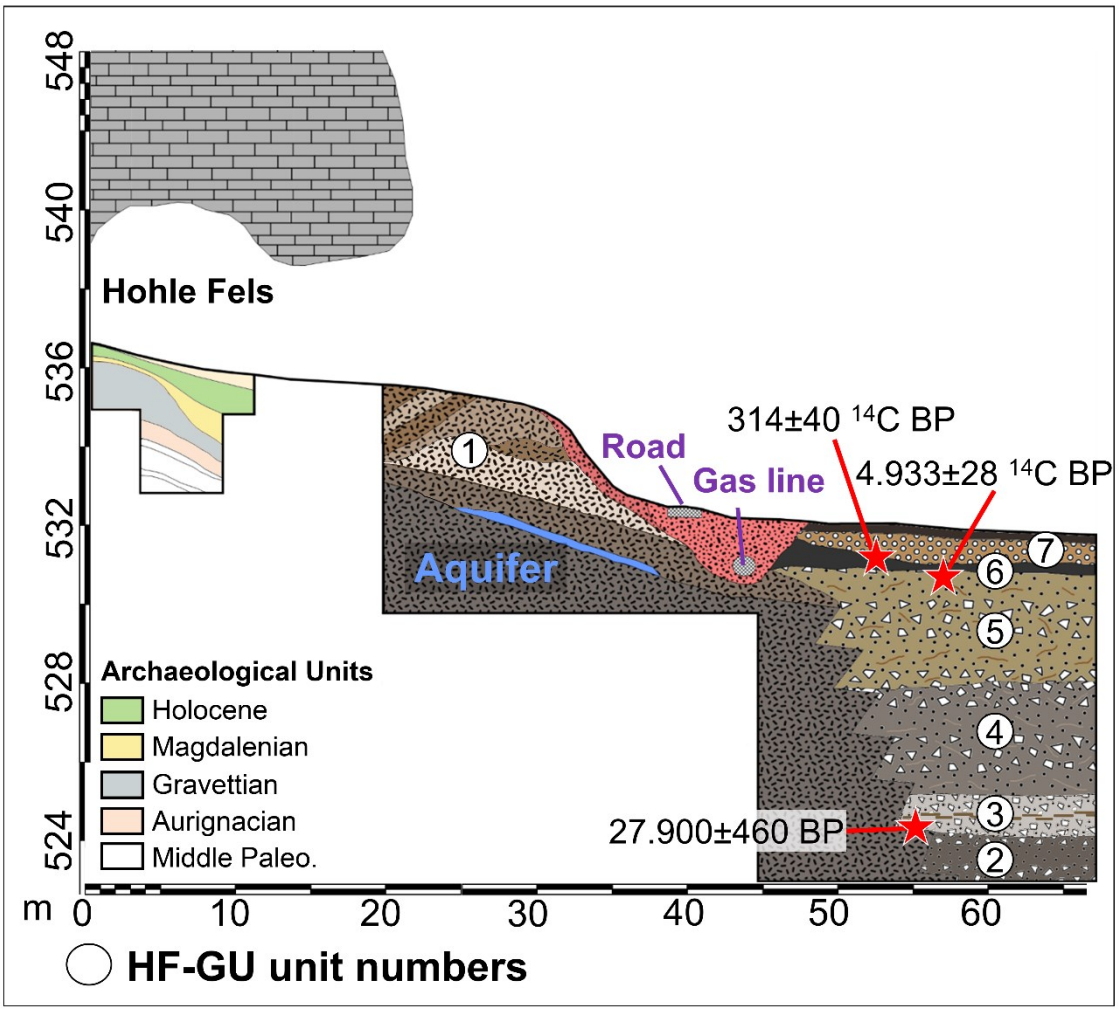

Fig. 5.20. The Ach Valley in front of Hohle Fels. Figure compiled from our results and data collected during the excavations conducted inside the cave (from Maria Malina). HF-GU unit numbers and ^{14}C dating are numbered on the drawing (figure modified from Barbieri et al. 2018).

II. Increasing loess deposition (LGM?)

Our macroscopic and micromorphological observations indicates that cave erosion was no longer occurring during the accumulation of the upper part of HF-GU3. This deposit lies underneath HF-GU4, which represents a gradual transition to the nearly gravel-free HF-GU5.

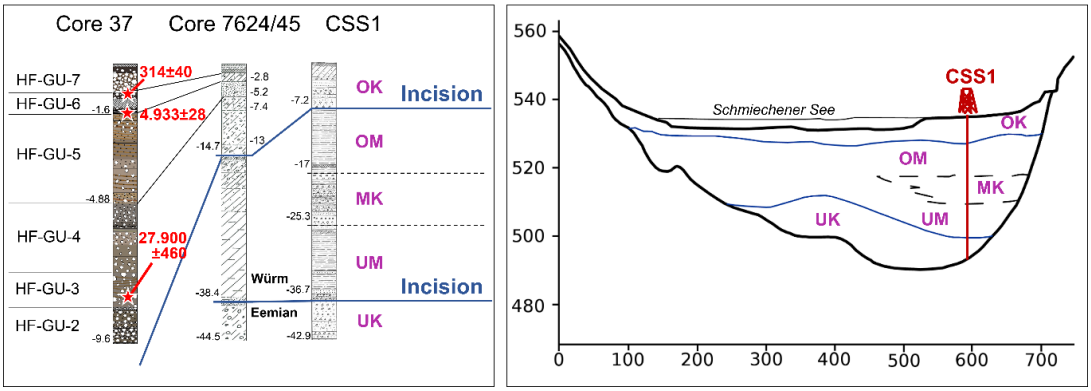

Fig. 5.21. The position of HF-GU2 in relation to previous river valley incision. ***On the left***, cross-correlation between our core 37, core 7624/45 recovered by Groschopf (1973) and CSS1 recovered by German (et al. 1995). HF-GU unit numbers are labelled in black along core 37. Results from ^{14}C dating are depicted in red, units from CSS1 are labelled in violet, and river incisions are marked in blue. ***On the right***, reconstruction of the deposits buried below the Schmiechener See in the Schmiech Valley (Fig. 5.1), modified from Brost (et al. 1987). CSS1 is depicted in red, units are labelled in violet and river incision are displayed in blue. Our cross-correlations indicate that HF-GU2 was deposited after a phase of valley incision.

HF-GU5 is largely composed of well-sorted, calcareous, coarse, reworked loess and calcite sand that are organized in graded laminations and lenses (Fig. 5.16, detail 1 and 3). Embedded in this matrix are rare limestone fragments, some displaying recognizable microfossils (Fig. 5.16, detail 4). Due to the lack of fragmented clay coatings, HF-GU5 can be regarded as a break in the sequence we recovered in core 37. We hypothesize that this unit resulted from the increasing deposition of reworked loess, which probably overprinted soil and bedrock erosion around the LGM (Barbieri et al. 2018). Reworked loess was accumulated in HF-GU5 by periodic liquefied mudflows as supported by the good sorting, graded laminations, and vesicles we observed in some layers of HF-GU5 (Fig. 5.16. Bertran and Texier 1999, Barbieri et al. 2018).

While the lower units we recovered in core 37 have been extensively gleyed, HF-GU5 appears rich in iron-manganese oxides. Such difference in sediment diagenesis might be related to fluctuation in the ground water level (Barbieri et al. 2018). Furthermore in HF-GU5 iron-managanese hypocoatings commonly occur around voids of likely biological origin (Fig. 5.16, detail 2). We conclude that after its deposition HF-GU5 might have undergone a phase of incipient soil formation.

II. Hillside and cave erosion (possibly Late Glacial)

Our GPR data revealed the presence of a preserved sedimentary sequence at the *Vorplatz* of Hohle Fels. Here, the deeper structure we identified is located about 4 m below the ground and corresponds to a surface which slopes gently from the Hohle Fels cave entrance towards the center of the Ach Valley (Fig. 5.5, detail A). The lower part of GL 229 (HF-GU1) rests in core 39 at depth comparable to this sloping surface. Our micromorphological results from this deposit revealed numerous sand-sized fragments of speleothems embedded in a non-decalcified, reworked loess (Fig. 5.9, detail 6). In this deposit we did not observe grains of phosphatized loess, bones, nor artifacts. We hypothesized that the exclusive occurrence of speleothem fragments in GL 229 might be explained with two alternative models. According to the first hypothesis, GL 299 resulted from the erosion of cave deposits that accumulated during a cold time period when Hohle Fels was less intensively occupied by humans and/or animals. Alternatively, the speleothem fragments we observed in GL 229 may have formed at the entrance of Hohle Fels or even inside small cavities located along the external wall of the cave. In this case GL 229 would have originated from the combined action of hillside mass-wasting and break-down of the exposed bedrock. The latter hypothesis appears to be supported by the occurrence of very fresh limestone fragments which display preserved microfossils.

Approximately 1-2 m below the ground of the *Vorplatz,* the GPR detected a second major reflector (Fig. 5.7, detail B). By examining the 3D geometry of this feature we hypothesized that it likely corresponds to a cone of colluvial material transported downhill from the hillside. This cone appears to dip towards the entrance to Hohle Fels, where it might have been shaped by sudden channel-scouring events originating from the external hillside and the cave of Hohle Fels (as described by Van Steijn et al. 1995, Blikra and Nemec 1998, Wilkerson and Schmid 2003, Sass and Krautblatter 2007, Onaca et al. 2016). The sediments we recovered from depths comparable with this colluvial cone appears composed of reworked loess and itis rich in fresh limestone gravel and free of speleothem fragments.

Our GPR data show that the potential disconformity we detected at the entrance of Hohle Fels is covered with densely stacked deposits that dip towards the cave and the Ach Valley (Fig. 5.7, detail C. Fig. 5.21). Blumentritt (personal communication) informed us that

Magdalenian artifacts were likely recovered from these deposits, in the course of an illegal excavation conducted along the external wall of the *Fels*. However, the geological layer (GL 227) that we recovered in core 39 from depths comparable with these finds show no evidence for archaeological material nor cave sediment. On the contrary, GL 227 is similar to the lower layers we recovered in core 39. The only relevant difference is represented by silty and sandy graded laminations which are indicative for some water transport (Fig. 5.9, detail 1).

The sequence we reconstructed for the Vorplatz of Hohle Fels has been truncated by more recent human activities related with the exploitation of the cave and its surroundings (Barbieri et al. 2018).

III. Lateral fluvial erosion (Early to Mid-Holocene)

HF-GU6 represents the most recent evidence for major landscape change in the Ach Valley (Barbieri et al. 2018). We hypothesize that this unit probably formed through processes similar to those that led to the formation of the so called "Black Floodplain Soil" (BFS), which is commonly reported in river valleys across Germany (Rittweger 2000). Combining data from various regions of Germany, Rittweger (2000) proposed that the BFS derived from phases of soil formation and erosion that took place during the early Holocene. The humin fraction present in the BFS was probably inherited from chernozem soils formed during the Boreal to early Atlantic. Towards the end of the Atlantic, the chernozem soil was eroded by lateral migration and minor river incisions, and was subsequently redeposited together with additional minerals. Today BFS is found as a relict complex of alluvial sequences with a range of Holocene ages (Rittwerger 2000).

Following the model proposed by Rittweger (2000) for the BFS, we hypothesize that the humin fraction present in HF-GU6 has been inherited from peats and soils formed around 5.000 ^{14}C BP (ID 58, Table 5.1). Later, the Ach river likely eroded this soil and redeposited it together with reworked loess and other mineral components. Redeposition of this material probably lasted until a few centuries ago (314 ± 40 ^{14}C BP, ID 57 in Table 5.1). Deposits comparable to our HF-GU6 have been documented discontinuously in the Ach, Blau and Schmiech valleys (Groschopf 1973, Gwinner 1989, Barbieri et al. 2018).

HF-GU6 was later covered with HF-GU7, which is rich in subangular to rounded limestone gravel, indicative of a more intensive sediment supply from the hillside. Based

on our GPR data (Aspiron and Aigner 1999) and sizing and roundness of the limestone gravel (Attal and Lavé 2009, Pearce 1971), we propose interpreting HF-GU7 as a high energy river deposit.

6 Implications of landscape and environmental changes for the interpretation of the archaeological record of the Ach and Lone valleys

In this chapter we address archaeological questions concerning the arrival of modern humans in the Swabian Jura (6.1); the depopulation of the region around the LGM and its recolonization by Magdalenian groups (6.2); and the occurrence of potential open-air sites in the region (6.3). After a short summary (6.4), we suggest potential further studies, which might help to clarify some of our findings (6.5).

6.1 Less intensive phosphatization of the Early Aurignacian deposit inside Hohlenstein-Stadel

A large portion of the Middle and Upper Paleolithic deposits accumulated inside the caves of Hohlenstein-Stadel in the Lone Valley (chapter 3.3.1) and Hohle Fels and Geißenklösterle in the Ach Valley (Goldberg et al. 2003, Miller 2015) is formed from reworked loess. Colluvial processes moved this sediment from the top of the Alb into the caves of the Ach and Lone valleys, and the originally calcareous loess has undergone a process of phosphatization. This diagenesis has not been constant, and, in particular, the early Aurignacian deposits of Hohlenstein-Stadel and Hohle Fels (Miller 2015) display less intensive calcite dissolution and minor apatite neoformation. The fact that the earliest Upper Paleolithic deposits within caves located 50 km apart present such similar diagenetic signatures could be considered the result of a regional process.

Calcite dissolution is regulated by different variables. Karstic water is the main agent involved in the dissolution of the limestone bedrock and it is more successful when its pH is between 6 and 4 (Plummer and Wigley 1976, Sjöberg and Rickard 1983, Sjöberg and Rickard 1984, Morse and Arvidson 2002). Increasing amounts of CO_2 and other chemical compounds resulting from the decomposition of organic matter (such as urea, uric acid, phosphates, sulfates and nitrates) might be responsible for the acidification of karstic water (Fairchild et al. 2006). Conversely, high concentrations of Ca^{2+}, Mg^{2+}, Sr^{2+}, Ba^{2+}, heavy metals, and silica might inhibit the dissolution of calcite (Plummer and Wigley 1976, Sjöberg 1976, Sjöberg and Rickard 1985, Morse and Arvidson 2002). The concentration of these chemical substances in karstic water depends on the biological activity of plants, *fungi*, land-snails and bacteria present inside the karst system and in its

surroundings (Folk et al. 1973, Castainer et al. 1999, Ehrlich and Newman 2008). Temperature also influences the rate of calcite dissolution, with a ratio of 1.3%/°C (Morse and Arvidson 2002).

In short, the decalcification process in cave sediments largely depends on water availability, rate of biological activity and temperature. The higher these variables, the higher the rate of calcite dissolution.

Apatite neoformation might take place when the acidification of karst water is caused by a high concentration of phosphoric acid (Karkanas et al. 2002). At Hohlenstein-Stadel we hypothesized that the phosphoric acid was released from decomposing animal carcasses and large carnivore excrements (possibly hyena). A similar model was previously discussed for some prehistoric caves in Switzerland and Spain (Braillard et al. 2004, Sanz et al. 2016, Sanz et al. in press). Bat or bird guano has been argued as the main factor responsible for the phosphatization of the deposits of Hohle fels (Goldberg et al. 2003, Miller 2015), Geißenhlösterle (Miller 2015) and many other cave sites (e.g. Karkanas et al. 2002, Shahack-Gross et al. 2004). All these studies indicate that animal use of caves during the Pleistocene played a significant role in the phosphatization of cave sediments.

Previous faunal analyses show that medium and large carnivores used less frequently the caves located in the Ach and Lone valleys during the transition from the Middle to the Upper Paleolithic, probably in response to the increasing presence of humans (Kitagawa et al. 2012). In addition to faunal data, this trend is also supported by micromorphological studies from Hohlenstein-Stadel, Hohle Fels and Geißenklösterle. In these caves fragments of coprolites are found at higher frequencies and in bigger sizes in the Middle Paleolithic than in Aurignacian deposits (Miller 2015 and data presented in chapter 3.3.1).

Data concerning the remains of avian fauna from Hohle Fels and Geißenklösterle show an opposite trend, with an increase in bird remains in deposits from the Middle to Upper Paleolithic (Conard et al. 2013). However, artifacts made out of bird bone (Conard et al. 2009), feather fragments on Aurignacian stone tools (Hardy et al. 2008), and cut marks on bird bone fragments indicate that the large majority of these remains was probably introduced into the caves by humans (especially at Hohle Fels, Conard et al. 2013).

Despite the likely decrease in animal use of the Swabian caves, the less intensive phosphatization of the early Aurignacian deposits inside Hohle Fels and Geißenklösterle

might have resulted from climatic change. Micromorphological analyses conducted on the earliest Aurignacian deposits of Hohle Fels revealed the presence of features related to the formation of ice lenses (Miller 2015). Inside Geißenklösterle the Middle Paleolithic sequence is truncated and covered with fresh non phosphatic loess, which contains early Aurignacian materials (Miller 2015). Miller (2015) hypothesized that the truncation of the Middle Paleolithic sequence might have been related to mass-wasting of the external hillside, while the subsequent deposition of loess might be regarded as an indicator of a colder and drier climate regime. We did not observe comparable features at Hohlenstein-Stadel, likely because the profile we analyzed using micromorphology was located too far back (ca. 50 m) from the cave entrance, leaving it less exposed to external climatic fluctuations. Therefore, in the case of Hohlenstein-Stadel we lack direct and consistent evidence supporting the occurrence of a colder climatic period during or after the accumulation of the early Aurignacian deposit.

In the Swabian Jura the appearance of the Aurignacian has been related with the arrival of early modern humans and the extinction of the endemic Neanderthals. Three models have been proposed to explain this evolutionary event: the "Population Vacuum", the "Danube Corridor" and the "*Kulturpumpe*" model (Conard 2000; Conard 2003; Conard and Bolus 2003; Conard et al. 2006; Conard and Bolus 2008). Particularly the first and the latter argue that the replacement of Neanderthals with early modern humans might have been facilitated by the occurrence of a cold climatic period (see chapter 1.2.1). Our results from Hohlenstein-Stadel cannot support or deny this hypothesis.

6.2 Landscape changes in Ach and Lone valleys

6.2.1 Fragmented clay coatings as indicators for landscape change

The micromorphological analysis of the sediments we recovered from the Lone and Ach valleys showed that these deposits are rich in fragmented clay coatings (Barbieri et al. 2018). Our findings contrast with the coring results as published for the Lone Valley by Schneidermeier (1999), who reported buried "red horizons" which he interpreted as potential paleosols preserved *in situ*.

The occurrence of fragmented clay coatings in the sequences we reconstructed for the Ach and Lone valleys is particularly useful to reconstruct the landscape history of this region. Clay coatings originate from the vertical movement of water into the ground,

which mobilizes clay particles in suspension. During this process, ceasing water supply or absence of available macropores prevent the mixture of clay and water to further infiltrate in the ground. Once the water is adsorbed into finer pores clay is filtrated out by the pore walls, leading to the formation of clay coatings (Kühn et al. 2010). Most of the clay pedofeatures we observed in our open-air sediments are laminated, thus they originated from multiple cycles of clay illuviation that took place over long-lasting periods of landscape stability (Kühn et al. 2010, Barbieri et al. 2018).

In situ clay coatings have been documented in paleosols that formed across Europe during cooler (Sedov et al. 2013) or warm interstadials of the Late Glacial (Van Vliet-Lanoë 1990, Kühn et al. 2006). Fragments of clay coatings have been documented in various colluvial sediments of Würm age (Buch and Zöller 1990, Antoine et al. 2001, Kühn et al. 2006, Sedov et al. 2013). Bertran and Texier (1999), Mücher (et al. 2010) and Kühn (et al. 2010) have regarded the occurrence of fragmented clay coatings as indicative for colluvial processes. Kühn (et al. 2010) has argued that also bioturbation is among the possible cause for the fragmentation of clay coatings. While Van Vliet-Lanoë (1990) and Huijzer (1993) have discussed the role of gelifluction and cryoturbation as potential process responsible for the disruption and deposition of these pedofeatures.

Among the fragmented clay coatings we studied, only those contained in HS-GU4 and HS-GU5 might have been disrupted and deposited by frost related processes (Barbieri et al. 2018). More in detail, in HS-GU4 we observed impregnated aggregates with star-shaped vughs and rounded aggregates with granostriated b-fabric that are comparable with frost-induced microstructures described by Van Vliet-Lanoë (Van Vliet-Lanoë 2010 p.84 and 90). On the other side, HS-GU5 contains well-rounded aggregates composed of medium and coarse calcite sand coated with alternating laminations of iron-stained clay and silt (Fig. 3.18). Huijzer (1993), Bertran and Texier (1999) and Van Vliet-Lanoë (2010) have described concentric aggregates similar to those we have identified in HS-GU5 in deposits influenced by solifluction and gelifluction. Although it is possible that HS-GU4 might have been affected by cryoturbation, our data do not fully support the hypothesis that HS-GU4 and HS-GU5 might have been deposited by gelifluction since this type of deposit commonly display diagnostic platy microstructure (Bertran and Texier 1999, Blikra and Nemec 1998), which is not present in HS-GU4 and 5 (Barbieri et al. 2018).

Interestingly, such micromorphological features are absent in nearly all the open-air sediment we investigated in the Ach and Lone valleys. Only HS-GU15 displays potential platy microstructure, gravel imbrication and possible folding/overturning which might have resulted from gelifluction (Bertran and Texier 1999). More consistent evidence of ground freezing during the colder periods of the Pleistocene come from the cave sites of Ach and Lone valleys, where micromorphological analyses revealed the occurrence of banded microfabrics and platy microstructures (Goldberg et al. 2003, Miller 2015, Barbieri and Miller in press, this dissertation chapter 3.3). We argue that such discrepancy between valley and cave deposits might be related to the different impact of cold climate on the sediments deposited in the open-air. For instance, during the colder periods of the Pleistocene the Ach and Lone valleys might have been covered with a thick snow pack, which might have isolated the ground surface from the colder atmosphere (Washburn 1979). Such isolation might have kept the ground temperature above freezing and/or might have impeded a regular water supply to the ground, preventing the formation and growth of ice crystals (Van Vliet-Lanoë 1998). Also higher gravel content and more continuous reworking might have impeded the formation and preservation of diagnostic frost-induced micromorphological features in the sediments deposited in the open-air (Van Vliet-Lanoë 2010, Barbieri et al. 2018).

According to her profile drawings, Geiling (et al. 2015) reported the occurrence of one ice wedge and involutions in the gravelly deposits that Bolus (et al. 1999) excavated in front of Hohlenstein, along the hillside opposite from our survey area. Considering these finds, we cannot reject the possibility that the nearly absence of frost-induced features in the sediments we recovered from Ach and Lone valleys might result from a methodological bias. For instance, limits in vertical and horizontal resolution of our coring and GPR data might not have allow us to detect and correctly interpret ice wedges and involutions comparable to those published by Geiling (et al. 2015). Furthermore, due to the core drilling, most of the sediments we recovered in our liners underwent a significant loss in porosity. We do not know if such sediment deformation might hinder the detection of platy microstructure, for instance. We conclude that further studies are needed to clarify our interpretation of the sediments deposited in the open-air of Ach and Lone valleys, particularly with trenching and experiments designed to evaluate the impact of core drilling on the preservation of specific micromorphological features.

Based on our data, we tend to exclude gelifluction and cryoturbation as major processes in the disruption of the numerous clay coatings observed in the sediments from the Ach and Lone valleys. Conversely we hypothesize that other processes (such as debris flow, mud flow, sheet flow and alluvial processes) might have been responsible for the erosion of the soils in which these pedofeatures originated (Barbieri et al. 2018).

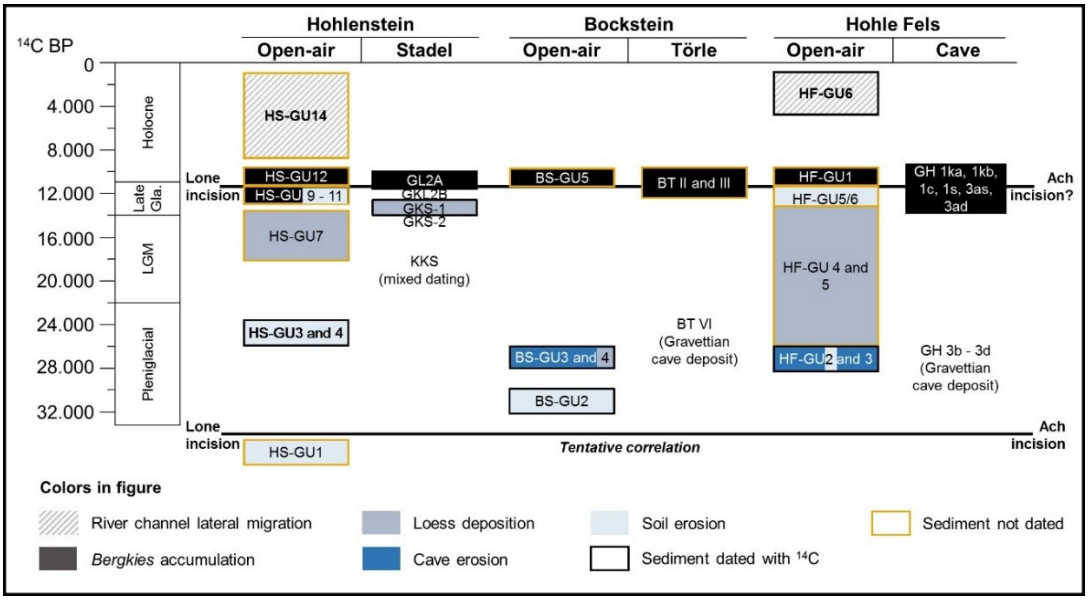

Fig. 6.1. Timetable. Chronological overview of the main geomorphological processes active in the Ach and Lone valleys (figure from Barbieri et al. 2018).

GL 315 (HS-GU1) lies around 1 m above the bedrock in the Lone Valley and displays fragmented, dusty clay coatings. Due to its stratigraphic position and its similarities with pre-Quaternary deposits (Ufrecht 2008a, Kösel 2016, Velliky personal communication), we argue that GL 315 likely represents the earliest evidence for soil formation and erosion in our study region (Fig. 3.9 and Fig. 3.11. Fig. 6.1. Barbieri et al. 2018). Based on our GPR and EC-logging data, we hypothesize that the deposition of HS-GU1 was followed by a phase of incision, during which the Lone River removed part of HS-GU1 from the center of the Lone Valley. Probably in the course of the same erosive phase, the Lone also carved the underlying limestone bedrock deepening its valley bottom of about 3.5 m (Fig. 3.10. Barbieri et al. 2018). Interestingly, previous coring and geophysical data from the Ach and Schmiech valleys revealed a comparable phase of valley incision, in the course of which Ach and Schmiech Rivers lowered their valley floors by ca. 10 m (Fig. 5.20. Groschopf 1973, Brost et al. 1987, German et al. 1995). Due to the lack of dating

for the deeper deposits preserved in Ach and Lone valleys, we cannot securely correlate these two phases of valley incision (Fig. 6.1. Barbieri et al. 2018).

The disconformities shaped during these erosional processes were covered with HS-GU3-4 (Fig. 3.17) and BS-GU2 (Fig. 4.7), in the Lone Valley, and HF-GU2 (Fig. 5.11), in the Ach Valley. From these deposits we reported fragments of limpid clay coatings displaying more distinct laminae in comparison with those deposited in GL 315 (Barbieri et al. 2018). Based on such difference in their internal organization, we hypothesize that HS-GU1, on one side, and HS-GU3-4, BS-GU2 and HF-GU2, on the other side, originated from the erosion of distinct and separate soils (Kühn et al. 2006. Barbieri et al. 2018). Radiocarbon determinations from HS-GU4, BS-GU2 and HF-GU2 indicate that these units deposited between 32.000 and 25.000 ^{14}C BP (Fig. 6.1).

After a hiatus (see section 6.2.3), further evidence for clay illuviation and soil erosion is documented in the units HS-GU9-11, from the Lone Valley, and HF-GU5, from the Ach Valley. In HS-GU8 and HS-GU9 phases of clay illuviation seem to have alternated with secondary calcite formation, which is documented by hypocoatings around voids, coatings around gravel fragments and calcified root cells (Fig.3.24 and Fig. 3.26). In the upper HS-GU11 we identified clay infillings, which appear only slightly disturbed (Fig. 3.30) and might have formed in the course of a more recent (possibly Holocene) phase of soil formation. In the bioturbated contact between HF-GU6 and HF-GU5 we observed very rare fragments of clay coatings. Micromorphological and ^{14}C dating show that HF-GU6 was affected by significant erosion and was likely redeposited in the course of the Holocene (314 ± 40 ^{14}C BP - 4933 ± 28 ^{14}C BP).

In conclusion, phases of soil formation and soil erosion have been the driving processes that have shaped the landscape of Ach and Lone valleys starting earlier than 32.000 ^{14}C BP (Barbieri et al. 2018). Most of the fragmented, laminated clay coatings that we observed in our sediments are the result of multiple cycles of illuviation (Kühn et al. 2010). Although weak clay translocation might have occurred also in the late summer of stadials, we hypothesize that the interstadials of the Pleniglacial offered conditions suitable for the formation of such pedofeatures (Clark 1988, Sedov et al. 2013, Barbieri et al. 2018). In fact these periods were characterized by deeper or absent permafrost, which facilitated the vertical drainage of meteoric water into the ground (Clark 1988),

and the spread of forest or forest-steppe vegetation (Jahnke 2013, Krönneck 2012, Kitagawa 2014, Riehl et al. 2015), which guaranteed long-lasting phases of landscape stability (Fig. 6.2).

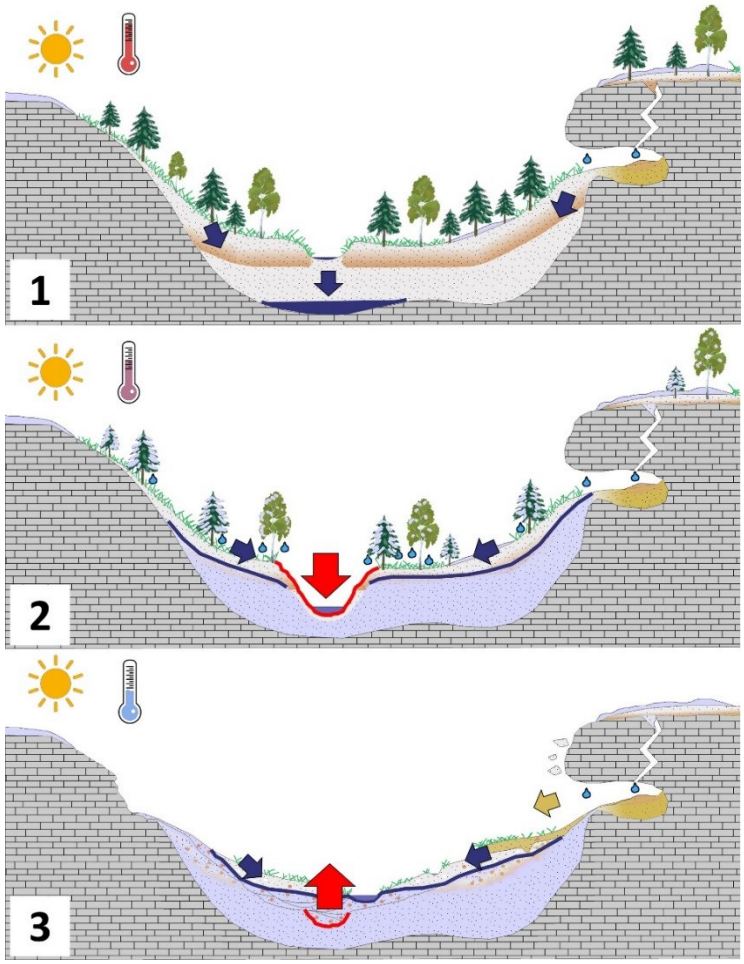

Fig. 6.2 Landscape formation processes. ***1***, in Ach and Lone valleys phase of climate amelioration were characterized by the spread of arboreal vegetation, hillside stability, deeper water drainage (blue arrows) and consequent clay illuviation. ***2***, periods of early climatic deterioration were characterized by a mixed forest-steppe vegetation, frozen ground (blue line), surface water (blue arrows) and valley incision (red arrow). ***3***, periods of advanced climate deterioration were dominated by the spread of grasslands, hillside and cave erosion (brown arrow) and consequent floodplain aggradation (red arrow. Figure from Barbieri et al. 2018).

Knox (1984) argued that in the passage from interstadials to stadials the vegetation adapted to climatic changes with a time lag of some 50-100 years. We conclude that this period of adaptation was characterized by shallower permafrost and sparse arboreal vegetation along the hillside and the riverbanks (Barbieri et al. 2018). In the late spring and early summer the water discharged from the melting snow was likely drained at the

surface in ephemeral river channels. Due to the increasing snow melting and the sparse arboreal coverage, water discharge was higher than the sediment load and might have promoted the incision of Ach and Lone valleys (Mol et al. 2000, Van Huissteden and Kasse 2001, Barbieri et al. 2018. Fig. 6.2).

After the complete adaptation of the vegetation to the stadial climate, the Ach and Lone valleys were covered with grassland (Jahnke 2013, Krönneck 2012, Kitagawa 2014, Riehl et al. 2015). In this altered setting, the valley flanks and riverbanks were no longer stabilized by the sparse arboreal vegetation. Therefore, in the late spring and early summer the water discharged from the melting snow possibly promoted the mass-wasting of the hillside and the erosion of the riverbanks. Both processes impeded further river incision and caused flood plain aggradation (Barbieri et al. 2018. Fig. 6.2).

6.2.2 Cave erosion, loess accumulation, human depopulation around the LGM

Together with reworked soil material the deposits of BS-GU3-4 (Fig. 4.10) and HF-GU2-3 (Fig. 5.11) contain isolated grains of phosphatized loess, fragments of speleothem and bones. Such components have been identified also inside the caves of Hohlenstein-Stadel (Barbieri and Miller, in press. 3.3.1), Hohle Fels and Geißenklösterle (Goldberg et al. 2003 and Miller 2015). Since loess phosphatization and speleothem formation occur inside caves, we conclude that BS-GU3-4 and HF-GU2-3 were deposited by erosional processes, which originated from the caves of Bockstein and Hohle Fels. This major phase of cave and landscape instability was possibly a consequence of the previous river valley incision, which lowered the bottom of the Ach and Lone valleys of several meters (Fig. 6.2, detail 3. Barbieri et al. 2018).

In our dataset we do not have evidence for sediment, faunal remains and artifacts being eroded from the caves of Hohlenstein and redeposited in the Lone Valley. This lack of evidence is expected considering that in comparison with the site of Hohlenstein the area we investigated with our coring is located on the other side of the Lone River, at a distance of about 150 m and slightly upstream in the valley (Barbieri et al. 2018). Archaeological investigations conducted at the *Vorplatz* of Hohlenstein-Stadel (Jahnke 2013) and our re-evaluation of the test pitting conducted by Bolus (et al. 1999) show that sediment moved outwards from the cave (section 6.3). We conclude that Hohlenstein-Stadel probably

experienced major phases of erosion around the LGM and during other periods of the Pleistocene (section 6.3).

From the contact between HF-GU2 and HF-GU3 we recovered one bone fragment, which we dated to 27.900 ± 460 ^{14}C BP. This fragment displays roundness and sizing comparable with the medium limestone gravel in which it was buried. We conclude that the contact between HF-GU2 and HF-GU3 does not represent the context of primary deposition for this bone, which was more likely eroded from upslope. The 27.900 ± 460 ^{14}C BP falls in the interval of 30.000 - 26.000 ^{14}C BP published for the Gravettian occupation at Hohle Fels (Taller and Conard 2016). Therefore, we hypothesize that this bone fragment might have been eroded from the Gravettian-aged deposits accumulated inside the nearby cave of Hohle Fels (Barbieri et al. 2018). Interestingly, previous micromorphological analysis conducted inside this cave appear to support the hypothesis that part of the Gravettian sequence has been removed by erosional processes (Miller 2015).

In BS-GU3, ca. 20 cm below thin section BS-31-01B (Fig. 4.8), radiocarbon measurement performed on a mixed sample of shell fragments yielded an age of 25.900 ± 200 ^{14}C BP (ID 69, Table 4.1). Since this radiocarbon determination was performed on shell fragments that we recovered from 2 ± 0.05 m below the ground surface, the age of 25.900 ± 200 ^{14}C BP has to be regarded as a range of ages. Furthermore, due to uncertainties related to the ^{14}C dating of gastropod shells (Goodfriend and Stipp 1983, Yates et al. 2002), the age of 25.900 ± 200 ^{14}C BP might be up to 3.000 radiocarbon years younger. Even taking all these problems into account, our age determination for the sample ID 69 appears to overlap the range of 21.000-31.000 ^{14}C BP published for the Gravettian occupation at Bockstein-Törle (Conard and Bolus 2003). Therefore we hypothesize that shortly after the time range 26.000-23.000 ^{14}C BP the Gravettian deposits originally accumulated inside the caves of Bockstein underwent a phase of erosion (Barbieri et al. 2018).

At the foothill of Bockstein the eroded cave material was buried together with reworked loess, which displays almost no fragmented clay coatings and rare gravel beds (BS-GU3 and 4. Barbieri et al. 2018). We documented increasing deposition of reworked loess also in front of Hohle Fels (HF-GU5) and in front of Hohlenstein (HS-GU7). Increasing loess

sedimentation and decreasing, or even ceased, deposition of reworked soil material might be regarded as indicative for a drier and colder climate period not interrupted by significant phases of soil formation (Barbieri et al. 2018). Additionally, decreasing deposition of limestone debris may be correlated with lower frequency of frost cycles, possibly due to temperatures more constantly below freezing (Barbieri et al. 2018). Alternatively, the near lack of limestone gravel might be related with the less intensive exposure of bare bedrock and the aggradation of deeper permafrost (Barbieri et al. 2018). Details apart, all these scenarios seem to indicate that BS-GU3 and 4, HF-GU5 and HS-GU7 accumulate during a climatic phase comparable with the LGM.

In sum, our results show that erosional processes have caused the removal of Gravettian-aged sediment from at least some of the cave sites located in Ach and Lone valleys. After and during this erosive process, increased loess sedimentation indicates that this region experienced a period of climate and landscape deterioration comparable with the LGM. Numerous scholars argue that humans left southwestern Germany around 26.000 ^{14}C BP due to the climate and landscape deterioration related with the approaching of the LGM (Jochim et al. 1999, Kind 2003, Conard and Moreau 2004, Moreau 2009b, Maier 2015, Taller and Conard 2016). According to a widely accepted model, southwestern Germany remained depopulated until ca. 13.500 ^{14}C BP when Magdalenian groups colonized this region (Jochim et al. 1999, Kind 2003, Terberger and Street 2002, Terberger 2003, Küßner and Terberger 2006, Maier 2015, Taller 2015). Our data show that the beginning of this long-lasting phase of apparent depopulation coincides with the occurrence of erosional phases at some cave sites (Bockstein). The existence of a causal link between cave erosion and Gravettian emigration needs to be further verified with additional investigations. Based on our results we propose two alternative scenarios:

1. Gravettian groups fled the caves of the Swabian Jura around 26.000 ^{14}C BP due to the onset of landscape instability and climatic deterioration. The region remained depopulated until the arrival of Magdalenian groups around 13.500 ^{14}C BP.
2. Human groups visited the Swabian Jura also during the time period 26.000-13.500 ^{14}C BP but subsequent erosional processes removed most of the archaeological evidence for such occupations. This hypothesis seems supported by few animal bones from the caves of Vogelherd, Bockstein and Fetzershaldenhöhle, in The

Lone Valley. These remains display signs of human modification (cut marks and fresh breaks) and dating between 26.000 and 21.000 ^{14}C BP (Conard and Bolus 2003, Moreau 2004, Maria Likoudí personal communication). These visits might have taken place in short-lived period of less intensive cave erosion.

The near lack of sterile sediment separating Gravettian from Magdalenian deposits inside the caves of the Swabian Jura seems to reinforce the hypothesis that this chronostratigraphic gap might result from erosive processes. Our micromorphological results from the *Vorplatz* of Hohlenstein-Stadel reveal that only shortly before the arrival of Magdalenian groups (14.000 ^{14}C BP, GKS-1) cave erosion was no longer active (Table 3.2).

6.2.3 Differential preservation of the Gravettian deposits in Ach and Lone valleys

The Gravettian record preserved in the cave sites of Ach and Lone valleys appears dissimilar. Lithic analyses conducted on the Gravettian stone tools recovered from various cave sites of the Ach Valley have discovered multiple refitting artefacts, which might indicate that this part of the Swabian Jura was repeatedly occupied by the same group of humans (Scheer 1986, 1993, Connard and Moreau 2004, Moreau 2009, 2010). Unlike the Ach Valley, evidence for the Gravettian period in the Lone Valley is sparse. This disparity in the archaeological record is remarking, particularly considered the homogeneity and richness of the Aurignacian record in this region (Moreau 2010). Results of ^{14}C dating performed on bone remains with cut marks from archaeological units originally assigned to the Aurignacian indicate a likely Gravettian presence at Vogelherd, Bockstein-Törle and potentially Hohlenstein-Stadel (Conard and Bolus 2003, Kitagawa 2014). In particular, more recent lithic analysis has led to the reassignment of the layers BT VI – BT IV from Bockstein-Törle to the Gravettian (Borges de Magalhães 2000). Such disparity in the Gravettian record preserved in the two valleys might indicate that our ancestors more frequently visited the Ach Valley or, conversely, that the caves located in the Lone Valley experienced more intensive erosional processes around the LGM. In the following paragraphs we test the latter hypothesis.

Cave size is a variable to be considered in evaluating the preservation of the Gravettian record of the two valleys. We hypothesize that the erosion of cave deposit was triggered by the intensive mass-wasting of the external hillside which likely occurred after a drop

in base level of Ach and Lone valleys (6.2.2). Thus, we assume the farther back from the cave entrance that sediment accumulated, the less it would have been exposed to erosional processes. Cave sites located in the Ach Valley, such as Brillenhöhle (back wall located max 23 m from drip line), Sirgenstein (max 40 m) and Hohle Fels (more than 40 m), are considerably longer than the majority of the cave sites of the Lone Valley (Fig. 6.3). At Bockstein most of the cavities is carved less than 10 m into the bedrock, while in the largest cave (Bocksteinhöhle) the back wall is located at a maximum of 15 m from the drip line (Fig. 6.3). Vogelherd is composed of a relatively long (40 m) karstic tunnel, which was completely accessible from the slope *via* entrances located at both its extremities (Fig. 6.3). In the Lone Valley only Hohlenstein hosts two phreatic tubes (Hohlenstein-Bärenhöhle and Hohlenstein-Stadel) which are more than 40 m long with one large opening, thus displaying sizing comparable with the larger sites of the Ach Valley (Fig. 6.3). Nevertheless, Hohlenstein displays a much poorer and highly reworked Gravettian record in comparison with Brillenhöhle, Geißenklösterle and Hohle Fels (Fig. 6.3). We conclude that cave size was probably not the dominant factor in controlling the intensity of cave erosion.

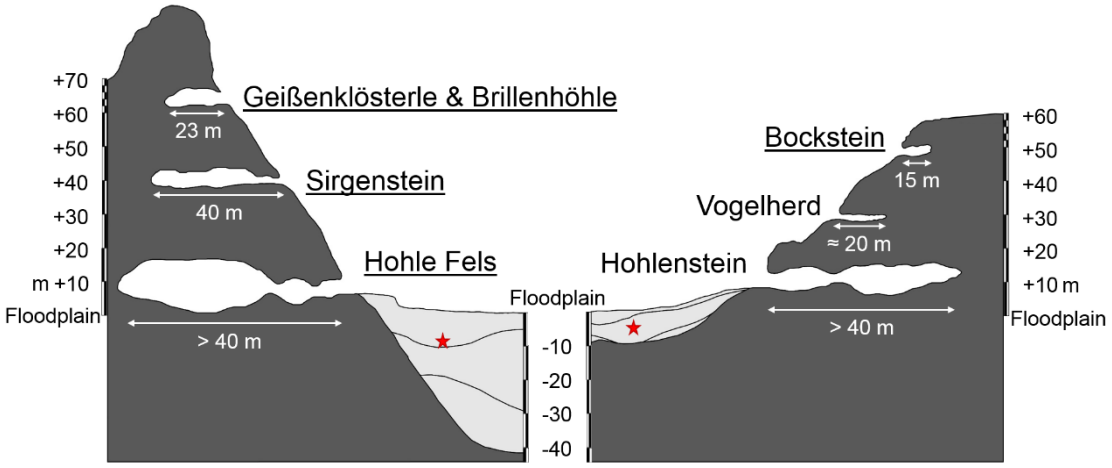

Fig. 6.3. Cave properties and preservation of the Gravettian record in Ach and Lone valleys. Idealized sections depicting max length (e.g. max distance from the drip line, white labels) and elevation above the floodplain (scale bar along the external sides of the sections) of the main cave sites located in Ach (on the left) and Lone valley (on the right). In the figure we underlined the name of the cave sites displaying preserved Gravettian deposits. Bedrock is depicted in dark gray, the sediments infilling the valleys are in light gray. Red stars indicate the depth of Gravettian ^{14}C ages in the valleys. This figure is further explained in section 6.2.3.

The relative elevation of the sites might also have contributed to the differential preservation of the Gravettian deposits (Fig. 6.3). In particular, we expect that slope

failure had a stronger impact on the caves located closer to the valley floor in comparison with those closer to the plateau. This model fits quite well when examining the two valleys separately. In the Ach Valley Hohle Fels is at the same time the site with the lowest relative elevation (12 m above the valley bottom, around the Gravettian period) and the cave which displays the clearest evidence for rills and gullies affecting the Gravettian deposits. All the other major sites of this valley do not display comparable erosional features and rest at much higher elevation from the valley bottom: during the Gravettian Geißenklösterle and Brillenhöhle rested at ca. 68 m and Sirgenstein at ca. 43 m (elevations reconstructed based on the depth of the bone fragment dated in core 37). In the Lone Valley Bockstein is the site with the highest relative elevation and the only cave at which a small Gravettian assemblage was preserved (Bockstein-Törle, Borges de Magalhães 2000, Conard and Bolus 2003).

However, when comparing the two valleys the importance of the relative elevation as a variable useful for justifying the various richness of the Gravettian record appears to be less significant. Our data show that, around the Gravettian, Bockstein was located at ca. 52 m above the valley floor (based on dating from core 31), thus ideally half way between the elevation of Sirgenstein and Geißenklösterle/Brillenhöhle. On the other hand Hohlenstein rested at ca. 10.6 m above the valley bottom (based on dating from core 12), a relatively elevation comparable with Hohle Fels (Fig. 6.3). We conclude that relative elevation cannot have been the sole and primary variable responsible for the non-homogeneous Gravettian record of Ach and Lone valleys.

Our data show that the Lone Valley displays a relatively shallow bedrock (max depth 9.5 m) and has been shaped by multiple “cuts and fills”. Conversely, in the Ach Valley the bedrock lies at around 40 m below the ground surface (German et al. 1995. Fig. 6.3), and floodplain aggradation seems to have been predominant since the LGM. Our geophysical data indicate that the old river channels buried in the Lone Valley have depths (1 - 1.5 m) and widths (10 – 15 m) comparable with the present day Lone. Our data from the Ach Valley are not sufficient to reconstruct the geometry of the river channels buried in this valley, and therefore a comparison between the water discharges of these two rivers during the Pleistocene is tentative. Several data, however, are not questionable. Hohlenstein is located towards the end of the Lone Valley at ca. 28 km from the source, while Hohle Fels rests at about 3.2 km from the spring of the Ach in Schelklingen. The

watershed of the Lone is ca. 331 km^2 and thus more than double that of the Ach (ca. 157 km^2). On the contrary, the fact that today the Lone River appears dry for most of the year while the Ach River displays apparent more constant and higher water discharge is likely the result of the Holocene aged, discontinuous, reworked peat (HF-GU6), which rests at shallow depths in the Ach Valley. This sediment is less permeable than the silty gravel deposits accumulated below the Lone valley floor and thus prevents the surface water from draining deep into the karstic system.

Based on the results from previous studies, we regard the current watershed of both rivers as representative also for the Late Pleistocene (German et al. 1995, Strasser et al. 2009). Therefore, we hypothesize that when the Swabian Alb was covered with permafrost, the water discharge might have been (at least occasionally) higher in the Lone than in the Ach River. As previously discussed, in both valleys the erosion of Gravettian deposits occurred during phases of hillside mass-wasting, which likely took place after a major river valley incision. We propose that the mass-wasting of the valley flanks resulted in a phase of floodplain aggradation which possibly occurred with different timing and/or intensity in the two valleys. More in detail, due to the higher sediment load, floodplain aggradation might have been faster in the Ach Valley. Therefore, the difference in elevation between valley bottom and caves would have been diminished in a lower amount of time, thus sediments accumulated along the hillsides and inside the caves would have achieved a new stability more quickly. Conversely, we hypothesize that, due to the higher water discharge, flood plain aggradation in the Lone Valley occurred either later in comparison with the Ach Valley or at a lower rate. As a result, the effect of the drop in base level lasted longer in the Lone Valley, promoting further erosion of the hillside and the Gravettian cave deposits.

6.2.4 River incision, minor cave erosion, *Bergkies* deposition and Magdalenian recolonization

After the LGM, sediments rich in gravel and fragmented clay coatings accumulated in both the Ach and Lone valleys (HS-GU9-11, BS-GU5, probably HF-GU1). We hypothesize that these deposits resulted from mass-wasting of the hillside alternating with phases of climate amelioration and soil formation (Barbieri et al. 2018).

At the *Vorplatz* of Hohlenstein-Stadel, the team of excavators lead by Kind and Beutelspacher reported a Magdalenian deposit (GL2B) overlaying the sterile unit of GKS-1. According to the excavators, GL2B was later eroded and covered with the Late Paleolithic deposit of GL2A (Jahnke 2013). Our micromorphological data from the *Vorplatz* of Hohlenstein-Stadel cannot support or deny the hypothesis that the Magdalenian occupation at this site was followed by an erosive phase. However, the clear archaeological break and the lack of pedogenesis at the contact between GKS-1 and GL2B might be regarded as indicative for some erosion (Barbieri and Miller in press). Data from microfaunal analysis conducted by Jahnke (2013) show that GL2A and GL2B accumulated in two distinct and separate climatic periods. More in detail GL2B exhibits microfanual remains comparable with a mixed forest-steppe while GL2A was rich in microfanual remains indicative of a steppe landscape (Jahnke 2013).

By integrating our data from the Lone Valley with field observations and faunal analyses from the *Vorplatz* of Hohlenstein-Stadel (Jahnke 2013), we hypothesize that that the sparse arboreal coverage of the cool Magdalenian interstadial might have offered conditions suitable for river valley incision (Barbieri et al. 2018). Probably in the course of this erosive phase the Lone River removed HS-GU4-11 from the center of the valley and thus lowered its floodplain by ca. 3 m (Fig. 3.35). Interestingly from the Danube Valley Heine (1999), Münzberger (2005) and Schellmann (2010) reported a phase of river valley incision which has been dated to 13.000-9.000 ^{14}C BP and thus might be contemporaneous with the downcutting we have identified for the Lone Valley (Barbieri et al. 2018). With a dynamic similar to the one we discussed for the erosion of the Gravettian-aged cave deposits, we hypothesize that in the subsequent stadial period this drop in base level might have triggered the occurrence of erosive processes at some cave sites in the Lone Valley (Barbieri et al. 2018). This erosion would have affected mainly cave entrances, as indicated by the partial removal of GL2B from the *Vorplatz* of Hohlenstein-Stadel. At this site GL2B was covered with *Bergkies* (GL2A), which displays lithology, bedding and calcite pedofeatures comparable with HS-GU12. Based on such correlation, we argue that the accumulation of *Bergkies* and other gravel-rich sediments in the Lone Valley prevented any further river incision and, conversely, promoted floodplain aggradation (Barbieri et al. 2018). Probably during the Holocene,

Bergkies and other slope sediments were affected by lateral fluvial erosion (Barbieri et al. 2018).

We cannot support or refute the occurrence of a major phase of incision in the Ach Valley during the Late Glacial (Barbieri et al. 2018). Nevertheless, our GPR data from the *Vorplatz* of Hohle Fels revealed a sequence comparable to the *Vorplatz* of Hohlenstein-Stadel. At the entrance of Hohle Fels, between 1 m to 2 m below the ground surface, we detected a large disconformity which likely resulted from the combined action of rock fall, debris flow and scouring events. This disconformity was later filled with sediments dipping towards the entrance of the cave. Such a shift in the geometry of these deposits is comparable to the passage from GL2B to GL2A, which we have discussed for the *Vorplatz* of Hohlenstein-Stadel (Barbieri et al. 2018). The sediments we recovered in our cores from the *Vorplatz* of Hohle Fels did not display materials suitable for dating. Nevertheless, accordingly to Blumentritt (personal communication), Magdalenian materials might have been recovered from above the large disconformity we identified by GPR (Barbieri et al. 2018). Interestingly, inside the cave of Hohle Fels, *Bergkies* has been reported from one Magdalenian-aged deposit (layer GH 3ad) but appears more common in Holocene-aged sediments (1ka, 1kb, 1c, 1s, 3as. Field descriptions from Maria Malina. Barbieri et al. 2018).

The stratigraphy of Sesselfelsgrotte provides further evidence for the deposition of *Bergkies* after the Magdalenian abandonment (Freund 1999). However, Magdalenian materials have been recovered in *Bergkies* deposits at numerous sites, such as Felsställe (Kind 1987), Burkhardtshöhle (Riek 1935), Spitalhöhle (Riek 1957), Vogelherd (Riek 1934), Bockstein (Wetzel and Bosinski 1969), Brillenhöhle (Riek 1973), Sirgenstein (Schmidt 1912) and possibly Sesselfelsgrotte (Freund 1999). We conclude that further research is required to clarify the chronological relation between *Bergkies* deposition and Magdalenian colonization/abandonment of the Swabian Jura (Barbieri et al. 2018).

In sum, our results indicate that the accumulation of fine, immature limestone gravel embedded in non-decalcified loess (*Bergkies* or similar deposits) appears to represent a geomorphological marker for the Late Glacial in the Lone and possibly Ach valleys (Barbieri et al. 2018). As argued by Riek (1934 and 1973) and Wolff (1962), the formation of *Bergkies* is related to the breaking-down of the limestone bedrock due to

repeated frost cycles. At the *Vorplätze* of Hohlenstein-Stadel and possibly of Hohle Fels the deposition of fresh loess and immature limestone gravel overprinted cave erosion and filled the cave entrances (Barbieri et al. 2018).

6.3 Occurrence of archaeological material in the Lone and Ach Valleys

From our cores we recovered only rare, mostly sand-sized fragments of charcoal and bones but no stone tools. Similar results were also obtained by Scheidermeier (1999), who performed coring in the area surrounding Bockstein and Hohlenstein in the Lone Valley and recovered archaeological materials exclusively in a 100 m^2 area located downslope from the cave complex of Hohlenstein.

Based on the results of his coring campaign, a team of archaeologists lead by Conard (Bolus et al. 1999) opened three test pits along this slope (opposite to the one we investigated). Below the soil, this team of excavators distinguished unit GE1, which was found to contain Mesolithic stone tools, metal artifacts and Roman pottery (Bolus et al. 1999). They also identified unit GE2, stratigraphically lower than GE1, in which 25 Middle-Paleolithic stone tools and numerous, up to coarse gravel-sized bone fragments were buried (Bolus et al. 1999, Geiling et al. 2015). Based on the study of the archaeological materials, Bolus (et al. 1999) interpreted GE1 as colluvial sediment, while he regarded GE2 as a potentially intact Middle Paleolithic deposit.

The presence of ice wedge and involutions reported by Geiling (et al. 2015) at the top of GE2 suggests, however, that this unit might have been affected by gelifluction. Furthermore, the amount of stone tools and bones recovered from this unit decreases downslope from the uppermost to the lowermost test pit (Bolus et al. 1999), likely indicating that these materials have been eroded from the uphill caves of Hohlenstein. After horse and reindeer, cave bear represents the third most recurrent class of faunal remains identified in the three test pits (94 fragments, Geiling et al. 2015). Only one of these fragments displays cut marks (Geiling et al. 2015), suggesting that the large majority of the cave bear bones belonged to animals that died naturally inside the caves of Hohelnstein (Münzel and Conard 2004). Most likely their remains were later eroded from the caves and redeposited in the valley (Kitagawa 2013).

In summary, despite the lack of geoarchaeological data from these excavations, the field documentation and data from the faunal analysis indicate that both GE2 and GE1 have been likely deposited by colluviation processes originating from the caves of Hohlenstein. Our micromorphological results from the Middle Paleolithic deposits exposed at the *Vorplatz* of Hohlenstein-Stadel support this hypothesis. In these sediments we identified numerous isolated grains of phosphatized loess, coprolites, and bones which have been moved from the back of the cave towards the Lone Valley (Fig. 3.39). We conclude that the bones and archaeological materials recovered by Bolus (et al. 1999) in the valley might represent the distal part of a colluvial cone which originated from the caves of Hohlenstein-Stadel and Hohlenstein-Bärenhohle.

Stone tools from the Paleolithic (a few dozen) and particularly Neolithic (several thousands) have been found scattered on the surface across the Swabian Jura in the course of occasional and systematic archaeological surveys (Floss and Schürch 2015). With the intent of further investigating the context of these findings, excavations were conducted at Speckberg (Hahn 1982 and Cep 2000), Wittlingen (Burkert et al 1992), Winterhalde bei Heidenheim-Schnaitheim (Floss and and Schürch 2015) and Börslingen-Eisenberg (Floss et al. 2012), which is located only 7 km West from Bockstein.

At Börslingen, Floss (et al. 2012) recovered Middle Paleolithic and Upper Paleolithic stone tools. In particular, he reported Aurignacian artifacts associated with a potential hearth (Floss et al. 2012). In the course of preliminary botanical analysis, Deckers identified a sample of charcoal from this potential hearth structure as combusted oak fragments, likely from the Holocene (Floss et al. 2012). Although Holocene artifacts were not recovered at the site, this preliminary botanical data could indicate that the Aurignacian tools were redeposited during the Holocene (Floss et al. 2012). Further ^{14}C dating and geoarchaeological investigations might help to assess the timing and the processes responsible for the accumulation of artifacts and sediment at Börslingen.

In summary, although we did not recover any from our cores, rare Paleolithic artifacts are buried in the open air sediments of Ach and Lone valleys. Nevertheless, the majority of these materials have been probably redeposited by colluvial processes during the Pleistocene and Holocene.

6.4 Summing up

Our research demonstrates that cave sequences can be successfully linked with open air sediment archives when the study focuses on depositional process, sediment source, and diagenesis at both micro and macroscopic scales. This success was only achieved by integrating our data with the results from previous investigations carried out in this region (Barbieri et al. 2018).

Most of the sediments we analyzed for this dissertation are younger than the Aurignacian time period. The exception is represented only by the deposits from the cave of Hohlenstein-Stadel, which we studied with micromorphology. Our results from the Middle Paleolithic sequence of this cave show that colluviation processes have periodically moved sediment and archaeological material from the back of the cave to the *Vorplatz* and eventually towards the center of the Lone Valley. Here Schneidermeier (1999) and Bolus (et al. 1999) recovered Middle Paleolithic stone tools and faunal remains, which we interpret as colluvial material originated from the caves of Hohlenstein-Stadel and Hohlenstein-Bärenhöhle.

In the deposits of Hohlenstein-Stadel the transition from Middle Paleolithic to Early Aurignacian is marked by the better preservation of calcite and less intensive phosphatization. The Middle/Upper Paleolithic transition at the caves of Hohle Fels and Geißenklösterle, in the Ach Valley, is marked by similar diagenetical signature, together with evidence of erosional processes (only at Geißenklösterle) and ground freezing (Miller 2015). Such micromorphological features might support the hypothesis that modern humans entered the Swabian Jura during a colder period (Miller 2015). We did not observe features indicative for ground freezing inside Hohlenstein-Stadel, likely because the profile we analyzed was located too far back (ca. 50 m) from the cave entrance, leaving it less exposed to external climatic fluctuations. Therefore in the case of Hohlenstein-Stadel we lack direct and consistent evidence supporting the occurrence of a colder climatic period at the time of the arrival of modern humans.

Thanks to the surveys we performed opposite from Hohlenstein, downhill from Bockstein and in front of Hohle Fels we reconstructed the impact of the landscape changes that took place in the Ach and Lone valleys on the archaeological record of this region.

Our results show that river valley incision and subsequent mass-wasting of the hillsides caused the erosion of Gravettian-aged deposits from the caves of Bockstein, Hohle Fels and possibly Hohlenstein-Stadel (Barbieri et al. 2018). During and after cave erosion increasing deposition rates of loess marked a shift towards colder and drier conditions corresponding with the LGM (Barbieri et al. 2018). Our data suggest that such landscape changes played a major role in shaping the record of human population of the region. In particular, the dissimilar Gravettian records preserved in the caves of the Ach and Lone valleys is largely the result of the more intensive erosion experienced in the latter. Additionally, due to such erosional processes it is not possible to verify the exact timing for the emigration of Gravettian groups from the Swabian Jura. Based on our results we hypothesize that human groups might have visited the Swabian Jura in the time period 26.000-13.500 ^{14}C BP but subsequent erosional processes might have destroyed the archaeological evidence for such occupations.

From the *Vorplatz* of Hohlenstein-Stadel unit GKS-1 represents one of the rare post-LGM data points for *in situ*, sterile deposits (only 1 Magdalenian artifact. Klaus-Joachim Kind, personal communication). Our micromorphological results from this deposit show that it is free of components indicative for cave erosion (such as isolated grains of phosphatized loess. Barbieri and Miller in press).

Only shortly after the deposition of GKS-1 (13.724 ± 105 ^{14}C), the Swabian Jura was colonized by Magdalenian groups in the time period 13.500-12.500 ^{14}C BP (Jahnke 2013, Taller 2015). According to our data Magdalenian deposits might have been partly eroded and covered with *Bergkies*, which filled the cave entrances marking the cessation of cave erosion (Barbieri et al. 2018).

In both valleys landscape erosion has occurred also in older and more recent times of the Pleistocene and Holocene. Therefore, further analyses are need to assess the integrity of the archaeological deposits exposed in the course of previous open-air excavations, since the archaeological material therein might have been affected by significant post-depositional disturbance.

6.5 Further Prospects

Our work is based on quite a large dataset. Nevertheless, the complexity of the deposits we studied definitely leaves room for further analyses.

Due to time and funding constrains we focused our micromorphological analysis on 25 of the 61 block samples we collected from our cores. Although completing the study of all the remaining samples is probably not necessary, we suggest analyzing a few more thin sections. In particular, we recommend focusing on the 4 block samples we collected from the river deposits HS-GU6 and HS-GU14, which have not yet been studied with micromorphology.

Furthermore, we recommend conducting additional micromorphological study of BS-GU4 and HS-GU7. BS-GU4 is composed of grains of phosphatized loess and bone fragments likely eroded from the Gravettian-aged deposits accumulated inside the caves of Bockstein. These observations are the result of the micromorphological analysis we performed on the thin section BS-31-1B, which was produced from the lower part of the block sample we collected from this unit. Given the relevance of this deposit, we propose completing the production and the study of the upper part of this block sample (BS-31-1A). HS-GU7, together with BS-GU4 and HF-GU5, mark a phase of increased loess deposition, likely indicative for colder and drier climate comparable with the LGM. We analyzed only one (HS-24-7) of the 4 block samples we recovered from this unit. We suggest investigating at least the upper most sample HS-24-4, from GL 100. This layer displays a darker matrix color possibly resulting from the processes of soil formation that took place in the climate amelioration subsequent to the LGM.

The sediments we recovered from the Ach and Lone valleys do not appear to contain much organic material suitable for ^{14}C measurements. In particular, the chronology of the sediments we recovered in front of Hohlenstein is based on only one ^{14}C age.

Our micromorphological analysis has revealed that the sediments recovered in the Lone Valley are often composed of *in situ* or displaced calcite cappings and pendants formed on gravel-sized fragments of limestone. Similar features have been successfully dated with ^{14}C (Courty et al. 1994, Pustovoytov 1998) and Uranium-Thorium series (Pustovoytov 1998). However, for the sediments of the Lone Valley, the major limit to

successfully date such components might be represented by their small dimensions (general thickness <1 mm).

The large majority of the deposits we recovered from Lone and Ach valleys is made of silt-sized grains of quartz, and therefore for further research in this region we strongly recommend performing sediment dating using luminescence methods.

The opening of trenches and deep soundings would surely improve the reconstruction of the subsurface that we have proposed in this dissertation. In particular, deep excavations might help in defining exactly which deposits have been affected by river incision in the Hohlenstein area. Furthermore, working on open sections would allow a more accurate sampling for luminescence dating and other analyses.

From the perspective of archaeologists, our results support new research projects inside cave sites rather than in the open landscape. In line with this consideration, the study of the Gravettian and Magdalenian deposits of Hohle Fels (also with micromorphology) should be a key aspect of further investigations. For geologists, it might be interesting to conduct a new, deeper (>10 m) coring campaign in the Ach valley, where the thicker colluvial valley filling might be indicative of a better preservation of Aurignacian- and even Middle Paleolithic-aged sediments. Additional research conducted downstream in the Danube drainage might help in framing the drop in base level that occurred in Ach and Lone valleys before the Gravettian within broader-scale geomorphological processes.

References

AG (ad-hoc-Arbeitsgruppe) Boden, 2005. Bodenkundliche Kartieranleitung. E. Schweizerbart, Hannover.

Annan, A.P., 2009. Electromagnetic principles of Ground Penetrating Radar. In Jol, H.M., Ed: Ground Penetrating Radar: Theory and Applications, Elsevier, pp. 3-40.

Antoine, P., Rousseau, D-D., Zöller, L., Lang, A., Munaut, A-V., Hatté, C., Fontugne, M., 2001. High-resolution record of the last Interglacial-glacial cycle in the Nussloch loess-palaeosol sequences, Upper Rhine Area, Germany. Quaternary International 76/77, pp. 211-229.

Antoine, P., Rousseau, D-D., Moine, O., Kunesch, S., Hatté, C., Lang, A., Tissoux, H., Zöller, L. 2009. Rapid and cyclic aeolian deposition during the Last Glacial in European loess: a high-resolution record from Nussloch, Germany. Quaternary Science Reviews 28, 25-26, pp. 2955-2973.

Antoine, P., Rousseau, D-D., Degeai, J-P., Moine, O., Lagroix, F., Kreutzer, S., Fuchs, M., Hatté, C., Gauthier, C., Svoboda, J.L., Lisá, L., 2013. High-resolution record of the environmental response to climatic variations during the Last InterglacialeGlacial cycle in Central Europe: the loess-palaeosol sequence of Dolní Vestonice (Czech Republic). Quaternary Science Reviews 67, pp. 17-38

Aspiron, U. and Aigner, T., 1999. Towards realistic aquifer models: three-dimensional georadar surveys of Quaternary gravel deltas (Singen Basin, SW Germany). Sedimentary Geology 129, pp. 281-297.

Attal, M. and Lavé, J., 2009. Pebble abrasion during fluvial transport: Experimental results and implications for the evolution of the sediment load along rivers. Journal of Geophysical research 114, F4, F04023, pp. 1-22, DOI 10.1029/2009JF001328

Barbieri, A., Miller, C., in press. Rekonstruktion der Fundplatzgenese der Hohlenstein-Stadel Höhle. In: Kind C.J. Ed.: Löwenmensch und mehr - Die Ausgrabungen 2008–2013 in den altsteinzeitlichen Schichten der Stadel-Höhle im Hohlenstein (Lonetal), Gemeinde Asselfingen, Alb-Donau-Kreis. Kerns Verlag.

Barbieri, A., Leven-Pfister, C., Toffolo, M.B., Hodgins, G.W.L., Kind, C.-J., Conard, N.J., Miller, C.E., 2018. Bridging Prehistoric caves with buried landscapes in the Swabian Jura (southwestern Germany). Quaternary International.

Barth, M., Conard, N.J., Münzel, S. C., 2009. Palaeolithic subsistence and organic technology in the Swabian Jura. In Fontana, L., Chauvière, F.-X., and Bridault, A. Ed.: In Search of Total Animal Exploitation. Case Studies from the Upper Palaeolithic and Mesolithic. Proceedings of the XVth UISPP Congress, Session C61, vol. 42, Lisbon, 4-9 September 2006. BAR International Series 2040, pp. 5-20.

Beck, D., 1996. Das Mittlepaläolithikum des Hohlenstein – Stadel un Bärenhöhle – im Lonetal. Universitätsforschungen zur prähistorischen Archäologie 56, Verlag Dr. Rudolf Habelt, Bonn.

Berger, J.-P., Reichenbacher, B., Becker, D., Grimm, K., Picot, L., Storni, A., Pirkenseer, C., Derer, C., Schaefer, A., 2005. Paleogeography of the Upper Rhine Graben (URG) and the Swiss Molasse Basin (SMB) from Eocene to Pliocene. International Journal of Earth Sciences 94, pp 697-710.

Bertran, P., 1992. Micromorphologie des grèzes Litées des Charentes et du Châtillonnais (France). Quaternaire 3,/1, pp. 4-15.

Bertran, P. and Francou, B., 1995. Stratified slope deposits: the stone-banked sheets and lobes model. In Slaymaker, O., Ed.: Steepland Geomorphology. John Wiley and Sons Ltd., pp. 147-169.

Bertran P. and Texier J.-P. 1999, “Facies and microfacies of slope deposits”, Catena 35, pp. 99-121.

Bertran, P., Coutard, J-P., Francou, B., Ozouf, J-C., Texier, J-P., 1992. Données nouvelles sur l´origine du lintage des grèzes: implications paléoclimatiques. Géographie physique et Quaternaire, 46/1, pp. 97-112.

Bertran, P., Coutard, J-P., Francou, B., Ozouf, J-C., Texier, J-P., 1994. New Data on Grèzes Bedding and their Paleoclimatic Implications. In Evans D.J.A. Ed.: Cold Climate Landforms. John Wiley & Sons Ltd.

Bertran, P., Hétu, B, Texier, J.-P., Van Steijn, H., 1997. Fabric characteristics of subaerial slope deposits, Sedimentology 44, pp. 1-16

Beutelspacher, T., Ebinger-Rist, N., Kind, C.-J., 2011. Neue Funde aus der Stadelhöhle im Hohlenstein, Archäologische Ausgrabungen in Baden-Württemberg 2010 Konrad Theiss Verlag, pp. 65-70.

Binder, H., 1988. Zur Geologie und Flußgeschichte des Lonetal. Lone und Lonetal-Ein Karst-Ökosystem auf dem Prüfstand, Ulmer Geographische Hefte 5, pp. 18-19

Binder, H., 1993. Die Trockentäler und Wildwässer. Karst und Höhle, Munich, pp. 279-289.

Bleich, K.E., 1993. Landoberflächen und Böden der Ostalb – ein Beitrag zur Landschaftsgeschichte. Karst und Höhle, Munich, pp. 95-111.

Blikra, L.H. and Nemec, W., 1998. Postglacial colluvium in western Norway: depositional processes, facies and palaeoclimatic record. Sedimentology 45, pp. 909-959.

Bolus, M., 2003. The cultural context of the Aurignacian of the Swabian Jura. In Zilhão, J. and d'Errico, F., Ed: The chronology of the Aurignacian and of the transitional technocomplexes: dating, stratigraphies, cultural implications. Proceedings of Symposium. Instituto Português de Arqueologia, Lisboa, pp. 152-163.

Bolus, M., 2004. Settlement analysis of sites of the Blattspitzen complex in central Europe. Settlement Dynamics of the Middle Paleolithic and Middle Stone Age II. Kerns Verlag, pp. 201-226.

Bolus, M. and Conard, N. J., 2001. The late Middle Paleolithic and earliest Upper Paleolithic in Central Europe and their relevance for the Out of Africa hypothesis. Quaternary International 75, pp. 29-40.

Bolus M, Conard N.J. and Kandel A.W. 1999. Grabungen vor dem Hohlenstein im Lonetal, Gemeinde Bissingen und Asselfingen, Alb-Donau-Kreis. Archäologische Ausgrabungen in Baden-Württemberg 1998, pp. 40-47.

Borges de Magalhães, J.C., 2000. Die Silexartefakte der Fundschichten IV–VII aus dem Bockstein-Törle im Lonetal, Ostalbkreis. Masters thesis, University of Tübingen.

Bosellini, A., Mutti, E., Ricci Lucchi, F., 1989. Rocce e successioni sedimentarie, Torino.

Bosinski, G., 1967. Die mittelpaläolithischen Funde im westlichen Mitteleuropa. Böhlau Verlag.

Bosinski, G., 1990. Homo sapiens. L´historie des chasseurs du Paléolithique supérior en Europe (40000-10000 av. J. C.). Paris: Édition Errance.

Bosinski, G. and Hahn, J., 1973. Der Magdalénien-Fund- platz Andernach. Rheinische Ausgrabungen 11, pp. 81–257

Bourgeois, O., Ford, M., Diraison, M., Le Carlier de Veslud, C., Gerbault, M., Pik, R., Ruby, N., Bonnet, S., 2007. Separation of rifting and lithospheric folding signatures in the NW-Alpine foreland. International Journal of Earth Sciences 96, pp. 1003-1031.

Braillard, L., Guelat, M., Rentzel, P., 2004. Effects of bears on rockshelter sediments at Tanay Sur-les-Creux, southwestern Switzerland. Geoarchaeology 19 (4), pp 343-367.

Brauer, A., Endres, C., Negendank, F.W.J., 1999. Lateglacial calendar year chronology based on annually laminated sediments from Lake Meerfelder Maar, Germany. Quaternary International 61, pp. 17-25.

Bridge, J., 2009. Advances in Fluvial Sedimentology using GPR. In Jol, H.M, Ed.: Ground Penetrating Radar Theory and Applications. Elsevier, pp. 323-359.

Bridge, J., Alexander, J., Collier, R.E.Ll., Gawthorpes, R.L., Jarvis, J., 1995. Ground penetrating radar and coring used to study the large-scale structure of point-bar deposits in three dimensions. Sedimentology 42, pp. 839-852.

Brost, E., Homilius, J., Koschyk, K., Villinger, E., 1987. Der Schmiecher See bei Schelklingen Geophysikalische und geologische Untersuchungen zur Erkundung seiner Entstehung. Geologische Jahrbuch, Reihe C, 49, pp. 38-60.

Buch, M.W. and Zöller, L., 1990. Gliederung und Thermolumineszenz-Chronologie der Würmlösse im Raum Regensburg. E&G Quaternary Science Journal 40, pp. 63-84.

Bullmann, H., 2010. Eigenschaften und Genese periglazialer Deckschichten auf Carbonatgesteinen des Muschelkalks inj einem Teilgebiet der ostthüringischen Triaslandschaft. Genesis and Properties of periglacial slope deposits on calcareous rocks of Muschelkalk in an area of eastern Thuringian Triassic landscape. PhD thesis, Leipzig University.

Bullmann, H. and Heinrich, J., 2013. Sensitivity of frost weathering and Aeolian deposit during genesis of Late Quaternary periglacial slope covers on calcareous rocks of Muschelkalk landscape, eastern Thuringian Basin, Germany. Catena 103, pp. 74-86.

Buoncristiani, J.F. and Campy, M., 2004. Expansion and retreat of the Jura ice sheet (France) during the last glacial maximum. Sedimentary Geology 165, pp. 253-264.

Burkert, W. and Floss, H., 2005. Lithic Exploitation Areas in the Upper Palaeolithic of West and Southwest Germany - A Comparative Study. In Körlin, G. and Weisgerber, G., Ed: Stone Age-Mining Age. Deutsches Bergbau-Museum, pp. 35-49.

Burkert, W., Çep B., Kind, C.-J., Pasda, C., Schrantz, M., Simon, U., 1992. Wittlingen Eine mittelpaläolithische Freilandfundstelle bei Bad Urach. Fundberichte aus Baden-Württemberg 17/1, pp. 1-110.

Burr, G.S., Edwards, R.L., Donahue D.J., Druffel E.R.M., Taylor, F.W., 1992. Mass spectrometric 14C and U–Th measurements in coral. Radiocarbon 34 (3), pp. 611-618.

Campen, I., 1990. Die Sedimente der Höhlen und Abris der Mittleren Schwäbischen Alb und ihre klimatische Ausdeutung. Universitätsbibliothek Publikation, Tübingen.

Campen, I., 1995. Abri- und Höhlensedimente. In Hahn, J., Ed: Urgeschichte in Oberschwaben und der mittleren Schäbischen Alb: Zum Stand neuerer Untersuchungen der Steinzeit-Archäologie. Archäologische Informationen aus Baden-Württemberg.

Castainer, S., Le Métayer-Levrel, G., Perthuisot, J.-P., 1999. Ca-carbonates precipitation and limestone genesis – the microbiogeologist point of view. Sedimentary Geology 126, pp. 9-23.

Chukanov, N.V., 2014. Infrared Spectra of Mineral Species – Extended Library, Springer Geochemistry/Mineralogy.

Clark, M.J., 1988. Periglacial hydrology. In Clark, M.J., Ed.: Advances in Periglacial Geomorphology. John Wiley & Sons Ltd, Great Britain.

Coltorti, M., Dramis, F., Pambianchi, G., 1983. Stratified Slope-Waste Deposits in the Esino River Basin, Umbria-Marche Apennines, Central Italy. Polarforschung 53, pp. 59-66.

Conard, N.J, 2003. Palaeolithic Ivory Sculptures from Southwestern Germany and the Origins of Figurative Art. Nature 426, pp. 830–832.

Conard, N.J., 2009. A female figurine from the basal Aurignacian of Hohle Fels Cave in southwestern Germany. Nature 459, pp. 248–252.

Conard, N.J., 2011. The stratigraphic, chronological and paleoecological context of the early Aurignacian in the Swabian Jura, Early anatomically modern humans in Eurasia: coping with climatic complexity, Buckinghamshire, UK.

Conard, N.J. and Fischer, B., 2000. Are there recognizable cultural entities in the German Middle Palaeolithic? In Ronen, A. and Weinstein-Evron, M. Ed.: Towards Modern Humans: The Yabrudian and Micoquian 400-50 k years ago Archaeopress, Oxford, pp. 7-21.

Conard, N. J. and Bolus, M., 2003. Radiocarbon dating the appearance of modern humans and the timing of cultural innovations in Europe: new results and new challenges. Journal of Human Evolution 44, pp. 331–371.

Conard, N. J., and Malina, M., 2004. Die Ausgrabungen 2004 in den frühen jungpaläolithischen Schichten des Hohle Fels bei Schelklingen, Alb-Donau-Kreis. Archäologische Ausgrabungen in Baden-Württemberg 2004, pp. 17-21.

Conard, N.J., Moreau, L., 2004. Current Research on the Gravettian of the Swabian Jura. Mitteilungen der Gesellschaft für Urgeschichte 13, pp. 29-59.
Conard, N. J. and Bolus, M., 2006. The Swabian Aurignacian and its place in European Prehistory. In Bar-Yosef, O. and Zilhão, J., Ed: Towards a definition of the Aurignacian. Proceedings of the Symposium held in Lisbon, Protugal, June 25-30, 2002. Trabalhos de Arquelogia 45, pp. 211-239.
Conard, N.J. and Bolus, M., 2008. Radiocarbon dating the late Middle Paleolithic and the Aurignacian of the Swabian Jura. Journal of Human Evolution 55, pp. 886–897.
Conard, N.J. and Malina, M., 2010. Neue Belege für dem Magdalénien vom Hohle Fels. Archäologische Ausgrabungen in Baden-Württemberg 2009, pp. 52-56.
Conard, N.J., Grootes, P.M., Smith. F.H., 2004. Unexpectedly recent dates for human remains from Vogelherd. Nature 430, pp. 198-201.
Conard, J. N, Bolus M., Goldberg P., Münzel, S.C., 2006. The last Neanderthals and first modern humans in the Swabian Jura. In Conard, J.N., Ed: When Neanderthals and modern humans met. Kenrs Verlag, pp. 305-341.
Conard, N.J, Malina, M., Münzel, S.C., 2009. New flutes document the earliest musical tradition in southwest Germany. Nature 460, pp. 737-740.
Conard, N.J., Bolus, M. and Münzel, S.C., 2012. Middle Paleolithic land use, spatial organization and settlement intensity in the Swabian Jura, southwestern Germany. Quaternary International 247, pp. 236-245.
Conard, N., Kitagawa, K., Krönneck, K., Böhme, M., Münzel, S., 2013. The importance of Fish, Fowl and Small Mammals in the Paleolithic Diet of the Swabian Jura, Southwestern Germany. In Clark, J.L. and Speth J.D. Ed.: Zooarchaeology and Modern Human Origins: Human Hunting Behavior during the Later Pleistocene. Vertebrate Paleobiology and Paleoanthropology, Springer, pp.173-190.
Courty, M.-A., Marlin, C., Dever, L., Tremblay, P., Vachier, P., 1994. The properties, genesis and environmental significance of calcitic pendents from the High Arctic (Spitsbergen). Geoderma, 61, pp. 71-102.
Cretin, C., 2007. Arrêt sur le Badegoulien: Historique, état de la question et perspectives. In Évin, L., Ed.: Un Siècle de Construction du discours scientifique en Préhistoire, Des Idées d'hier, Actes du 26eme Congrès Préhistorique de France, Avignon 2004, vol. 1, Société préhistorique française, pp. 367–378.
Cupillard, C., Magny, M., Bocherens, H., Bridault, A., Bégeot, C., Bichet, V., Bossuet, G., Drucker, D.G., Gauthier, E., Jouannic, G., Millet, L., Richard, H., Rius, D., Ruffaldi, P., Walter-Simmonet, A-W., 2015. Changes in ecosystems, climate and societies in the Jura Mountains between 40 and 8 ka cal BP. Quaternary International 378, 40-72
Czarnetzki, A., 1983. Zur Entwicklung des Menschen in Südwestdeuchlan. In Müller-Beck, H., Ed.: Urgeschichte in Baden-Württemberg. Konrad Theiss Verlag, pp. 217–240
Çep, B., 2000. Die mittelpaläolithischen Steinartefakte des Speckbergs bei Meilenhofen. Ein Beitrag zur Frage der Inventarausprägungen in Höhlen und Freilandstationen im Mittelpaläolithikum Süddeutschlands. Unpublished Dissertation.
Çep, B. and Waiblinger, J., 2001. The use of cave and open-air sites in southern Germany. Kerns Verlag Tübingen, Tübingen.
Çep, B., Burkert, W. and Floss, H., 2011. Zur mittelpaläolithischen Rohmaterialversorgung im Bockstein (Schwäbische Alb). Mitteilungen der Gesellschaft für Urgeschichte 20, pp. 33-52.
Davis, J. L. and Annan, A. P., 1989. Ground-Penetrating Radar for high resolution mapping for soil and rock stratigraphy. Geophysical Prospecting 37, pp. 531-551.
Delagnes, A., Jaubert, J., Meignen, L, 2007. Les technocomplexes du paléolithique moyen en Europe occidentale dans leur cadre diachronique et géographique. In Vandermeersch B. and Maureille B. Ed.: Les neandertaliens. Biologie et cultures. Editions du CTHS, Paris, pp. 213–229.

Demoulin, A., Launoy, T., Zippelt, K., 1998. Recent crustal movements in the southern Black Forest (western Germany). Geol Rundsch 87, pp. 43-52.
Deshaies, M., Ghanini, S., Harmand, D., Weisrock, A., 1995. The Lorraine Grèzes Litées Deposits. Permafrost and Periglacial Processes 6, pp. 119-123.
Dongus, H., 1974. Die Oberflächenformen der Schwäbischen Ostalb. Abhandlungen zur Karst- und Höhlenkunde, Munich.
Durand, N., Monger, C.H., Canti, M.G., 2010 Calcium Carbonate Features. In Stoops, G., Marcellino, V., Mees, F., Ed.: Interpretation of micromorphological features of soils and regoliths. Elsevier, pp. 149-194.
Eberle, J., Eitel, B., Blümel, W.D., and Wittman, P., 2010. Deutschlands Süden - Vom Erdmittelalter zur Gegenwart. Spektrum Akademischer Verlag.
Ehrlich, H.L. and Newman, D.K., 2008. Geomicrobiology. CRC Press.
Fairchild, I.J., Smith C.L., Baker, A., Fuller, L., Spötl, C., Mattey, D., McDermott F., E.I.M.F., 2006. Modification and preservation of environmental signals in speleothems. Earth-Science Reviews 75 (1-4), pp. 105-153.
Fiebig, M., Ellwanger, D., Doppler, G., 2011. Pleistocene Glaciations of Southern Germany. In Ehlers, J., Gibbard, P.L., Hughes, P.D Ed.: Quaternary Glaciations - Extent and Chronology: A Closer Look. Elsevier, pp. 163-174.
Fitzpatrick, E., A., 1983. Soils. Their Formation, Classification and Distribution.
Floss, H. and Terberger, T., 2002. Die Steinartefakte des Magdalénien von Andernach (Mittelrhein), Die Grabungen 1979-1983. Leidorf.
Floss, H. and Kieselbach, P., 2004. The Danube Corridor after 29,000 BP–New results on raw material procurement patterns in the Gravettian of southwestern Germany. Mitteilungen der Gesellschaft für Urgeschichte 13, pp. 61-78.
Floss, H. and Schürch, B., 2015. Paläolitische Oberflächenfunde von der Blaubeurer Alb. Mitteilungen der Gesellschaft für Urgeschichte 24, pp. 121- 140.
Floss, H., Hoyer, C., Dutkiewicz, E., Frick, J., Poenicke, H-.W., 2012. Eine neu entdeckte paläolitische Freilandfundstelle auf der Schwäbischen Alb – Sondagegrabungen in Börslingen. Archäologische Ausgrabungen in Baden-Württemberg 2011, pp. 71-73.
Folk, R.L., Roberts, H.H., Moore, C.N., 1973. Black phytokarst from Hell, Cayman Islands, British West Indies. Geological Society of America Bulletin 87, pp. 2351-2360
Fraas, O., 1862. Der Hohlenstein und der Höhlenbär. Jahreshefte des Vereins für vaterländische Naturkunde in Württemberg 18, pp. 156-188.
Freund, G., 1999. Sesselfelsgrotte I: Grabungsverlauf und Stratigraphie. Quartär-Bibliothek, Saarbrücker Druckerei und Verlag.
Gamble, C., 1999. The Hohlenstein-Stadel Revisited. In Foundation, E.S., Ed.: The role of early humans in the accumulation of European Lower and Middle Palaeolithic bone assemblages: Ergebnisse eines Kolloquiums. Habelt, Bonn, pp. 305-324.
Geiling, J.M., Bolus, M., Conard, N.J., 2015. The Archaeological Significance of the Reindeer Antlers from the Hohlenstein-Complex in the Lone Valley of Southwestern Germany. Mitteilungen der Gesellschaft für Urgeschichte 24, pp. 97-119.
German, R., Grüger, E., Schreiner, A., Strayle, G., Villinger, E., 1995. Geologie: Die Entstehung des Schmiechener Sees aufgrund der Bohrung "Schmiechener See 1". Der Schmiecher See- Naturkunde eines Naturschutzgebietes auf der Schwäbischen Alb, Beih. Veröff. Naturschutz Landschaftspflege Bad.-Württ. 78, pp. 31-98.
Geyer, F.O. and Gwinner, M.P., 1991**.** Geologie von Baden-Württemberg. E. Schweizerbart´sche Verlagsbuchhandlung (Nägele u. Obermiller), Stuttgart.
Geyer, M and Villinger, E., 2001. Geologische Karte Von Baden-Württemberg 1:25000, Blatt 7624 Schelklinge. Landesamt für Geologie, Rohstoffe und Bergbau Baden-Württemberg, Freiburg.
Goldberg, P., 1979. Micromorphology of Pech de l'Azé II sediments. Journal of Archaeological Science 6, pp. 17-47.

Goldberg, P., Schiegl, S., Meligne, K., Dayton, C., Conard, N.J., 2003. Micromorphology and Site Formation at Hohle Fels Cave, Swabian Jura, Germany. E&G Quaternary Science Journal 53, pp. 1-25.
Goodfriend, G.A. and Stipp, J.J., 1983. Limestone and the problem of radiocarbon dating of land-snail shell carbonate. Geology 11, pp. 575–577
Groschopf, P. 1963. Die geologischen Voraussetzungen für die Erschließung von Karstwasser im Blautal. Jh. Karst- u. Höhlenkde. 4, pp. 71-79.
Groschopf, P., 1969. Bohrungen 7624/45, 47, 49, 51, Geologische Landesamt Baden-Württemberg Archiv.
Groschopf, P., 1973. Geologischer Bau. Der Stadt- und der Landkreis Ulm, Amtlicher Kreisbeschreibung. Süddeutsche Verlagsgesellschaft, 5-38.
Gwinner, M.P., 1989. Erläuterungen zu Blatt 7524 Blaubeuren. Geoilogische Karte von Baden-Württemberg, Stuttgart.
Haas, S., 1991. Neue Funde menschlicher Skelettreste und ihre Ergebnisse. In Hahn, J., Kind, C.-J., Ed.: Urgeschichte in Oberschwaben und der mittleren Schwabischen Alb. Zum Stand neuerer Untersuchungen der Steinzeit-Archaologie. Gesellschaft fur Vor- und Fruhgeschichte in Wurttemberg und Hohenzollern (Archaologische Informationen aus Baden-Wurttemberg) 17, pp. 37–38.
Hahn, J., 1982. Der Speckberg bei Meilenhofen. Teil II: Archäologie des Jungpaläolithikums. Kataloge der Prähistorischen Staatssammlung 20. Kallmünz/Opf: Lassleben.
Hahn, J., 1988. Die Geißenklösterle-Höhle im Achtal bei Blaubeuren I. Fundhorizontbildung und Besiedlung im Mittelpaläolithikum und im Aurignacien. Forschungen und Berichte zur Vor- und Frühgeschichte in Baden-Württemberg 26. Konard Theiss Verlag, Stuttgart.
Hahn, J. and Koenigswald, W.v., 1977. Die steinzeitlichen Funde und die spätglaziale Nagetierschicht aus der kleinen Scheuer am Hohlenstein im Lonetal. Fundberichte aus Baden-Württemberg 3, pp. 51-75.
Hahn, J. and Kind, C.-J., 1997: Besiedlungsgeschichte Südwestdeutschlands als klimagekoppelter Prozess. Sonderforschungsbereich 275: Klimagekoppelte Prozesse in meso- und känozoischen Geoökosystemen, Teilprojekt C5: Bericht 1994-1997, vol. 2, pp. 341-354.
Hahn, J., Müller-Beck, H. and Taute, W., 1985. Eiszeithöhlen im Lonetal: Archäologie einer Landschaft suf der Schwäbischen Alb. Konrad Theiss.
Hantke, R., 1974. Zur Vergletscherung der Schwäbische Alb. Eiszeitalter und Gegenwart 25, p. 214.
Hantke, R., 1978. Eiszeitalter – Band I. Ott Verlag AG Thum.
Hantke, R. and Rahm, G., 1976. Das frühe Spätglazial in den Quellästen der Alb (Südlicher Schwarzwald). Vierteljahrsschrift der Naturforschendengesellschaft in Zürich, Druck und Verlag Leeman AG Zürich, pp. 293-299.
Habbe, K.A., 2007. Stratigraphische Begriffe für das Quartär des süddeutschen Alpenvorlandes. Eiszeitalter und Gegenwart 56, 1/2, pp. 3-6.
Harris, S., 1975. Petrology and Origin of Stratified Scree in New Zealand. Quaternary research 5, pp. 199-214.
Hassler, H., Hoang-Trong, P., Schick, R., Schneider, G., Strobach, K., 1980. The September 3, 1978, Swabian Jura earthquake. Tectonophysics, 68, pp. 1-14.
Hatté, C., Pessenda, L.C., Lang, A., Paterne, M., 2001. Development of accurate and reliable 14C chronologies for loess deposits: application to the loess sequence of Nussloch (Rhine valley, Germany). Radiocarbon 43 (2B), pp. 611–618.
Heine, K., 1999. Fluvial response of the Danube river to climate change in Bavaria during the Weichselian and the Holocene. Boletim Goiano de Geografia 19 (1), pp. 82-93.
Heinz, J., 2001. Sedimentary geology of glacial and periglacial gravel bodies (SW-Germany): dynamic stratigraphy and aquifer sedimentology. Unpubl. PhD Thesis, Uni. Tübingen.
Heiri, O., Koinig, K.A., Spötl, C., Barrett, S., Brauer, A., Drescher-Schneider, R., Gaar, D., Ivy-Ochs, S., Kreschner, H., Leutscher, M., Moran, A., Nicolussi, K., Preusser, F., Schmidt, R., Schoeneich, P., Schwörer, C., Sprafke, T., Terhorst, B., Tinner, W., 2014.

Paleoclimate records 60-8 ka in the Austrian and Swiss Alps and their forelands. Quaternary Science Reviews 106, pp. 186-205.
Mücher, H., van Steijn, H., Kwaad, F., 2010. Colluvial and Mass Wasting Deposits. In Stoops, G., Marcellino, V., Mees, F., Ed.: Interpretation of micromorphological features of soils and regoliths. Elsevier, pp. 37-48.
Hétu, B. and Gray, J.T., 2000. Effects of environmental change on scree slope development throughout the postglacial period in the Chic-Choc Mountains in the northern Gaspé Peninsula, Québec. Geomorphology 32, pp. 225-255.
Higham, T., Basell, L., Jacobi, R., Wood, R., Bronk Ramsey, C., Conard, N.J., 2012. Testing models for the beginnings of the Aurignacian and the advent of figurative art and music: The radiocarbon chronology of Geißenklösterle. Journal of Human Evolution 62(6), pp. 664-76.
Horwitz, L.K. and Goldberg, P., 1989. A study of Pleistocene and Holocene Hyena Coprolites. Journal of Archaeological Science 16, pp. 71-94.
Hublin, J.J., 2009. The origin of Neandertals. PNAS 106 (38), pp. 16022–16027.
Huijzer, A.S., 1993. Cryogenic microfabrics and macrostructures: interrelations, processes and palaeoenvironmental significance. PhD-Thesis Vrije Universiteit Amsterdam.
Illies, J.H. and Greiner, G., 1979. Holocene movements and state of stress in the Rhinegraben rift system. Tectonophysics 52, pp. 349-359.
Ivy-Ochs, S., Kerschner, H., Reuther, A., Preusser, F., Heine, K., Maisch, M., Kubik, P.W., Schlüchter, C., 2008. Chronology of the last glacial cycle in the European Alps. Journal of Quaternary Science 23, pp. 559-573.
Jahnke, T., 2013. Vor der Höhle. Zur Fundplatzgenese am Vorplatz des Hohlenstein-Stadle (lonetal). Unpublished Magisterarbeit, Eberhard Karls Universität, Tübingen.
Jochim, M., Herhan, C., Starr, H., 1999. The Magdalenian Colonization of Southern Germany. American Anthropologist 101 (1), pp. 129-142.
Jornaux, A., 1976. Les Grèzes Litées du Châtillonnais. Bulletin de l´Association français pour l´étude du quaternaire, 13/3-4, pp. 123-138.
Jull, A.J.T., Burr, G.S., Hodgins, G.W.L., 2013. Radiocarbon dating, reservoir effects, and calibration. Quaternary International 299, pp. 64-71.
Karkanas, P., Bar-Yosef, O., Goldberg, P., Weiner, S., 2000. Diagenesis in Prehistoric Caves: the Use of Minerals that Form In Situ to Assess the Completeness of the Archeological Record. Journal of Archaeological Science 27, pp. 915-929.
Karkanas, P., Rigaud, J-P., Simek, J.F., Albert, R.M., Weiner, S., 2002. Ash Bones and Guano: a Study of the Minerals and Phytoliths in the Sediments of Grotte XVI, Dordogne, France. Journal of Archaeological Science 29, pp. 721-732.
Karte, J., 1983. Grèzes Litées as a Special Type of Periglacial Slope Sediments in the German Highlands. Polarforschung 53/2, pp. 67-74.
Kaufmann, G. and Romanov, D., 2008. Cave development in the Swabian Alb, south-west Germany: A numerical perspective. Journal of Hydrology 349, pp. 302-317.
Kind, C.J., 1987. Das Felsställe. Landesamt Baden-Württemberg, Konard Theiss Verlag Stuttgart.
Kind, C.J., 2003. Die absolute Datierung des Magdalenines und des Mesolithikums in Süddeutschland. Veröffentlichungen des Landesamtes für Archäeologie, Band 57, pp. 303-319.
Kind, C.-J., Beutelspacher, T., 2010. Ausgrabungen 2009 im Stadel am Hohlenstein im Lonetal. Archäologische Ausgrabungen in Baden- Württemberg 2009. Konrad Theiss, Stuttgart, pp. 62-69.
Kind, C.J., Ebinger-Rist, N., Wolf, S., Beutelspacher, T., Wehrberger, K., 2014. The Smile of the Lion Man. Recent Excavations in Stadel Cave (Baden-Württemberg, south-western Germany) and the Restoration of the Famous Upper Palaeolithic Figurine. Quartär 61, pp. 129-145.
Kitagawa, K., 2014. Exploring hominins and animals in the Swabian Jura: Study of Paleolithic fauna from Hohlenstein-Stadel. Universitätsbibliothek Publikation, Tübingen.

Kitagawa, K., Krönneck, P., Conard, N.J., Münzel, S.C., 2012. Exploring Cave Use and Exploitation Among Cave Bears, Carnivores and Hominins in the Swabian Jura, Germany. Journal of Taphonomy 10 (3-4), pp. 439-461.

Kleber, A., 1992. Periglacial slope deposit and their pedogenic implications in Germany. Palaeogeography, Palaeoclimatology and Palaeoecology 99, pp.361-371.

Knox, J.C., 1984. Responses of river systems to Holocene climates. In: Wright, H.E. (Eds.), Late Quaternary Environments of the United States. Longman, London, pp. 26–41.

Kozlowski, J.K. and Ptte, M., 2000. The Formation of the Aurignacian in Europe. Journal of Anthropological Research 56, pp. 513-534.

Kölbl, S. and Conard, N.J., 2003. Eiszeitschmuck: Status und Schönheit, Museumsheft 6, Urgeschichtliches Museum Blaubeuren.

Koenigswald, W., 1999. Palökologie und Vorkommen des pleistozänen Auerochsen (Bos primigenius Bojanus, 1827) im Vergleich zu den grossen Rindern des Pleistozäns. In Weniger, G.C. Ed.: Archäologie und Biologie des Auerochsen. Neanderthal Museum, Mettman, pp. 93-102.

Kösel, M., 2016. Paläoböden in quartärgeologischen Sequenzen und als Bestandteile des Solums rezenter Oberflächenböden – Beispiele aus dem Grenzbereich von Schichtstufenlandschaft und Alpenvorland (Südrand Schwäbische Alb, Donautal, nördliche Iller-Riß-Platte). RPF-LGRB 1.

Krönneck, P., 2012. Die pleistozäne Makrofauna des Bocksteins (Lonetal – Schwäbische Alb) Ein neuer Ansatz zur Rekonstruktion der Paläoumwelt. Universitätsbibliothek Publikation, Tübingen.

Kunter, M., and Wahl J., 1992. Das Femurfragment eines Neandertalers aus der Stadelhöhle des Hohlensteins im Lonetal. Fundberichte aus Württemb. 17 (1), pp. 111–124.

Kühn, P., Terhorst, B., Ottner, F., 2006. Micromorphology of middle Pleistocene paleosols in northern Italy. Quaternary International 156-157, pp. 156-166.

Kühn, P., Aguilar, J., Miedema, R., 2010. Textural Pedofeatures and Related Horizons. In Stoops, G., Marcellino, V., Mees, F., Ed.: Interpretation of micromorphological features of soils and regoliths. Elsevier, pp. 149-194.

Küßner, M., 2007. Mitteldeutsche Fundstellen der Zeit zwischen dem Weichsel-Pleniglazial und dem Ende des Alleröd im Kartenbild. In A.G.I. Thüringen Ed.: Terra Praehistorica. Festschrift für Klaus-Dieter Jäger zum 70. Geburtstag. Beier and Beran, pp. 211-223.

Küßner, M., and Terberger, T., 2006. Die Fundstelle Gera-Zoitzberg und die Zeit zwischen Gravettien und Magdalénien in Mitteldeutschland. Alt-Thüringen 39, pp. 69-120.

Laville, H. and Hahn, J., 1981. Les depots de Geißenklösterle et l´évolutions du climat en Jura souable entre 36-23.000 BP. C. R. Acad. Sc. Paris 292, pp. 225-227.

Leven, C., Weiss, H., Vienken, T., Dietrich., P., 2011. Direct Push technologies-an efficient investigation method for subsurface characterization. Grundwasser 16 (4), pp. 221-234.

Lin-Vien, D., Colthup, N.B., Fateley, W.G., Grasselli, J.G., 1991. The Handbook of Infrared and Raman Characteristic Frequencies of Organic Molecules. London: Academic Press.

Liolios, D., 2006. Reflections on the role of bone tools in the definition of the Early Aurignacian. In Bar-Yosef, O. and Zilhão, J., Ed.: Towards a Definition of the Aurignacian. Instituto Português de Arqueologia, Lisboa, pp. 37-51.

Litt, T., 2007. Das Quartär als chronostratigraphische Einheit. Eiszeitalter und Gegenwart 56, 1/2, pp. 3-6.

Litt, T., Brauer, A., Goslar, T., Merkt, J., Balaga, K., Müller, H., Ralska-Jasiewiczowa, M., Stebich, M., Negendank, J.F.W., 2001. Correlation and synchronisation of Lateglacial continental sequences in northern central Europe based on annually laminated lacustrine sediments. Quaternary Science Reviews 20, pp. 1233-1249.

Lotter, A.F., Heiri, O., Brooks, S., van Leeuwen, J.F.N., Eicher, U., Ammann, B., 2012. Rapid summer temperature changes during Termination 1a: high-resolution multi-proxy climate reconstruction from Gerzensee (Switzerlamd). Quaternary Science Reviews 36, pp. 103-113.

Lu, Q. and Sato, M., 2007. Estimation of Hydraulic Property of an Unconfined Aquifer by GPR. Sensing and Imaging (8) 83. doi:10.1007/s11220-007-0035-x.
Maier, A., 2015. The Central European Magdalenian – Regional Diversity and Internal Variability. Springer.
Mailänder, R. and Veit, H., 2001. Periglacial cover-beds on the Swiss Plateau: indicators of soil, climate and landscape evolution during Late Quaternary. Catena 45, pp. 251-272.
Mall, W. and Geyer, M., 2004. Geologische Karte Von Baden-Württemberg 1:25000, Blatt 7426 Langenau. Landesamt für Geologie, Rohstoffe und Bergbau Baden-Württemberg, Freiburg.
Martini, I.P., Kwong, J.K., Sadura, S., 1993. Sediment ice rafting and cold climate fluvial deposits: Albany River, Ontario, Canada. In Marzo, M. and Puigdefábregas, C., Ed.: Alluvial Sedimentation. Special Publications of the International Association of Sedimentologists 17. Blackwell Scientific Publications, The Alden Press, pp.63-76.
McGeehin, J., Burr, G.S., Jull, A.J.T., Reines, D., Gosse, J., Davis, P.T., Muhs, D., Southon, J.R., 2001. Stepped- combustion 14C dating of sediment: a comparison with established techniques. Radiocarbon 43 (2A), pp. 255–261.
Mentlík, P., Minár, J, Břízová, E., Lisá, L., Tábořík, P, Stacke, V., 2010. Glaciation in the surroundings of Prášilské Lake (Boehiman Forest, Czech Republic). Geomorphology 117, pp. 181-194.
Miller, C.E., 2015. A Tale of Two Swabian Caves – Geoarchaeological Investigations at Hohle Fels and Geißenklösterle. Kerns Verlag Tübingen.
Mol, J., Vandenberghe, J., Kasse, C., 2000. River response to variations of periglacial climate in mid-latitude Europe. Geomorphology 33, pp. 131-148.
Montet-White, A., 1994. Alternative interpretations of the later upper Paleolithic in central Europe. Annual Review of Anthropology 23, pp. 485-508.
Moreau, L., 2009a. Das Siedlungsmuster im Achtal zur Zeit des älteren Gravettien. Zum Beitrag einer neuen Zusammensetzung zwischen der Brillenhöhle und dem Geißenklösterle (Schwäbische Alb, Alb-Donau Kreis). Archäologisches Korrespondenzblatt 39 (1), pp. 1-20.
Moreau, L., 2009b. Geißenklösterle. Das Gravettien der Schwabischen Alb im europaischen Kontext. Kerns Verlag Tübingen, Tübingen.
Moreau, L., 2010. Geißenklösterle. The Swabian Gravettian in its European context. Quartär 57, pp. 79-93.
Morse, J.W. and Arvidson, R.S., 2002. The dissolution kinetics of major sedimentary carbonate minerals. Earth-Science Reviews 58, pp. 51-84.
Mücher, H., van Steijn, H., Kwaad, F., 2010. Colluvial and Mass Wasting Deposits. In Stoops, G., Marcellino, V., Mees, F., Ed.: Interpretation of Micromorphological Features of soils and regoliths. Elsevier, pp.37-48
Müller, U., Pross, J., Bibus, E., 2003. Vegetation response to rapid climate change in Central Europe during the past 140,000 yr based on evidence from the Füramoos pollen record. Quaternary Research 59, pp. 235-245.
Münzberger, P., 2005. Jungquartäre Talgeschichte der Donau und ihrer Nebenfüsse im Raum Straubing – Deggendorf in Abhängigkeit von natürlichen und anthropogenen Einfüssen. Regensburger Beiträge zur Bodenkunde, Landschaftsökologie und Quartärforschung 8, Regensburg.
Münzel, S. 1997. Seasonal activities of human and Non-human inhabitants of the Geißenklösterle Cave near Blaubeuren, Alb-Danube District. Anthropozoologica. 25-26, pp. 355-361.
Münzel, S. C. and Conard, N. J. 2004. Cave bear hunting in Hohle Fels Cave in the Ach valley of the Swabian Jura. Revue de Paléobiologie 23(2), pp. 877–885.
Münzel, S., Seeberger, F., Hein, W., 2002. The Geißenklösterle Flute-Discovery, Experiments, Reconstruction. Studien zur Musikarchäologie III, pp. 107-118.

Münzel, S. C., Wolf, S., Drucker, D. G., Conard, N.J., in press. The exploitation of mammoth in the Swabian Jura (SW-Germany) during the Aurignacian and Gravettian period. Quaternary International.

Møller, I., 2006. Methods for mapping and characterizing buried valleys: Ground Penetrating Radar. In Kirsch, R., Rumpel, H.-M., Scheer, W., Wiederhold, H., Ed.: Groundwater Resources in Buried Valleys – A Challenge for Geosciences. Leibniz Institute for Applied Geosciences, pp. 99-106.

Neal, A., 2004. Ground-penetrating radar and its use in sedimentology: Principles, problems and progress. Earth Science Reviews 66 (3), pp. 261-330.

Neugebauer, I., Brauer, A., Dräger, N., Dulski, P., Wulf, S., Plessen, B., Mingram, J., Herzschuh, U., Brande, A., 2012. A Younger Dryas varve chronology from Rehwiese paleolake record in NE-Germany. Quaternary Science Reviews 36, pp. 91-102.

Niven, L., 2006. The Palaeolithic occupation of Vogelherd Cave : implications for the subsistence behavior of late Neanderthals and early modern humans. Kerns Verlag.

Niven, L., 2007. From carcass to cave: Large mammal exploitation during the Aurignacian at Vogelherd, Germany. Journal of Human Evolution 53, pp. 362-382.

Onaca, A., Ardelean, A.C., Urdea, P., Ardelean, F., Sărășan, A., 2016. Genetic typologies of talus deposits derived from GPR measurements in the Alpine Environment of the Făgăraș Mountains. Carpathian Journal of Earth and Environmental Sciences 11 (2), pp. 609-616.

Orschiedt, J., 2000. Germany. Hominin Remains - an Up-Date 10. Brussels.

Otte, M., 1992. Processus de diffusion à long ter,e au Magdalénien. IN Rigaud, J.-P., Ed.: Le peuplement magdalénien. Actes du colloque de Chancelade 1988. Eds du CTHS, pp. 399-416.

Owen, L., 2013. Fish in the Magdalenian of Southwest Germany. Emergency Food or Important Resource? In Pastoors, A., Auffermann, B. Ed.: Plesitocene foragers: their culture and environment. Neanderthal Museum, pp. 85-100.

Ozouf, J-C., Coutard, J-P., Lautridou, J-P., 1995. Grèzes, Gèzes Litées: Historique des Définitions. Permafrost and Periglacial Processes 6, pp. 85-87.

Pawelec, H., 2006. Origin and palaeoclimatic significance of the Pleistocene slope covers in the Cracow Upland, southern Poland. Geomorphology 74, pp. 50-69.

Pawellek, T. and Aigner, T., 2003. Apparently homogenous „reef"-limestone built by high-frequency cycles: Upper Jurassic, SW-Germany. Sedimentary geology 160, pp. 259, 284.

Pearce, T.H., 1971. Short Distance Fluvial Rounding of Volcanic Detritus. Journal of Sedimentary Petrology 41, 4, pp. 1069-1072

Pessenda, L.C.R., Gouveia, S.E.M., Aravena, R., 2001. Radiocarbon dating of total soil organic material and humin fraction and its comparison with 14C ages of fossil charcoal. Radiocarbon 43 (2B), pp. 595-601.

Pfeffer, K.-H., 2004. Zur Bodengeographie der Schwäbische Alb – eine Bilanz aus Literatur- und Geländebefunden. Tübinger Geowissenschaftliche Arbeiten 10, pp. 73-93.

Plummer, L.N. and Wigley, T.M.L., 1976. The dissolution of calcite in CO2-saturated solutions at 35°C and 1 atmosphere total pressure. Geochimica and Cosmochimica Acta 40, pp. 191-202.

Posth, C., Wißing, C., Kitagawa, K., Pagani, L., van Holstein, L., Wehrberger, K., Conard, N.J., Kind, C-J., Bocherens, H., Krause, J., 2017. Deeply divergent archaic mitochondrial genome provides lower time 4 boundary for African gene flow into Neandertals. Nature Communications 8,16046 doi: 10.1038/ncomms16046.

Pustovoytov, K., 1998. Pedogenic carbonate cutans as a record of the Holocene history of relict tundra-steppes of the Upper Kolyma Valley (North-Eastern Asis). Catena 34, pp. 185-195.

Raab, T. and Völkel, J., 2003. Late Pleistocene glaciation of the Kleiner Arbersee area in the Bavarian Forest, South Germany. Quaternary Science Reviews 22, pp. 581-593.

Reiff, W., 1993. Geologie und Landschaftsgeschichte der Ostalb. Karst un Höhle, Münich, pp. 71-92.

Richter, D., Waiblinger, J., Rink, W.J, Wagner G.A., 2000. Thermoluminescence, Electron Spin Resonance and ^{14}C-dating of the Late Middle and Early Upper Palaeolithic Site of Geißenklösterle Cave in Southern Germany. Journal of Archaeological Science 27, pp. 71-89.

Riehl, S., Marinova, E., Deckers, K., Malina, M., Conard, N.J., 2015. Plant use and local vegetation patterns during the second half of the Late Pleistocene in southwestern Germany. Archaeol Anthropol Sci (7) 151. doi:10.1007/s12520-014-0182-7

Riek, G., 1934. Die Eiszeitjägerstation am Vogelherd im Lonetal I: Die Kulturen. Akademische Verlagsbuchhandlung Franz F. Heine, Tübingen

Riek G. 1935, "Kulturbilder aus der Altsteinzeit Württembergs", Franz. F. Hein, Verlagsbuchhandlung, Tübingen.

Riek, G., 1938. Ein Beitrag zur Kenntnis des süddeutschen Solutréen. Germania 22, pp. 147-150.

Riek, G., 1957. Drei jungpaläolithische Stationen am Bruckersberg in Giengen an der Brenz. Veröffentlichungen des Staatl.amtes für Denkmalpflege Stuttgart, Verlag Silberburg – Kommissionsverlag, Stuttgart.

Riek, G., 1959. Ein magdalenienzeitlicher Rastplatz unter der Südwand des Sirgensteinfelsens (Markung Weiler, Kr. Ulm). Sonderdruck aus Fundberichte aus Schwaben, Neue Folge 15, pp. 30-42.

Riek, G., 1973. Das Paläolithikum der Brillenhöhle bei Blaubeuren (Schwäbische Alb) I. Landesdenkmalamt Baden-Württemberg, Verlag Müller & Gräff – Kommissionsverlag Stuttgart.

Rittweger, H., 2000. The "Black Floodplain Soil" in the Amöneburger Becken, Germany: a lower Holocene marker horizon and indicator of an upper Atlantic to Subboreal dry period in Central Europe? Catena 41 (1-3), pp. 143-164.

Rose, J., Lee, J.A., Kemp, R.A., Harding, P.A., 2000. Paleoclimate, sedimentation and soil development during the Last Glacial Stage (Devensian), Hearthrow Airport, London, UK. Quaternary Science Reviews 19, pp. 827-847.

Rosendahl, G., 2011. Technological Analysis of the Bifacial Tools from La Micoque and Its Implications. In: Conard, N.J. and Richter, J., Ed.: Neanderthal Lifeways, Subsistence and Technology. Springer Netherlands, pp. 133-138.

Ruebens, K., 2007. Bifacial Elements in Continental Northwestern Europe during the Last Glacial Cycle (MIS5d-3): The Relationship between Mousterian, Micoquian and 'Mixed'Assemblages. Papers from the Institute of Archaeology 18, pp. 84-10

Sala, N. and Conard, N.J., 2016. Taphonomic analysis of the hominin remains from Swabian Jura and their implications for the mortuary practices during the Upper Paleolithic. Quaternary Science Reviews Volume 150, pp. 278–300.

Sanz, M., Daura, J., Égüez, N., Brugal, J.-P., 2016. Not only hyenids: A multi-scale analysis of Upper Pleistocene carnivore coprolites in Cova del Coll Verdaguer (NE Iberian Peninsula). Paleogeography, Paleoclimatology, Paleoecology 443, pp. 249-262.

Sanz, M., Daura, J., Égüez, N., Cabanes, D., in press. On the track of anthropogenic activity in carnivore dens: Altered combustion structures in Cova del Gegant (NE Iberian Peninsula). Quaternary International.

Sass, O. and Krautblatter, M., 2007. Debris-flow-dominated and rockfall-dominated scree slopes: genetic models and process rates derived from GPR measurements. Geomorphology 86 (1), pp. 176-192. doi:10.1016/j.geomorph.2006.08.012.

Sauer, D., Kadereit, A., Kühn, P., Miller, E.C., Shinonaga, T., Kreutzer, S., Hermann, L., Fleck, W., Starkovich, B.M., Stahr, K., 2016. The loess-paleosol sequence of Datthausen, SW Germany: Characteristics, chronology, and implications for the use of the Lohne Soil as a marker soil. Catena 146, 10-29.

Schall, W., 2002. Erläuterungen zum Blatt 7425 Lonsee. Landesamt für Geologie, Rohstoffe und Bergbau Baden-Württemberg.

Scheer, A., 1986. Ein Nachweis absoluter Gleichzeitigkeit von paläolithischen Stationen? Archäologisches Korrespondenzblatt 16, pp. 383-391.

Scheer, A., 1993. The Organization of Lithic Resource Use during the Gravettian in Germany. In: Knecht, H., Pike-Tay, A., White, R., Ed.: Before Lascaux: the complex record of the Early Upper Paleolithic. Boca Raton: CRC Press, pp. 193-210.

Schellmann, G., 2010. Neue Befunde zur Verbreitung, geologischen Lagerung und Altersstellung der würmzeitlichen (NT 1 bis NT3) und holozänen (H1 bis H7) Terrassen im Donautal zwischen Regensburg und Bogen. Bamberger Geographische Schriften 24, pp. 1-77.

Schiegl, S., Goldberg, P., Pfretzschner, H.-U., Conard, N., 2003. Paleolithic Burnt Bone Horizons from the Swabian Jura: Distinguishing between In situ Fireplaces and Dumping Areas. Geoarchaeology 18, pp. 541-565.

Schielein, P., Schellmann, G., and Lomax, J., 2011. Stratigraphy of Late Quaternary fluvial terraces at the confluence of the Lech and Danube valleys. Quaternary Science Journal 60, 4, pp. 414-424.

Schmidt, R.R., 1912. Die Diluviale Vorzeit Deutschlands. E. Scweizerbartsche Verlasbuchhadlung Nägele und Dr. Spoesser, Stuttgart.

Schneider, G., 1967. Erdbeben und Tektonik in Südwet-Deutschland. Tectonophysics 5, pp. 459-511.

Schneider, G., 1979. The earthquake in the Swabian Jura of 16 November 1911 and present concepts of Seisotectonics. Tectonophysics 53, pp. 279-288.

Schneidermeier, T., 1999. Paläolithische Fundschichten in quartären Locksedimenten (Südwestdeutschland): Prospektionsmethoden, Stratigraphie und Paläoökologie. Tübinger Geowissenschaftliche Arbeiten (Reihe A, Band 57). Attempto Service GmbH, Tübingen.

Schreiner, A., 1989. Vulkanischer Tuff (Miozän). In Gwinner, M.P., Ed.: Erläuterungen zu Blatt 7524 Blaubeuren. Geoilogische Karte von Baden-Württemberg, Stuttgart.

Shahack-Gross, R., Berna, F., Karkanas, P., Weiner, S., 2004. Bat guano and preservation of archaeological remains in cave sites. Journal of Archaeological Science 31, pp. 1259-1272.

Sedov, S., Sycheva, S., Targulian, V.P.T., Díaz, J., 2013. Last Interglacial paleosols with Argic horizons in Upper Austria and Central Russia – peodgenetic and paleoenvironmental inferences from comparison with the Holocene analogues. E&G Quaternary Science Journal 62 (1), pp. 44-58.

Semmel, A. and Terhost, B., 2010. The concept of the Pleistocene periglacial cover beds in central Europe: A review. Quaternary International 222, pp. 120-128.

Sjöberg, E.L., 1976. A fundamental equation for calcite dissolution kinetics. Geochimica et Cosmochimica Acta 40, pp. 441-447.

Sjöberg, E.L. and Rickard, D.T., 1983. Temperature dependence of calcite dissolution kinetics between 1° and 62 °C at pH to 8.4 in aqueous solutions. Geochimica et Cosmochimica Acta 48, pp. 485-493.

Sjöberg, E.L. and Rickard, D.T., 1984. Calcite dissolution kinetics: surface speciation and the origin of the variable pH dependence. Chemical Geology 42, pp. 119-136.

Sjöberg, E., L., Rickard, D., T., 1985. The effect of added dissolved calcium on calcite dissolution kinetics in aqueous solutions at 25°C. Chemical Geology 49, 405-413.

Soergel-Rieth, E., 2011. Eine diluviale Nagetierschicht und ihre Bedeutung für die Klimafrage. Kerns Verlag.

Starnberger, R., Drescher-Schneider, R., Reitner, J.M., Rodnight, H., Reimer, P.J., Spötl, C., 2013. Late Pleistocene climate change and landscape dynamics in the Eastern Alps: the Inner-alpine Unterangberg record (Austria). Quaternary Sceince Reviews 68, pp. 17-42.

Stoops, G., 2003. Guidelines for Analysis and Description of Soil and Regolith Thin Sections. Soil Science Society of America, Inc. Madison.

Strasser, M., Strasser, A., Pelz, K., Seyfried, H., 2009. A mid Miocene to early Pleistocene multi-level cave as a gauge for tectonic uplift of the Swabian Alb (Southwest Germany). Geomorphology 106, pp. 130-141.

Svoboda, J., Ložek, V., Vlček, E., 1996. Hunters between east and west. The Paleolithic of Moravia. Plenum Press.
Taller, A., 2015. Das Magdalenian des Hohle Fels: Chronologische Stellung, Lithische Technologie und Funktion der Rückenmesser. Kerns Verlag.
Taller, A. and Conard, N.J., 2017. Das Gravettien der Hohle Fels-Höhle und seine Bedeutung für die kulturelle Evolution des europäischen Jungpaläolithikums. Quartär 63, pp. 89 – 123.
Taller, A., Beyries, S., Bouls, M., Conard, N. J., 2012. Are the Magdalenian backed pieces from Hohle Fels just projectiles or part of a multifunctional toolkit? Mitteilungen der Gesellschaft für Urgeschichte 21, pp. 37–54.
Taller, A., Bolus, M., Conard, N.J., 2014. The Magdalenian of Hohle Fels Cave and the resettlement of the Swabian Jura after the LGM. Modes de contacts et de déplacements au Paléolithique Eurasiatique - Modes of contact and displacements during the Eurasian Palaeolithic, Actes du Colloque international de la commission 8 (Paléolithique supérieur) de l´UISPP, Université de Liège, 28-31 Mai 2012, pp. 383-402.
Temmler, H., Beinroth, F., Geyer, M., 2003. Geologische Karte Von Baden-Württemberg 1:25000, Blatt 7427 Sontheim an der Brenz. Landesamt für Geologie, Rohstoffe und Bergbau Baden-Württemberg, Freiburg.
Terberger, T., 2003. Vom Gravettien zum Magdalénien in Mitteleuropa. Aspekte der menschlichen Besiedlungsgeschicte in der Zeit um das zweite Kältemaximum der letzten Eiszeit. Archäologisches Nachrichtenblatt 8, pp. 55-62.
Terberger, T., and Street, M., 2002. Hiatus or continuity? New results for the question of pleniglacial settlement in central Europe. Antiquity 76 (291), pp. 691-698.
Terhorst, B., Kühn, P., Damm, B., Hambach, U., Meyer-Heintze, S., Sedov, S., 2014. Paleoenvironmental fluctuations as recorded in the loess-paleosol sequence of the Upper Paleolithic site Krems-Wachtberg. Quaternary International 351, pp. 67-82.
Thost, G., 1986. Klima- und witterungsbedingte Besonderheiten im Bereich des Blautals. Das Blautal, Ulmer Geographische Hefte 4, pp 28-31.
Torres-Giron, M. L. and Recio-Espejo, J.M., 1992. Periglacial features of the Subbetic Mountains of southern Spain (Córdoba Province). Journal of Quaternary Science 12, pp. 275-282.
Torke, W., 1998. Fische aus jungpleistozänen und holozänen Siedlungsplätzen in Baden-Württemberg. Naturkunde Württemberg 154, pp. 231- 259.
Turkonovsky, J. and Schneider, G., 1982. The seismotectonic character of the September 3, 1978, Swabian Jura earthquake series. Tectonophysics 83, pp. 151-162.
Ufrecht, W., 2008a. Evaluating landscape development and karstification of the Central Schwäbische Alb (Souhwest Germany) by fossil record of karst fillings, Zeitschrift für Geomorphologie 52, 4, pp. 417-436.
Ufrecht, W., 2008b. Geologie und Hydrologie im Gebiet des Kartenblatts 7521 Reutlingen (1:25.000)- ein Überblick. Laichinger Höhlenfreund 43. Jahrgang, pp. 9 – 18.
Valoch, K., 1996. Le Paléolithique en Tchéquie et en Slovaquie. Jérome Millon.
Vanderberghe, J., 2015. River terraces as response to climate forcing: Formatting processes, sedimentary characteristics and sites for human occupation. Quaternary International 370 (3), pp. 3-11
Van der Marel, H.W. and Beutelspacher, H., 1976. Atlas of Infrared Spectroscopy of Clay Minerals and their Admixtures, Elsevier Scientific Publishing Company.
Vanhaeren, M. and d'Errico, F., 2006. Aurignacian ethno-linguistic geography of Europe revealed by personal ornaments. Journal of archaeological science 33, pp. 1105-1128.
Van Huissteden, J. and Kasse, C., 2001. Detection of rapid climate change in Last Glacial fluvial succession in the Netherlands. Global and Planetary Change 28, pp. 319-339.
Van Steijn, H., Bertran, P., Francou, B., Hétu, B., Texier, J.P., 1995. Models for the Genetic and Environmental Interpretation of Stratified Slope deposits: Review. Permafrost and Periglacial Processes 6, pp. 125-146.
Van Vliet-Lanoë, B., 1990. The genesis and age of the argillic horizon in Weichselian loess of Northwestern Europe. Quaternary International 5, pp. 49-56.

Van Vliet-Lanoë, B., 1998. Frost and soils: implications for paleosols, paleoclimates and stratigraphy. Catena 34, pp. 157-183.
Van Vliet-Lanoë B. 2010. Frost Action. In Stoops, G., Marcellino, V., Mees, F., Ed.: Interpretation of Micromorphological Features of soils and regoliths. Elsevier, pp.81-108
Verpoorte, A., 2005. The first modern humans in Europe? A closer look at the dating evidence from the Swabian Jura (Germany). Antiquity 79, pp. 269-279
Vepraskas, M.J., Wilding, L.P., Drees, L.R., 1993. Aquic conditions for Soil Taxonomy: concepts, soil morphology and micromorphology. Dev. Soil Sci. (1993). doi:10.1016/S0166-2481(08)70402-1
Villinger, E., 2003. Zur Paläogeographie von Alpenrhein und oberen Donau. Zeitschrift der Deutschen Geologischen Gesellschaft 154, 2/3, pp. 193-253.
Vos, C., Don, A., Prietz, R., Heidkamp, A., Freibauer, A., 2016. Field-based soil-texture estimates could replace laboratory analysis. Geoderma 267, pp. 215-219.
Wagner, E., 1983. Das Mittelpaläolithikum der Grossen Grotte bei Blaubeuren (Alb-Donau-Kreis). Theiss, Stuttgart.
Wang, S.-L., Burr, G.S., Chen, Y.-G., Lin Y., Wu, T.-S., 2013. Low-Temperature and temperature stepped-combustion of terrace sediments from Nanfu, Taiwan. Radiocarbon 55 (2-3), pp. 553-562.
Washburn, A.L., 1979. Geocryology – A survey of periglacial process and environments. Edward Arnold, London.
Weiner, S., Bar-Yosef, O., 1990. States of preservation of bones from prehistoric sites in the Near East: a survey. Journal of Archaeological Science 17, pp. 187-196.
Weniger, G.C., 1987. Magdalenian Settlement and Subsistence in South-West Germany. Proceedings of the Prehistoric Society 53, pp. 293-307.
Wetzel, R., 1958. Die Bocksteinschmiede mit dem Bocksteinloch, der Brandplatte und dem Abhang sowie der Bocksteingrotte. Veröffentlichungen aus der prähistorischen Abteilung des Ulmer Museums 1, Kohlhammer, Stuttgart.
Wetzel, R., 1961. Der Hohlestein im Lonetal. Dokumente alteuropäischer Kulturen vom Eiszeitalter bis zur Völkerwanderung. Mitteilungen des Vereins für Naturwissenschaft und Mathematik in Ulm (Donau) 27, pp. 21-75.
Wetzel, R. and Bosinski, G., 1969. Die Bocksteinschmiede im Lonetal (Markung Rammingen, Kreis Ulm) I. Veröffentlichungen des Staatlichen Amtes für Denkmalpflege Stuttgart, Verlag Müller 6 Gräff – Komissionsverlag, Stuttgart.
Wilkerson, F.D. and Schmid, G.L., 2003. Debris flows in Glacier National Park, Montana: geomorphology and hazards. Geomorphology 55 (1-4), pp. 317–328.
Wolf, S., 2015. Schmuckstücke – Die Elfenbeinbearbeitung im Schwäbischen Aurignacien. Kerns Verlag.
Wolff, W., 1962. Periglazial-Erscheinungen auf der Albhochfläche. Die Reprografie – Karl Mayer KG, Stuttgart.
Yates, T.J.S, Spiro, B.F, Vita-Finzi, C., 2002. Stable isotope variability and the selection of terrestrial mollusc shell samples for ^{14}C dating. Quaternary International 87 (1), pp. 87-100.
Ziegler, P. A. and Fraefel, M., 2009. Response of drainage systems to Neogene evolution of the Jura fold thrust belt and Upper Rhine Graben. Swiss Journal of Geoscience 102, pp. 57-75.
Zilhão, J., 2001. Anatomically Archaic, Behaviorally Modern: The Last Neanderthals and Their Destiny. Drieentwintigste Kroon-Voordacht gehouden voor de Stichting Nedrlands Museum vor Anthropologie en Praehistorie te Amsterdam.
Zilhão, J. and d'Errico F., 1999. The Chronology and Taphonomy of the Earliest Aurignacian and Its Implications for the Understanding of Neandertal Extinction. Journal of World Prehistory 13, pp. 1-68.

Zilhão, J. and d'Errico, F., 2003. An Aurignacian «garden of Eden» in southern Germany? An alternative interpretation of the Geissenklösterle and a critique of the Kulturpumpe model. PALEO Revue d'archéologie préhistorique 15, pp. 1-28.

Appendix I - Processing of the geophysical data and 3D Modelling

7.1 DTM data

Hohlenstein

We reconstructed the topography of the river terrace located in front of Hohlenstein by interpolating DGPS and LIDAR points (thanks to Felix Bachover and Geraldine Quénéhervé). The elevation values acquired with the two methods are generally comparable, however the two datasets present different advantages and disadvantages. The digital terrain model (DTM) based on the DGPS points displays a resolution of 0.5 m and thus can successfully resolve the break-in-slope between the terrace and the floodplain. However the DGPS dataset present significant artifacts due to the method used for data acquisition (points have been collected while the operator was walking along "zig-zag" lines. Fig. 7.1 detail 1). Additionally the area close to the forest margin display elevation values higher than expected, likely due to the not optimal connection of the DGPS with the satellite. On the opposite, the LIDAR data present consistent elevation values and no significant artifacts. However, the LIDAR dataset displays lower resolution (1 m per cell) which results in a less sharp image (Fig. 7.1 detail 2). Here is the working flow we used to interpolate these two datasets with the software Saga:

1- We created a DTM (grid) starting from the LIDAR points
2- We created a second grid starting from the DGPS points;
3- Basing on the latter we produced a slope map;
4- After a visual and interactive examination of this map we defined the cells with a value higher than 10° as potential artifacts;
5- We sat the value of these "artifact cells" to 5000 (any other number with 4 digits could have been used instead, the goal of this step was to define all these cells with a univocal value).
6- We changed the value of all the other "non-artifact" cells to -99999, which corresponds to the Null value in Saga. By doing so, we deleted all the "non-artifact" cells.
7- We clipped the slope map to the break-in-slope area where artifact features were more evident.

8- We assigned to all the “artifact cells” the value 0 and summed them to the LIDAR grid.

9- We merged (with B-spline interpolation) the result of step 8 with the original DGPS grid of step 2. By doing so, we replaced the “artifact cells” with more reliable elevation values from the LIDAR grid.

10- As a final step we applied a simple filter to the new grid to smooth the data (Fig. 7.1 detail 3 and 4).

We used the grid resulting from step 10 for the topo-correction of the GPR data and to assess the elevation of the EC-logging and the cores. From Saga we exported this DTM into .xyz format so to be imported in GOCAD, where we created a TIN surface.

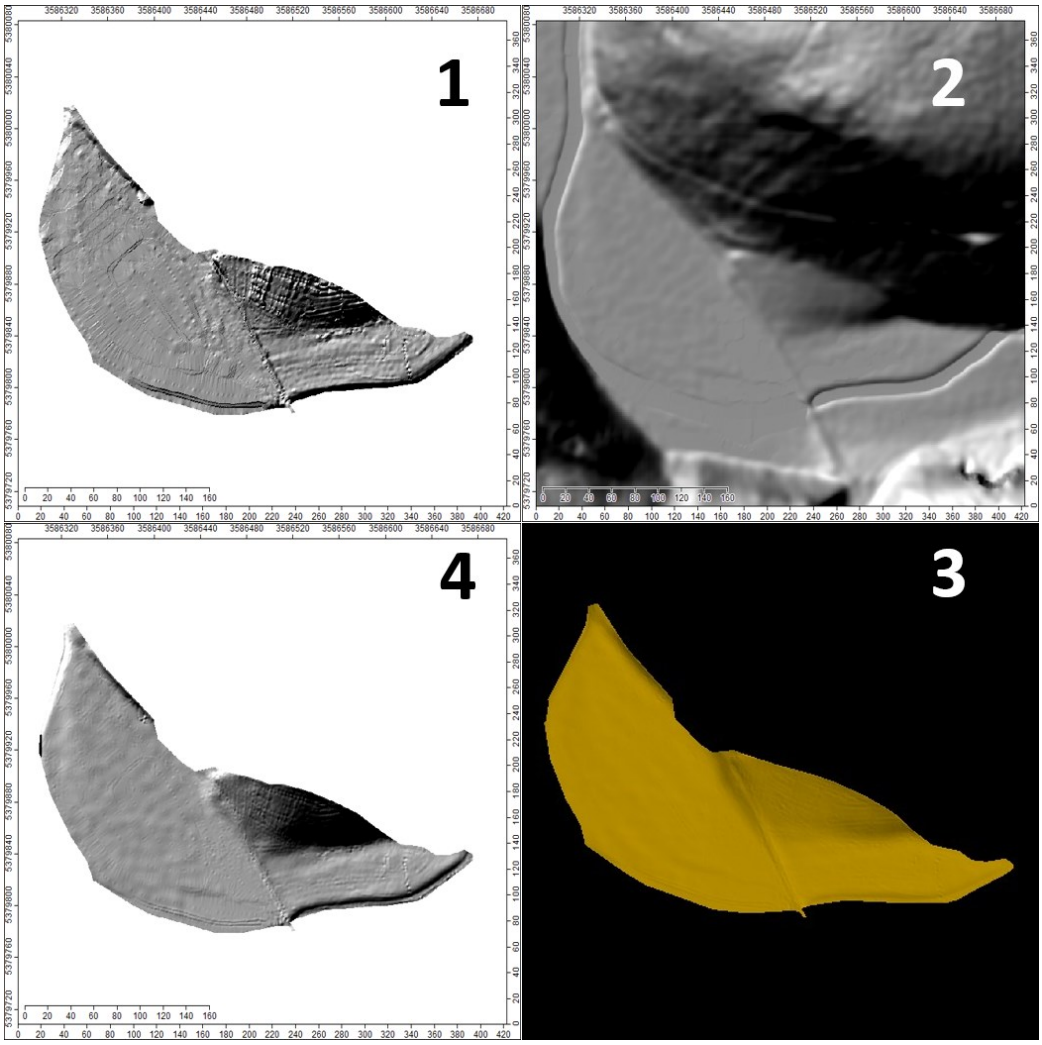

Fig 7.1. DTM of the area opposite from Hohlenstein. Hillshade maps produced out of DGPS points (***1***), LIDAR data (***2***) and the interpolation between the two data sets (***3***). The interpolated DTM visualized in GOCAD.

Bockstein

At Bockstein we carried a less intensive survey in comparison with the prospection we conducted at Hohlenstein and Hohle Fels. For this part of the Lone Valley we relied on the LIDAR data (1 m resolution) without any further interpolation.

Hohle Fels

The *Vorplatz* of Hohle Fels appears poorly visible in the LIDAR data (1m resolution. Fig. 7.2, detail 2). This is likely due to the relatively small extent of the *Vorplatz* (ca. 350 m^2) and the very high limestone outcrop of Hohle Fels. With the intent to obtain a more detailed topography, we covered the Vorplatz with 166 total station points. Based on such dataset we produced a DTM displaying 30 cm of resolution (Fig. 7.2, detail 1). Since our coring and geophysical data do not come exclusively from the *Vorplatz* we interpolated this DTM with LIDAR data (1 m resolution) from the hillside and the Ach floodplain. We merged the two datasets in GOCAD. The resulting surface is displayed in Fig. 7.2, detail 3.

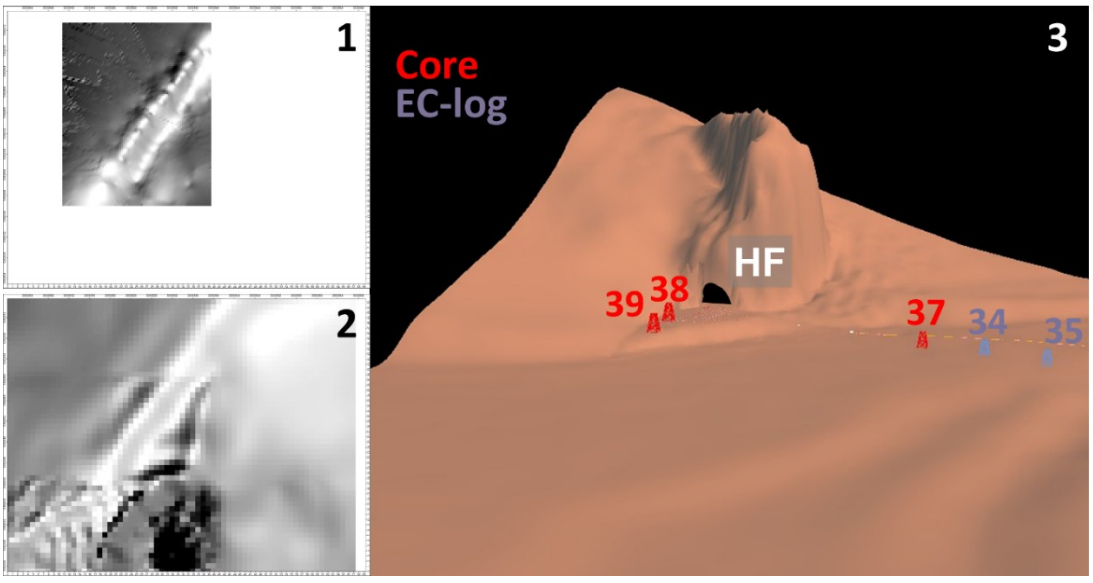

Fig. 7.2. DTM of the area surrounding Hohle Fels. Hillshade maps produced from the points collected with total station (***1***) and LIDAR data (***2***). ***3***, DTM visualized in GOCAD.

7.2 Processing of GPR data

As mentioned in Chapter 2, all the GPR data from our survey areas have been processed in the software Reflex 7.5. In this section we illustrate which filters have been employed:

1. *Remove Header Gain* (Fig. 7.3, detail 1). In order to be properly visualized GPR data needs to be amplified with a filter, which is called "gain". The gain filter is already applied during data collection so to verify that data are acquired properly. The setting of the gain in the field is problematic particularly due to the low quality of the unit screen. As result raw GPR data are not properly amplified. With this step of our processing flow we removed the gain filter applied in the field and, in step 3, we applied a new one.

2. *Move start time to the first direct wave* (Fig. 7.3, detail 2). When GPR profiles are collected in distance mode the antenna might encounter obstacles (rough ground surface, patches with higher grass vegetation, etc.) that might cause variations in the antenna airgap. The resulting GPR profile will display jumps in the air/ground wavelet first arrival (Cassidy 2009). Also thermal drift and electronic instability might cause similar artifacts in the data (Cassidy 2009). In order to remove them, all the traces within a GPR profile need to be moved to a common reference point. In our case we moved the traces to the first break point of the first direct wave.

3. *Manual Gain* (Fig. 7.3, detail 3). After having set a common reference for all the traces we applied a new gain filter.

4. *Band Pass Butterworth* (Fig. 7.3, detail 4). Although frequency filters are applied already during data acquisition, GPR data commonly display some disturbance (noise). This results from interference with electromagnetic fields produced by the GPR itself and other external sources. With this step we applied a high- and low-pass filter to our GPR data, thus removing all the frequencies higher and lower than the main bandwidth of the GPR signal (Cassidy 2009).

5. *Average xy* (Fig. 7.3, detail 5). This filter sum to each trace the horizontal (x) and vertical (y) mean calculated over a number of traces, this filter is effective in removing high frequency noise (Jens Hornung, personal communication) and emphasizes continuous reflectors (Cassidy 2009).

6. *Subtracting the average* or *background removal* (Fig. 7.3, detail 6). Horizontal bands are a type of artifact very common in GPR data (signal ringing, Cassidy 2009). We removed these artifacts by subtracting the average of a given number of traces from each individual trace in a sequence. Alternatively we applied the

background removal filter, which subtracts from each trace the average of the entire GPR profile.

7. *Kirchhoff Hyperbolae migration* (Fig. 7.3, detail 7). Particularly the GPR profiles collected on top of coarse-grained sediments (for instance those from the *Vorplatz* of Hohle Fels) display numerous diffraction hyperbolae. In order to obtain a more realistic image of the underground, we migrated the hyperbolae present in our GPR data. Before the migration, we realized 2D-velocity models for the GPR data. These models are based on the velocity analysis of the GPR measurements combined with the study of our EC-logging and coring data. These 2D-velocity models have been used for the migration of the GPR data (2D-migration). More rarely migration was performed using only one average velocity for the entire GPR profile (1D-migration).
8. *Time-depth correction* (Fig. 7.3, detail 8). As discussed in chapter 2.1, GPR data are acquired versus time. With this step we converted the time into depth. This filter was based on the 2D-velocity models used for the migration.
9. Topography correction using the traceheaders (Fig. 7.3, detail 9). We performed this filter after having assigned to each trace *x*, *y* and *z* coordinates (see p. 170).

Although we used the same filters for all the GPR data, we often changed the filter settings in order to achieve a better processing. As a common practice, for each grid we selected two representative profiles, one collected along the *x* and one along the *y* axis. On these profiles we experimented with the filter settings. Once we reached a satisfactory result, we saved the most successful processing flow as a sequence processing file (.spf), which was later used to process automatically the rest of the Grid. Although largely automatized, data processing still needed some regular manual inputs. In particular velocity and topography models have to be loaded manually, therefore sequence processing was interrupted at steps 7, 8 and 9. After the sequence processing, an average of 2 to 5 GPR profiles per Gird was not appropriately processed. These GPR profiles have been reprocessed individually.

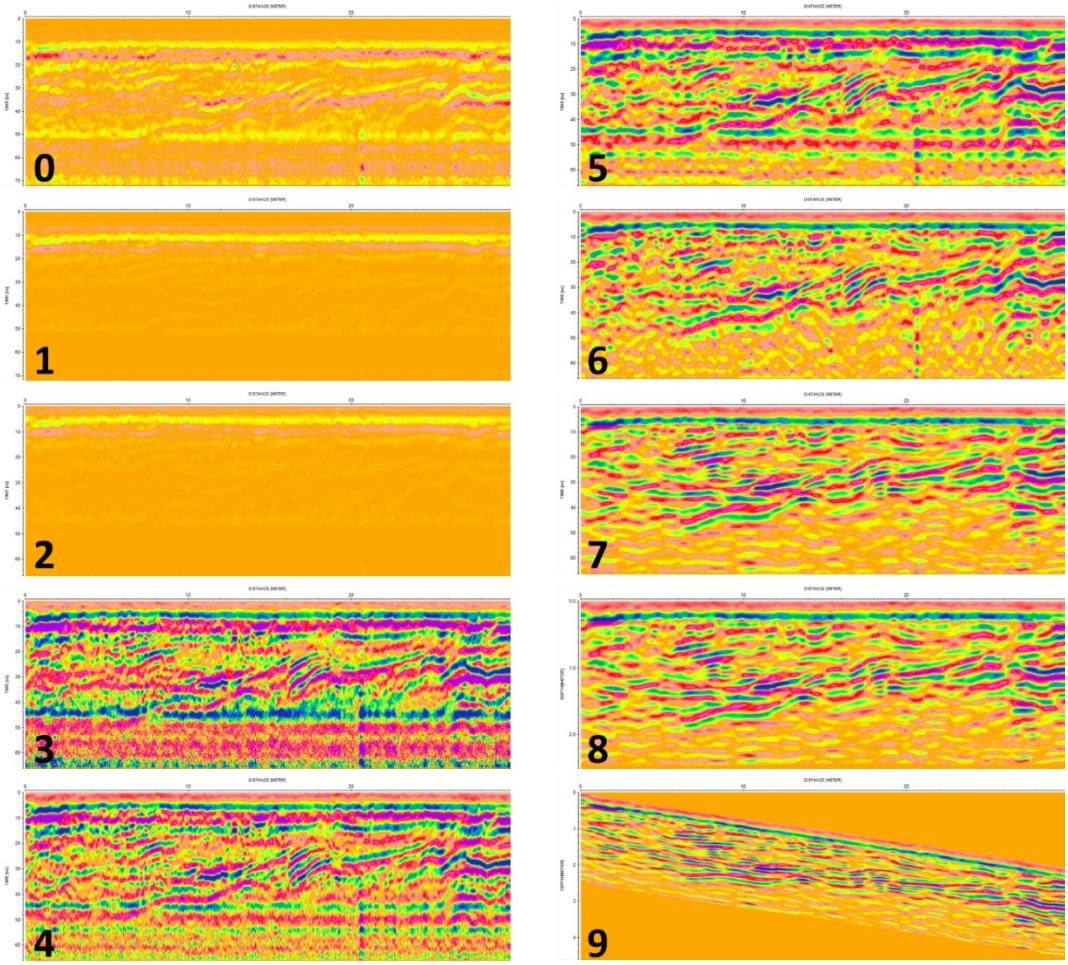

Fig. 7.3. GPR data processing. ***0***, Raw data from Hoholenstein Grid1_y_36; ***1***, Remove Header Gain; ***2***, Move Start Time; ***3***, Manual Gain; ***4***, Band Pass Butterworth; ***5***, Average xy; ***6***, Subtracting The Average; ***7***, Kirchoff Migration; ***8***, Time-depth Correction; ***9***, Topography Correction.

In order to import the GPR data in a 3D geographic system, we needed to assign 3D geographic coordinates to each individual scan within each GPR profile. Unfortunately this was not entirely possible in the field, since DGPS and total station were available only for few days at the end of each survey campaign. Therefore we located the position of our GPR data in two steps. In the field we recorded exclusively the geographic coordinates of the gird corners (DHDN 3 Gauss Zone 3; EPSG: 31467), while later, starting from these points, we reconstructed the location of the GPR scans. Here we present in detail the protocol we followed to assign geographic coordinated to our GPR data:

1. In Saga, we built lines connecting the grid corners measured in the field (Fig 7.4, upper left). Start and end of GPR profiles need to be located along these lines.
2. In order to do so, we ran the module “Convert lines to points”, which allows to convert a polyline into points also adding regularly spaced (for instance each 1 m) extra points (Fig 7.4. Lower right).
3. After having named the points created with step 2 (either manually or via code in R), by the use of the module “Convert points to line” we built the GPR profiles (Fig. 7.4 lower left).

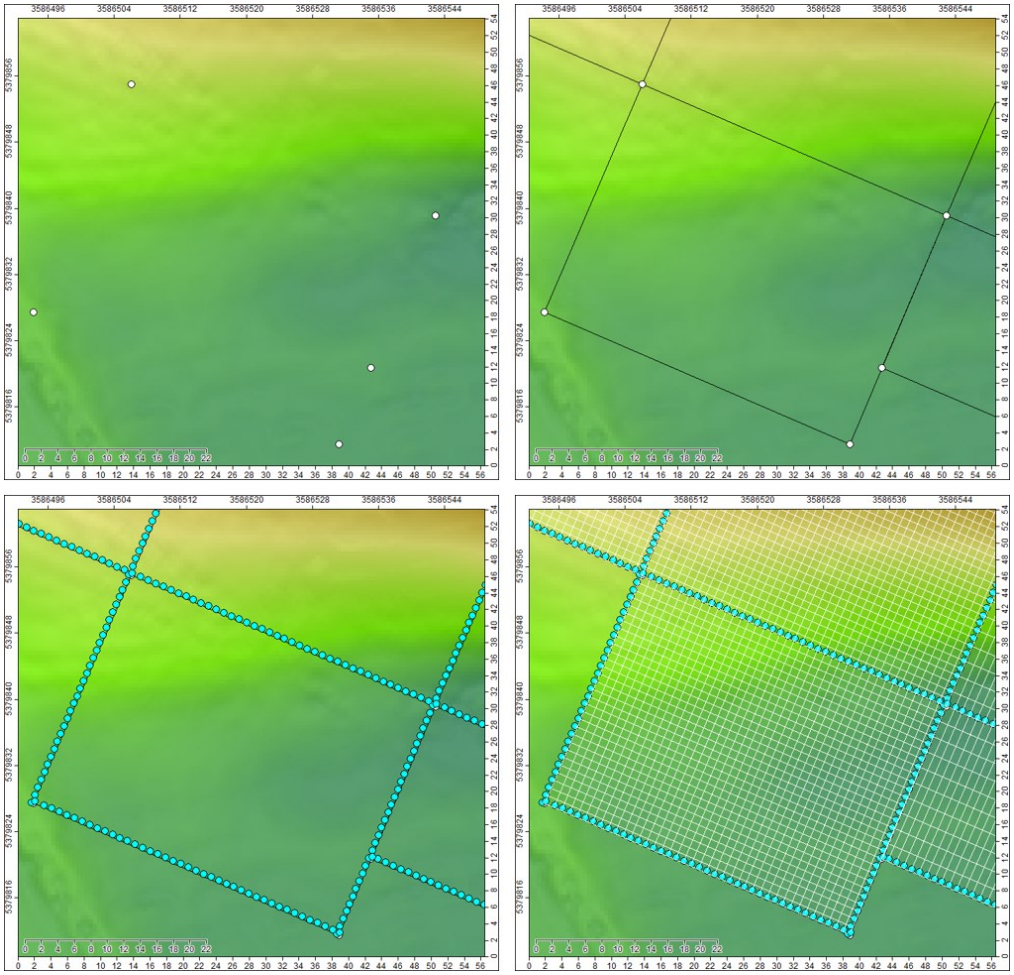

Fig. 7.4. Assigning geographic coordinates to GPR data – part one. ***Upper left***, the corner points of a grid; ***Upper right***, the 4 lines have been created on the border of the grid; ***Lower left***, the start and end points of each GPR profiles have been created; ***Lower right***, all the GPR profiles have been created.

4. Starting from the result of step 3 and using again the module “Convert lines to points”, along each GPR profile we built as many points as many scans we collected in the field (Fig. 7.5, on the left). The value to be insert in the “add extra

points" option of the module "Convert lines to points" corresponds to the trace increment, which might be found in the fileheaders of the GPR measurements (this was checked in Relfex).

5. Using the module "Add grid value to points" we added the *z* coordinate from our DTM to the points created in the previous step.
6. The result of step 5 was then exported in .txt format with 5 columns: ID, GPR profile name, x, y and z.

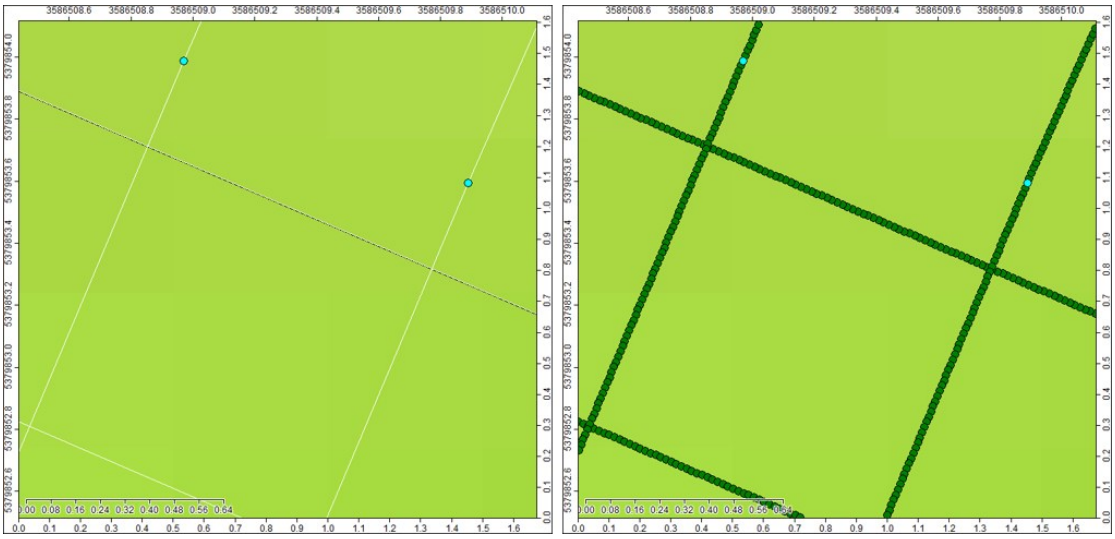

Fig. 7.5. Assigning geographic coordinates to GPR data – part two. ***On the left*** the lines representing the GPR profiles, ***on the right*** they have been transformed into points with the spacing of the scan/units. Therefore the points represent the location of the traces.

Additional information:

a- A separate trace file (.txt) was created for the GPR measurements collected at Hohlenstein, Hohle Fels and Bockstein;

b- For the GPR measurements collected at Hohlenstein we decided to relocate the start and the end points of the profiles 30 cm (half of the length of the 200 MHz antenna) backwards from the Grid border, since in the field we placed the front side of the antenna, and not the center, on the grid borders.

We did not apply this correction to the GPR measurements collected at Hohle Fels and Bockstein because at these sites grid corners were measured only weeks after the survey, when they were jet partly displaced (Bockstein) or partly removed (Hohle Fels).

Nevertheless in GOCAD we could verify that in great majority our reconstruction of the location of the GPR data was quite accurate, probably due to the not very high scan/units setting (50 to 60), the not dense spacing between GPR profiles (1 to 3 m) and the size of the feature we were interested in (tens of meters).

c- In general we estimate that the geographical position of our GPR data is precise within 0.5 m.

With the intent of extracting the tracheader for each GPR profile from the .txt file that we built in SAGA, we wrote a script with the software R:

```
traces<-read.table("traces.txt")
options(digits=11)
n<-0
for (n in seq(0,30,by=1))
# this is true if the x axis of the Grid is 30 m long and the spacing is 1
{location_name<-grep(paste("^Grid5_x_",n,"$",sep=""),as.vector(traces[,2]))
# as example we are asking the program to look for all the traces of Grid5, axis x
name<-as.vector(traces[,2])[location_name]
x<-as.numeric(as.vector(traces[location_name,3]))
y<-as.numeric(as.vector(traces[location_name,4]))
z<-as.numeric(as.vector(traces[location_name,5]))
temporary<-data.frame(name,x,y,z)
temporary<-temporary[order(temporary[,2]),]
# The last line is needed to define the direction of the profile,
# since when saving and exporting Saga does not archive data in order.
# The order we want depends on how the Grid was sat and how we collected the data
# (we can check this in GIS).
# In this case we ask the program to order traces from the smallest to the highest x coordinate.
# If we wanted to order the data with an opposite trend, the command would have been:
# temporary<-temporary[order-(temporary[,2]),] if it´s decreasing
step<-c(0.01818181761*(1:length(z)))
# 0.01818181761 is the trace increment, this value might be found in the fileheaders in Reflex.
zero_column<-(rep(0,length(z)))
top<-data.frame(step,zero_column,temporary[,4])
write.table(top,paste("Top_Grid5_x_",n,".ASCII",sep=""),sep="\t",row.names=F,col.names=F)
# These files can be used instead of the traceheadres for topo-correction.
max_min<-c(max(z),min(z))
write.table(max_min,paste("max&min_z_Grid5_x_",n,".txt",sep=""),row.names=F,col.names=F)
# Again we should remember to change the name of what the program is supposed to look for
trace_number<-(1:length(z))
traceheader<-
data.frame(tracenumber=trace_number,distance=step,shotx=temporary[,2],shoty=temporary[,3],
recx=temporary[,2],recy=temporary[,3],shotz=temporary[,4],recz=temporary[,4])
write.table(traceheader,paste("Table_Grid5_x_",n,".DST",sep=""),sep="\t",row.names=F)
# As before we should remember to change the name of what the program is supposed to look for.
# This command creates one table per each GPR profile collected in Grid 5 along the x axis.
# Each table contains the new traceheader for each GPR profile.
# All the tables can be opened in Reflex, where the traceheaders can be modified.
# Unfortunately there is no way to do this step with the sequence processing,
# so traceheaders needs to be changed for one GPR profile at the time.
n<-n+1
# change 1 to 2 or 3 if the spacing is 2m or 3m.
```

```
}
# The comments above are valid for the lower part as well, the code is split in two cycles,
# the lower part is for the y. Some of our GPR grids have different spacing along the two axis.
# Splitting the code in two was to facilitate the writing of the code.
# Also for this code we should remember to change the name of the grid (e. g. Grid_5).
n<-0
for (n in in seq(0,40,by=1){
location_name<-grep(paste("^Grid5_y_",n,"$",sep=""),as.vector(traces[,2]))
name<-as.vector(traces[,2])[location_name]
x<-as.numeric(as.vector(traces[location_name,3]))
y<-as.numeric(as.vector(traces[location_name,4]))
z<-as.numeric(as.vector(traces[location_name,5]))
temporary<-data.frame(name,x,y,z)
temporary<-temporary[order(temporary[,2]),]
step<-c(0.01818181761*(1:length(z)))
zero_column<-(rep(0,length(z)))
top<-data.frame(zero_column,step,temporary[,4])
write.table(top,paste("Top_Grid5_y_",n,".ASCII",sep=""),sep="\t",row.names=F,col.names=F)
max_min<-c(max(z),min(z))
write.table(max_min,paste("max&min_z_Grid5_y_",n,".txt",sep=""),row.names=F,col.names=F)
trace_number<-(1:length(z))
traceheader<-
data.frame(tracenumber=trace_number,distance=step,shotx=temporary[,2],shoty=temporary[,3],
recx=temporary[,2],recy=temporary[,3],shotz=temporary[,4],recz=temporary[,4])
write.table(traceheader,paste("Table_Grid5_y_",n,".DST",sep=""),sep="\t",row.names=F)
n<-n+1}
```

After letting run this script in R we obtained as many "Table_Grid*n_x*/*y_n*.DST" files as many GPR profiles we measured for the *n* Grid. This code has to be run as many times as many grids have been collected in the field. All the ".DST" files written by R are designed to be compatible with Reflex.

In Reflex the traceheader of each GPR profile was changed at latest before applying the topo-correction filter, ideally even before starting the entire sequence processing so to be able to import in GOCAD the GPR data at any stage of processing.

The script we wrote in R also creates ".txt" files which contain the two traces displaying respectively the highest and the lowest z coordinates for each GPR profiles. These files might be useful to check the result of the topo-correction. More in detail when performing this filter Reflex migrates the traces using a default velocity of 0.1 m/ns. However often this value needs to be modified otherwise the software would deform the actual topography. In order to check whether the topo-corrected profile respected the actual topography, we usually verified that the difference in elevation between the highest and the lowest trace in the topo-corrected profile was the same as in the ".txt" file we created with the R script.

Once the topo-correction was performed, the data were exported from R using the ASCII 4 column format making sure to include the traceheader coordinates and adding "points" as "addition for output filename". The exported files include *x*, *y* (both of them geographic coordinates), depth (m from top) and amplitude. However to be displayed correctly in GOCAD the depth values have to be replaced with elevation values. This substitution was operated in R via this script:

```
options(digits=11)
n<-0
for (n in seq(0,30,by=1))
# Similarly to previous code, we need to change this line if the x axis is shorter
# and if the spacing is different than 1 m.
{asc<-read.table(paste("GRID5_X_",n,"points.ASC",sep=""))
# As example we are still working on Grid 5.
first<-asc[,1]
x<-asc[,1]
y<-asc[,2]
z<-(read.table(paste("max&min_z_Grid5_x_",n,".txt",sep=""))[1,])-as.numeric(paste(asc[,3]))
a<-asc[,4]
write.table(data.frame(x,y,z,a),paste("Grid5_x_",n,"_gocad.ASC",sep=""),sep="\t",row.names=F)
# Remember to change the name of the grid.
# This command line creates the file that we will import in GOCAD.
n<-n+1
# Remember to change 1 with 2 or 3, if the spacing is 2 m or 3 m.
}
# The comments above are valid for the lower part as well, the code is split in two for cycles
# because spacing along x and y axes might be different. Also the rest of the code is compiled
# as example for Grid 5.
n<-0
for (n in seq(0,40,by=1)) {
asc<-read.table(paste("GRID5_Y_",n,"points.ASC",sep=""))
first<-asc[,1]
x<-asc[,1]
y<-asc[,2]
z<-(read.table(paste("max&min_z_Grid5_y_",n,".txt",sep=""))[1,])-as.numeric(paste(asc[,3]))
a<-asc[,4]
write.table(data.frame(x,y,z,a),paste("Grid5_y_",n,"_gocad.ASC",sep=""),sep="\t",row.names=F)
n<-n+1
}
```

7.3 Import in GOCAD

The GPR data

The R script we report at the end of the previous section creates one "_gocad.ASC" file per GPR profile. These files can be imported in GOCAD2.1.6 as points, through the dedicated import tool ("import as column file"). In GOCAD we also designed a special color palette in order to better display the GPR data. Subsequently we have picked the most interesting reflected phases with the picking tool. Once done with the picking, we

created TIN surfaces basing on the picked points. Often the resulting surfaces need some manual adjustments (such as fitting better to the GPR data and deleting all the extra triangles that software might have created).

Unfortunately working with GOCAD was often challenging, mainly due to the frequent crashing and memory issues of the software itself. In particular GOCAD has limitations in dealing with a large amount of point sets, usually loading more than ca. 30 GPR profiles at the time would result in memory issues. With the intent of solving this issue, we converted at least some of the GPR profiles from points into voxels, however GOCAD often created voxels with large blank areas. Furthermore picking on voxels appeared more problematic than on point clouds, since the program often failed to locate precisely the points we would pick. In conclusion for further researches we would encourage either to try newer versions of GOCAD or experiment alternative software solutions.

The Coring data

In order to import the coring data in GOCAD we created a ".txt" file with two rows in which we inserted respectively *x*, *y* and *z* for the top and the bottom of each borehole. We imported the so created file in GOCAD as a "well object" through the dedicated tool (import from column file) choosing the option "X-Y-TVDSS", which allows the program to classify the columns as *x*, *y* and elevation data. We saved the cores in the native GOCAD format ".WL". Subsequently we opened the ".WL" files in notepad and after the row "ZM_NPTS 2" we added new rows as in the example:

ZONE GL1 0 0.3 1
ZONE GL2 0.3 0.66 2
ZONE GL3 0.66 1.22 3

After "*ZONE*", the first column indicates the name of the geological layer (GL), the second and third columns indicate the top and the bottom of each layer (in meters as distance from the top of the borehole) and the last column is an ID value. In GOCAD the zones are visualized as segments of different colors along the well path.

Information regarding dating samples have been insert directly in GOCAD as Markers along the well path by the dedicated tool ("Add Marker").

The EC-loggings data

We have imported the EC-loggings in GOCAD without any processing. In order to have the EC-loggings in a format compatible with GOCAD we wrote the script:

```
options(digits=11)
depth<-read.table("no10-EC0459.dat")[,4]
ec<-read.table("no10-EC0459.dat")[,2]
# no10-EC0459.dat is the original name for the EC-logging 10,
# we changed this variable for the other loggings.
x<-3586393.956
y<-5379853.921
z<-467.927317-depth
# We entered manually the coordinates for each EC-logging
write.table(data.frame(x,y,z,ec),"no10.dat",sep="\t",row.names=F,col.names=F)
# Of course we changed the name of the output file for the other EC-loggings
```

The program wrote for each EC-logging a ".DAT" file with 4 columns (*x*, *y*, *z*, *ec*). We imported the ".DAT" files as "well objects" in GOCAD through the tool "import from column file". Also in this case while importing the files we choose the option X-Y-TVDSS (see above) and we added a column for the *EC* values. Once imported we selected to display the EC data as "logging data".

References

Cassidy, N.J., 2009. Ground Penetrating Radar Data Processing, Modelling and Analysis. In Jol, H.M., Ed.: Ground Penetrating Radar Theory and Applications. Elsevier, pp. 141-176.

Appendix II - Surface mapping in the Lone Valley

We studied the shallow deposits and the main geomorphological features located in the Lone Valley between the cave sites of Vogelherd and Bockstein by augering and grain size analysis.

8.1 Methods

8.1.1 Core recovering and sediment description

Sediments were recovered with a German auger down to a maximal depth of 1 m. The position of cores (126) and outcrops (ca. 10) was recorded with a Garmin GPS (Fig. 8.1). For each core we described the date and weather condition at the moment of recovery, depth, texture, Munsell color and composition of the sediments (Fig. 8.2). Most of the cores have been sampled (ca. 2 g of loose sediment) for further analysis. In the field all our observations were reported in a specifically suited Libre Office DB form (Fig. 8.2, see section 1.3).

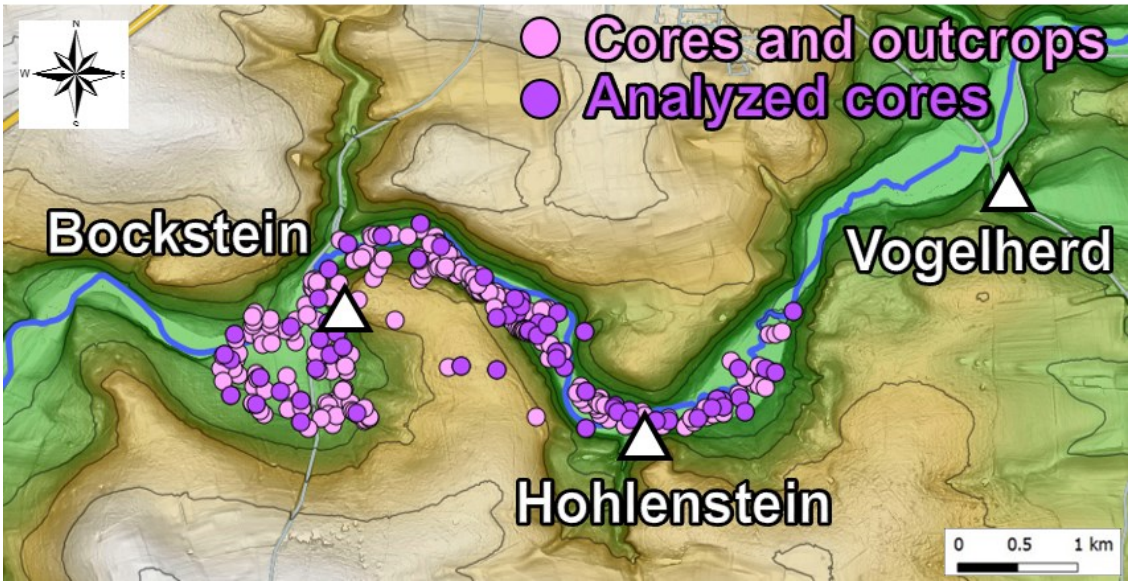

Fig. 8.1. Location of described cores and outcrops in The Lone Valley.

8.1.2 Grain size analysis

We selected 70 samples for grain size analysis. After drying in the oven at 40 °C for few days, we broke these sediment samples into individual particles by the use of a mortar. We sieved out and described the coarser fraction (>2 mm) in order to assess its petrography, morphology and grainsize. For each sample we transferred a total of 20 ±

0.01 g (< 2 mm) of the remaining fine fraction in two separate glass beakers, placing 10 ± 0.005 g of sediment in each beaker. One glass was used for reference (reference beaker) and one for grain size analysis (analysis beaker). In order to eliminate the organic fraction we poured into the beakers 50 ml of 30% hydrogen peroxide (H_2O_2), beakers were immerged in a water bath, filled with distilled water and covered overnight. In the next day they were placed under the fume-hood in a heated sand-bath, where they cooked for about 6 hours until no more reaction was observed. After this step the reference beakers and the analysis beakers were processed differently. Reference beakers were placed in the oven at 105 ˚C until the solution was completely evaporated, subsequently they were cooled down in the desiccator and weighted to estimate the amount of organic matter originally present in the sediment. After cooking, with the use of distilled water and a rubber scraper, the sediment and the solution left in the analysis beakers were transferred into 500 ml PE-Erlenmeyer flasks. We added 10 ml of sodium pyrophosphate solution ($Na_4P_2O_7 \cdot 10 \cdot H_2O$) to the flasks, we closed them and placed them in the mechanical shaker for 6 hours. After shaking, sand and coarse silt were manually sieved with the help of distilled water (mesh sizes 0.63 mm; 0.2 mm; 0.125 mm; 0.063 mm). After complete separation of the grains, we transferred the content of each sieve into crystallizing dishes which were dried in the oven at 105 ˚C overnight. Once the solution was completely evaporated, we cooled the crystallizing dishes in the desiccator and weighted them within an accuracy of 0.0001 g in order to assess the content of sand and coarse silt fractions. During sieving the finer silt and clay fractions were collected inside 800 ml beakers, which were subsequently place in the oven until only 50-60 ml of suspension was left. After transferring this material in smaller beakers we established the medium and fine silt and clay content with the Sedigraph.

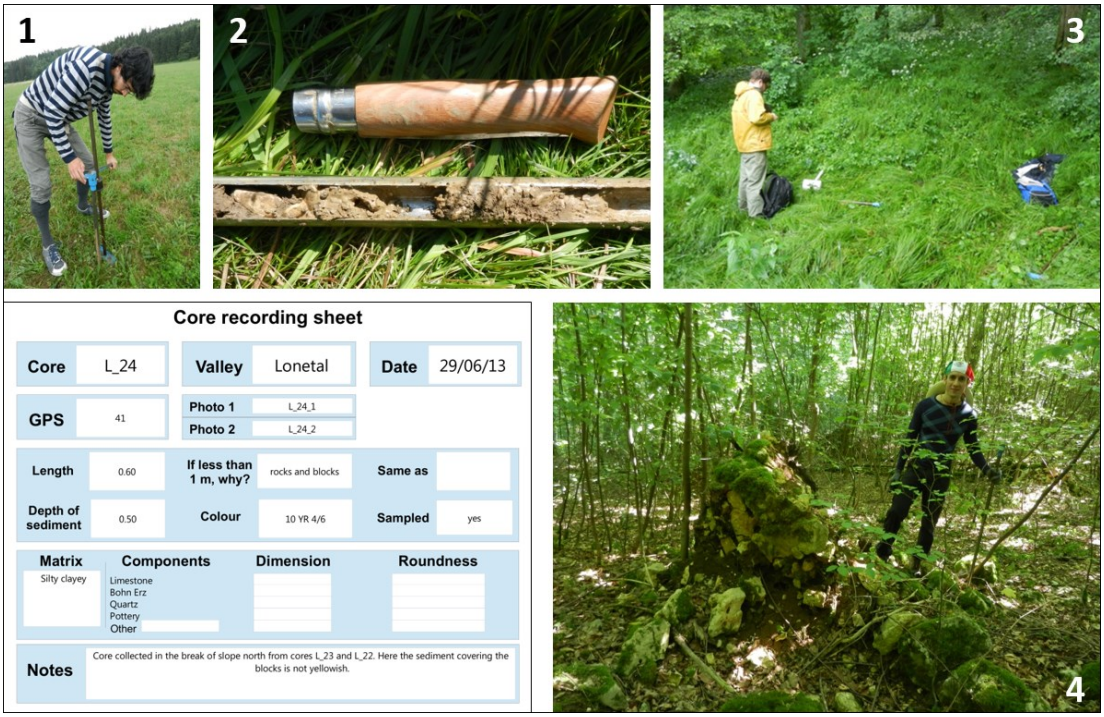

Fig 8.2. Surface Mapping. ***1***, Core recovering; ***2***, detail of photograph of recovered sediment; ***3***, sediment description; ***4***, outcropping sediment under fallen tree. ***On the left***, the core recording sheet used in the field and designed in Libre Office DB.

8.1.3 Data management

In order to perform further statistical and spatial analyses, we insert our field observations and the results of our grain size analysis in an integrated spatial data base (Fig. 3).

As a first step we created a database table in PostGIS:

```
CREATE TABLE public.core_recording_sheet
(
  core character varying(10) NOT NULL,
  valley character varying(20),
  date date,
  gps character varying(10),
  photo_1 text,
  photo_2 text,
  total_length double precision,
  why text,
  depth_sediment_m double precision,
  coulour character varying(20),
  matrix text,
  limestone character varying(10),
  quartz character varying(10),
  bon_herz character varying(10),
  pottery character varying(10),
  other_name character varying(20),
  other_dimension character varying(10),
  limestone_roundness character varying(15),
  quartz_roundness character varying(15),
```

```
 bon_herz_roundness character varying(15),
 pottery_roundness character varying(15),
 other_roundness character varying(15),
 notes text,
 point geometry,
total_weight double precision;
fine_fraction_percent double precision;
coarse_fraction_percent double precision;
organic_matter_percent double precision;
fine_fraction double precision;
coarse_fraction double precision;
check_1 double precision;
processed character (5);
problems character (5);
analyzed_fine_fraction double precision;
left_fine_fraction double precision;
medium_gravel double precision;
fine_gravel double precision;
coarse_sand double precision;
medium_sand double precision;
fine_sand double precision;
very_fine_sand double precision;
coarse_silt double precision;
medium_silt double precision;
fine_silt double precision;
coarse_clay double precision;
medium_and_fine_clay double precision;
medium_gravel_cum double precision;
fine_gravel_cum double precision;
coarse_sand_cum double precision;
medium_sand_cum double precision;
fine_sand_cum double precision;
very_fine_sand_cum double precision;
coarse_silt_cum double precision;
medium_silt_cum double precision;
fine_silt_cum double precision;
coarse_clay_cum double precision;
medium_and_fine_clay_cum double precision;
sand_tot double precision;
silt_tot double precision;
clay_tot double precision;
stat_mode double precision;
stat_mean double precision;
stat_sd double precision;
stat_skewness double precision;
stat_kurtosis double precision;
coarse_roundness character;
limestone_per double precision;
bohnerz_per double precision;
quartz_per double precision;
 CONSTRAINT core_recording_sheet_pkey PRIMARY KEY (core)
)
WITH (
 OIDS=FALSE
);
ALTER TABLE public.core_recording_sheet
 OWNER TO postgres;
```

Subsequently, in Libre Office DB we created a connection with the software PostgreSQL and we designed the form depicted in Fig. 8.3 (on the left), which we used to insert in the database all the information we collected in the field.

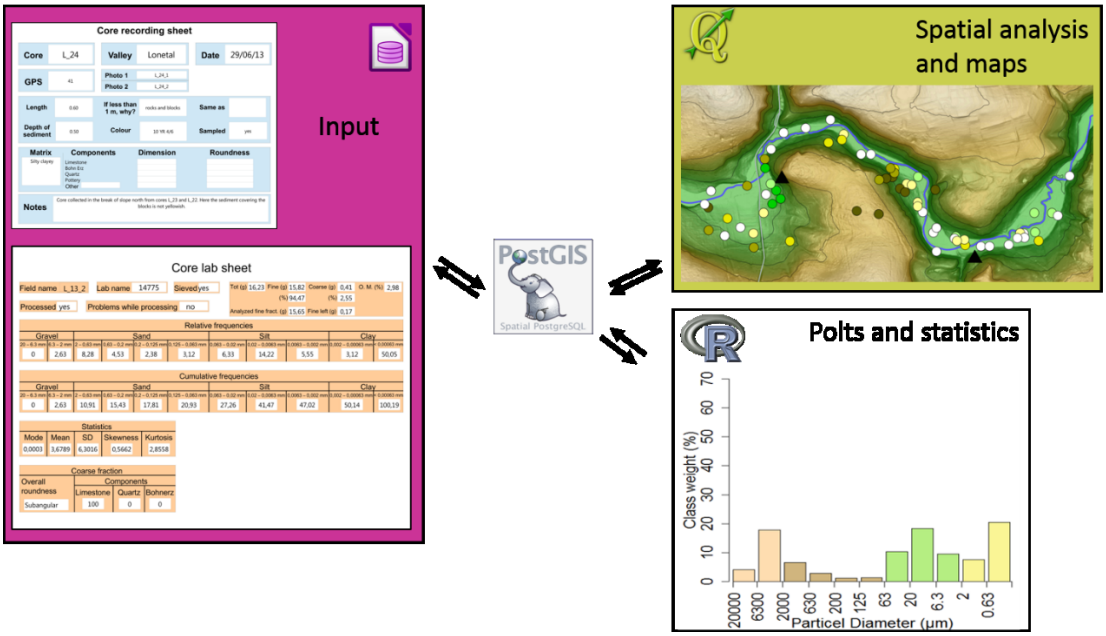

Fig. 8.3. Data management. The architecture of the integrated spatial database we used for our surface mapping.

In order to transfer the GPS points into the database we downloaded them from the GPS device by the use of the free software Easy GPS. Once downloaded, the points have been saved first in the GPS Exchange File format (*.gpx*) and later (through Notepad) as ".csv". Since name, *x*, *y* and *z* coordinates of each point are located respectively in the 1st, 3rd, 4th and 5th columns of these ".csv" files, we wrote the following script in R in order to extract them:

```
csv<-read.csv("13_07_27-28.csv",sep=" ")
# example name of the ".csv" file containing the GPS coordinates
coordinates<-which((csv[,1]) %in% "<wpt")
latitude<-csv[,2][coordinates]
longitude<-csv[,3][coordinates]
longitude<-as.factor(unlist(strsplit(as.character(longitude), ">")))
z<-which(substr(as.character(csv[,1]),1,4) %in% "<ele")
elevation<-(csv[z,1])
elevation<-(unlist(strsplit(as.character(elevation), "<ele>")))
elevation<-as.factor(unlist(strsplit(as.character(elevation), "</ele>")))
n<-which(substr(as.character(csv[,1]),1,5) %in% "<name")
name<-(csv[n,1])
name<-(unlist(strsplit(as.character(name), "<name>")))
name<-as.factor(unlist(strsplit(as.character(name), "</name>")))
d.f.<-data.frame(name,longitude,latitude,elevation)
```

```
write.table(d.f., "13_07_27-28.txt", sep=" ", row.names=F, col.names=T)
```

In the field we measured with the GPS not only the location of the cores but also the position of outcrops and other main geomorphological features. Therefore we decided to insert all the GPS points in a separate database table, from which we would have later transferred only the points of the cores into the core_recording_sheet. We created the table for the GPS coordinates with the following command:

```
CREATE TABLE public.gps
 (
   name text,
   x numeric (10,8),
   y numeric (10,8),
   z numeric (6,3),
   notes text,
   point geometry,
   id bigserial,
   core text
    CONSTRAINT gps_pkey PRIMARY KEY (id)
)
WITH (
OIDS=FALSE);
```

In order to be displayed in GIS, GPS points have to be converted in double precision values with the command:

```
UPDATE public.gps SET point=ST_MakePoint(x,y,z);
UPDATE public.gps
   SET cored='no'
 WHERE public.gps.notes<>'Null';
UPDATE public.gps
   SET cored=public.core_recording_sheet.core from public.core_recording_sheet
 WHERE public.core_recording_sheet.gps=public.gps.name;
```

Finally we transferred the GPS points into the core_recordin_sheet table:

```
UPDATE public.gps SET point=ST_MakePoint(x,y,z);
UPDATE public.gps
   SET cored='no'
 WHERE public.gps.notes<>'Null';
UPDATE public.gps
   SET cored=public.core_recording_sheet.core from public.core_recording_sheet
 WHERE public.core_recording_sheet.gps=public.gps.name;
UPDATE public.core_recording_sheet
   SET gps= public.gps.id from public.gps
 WHERE public.core_recording_sheet.gps=public.gps.name;
UPDATE public.gps
   SET name= public.gps.id;
UPDATE public.core_recording_sheet
   SET point= public.gps.point from public.gps
 WHERE public.core_recording_sheet.gps=public.gps.name;
```

We added the results of the Grain size analysis to the database by exploiting the *UPDATE* function. Taking advantage of the dedicated QGIS tool, we connected our Postgis database to a GIS environment where we could display the cores, their attributes and perform further spatial analysis.

8.2 Results

As discussed in chapter 1.1.1 the Swabian Jura was covered with loess during the Würm Glaciations (Riek 1957, Gwinner 1989, Schall 2002, Goldberg et al. 2003, Miller 2015). Few *in situ* loess sequences are documented mainly south of the Cliff line, in the so called *Flächen Alb*, while the loess deposits originally accumulated northwards from this area have been reworked by colluvial processes shortly after their deposition (Schall 2002, Sauer et al. 2016). This post-depositional sedimentary disturbance was likely combined with decalcification, especially during warm periods, and led to the formation of 1-2.5 m thick deposits variously named as *Alblehm*, *Lößlehm* or *Quartär Lehm* (Riek 1957, Gwinner 1989 and Schall 2002). These deposits are also mapped within the part of The Lone Valley which we investigated with the surface mapping and the grain size analysis (Temmler et al. 2003, Mall and Geyer 2004).

Interestingly our results from the grain size analysis downsize considerably the presence of loamy deposits in the Lone Valley (Fig. 4, detail 1). More in detail, only the 7% of the samples we have analyzed might be considered as loamy, namely loam (2.85%), silty loam (2.85%) and clay loam (1.42%). On the opposite the large majority of our samples (77.14%) resulted to be composed of either silty clay or clay silt, while the remaining 15.71% is made of clay. Similarly to silt and clay, among the components of the gravel fraction, quartz and limestone fragments appear to be very present in the investigated area. Based on further statistical and spatial analyses (Fig. 8.4, details 3 and 4), we distinguished 7 main sedimentological units (Fig. 8.5):

1. Unit A: limestone bedrock. Outcrops are located along the hillsides and around the cave sites. Most likely bedrock is laying below the soil on top of the plateau, particularly from Bockstein to Hohlenstein, where with our auger we encountered abrupt refusal at approximately 10-20 cm.

2. Unit B: our data indicate that the soil appears slight more developed (usually not more than 30 cm) along the hillsides. Particularly along the southern hillside of the valley in between Hohlenstein and Bockstein we observed multiple outcrops of cobbles and boulders of limestone.
3. Unit C: in this unit we grouped all the sediments that contain more than the 30% of clay and display high percentage of gravel-sized fragments of Bohnerz. These sediments are mainly located along the hillsides, starting from the plateau down into the valley, and might result from the rework of relict deposits of the Bohnerz formation (Schall 2002, Ufrecth 2008).
4. Unit Da/Db: these sediments are rich in clay, angular gravel of limestone and angular gravel of Bohnerz (particularly Unit Db is richer in Bohnerz fragments). They are located at the foothill, are laterally continuous and very common along the valley. Based on their distribution and angularity, we interpret these sediments as colluvial deposits.
5. Unit E: sediments richer in medium silt and free from gravel-sized fragments, they are localized at the foothill, particularly in the area of Bockstein. We have interpreted these deposits as largely composed of reworked loess (see chapter 4).
6. Unit F: sediments composed of elongated and rounded limestone gravel. Due to their high roundness and location along the valley bottom, we interpret these sediments as potential shallow paleo-channel deposits.
7. Unit G: in these sediment the amount of silt and clay is almost even, they are usually free from gravel and are located in the floodplain. Based on their lithological properties these sediments correspond probably to Holocene alluvial deposits.

8.3 Conclusions

Thanking this surface mapping we traced the paleo-channel deposits buried opposite from Hohlenstein and the loess rich deposits accumulated at the foothill of Bockstein. On these features we focused our further coring and GPR surveys (chapters 3 and 4, respectively). However, the presence of shallow sediments rich in gravel and even coarser fragments of

limestone has limited our capability to investigate large portions of the Lone Valley (for instance the areas we mapped as Unit B).

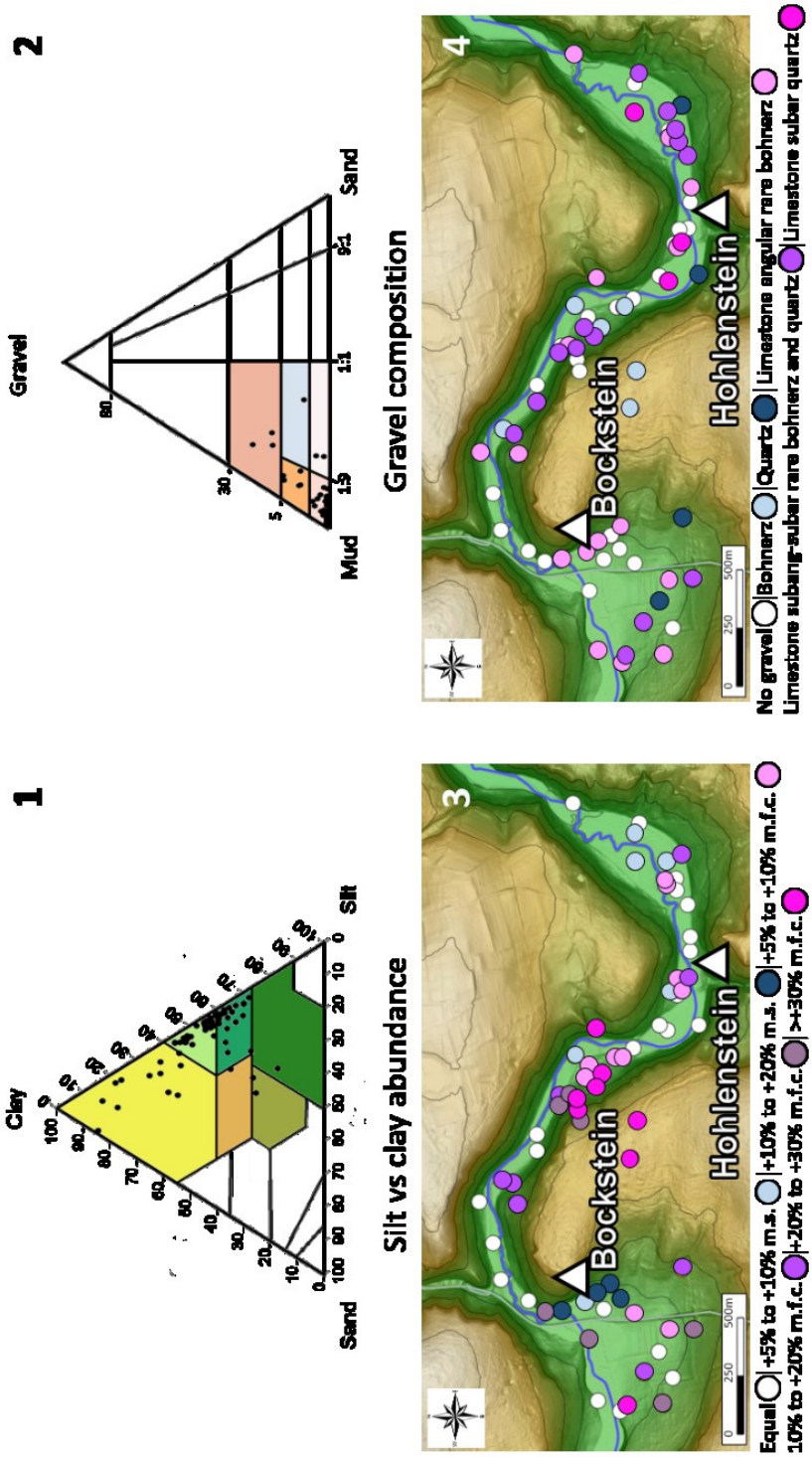

Fig. 8.4. Analysis of the surface mapping data. ***1***, results of the grainsize analysis plotted in a textural triangle graph accordingly to Shepard´s classification system (in GRADISTAT_V8). ***2***, results of the grainsize analysis plotted in a textural triangle graph accordingly to Folk´s classification system (in GRADISTAT_V8). ***3***, spatial analysis based on the silt vs clay abundance. Abbreviations, ***m.s***, medium silt; ***m.f.c***, medium and fine clay. ***4***, spatial analysis based on the gravel composition.

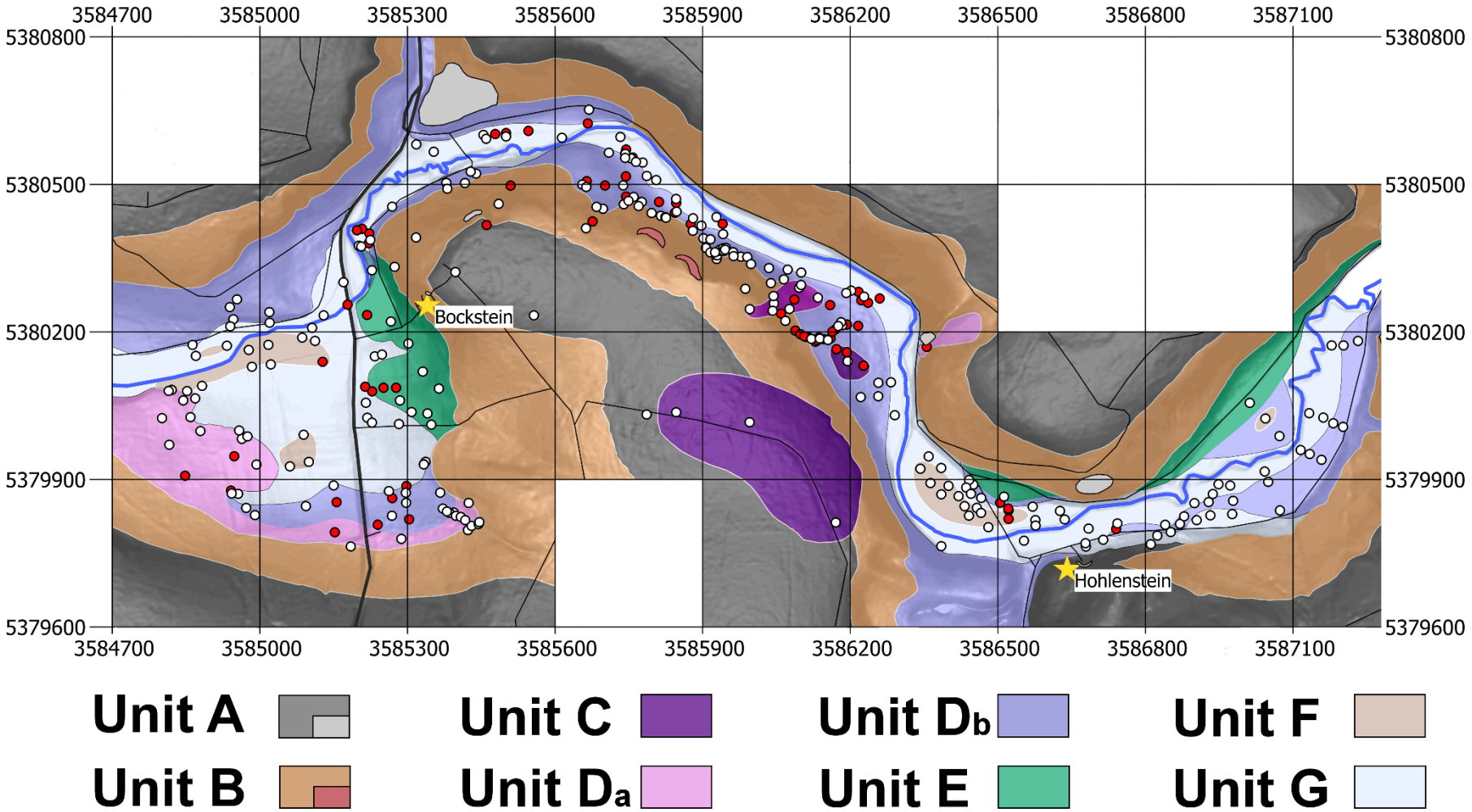

Fig. 8.5. Sedimentological map of the Lone Valley. Dots indicate the location of cores and sediment outcrops. Sediments studied with grain size analysis are marked in red. Details in the text.

References

Goldberg, P., Schiegl, S., Meligne, K., Dayton, C., Conard, N.J., 2003. Micromorphology and Site Formation at Hohle Fels Cave, Swabian Jura, Germany. E&G Quaternary Science Journal 53, pp. 1-25.

Gwinner, M.P., 1989. Erläuterungen zu Blatt 7524 Blaubeuren. Geoilogische Karte von Baden-Württemberg, Stuttgart.

Mall, W. and Geyer, M., 2004. Geologische Karte Von Baden-Württemberg 1:25000, Blatt 7426 Langenau. Landesamt für Geologie, Rohstoffe und Bergbau Baden-Württemberg, Freiburg.

Miller, C.E., 2015. A Tale of Two Swabian Caves – Geoarchaeological Investigations at Hohle Fels and Geißenklösterle. Kerns Verlag Tübingen.

Riek, G., 1957. Drei jungpaläolithische Stationen am Bruckersberg in Giengen an der Brenz. Veröffentlichungen des Staatl.amtes für Denkmalpflege Stuttgart, Verlag Silberburg – Kommissionsverlag, Stuttgart.

Schall, W., 2002. Erläuterungen zum Blatt 7425 Lonsee. Landesamt für Geologie, Rohstoffe und Bergbau Baden-Württemberg.

Temmler, H., Beinroth F., Geyer, M., 2003 Geologische Karte Von Baden-Württemberg 1:25000, Blatt 7427 Sontheim an der Brenz. Landesamt für Geologie, Rohstoffe und Bergbau Baden-Württemberg, Freiburg.

Ufrecht, W., 2008. Evaluating landscape development and karstification of the Central Schwäbische Alb (Souhwest Germany) by fossil record of karst fillings, Zeitschrift für Geomorphologie 52, 4, pp. 417-436.

Appendix III – Descriptions of the Geological Layers

In this appendix we present the description of all the Geological layers (GL) that we distinguished in the course of our analysis of the cores recovered from the Lone and Ach valleys. For each GL we listed survey area (**Location**), **Core**, **Liner**, **Depth** (m) and **Contact** to the lower GL (accordingly to Fitzpatrick 1983; sharp, clear, gradual, diffuse, mixed). We reported amount (Chilingar et al. 1967), color (Munsell soil color chart), texture (Vos et al. 2016) and, when possible, composition of the fine fraction. We listed content (Chilingar et al. 1967) and composition of the coarse fraction. For the gravel we described color, size (ISO 14688-1:2002 standard), shape (Stoops 2003, p. 51), roundness (Bosellini et al. 1989) and frequency (Chilingar et al. 1967) of the components. In the chapters 3, 4 and 5 the roundness of the components has been described with the terms "angular", "subangular", "subrounded", "rounded", and "well rounded". These terms correspond to the values 0.1-0.2, 0.3, 0.4, 0.5-0.6, and 0.7-0.8, respectively, published by Bosellini (et al. 1989). For this Appendix we used this classification system since it allows to describe also more subtle variations in the roundness and it can be more easily summarized in a table.

List of abbreviations used in the following pages
f: fine
m: medium
c: coarse
g: gravel
pb: pebbles
grad. gradual
diff.: diffuse
plan: planar
obl: oblate
prol: prolate
tria: triaxial
equ: equant
w: white
y: yellow
gr: gray
br: brown
b: black
p: pink

Location:	HS	**Core:**	5	**Liner:**	1	**Depth:**	0.66	**GL:**	300	**Contact:**	sharp
	Fine:	95%	10 YR 4/4	Clayey silt with coarse limestone sand							
	Coarse:	5%	Limestone	y	fg	obl	0.4	100%			

Location:	HS	**Core:**	5	**Liner:**	1, 2	**Depth:**	1.98	**GL:**	301	**Contact:**	grad.
	Fine:	15%	10 YR 5/4		Sandy silt with little coarse to fine calcite sand						
	Coarse:	85%	Limestone		y	fg	obl			0.4	50%
			Chert		r	fg	tria			0.1	1 fr
			Limestone		w to y	mg	obl, tria			0.4 to 0.6	40%
			Limestone		dark gr	mg	tria			0.1	2%
			Limestone		w	mg	obl, tria			0.3	8%
			Some of the limestones gravel has black possibly iron-manganese nodules (sampled).								
Location:	HS	**Core:**	5	**Liner:**	2	**Depth:**	2.12	**GL:**	302	**Contact:**	sharp
	Fine:	95%	10 YR 7/3		Silty clay						
	Coarse:	5%	Limestone		gr	fg	obl, prol			0.8	45%
			Bohnerz		b	fg	prol, tria			0.3	few fr.
			Limestone		gr, br	mg	obl, prol, tria			0.5 to 0.9	ca. 55%
Location:	HS	**Core:**	5	**Liner:**	2	**Depth:**	2.30	**GL:**	303	**Contact:**	sharp
	Fine:	0%	/		/						
	Coarse:	100%	Limestone		w	fg	plan, obl, prol, tria			0.2 to 0.5	100%
Location:	HS	**Core:**	5	**Liner:**	2	**Depth:**	2.40	**GL:**	304	**Contact:**	sharp
	Fine:	90%	10 YR 7/3		Sandy clay						
	Coarse:	5%	Limestone		gr	fg, mg	equ			0.8	40%
			Bohnerz		b	fg, mg	obl, prol, tria			0.9	2%
			Limestone		gr	mg	obl, prol, tria			0.4	58%
			Chert		p	mg	plan, prol			0.5	few fr.
			chert has been sampled								
Location:	HS	**Core:**	5	**Liner:**	3	**Depth:**	2.97	**GL:**	305	**Contact:**	sharp
	Fine:	10%	10 YR 5/4		Sand						
	Coarse:	90%	Bohnerz		black	fg	tria, equ			0.7 to 0.9	10%
			Limestone		gr to y	fg	tria, obl			0.4 to 0.7	50%
			Limestone		gr to y	mg	tria, prol			0.4 to 0.5	40%
Location:	HS	**Core:**	5	**Liner:**	3	**Depth:**	3.25	**GL:**	306	**Contact:**	sharp
	Fine:	10%	Silty clay with little sand of bohnerz and calcite. The upper part is darker in colour (10YR 3/3); the lower part is richer in medium and fine gravel also richer in clay and is lighter in colour (10YR 5/6). The transition is around -3.12 m.								
	Coarse:	90%	Limestone		gr, y, w	fg	tria			0.3	60%
			Limestone		gr, y, w	mg	tria			0.2 (rare 0.6)	40%
Location:	HS	**Core:**	5	**Liner:**	3	**Depth:**	3.44	**GL:**	307	**Contact:**	sharp

Fine:	15%	10 YR 5/6	Silty clay with little medium to coarse sand of calcite and bohnerz					
Coarse:	85%	Limestone	y	fg	obl, tria	0.5, 0.6	10%	
		Limestone	y, gr	mg	obl, tria	0.3, 0.4	30%	
		Limestone	w, gr	mg	tria	0.3	60%	
		Limestone	w	mg	plan	0.3	few fr.	

Location:	HS	**Core:**	5	**Liner:**	3	**Depth:**	3.54	**GL:** 308	**Contact:**	sharp
Fine:	0%	/		/						
Coarse:	100%	Limestone		w	fg	tria, plan, prol	0.1 to 0.3	10%		
		Limestone		w	mg, cg	tria	0.1 to 0.3	70%		
		Bohnerz		b	fg	equ	0.9	20%		

Location:	HS	**Core:**	5	**Liner:**	3	**Depth:**	3.60	**GL:** 309	**Contact:**	sharp
Fine:	5%	10 YR 6/4	Silt with little coarse sand of claicte and Bohnerz							
Coarse:	95%	Limestone		w	fg	tria, obl	0.3, 0.4	80%		
		Limestone		w	mg	tria, obl	0.3, 0.4	20%		

Location:	HS	**Core:**	5	**Liner:**	4	**Depth:**	4.18	**GL:** 310	**Contact:**	clear
Fine	60%	10 YR 5/6	Silt with little medium sand of calcite and Bohnerz							
Coarse	40%	Limestone		y	fg	tria	0.5	35%		
		Limestone		y	mg	tria	0.2 to 0.4	65%		
		Bohnerz		b	fg	tria	0.9	few fr		

Location:	HS	**Core:**	5	**Liner:**	4	**Depth:**	4.49	**GL:** 311	**Contact:**	sharp
Fine:	30%	10 YR 6/4	Silt with calcite and Bohnerz sand, in particular the last 4 cm are characterized by an increasing in medium and fine sand.							
Coarse:	70%	Limestone		y	fg	tria, prol	0.3, 0.4	30%		
		Limestone		y	mg	tria, obl	0.4, 0.5	70%		
		Quartz		w, p	mg	tria	o.6	1 fr		
		Limestone		w, p	mg	tria, obl	0.2, 0.3	few fr.		
		Bohnerz		b	mg	tria	0.4	1 fr.		

Location:	HS	**Core:**	5	**Liner:**	4	**Depth:**	4.54	**GL:** 312	**Contact:**	grad.
Fine:	95%	Silty clay with rare medium sand of calcite and quartz. The main color is 7.5 YR 5/6, reddish zones are 5 YR 5/6								
Coarse:	5%	Limestone		y	fg	tria	0.5, 0.6	very rare		
		Limestone		b	cg	tria	0.3	1 fr		

Location:	HS	**Core:**	5	**Liner:**	4	**Depth:**	4.76	**GL:** 313	**Contact:**	grad.
Fine:	0%	/		/						
Coarse:	100%	Limestone		w	cg, pb	nd	0.3	100%		

Location:	HS	**Core:**	5	**Liner:**	5	**Depth:**	5.14	**GL:** 314	**Contact:**	grad.
Fine:	80%	10 YR 5/6	Silty clay. Small clay aggregates from the lower GL 315							
Coarse:	20%	Limestone		nd	fg	obl	0.3, 0.4	60%		
		Limestone		nd	mg	tria	0.2, 0.3	40%		

Location:	HS	**Core:**	5	**Liner:**	5	**Depth:**	5.35	**GL:**	315	**Contact:**	sharp
	Fine:	95%	7.5 R 4/6		Clay with coarse sand of black calcite, coming from the lower GL 316. Zoning and veins of different color: 10YR 6/6 and 2.5 YR 7/3. In particular two veins are coming downwards from the contact with GL 314 (crack, wedge?).						
	Coarse:	5%	Limestone		b	fg	obl, tria		0.3, 0.4		40%
			Limestone		b	mg	obl, tria		0.3-0.4		60%
Location:	HS	**Core:**	5	**Liner:**	5	**Depth:**	5.39	**GL:**	316	**Contact:**	sharp
	Fine:	20%	10 YR 6/6		Silty clay						
	Coarse:	80%	Limestone		b	fg	obl		0.3, 0.4		10%
			Limestone		b	mg	tri		0.2, 0.3		90%
Location:	HS	**Core:**	5	**Liner:**	5	**Depth:**	5.67	**GL:**	317	**Contact:**	sharp
	Fine:	40%	10 YR 6/6		Silty clay with increasing content of coarse (calcite?) sand towards the bottom. Zoning and aggregates (sandy/silty clay) of different colors, 10 YR 8/1 and 2.5Y 7/3						
	Coarse:	60%	Limestone		w, y, b	fg	obl, tria		0.3 to 0.5		40%
			Limestone		w, y, b	mg	tria		0.4		60%
Location:	HS	**Core:**	5	**Liner:**	5	**Depth:**	5.74	**GL:**	318	**Contact:**	sharp
	Fine:	20%	10 YR 5/8		Silty clay with medium and fine sand of calcite (?)						
	Coarse:	80%	Limestone		y	fg	tria		0.4		60%
			Limestone		y	mg	equ, tria		0.5		40%
Location:	HS	**Core:**	5	**Liner:**	5	**Depth:**	5.80	**GL:**	319	**Contact:**	grad.
	Fine:	5%	10 YR 5/6		Silty clay with rare medium sand of white-yellowish calcite						
	Coarse:	95%	Limestone		w	fg to cg	tria, obl		0.3, 0.4		100%
Location:	HS	**Core:**	5	**Liner:**	5	**Depth:**	5.84	**GL:**	320	**Contact:**	sharp
	Fine:	5%	10 YR 5/6		Silty clay with rare coarse sand of yellowish calcite						
	Coarse:	95%	Limestone		fg to cg		as GL 319				
Location:	HS	**Core:**	5	**Liner:**	5	**Depth:**	5.92	**GL:**	321	**Contact:**	sharp
	Fine	5%	10 YR 4/6		as GL 320						
	Coarse	95%	Limestone		y	mg	tria		0.5		100%
Location:	HS	**Core:**	5	**Liner:**	6	**Depth:**	6.12	**GL:**	322	**Contact:**	nd
	Fine:	30%	Mainly silty clay (10 YR 5/6) with rare coarse sand of calcite. Zoning with clay aggregates and various matrix color, 2.5 YR 5/6, 2.5Y 7/4.								
	Coarse:	70%	Limestone		y	fg	tria, obl		0.5		40%
			Limestone		y	mg	tria		0.3-0.4		60%
Location:	HS	**Core:**	9	**Liner:**	1	**Depth:**	0.62	**GL:**	1	**Contact:**	grad.

	Fine	99.1%	10 YR 4/3; from -0.5, 10 YR 4/4		Clayey silt with medium sand of yellowish limestone				
	Coarse	0.1%	Pottery	nd	fg	nd	nd	1 fr.	

Location:	HS	**Core:**	9	**Liner:**	1	**Depth:**	0.70	**GL:**	2a	**Contact:**	sharp
	Fine:	5%	10 YR 4/4		Clayey silt with medium to fine sand of white-yellow limestone						
	Coarse:	95%	Limestone		w		fg	tria		0.3	20%
			Limestone		w		mg	tria		0.3	80%

Location:	HS	**Core:**	9	**Liner:**	1	**Depth:**	0.74	**GL:**	2b	**Contact:**	sharp
	Fine:	30%	10 YR 4/3		Silty clay richer in medium to fine sand of white-yellow limestone						
	Coarse:	70%	Limestone		w		mg	tria, obl, prol		0.5 to 0.7	100%

Location:	HS	**Core:**	9	**Liner:**	1	**Depth:**	0.79	**GL:**	2c	**Contact:**	clear
	Fine:	20%	10 YR 4/3		Silty clay						
	Coarse:	80%	Limestone		w		fg	tria		0.5	30%
			Limestone		w		mg	tria		0.6	70%

Location:	HS	**Core:**	9	**Liner:**	1	**Depth:**	0.89	**GL:**	2d	**Contact:**	clear
	Fine:	20%	7.5 YR 4/4		Sandy silty with medium to fine sand of white-yellow limestone						
	Coarse:	80%	Limestone		w		fg	obl, equ		0.5	30%
			Limestone		w		mg	obl, equ		0.6	70%

Location:	HS	**Core:**	9	**Liner:**	1	**Depth:**	0.92	**GL:**	2e	**Contact:**	sharp
	Fine:	5%	10 YR 6/4		Sand						
	Coarse:	90%	Limestone		w		fg	obl, equ		0.5	30%
			Limestone		w		mg	obl, equ		0.6	70%

Location:	HS	**Core:**	9	**Liner:**	1	**Depth:**	1.10	**GL:**	2f	**Contact:**	clear
	Fine:	40%	10 YR 5/4		Silty sand						
	Coarse:	60%	Limestone		w, y		fg	tria, prol		0.4 to 0.7	30%
			Quartz		w		fg	tria		0.2	few fr.
			Limestone		w, y		mg	obl, tria		0.4 to 0.6	70%

Location:	HS	**Core:**	9	**Liner:**	1	**Depth:**	1.14	**GL:**	3	**Contact:**	sharp
	Fine:	10%	10 YR 5/4		Sand						
	Coarse:	90%	Limestone		w		fg	obl, tria		0.2	65%
			Limestone		w		mg	obl, tria		0.4, 0.3	35%

Location:	HS	**Core:**	9	**Liner:**	1	**Depth:**	1.22	**GL:**	4	**Contact:**	clear
	Fine:	20%	10 YR 7/3		Sandy clay with coarse sand of calcite and Bohnerz						
	Coarse:	80%	Limestone		w		fg	tria, prol		0.7	80%
			Limestone		w		mg	obl, tria		0.4, 0.5	20%

Location:	HS	**Core:**	9	**Liner:**	2	**Depth:**	1.64	**GL:**	5	**Contact:**	clear

Fine:	20%	10 YR 5/4	Silty sand with coarse to fine calcite sand					
Coarse:	80%	Limestone	y	fg	obl, tria	0.4	39%	
		Bohnerz	b	fg	equ	0.8	0.5%	
		Cherty limestone	gr	fg	obl	0.2	0.5%	
		Limestone	w, gr	mg	obl, tria, prol	0.3 to 0.5	60%	

Location:	HS	**Core:**	9	**Liner:**	2	**Depth:**	2.15	**GL:**	6	**Contact:** clear
Fine:	10%	10 YR 6/4	Silty sand, more coarse sand than previous sediment. Also Bohnerz in the sand fraction							
Coarse:	90%	Limestone	y	fg	tria	0.4, 0.5	30%			
		Bohnerz	b	fg	tria	0.4	5%			
		Limestone	w, gr	mg	tria	0.2, 0.4	65%			

Location:	HS	**Core:**	9	**Liner:**	2	**Depth:**	2.44	**GL:**	7	**Contact:** nd
Fine:	10%	10 YR 5/6	Silty sand							
Coarse:	90%	Limestone	y	fg	tria	0.4, 0.5	40%			
		Limestone	w, gr	mg	tria	0.2, 0.4	60%			

Location:	HS	**Core:**	12	**Liner:**	1	**Depth:**	0.31	**GL:**	19	**Contact:** diff.
Fine:	100%	10 YR 3/2	Clayey silt with medium to coarse sand of calcite							
Coarse:	0%	/	/	/	/	/	/			

Location:	HS	**Core:**	12	**Liner:**	1	**Depth:**	0.53	**GL:**	20	**Contact:** clear
Fine:	40%	10 YR 4/3	Clayey silt with coarse sand of calcite							
Coarse:	60%	Limestone	y, w	fg	tria	0.2	30%			
		Limestone	y, w	mg	tria	0.1, 0.2	70%			

Location:	HS	**Core:**	12	**Liner:**	1	**Depth:**	0.69	**GL:**	21	**Contact:** sharp
Fine:	70%	7.5 YR 4/4	Clay with little silt and coarse to fine sand of calcite and Bohnerz							
Coarse:	30%	Limestone	y	fg	tria, obl	0.2 to 0.4	40%			
		Limestone	y	mg	tria, obl	0.2	60%			
		Bohnerz	b	mg	equ	0.8	1 fr			

Location:	HS	**Core:**	12	**Liner:**	1	**Depth:**	0.71	**GL**	22	**Contact:** sharp
Fine:	100%	10 YR 4/3	Silt							
Coarse:	0%	/	/	/	/	/	/			

Location:	HS	**Core:**	12	**Liner:**	1	**Depth:**	1.01	**GL:**	23	**Contact:** diff.
Fine:	75%	10 YR 4/6	Sandy silt with clay. The sand is medium to fine and is composed of calcite and Bohnerz							
Coarse:	25%	Limestone	y, w	fg	tria	0.2 to 0.3	60%			
		Bohnerz	b	fg	obl, tria	0.8	1 fr			
		Limestone	y, w	mg	tria	0.7 to 0.3	40%			

Location:	HS	**Core:**	12	**Liner:**	1	**Depth:**	1.22	**GL:**	24	**Contact:** diff.

	Fine:	60%	10 YR 5/6	Sandy silt with little clay. In comparison with GL 23, GL 24 is richer in medium sand.					
	Coarse:	40%	Limestone	y	fg	tria, obl	0.3	40%	
			Limestone	y	mg	tria	0,1-0.2	60%	

Location:	HS	**Core:**	12	**Liner:**	2	**Depth:**	1.55	**GL:**	25	**Contact:**	clear
	Fine:	20%	10 YR 5/6	Clayey silt with coarse sand of calcite							
	Coarse:	80%	Limestone	y	fg	tria	0.3	20%			
			Limestone	y	mg	tria	0.2, 0.3	80%			

Location:	HS	**Core:**	12	**Liner:**	2	**Depth:**	1.81	**GL:**	26	**Contact:**	clear
	Fine:	10%	7.5 YR 4/6	Sandy clay with coarse sand of calcite							
	Coarse:	90%	Limestone	y	fg	obl, tria	0.2, 0.3	30%			
			Limestone	y	mg	obl, tria	0.2, 0.4	70%			

Location:	HS	**Core:**	12	**Liner:**	2	**Depth:**	2.22	**GL:**	27	**Contact:**	clear
	Fine:	70%	10 YR 5/4	Sandy silty.							
	Coarse:	30%	Limestone	y	fg	tria	0.2, 0.3	40%			
			Limestone	y	mg	tria	0.1 to 0.3	60%			

Location:	HS	**Core:**	12	**Liner:**	2	**Depth:**	2.44	**GL:**	28	**Contact:**	clear
	Fine:	85%	10 YR 5/4	Clayey sand. At - 2.33 m large sandy area 2.5 Y 6/4 in color							
	Coarse:	15%	Limestone	y	fg	tria	0.2, 0.3	40%			
			Limestone	y	mg	tria	0.2, 0.3	60%			

Location:	HS	**Core:**	12	**Liner:**	3	**Depth:**	2.98	**GL:**	29	**Contact:**	grad.
	Fine:	85%	10 YR 5/6	Alternating laminations of clayey silt and silty clay. Main matrix color reported on the left, laminations are also 2.5 Y 6/4							
	Coarse:	15%	Limestone	y	fg	tria	0.4, 0.5	10%			
			Limestone	y	mg	obl, tria	0.1 to 0.4	90%			

Location:	HS	**Core:**	12	**Liner:**	3	**Depth:**	3.16	**GL:**	30	**Contact:**	grad.
	Fine:	60%	10 YR 6/4	Clayey silt with medium and coarse sand of limestone and Bohnerz							
	Coarse:	40%	Limestone	y, b	fg	tria, prol	0.8	40%			
			Limestone	y, b	mg	obl, tria	0.4, 0.6, 0.8	60%			
			The gravel display some graded bedding.								

Location:	HS	**Core:**	12	**Liner:**	3	**Depth:**	3.49	**GL:**	31	**Contact:**	sharp
	Fine:	30%	10 YR 4/6	Silty sand, of calcite and Bohnerz.							
	Coarse:	70%	Limestone	y	fg	tria, obl	0.5, 0.6	20%			
			Limestone	y, b, br	mg	tria	0.3, 0.4, 0.6	80%			
			Still some grading. Down to -3.39 the sediment is richer in medium gravel, towards the bottom of the unit it is richer in fine gravel and sand.								

Location:	HS	**Core:**	12	**Liner:**	3	**Depth:**	3.53	**GL:**	32	**Contact:**	sharp

Fine:	10%	7.5 YR 4/6	GL 32 is like a sandwich. Upper part and lower part are silty clayey (10 YR 4/6) with little MG. The central part is a way much richer in FG and is more reddish 7.5 YR 4/6.	
Coarse:	90%			

Location:	HS	**Core:**	12	**Liner:**	3, 4	**Depth:**	4.20	**GL:**	33	**Contact:**	sharp
Fine:	30%	nd	Silty clay								
Coarse:	70%	Limestone	y	fg	tria	0.2, 0.3	20%				
		Limestone	y	mg	tria	0.2 to 0.6	60%				
		The medium gravel is well sorted being smaller than 1 cm.									

Location:	HS	**Core:**	12	**Liner:**	4	**Depth:**	4.40	**GL:**	34	**Contact:**	clear
Fine:	95%	10 YR 5/6	Silty clay. Matrix rich in potential, soft iron nodules								
Coarse:	5%	Limestone	y	fg	tria	0.3-0.4	100%				

Location:	HS	**Core:**	12	**Liner:**	4	**Depth:**	4.55	**GL:**	35	**Contact:**	clear
Fine:	40%	10 YR 5/6	Clay with coarse sand of calcite								
Coarse:	60%	Limestone	y	fg	obl, tria	0.3	23%				
		Limestone	y	mg	tri	0.2 to 0.6	70%				
		Bohnerz	b, r	mg	tria	0.3	ca.7%				
		Cherty limestone	gr, y	mg	tria	0.2	few fr.				

Location:	HS	**Core:**	12	**Liner:**	4	**Depth:**	4.66	**GL:**	36	**Contact:**	clear
Fine:	30%	10 YR 6/6	Sandy silty. Fine to coarse sand of calcite and Bohnerz								
Coarse:	70%	Limestone	y	fg	tria	0.3	30%				
		Limestone	y	mg	tria	0.3 to 0.5	70%				
		Gravel is well sorted, largely smaller than 1 cm									

Location:	HS	**Core:**	12	**Liner:**	4	**Depth:**	4.68	**GL:**	37	**Contact:**	sharp
Fine:	60%	5YR 4/6	Medium to coarse sand of calcite, quartz, Bohnerz								
Coarse:	40%	Limestone	y,g	mg	tria	0.3 to 0.5	100%				

Location:	HS	**Core:**	12	**Liner:**	4	**Depth:**	4.70	**GL:**	38	**Contact:**	sharp
Fine:	100%	7.5 YR 3/3	Medium to fine sand of quartz and calcite with little silt								
Coarse:	0%	/	/	/	/	/	/				

Location:	HS	**Core:**	12	**Liner:**	4	**Depth:**	4.72	**GL:**	39	**Contact:**	sharp
Fine:	100%	7.5 YR 4/4	Clayey silt with medium to fine calcite sand								
Coarse:	0%	/	/	/	/	/	/				

Location:	HS	**Core:**	12	**Liner:**	4	**Depth:**	4.73	**GL:**	40	**Contact:**	sharp
Fine:	100%	10 YR 4/6	Silty fine to medium sand of calcite and quartz.								
Coarse:	0%	/	/	/	/	/	/				

Location:	HS	**Core:**	12	**Liner:**	4	**Depth:**	4.77	**GL:**	41	**Contact:**	sharp
Fine:	20%	10 YR 3/3	Sandy silt. Sand composed of fine to coarse sand-sized grains of quartz.								

Coarse:	80%	Limestone	y	fg	tria	0.2 to 0.4	18%
		Quartz	nd	fg	tria	0.2	1 fr.
		Iron nodules	b	fg	nd	n.d	2%
		Limestone	y	mg	tria	0.2 to 0.4	80%

Location:	HS	**Core:**	12	**Liner:**	4, 5	**Depth:**	5.02	**GL:**	42	**Contact:**	clear
Fine:	15%	10 YR 4/6	Clayey silt								
Coarse:	85%	Limestone	w,y	fg	tria	0.4 to 0.6	25%				
		Bohnerz	b	fg	obl, tria	0.3	5%				
		Limestone	w,y	mg	obl, tria	0.4 to 0.6	70%				

Location:	HS	**Core:**	12	**Liner:**	5	**Depth:**	5.17	**GL:**	43	**Contact:**	sharp
Fine:	60%	10 YR 4/6	Sandy clay. Fine to Coarse sand of calcite and Bohnerz.								
Coarse:	40%	Limestone	y, b	fg	tria	0.5	28%				
		Bohnerz	b	fg	equ	0.8	2%				
		Limestone	y, b	mg	tria, obl	0.4	70%				
		Gravel well sorted, largely smaller than 1 cm.									

Location:	HS	**Core:**	12	**Liner:**	5	**Depth:**	5.25	**GL:**	44	**Contact:**	sharp
Fine:	95%	In-between 10 YR 5/6 and 2.5 Y 6/6.	Silty clay with few reddish (7.5 YR 5/6) laminations.								
Coarse:	5%	Limestone	y	fg	obl, tria	0.3	100%				

Location:	HS	**Core:**	12	**Liner:**	5	**Depth:**	5.36	**GL:**	45	**Contact:**	sharp
Fine:	95%	In-between 10 YR 5/6 and 2.5 Y 6/6.	Silty clay.								
Coarse:	80%	Limestone	y	fg	tria	0.2, 0.3	10%				
		Limestone	y, w	mg	tria	0.2, 0.3	90%				

Location:	HS	**Core:**	12	**Liner:**	5	**Depth:**	5.60	**GL:**	46	**Contact:**	sharp
Alteration of sandy gravels and gravelly sands. Gravels generally fine, rare medium; subangular (0,3 - 0,4). Components of the sand are limestone, quartz and bohnerz											

Location:	HS	**Core:**	12	**Liner:**	5	**Depth:**	5.70	**GL:**	47	**Contact:**	nd
Fine:	30%	10 YR 5/6	Sandy silt								
Coarse:	70%	Limestone	y	fg	tria	0.4	15%				
		Bohnerz	b	fg	equ	0.6	1 fr				
		Limestone	y	mg	tria	0.5, 0.6	60%				
		Limestone	w, y	cg	tria	0.4	25%				

Location:	HS	**Core:**	15	**Liner:**	1	**Depth:**	0.48	**GL:**	48	**Contact:**	diff
Fine:	20%	10 YR 3/6	Silty clay								
Coarse:	80%	Limestone	y	fg, mg	tria	0.2	100%				

Location:	HS	**Core:**	15	**Liner:**	1	**Depth:**	0.95	**GL:**	49	**Contact:**	clear
Fine:	20%	10 YR 5/6	Sandy silt								
Coarse:	80%	Limestone	w, y	fg	tria	0.2, 0.1	40%				
		Limestone	w, y	mg	tria	0.2, 0.1	60%				

Location:	HS	**Core:**	15	**Liner:**	1, 2	**Depth:**	1.51	**GL:**	50	**Contact:**	sharp
	Fine:	15%	10 YR 4/6		Silty clay with medium to coarse calcite sand						
	Coarse:	85%	Limestone		w, y	fg	tria			0.2, 0.1	70%
			Limestone		w, y	mg	tria			0.2, 0.1	10%
			Limestone		w, y	cg	tria			0.3	20%
Location:	HS	**Core:**	15	**Liner:**	2	**Depth:**	1.64	**GL:**	51	**Contact:**	sharp
	Fine:	90%	10 YR 3/6		Silty clay with possibly secondary calcite pedofeatures.						
	Coarse:	10%	Chert		w, b	mg	obl			0.1	80%
			Limestone		y	mg	nd			nd	20%
Location:	HS	**Core:**	15	**Liner:**	2	**Depth:**	1.74	**GL:**	52	**Contact:**	clear
	Fine:	5%	10 YR 3/6		Clayey silt with medium to coarse sand of calcite and Bohnerz.						
	Coarse:	95%	Limestone		y	fg	tria			0.4, 0.5	40%
			Limestone		y	mg	tria, obl			0.2 to 0.4	60%
Location:	HS	**Core:**	15	**Liner:**	2	**Depth:**	1.78	**GL:**	53	**Contact:**	clear
	Fine:	60%	10 YR 4/6		Sandy silt, medium sand of calcite and Bohnerz.						
	Coarse:	40%	Limestone		y	fg	tria			0.6	18%
			Bohnerz		b	fg	obl, tria			0.2	1%
			Limestone		y, gr	mg	tria, obl			0.2	80%
			Chert		y	mg	triax			0.4, 0.5	1%
Location:	HS	**Core:**	15	**Liner:**	2	**Depth:**	1.93	**GL:**	54	**Contact:**	sharp
	Fine:	5%	10 YR 3/4		Sandy silt, medium to coarse sand of calcite, quartz and Bohnerz.						
	Coarse:	95%	Limestone		y	fg	tria			0.5 to 0.7	50%
			Limestone		y, w	mg	tria			0.3, 0.4	30%
			Limestone		w	cg	oblate			0.5	20%
Location:	HS	**Core:**	15	**Liner:**	2	**Depth:**	2.27	**GL:**	55	**Contact:**	diff.
	Fine:	70%	10 YR 5/6		Silt with rare medium sand of bohnerz and quartz.						
	Coarse:	30%	Limestone		nd	fg	tria			0.2, 0.3	40%
			Limestone		nd	mg	obl, tria			0.3	60%
Location:	HS:	**Core:**	15	**Liner:**	2	**Depth:**	2.44	**GL:**	56	**Contact:**	nd
	Fine	95%	10 YR 5/6		Silt.						
	Coarse	5%	Limestone		nd	fg	tria			0.3	60%
			Limestone		nd	mg	obl, tria			0.3	40%
Location:	HS	**Core:**	15	**Liner:**	3	**Depth:**	2.82	**GL:**	57	**Contact:**	sharp
	Fine:	90%	10 YR 5/6		Clayey silt.						
	Coarse:	10%	Limestone		y	fg	tria, prol			0.2	100%
Location:	HS	**Core:**	15	**Liner:**	3	**Depth:**	3.02	**GL:**	58	**Contact:**	sharp
	Fine:	10%	nd		Fine to medium sand of calcite, quartz and Bohnerz with rare silt.						
	Coarse:	90%	Limestone		w, y	fg	tria			0.5	10%

			Limestone	w, y	mg	tria	0.3 to 0.5	30%		
			Limestone	w, y	cg	tria	0.3	60%		

Location:	HS	**Core:**	15	**Liner:**	3	**Depth:**	3.16	**GL:**	59	**Contact:** clear
	Fine:	10%	nd	Fine to medium sand of calcite, quartz and Bohnerz with rare silt.						
	Coarse:	90%	Limestone	w, y	fg	tria	0.5	10%		
			Limestone	w, y	mg	tria	0.3 to 0.5	30%		
			Limestone	w, y	cg	tria	0.3	60%		

Location:	HS	**Core:**	15	**Liner:**	3, 4	**Depth:**	4.03	**GL:**	60	**Contact:** clear
	Fine:	5%	10 YR 5/6 and 4/6	Fine to coarse sand of calcite, Bohnerz and quartz						
	Coarse:	95%	Limestone	y	fg	tria, obl	0.6	18%		
			Bohnerz	b	fg	tria, equ	0.7, 0.8	2%		
			Limestone	w, y	mg	tria, obl	0.6, 0.7	80%		

Location:	HS	**Core:**	15	**Liner:**	4	**Depth:**	4.42	**GL:**	61	**Contact:** grad
	Fine:	30%	10 YR 5/6	Silt with rare fine to medium sand of calcite and Bohnerz						
	Coarse:	70%	Limestone	y	fg	tria, obl	0.6, 0.7, rare 0.3	15%		
			Bohnerz	b	mg	tria	0.7	5%		
			Limestone	y, b	mg	tria, obl, prol	0.5 to 0.7	80%		

Location:	HS	**Core:**	15	**Liner:**	4	**Depth:**	4.51	**GL:**	62	**Contact:** clear
	Fine:	15%	10 YR 5/6	Silty sand, the latter is composed of calcite and Bohnerz						
	Coarse:	85%	Limestone	y	fg	tria, obl	0.5	19%		
			Bohnerz	b	fg	tria	0.5	1%		
			Limestone	y, b	mg	obl	0.6, 0.7	80%		

Location:	HS	**Core:**	15	**Liner:**	4	**Depth:**	4.66	**GL:**	63	**Contact:** sharp
	Fine:	5%	7.5 YR 5/4; 10 YR 5/4	Silt clay with coarse sand of calcite and Bohnerz.						
	Coarse:	95%	Limestone	y	fg	tria, obl	0.3, 0.2	60%		
			Limestone	y	mg	tria	0.3, 0.2	40%		
			Most of the limestone gravel is between 0.6 and 1 cm large.							

Location:	HS	**Core:**	15	**Liner:**	4	**Depth:**	4.76	**GL:**	64	**Contact:** sharp
	Fine:	30%	7.5 YR 4/6; 10 YR 4/6	Silty clay						
	Coarse:	70%	Limestone	y	fg	tria	0.2, 0.3	40%		
			Limestone	y	mg	tria	0.2 to 0.6	60%		

Location:	HS	**Core:**	15	**Liner:**	4	**Depth:**	4.88	**GL:**	65	**Contact:** nd
	Fine:	95%	10 YR 5/6	Silt clay, displaying medium to coarse sand-sized aggreagtes of silty clay 5YR 5/6 in color.						
	Coarse:	5%	Limestone	w, y	mg	tria, obl	0.5	100%		

Location:	HS	**Core:**	15	**Liner:**	5	**Depth:**	5.07	**GL:**	66	**Contact:**	sharp
	Fine:	5%	10 YR 5/6		Sandy silt, composed of calcite and Bohnerz.						
	Coarse:	95%	Limestone		y	fg	tria,		0.4		100%

Location:	HS	**Core:**	15	**Liner:**	5	**Depth:**	5.36	**GL:**	67	**Contact:**	clear
	Fine:	70%	10 YR 4/6		Sandy silt. Sand coarser than previous GL, similar composition.						
	Coarse:	30%	Limestone		y	fg	tria, obl		0.3, 0.6		30%
			Limestone		y	mg	tria		0.3, 0.2		69%
			Bohnerz		b	mg	tria		0.3		1%

Location:	HS	**Core:**	15	**Liner:**	5	**Depth:**	5.80	**GL:**	68	**Contact:**	nd
	Fine:	10%	10 YR 6/6		Coarse silty sand of calcite and Bohnerz.						
	Coarse:	90%	Limestone		y	fg	tria		0.3, 0.2, rare 0.4		30%
			Limestone		y	mg	tria		0.4 to 0.6		70%

Location:	HS	**Core:**	24	**Liner:**	1	**Depth:**	0.93	**GL:**	90	**Contact:**	diff.
	Fine:	97%	10 YR 4/3 (upper part), 7.5 YR 4/6 (lower part)		Clayey silt to silty clay						
	Coarse:	3%	Limestone		w	mg	tria		0.3, 0.2		100%

Location:	HS	**Core:**	24	**Liner:**	1	**Depth:**	1.13	**GL:**	91	**Contact:**	sharp
	Fine:	40%	10 YR 5/4		Silt with rare coarse calcite sand						
	Coarse:	60%	Limestone		y	fg	tria		0.3, 0.2		20%
			Limestone		y	mg	tria		0.2		80%

Location:	HS	**Core:**	24	**Liner:**	1, 2	**Depth:**	1.62	**GL:**	92	**Contact:**	sharp
	Fine:	40%	10 YR 5/4		Silt with rare coarse calcite sand						
	Coarse:	60%	Limestone		y	fg	tria		0.3, 0.2		20%
			Limestone		y	mg	tria		0.2		60%
			Limestone		y	cg	nd		nd		20%

Location:	HS	**Core:**	24	**Liner:**	2	**Depth:**	1.67	**GL:**	93	**Contact:**	grad.
	Fine:	80%	10 YR 5/6		Silt with rare coarse calcite sand						
	Coarse:	20%	Limestone		y	fg	tria		0.3		30%
			Limestone		y	mg	tria		0.2, 0.3		70%

Location:	HS	**Core:**	24	**Liner:**	2	**Depth:**	1.93	**GL:**	94	**Contact:**	clear.
	Fine:	15%	10 YR 4/6		Clayey silt with rare medium calcite sand.						
	Coarse:	85%	Limestone		y	fg	tria, obl		0.2, 0.3		30%
			Limestone		y, w	mg	tria, equ		0.2		70%

Location:	HS	**Core:**	24	**Liner:**	2	**Depth:**	2.05	**GL:**	95	**Contact:**	sharp
	Fine:	5%	7.5 YR 4/6		Clayey silt with rare medium to fine calcite sand.						

Coarse	95%	Limestone	y	fg	tria	0.3, 0.4	20%
		Limestone	y	mg	tria, obl	0.2, 0.3	80%

Location:	HS	**Core:**	24	**Liner:**	2	**Depth:**	2.08	**GL:**	96	**Contact:**	clear
Fine:	70%	10 YR 4/6				Silty clay.					
Coarse:	30%	Limestone		y		mg	tria, obl		0.4		100%

Location:	HS	**Core:**	24	**Liner:**	2	**Depth:**	2.34	**GL:**	97	**Contact:**	sharp
Fine:	30%	10 YR 4/6				Silty clay with coarse calcite sand. Roots from modern vegetation.					
Coarse:	70%	Limestone		y		fg	tria		0.3		40%
		Limestone		y		mg	tria		0.2		60%
		This layer exhibits downward increasing grain size.									

Location:	HS	**Core:**	24	**Liner:**	2, 3	**Depth:**	3.01	**GL:**	98	**Contact:**	sharp
Fine:	40%	7.5 YR 4/6				Silty clay, richer in clay than previous GL.					
Coarse:	60%	Limestone		y		fg	tria		0.2, 0.3		10%
		Limestone		y		mg	tria		0.3		90%

Location:	HS	**Core:**	24	**Liner:**	3	**Depth:**	3.11	**GL:**	99	**Contact:**	sharp
Fragmented limestone cobble/pebble											

Location:	HS	**Core:**	24	**Liner:**	3	**Depth:**	3.66	**GL:**	100	**Contact:**	nd
Fine:	98%	In-between 10 YR 4/4 and 2.5 Y 6/4				Silty. In the lowermost 30 cm GL 100 exhibits clay aggregates.					
Coarse:	2%	Limestone		y, w		mg	prol, tria		0.3, 0.4		90%
		Bohnerz		b		mg	tria		0.6		10%

Location:	HS	**Core:**	24	**Liner:**	4	**Depth:**	4.05	**GL:**	101	**Contact:**	sharp
Fine:	98%	This layer exhibits laminations different in color and texture, clayey silt 7.5 YR 4/4; silt 2.5 Y 6/3 (main color of the layer); clayey silt 10 YR 6/6.									
Coarse:	2%	Limestone		y		fg	tria		0.2		40%
		Limestone		y		mg	obl		0.5		60%
		Limestone gravel marks the upper contact of this layer.									

Location:	HS	**Core:**	24	**Liner:**	4	**Depth:**	4.32	**GL:**	102	**Contact:**	clear
Fine:	100%	Similarly to previous layer also GL 102 is composed of laminations: silt 2.5 Y 6/4 (main sediment), silt 2. 2.5 Y 7/2; silt 10 YR 6/6; silt 10 YR 5/6									
Coarse:	0%	/		/		/	/		/		/

Location:	HS	**Core:**	24	**Liner:**	4	**Depth:**	4.35	**GL:**	103	**Contact:**	clear
Fine:	100%	10 YR 5/6				Clayey silt					
Coarse:	0%	/		/		/	/		/		/

Location:	HS	**Core:**	24	**Liner:**	4	**Depth:**	4.58	**GL:**	104	**Contact:**	clear

	Fine:	100%	GL 103 is composed of 10 YR 7/2 clayey silt intercalating with 10 YR 5/6 laminations rich in large impregnations of iron-manganese oxides.									
	Coarse:	0%	/		/		/		/		/	/

Location:	HS	**Core:**	24	**Liner:**	4	**Depth:**	4.60	**GL:**	105	**Contact:**	sharp	
	Fine:	40%	10 YR 5/6			Clayey silty.						
	Coarse:	0%	/		/		/		/		/	/

Location:	HS	**Core:**	24	**Liner:**	4	**Depth:**	4.76	**GL:**	105	**Contact:**	sharp	
	Fine:	40%	10 YR 5/6			Clayey silty. Much richer than the previous in large impregnations of iron-manganese oxides.						
	Coarse:	0%	/		/		/		/		/	/

Location:	HS	**Core:**	24	**Liner:**	4	**Depth:**	4.88	**GL:**	106	**Contact:**	nd	
Coarse gravel sized limestone fragment at the bottom of core 24.												

Location:	HS	**Core:**	27	**Liner:**	1	**Depth:**	0.71	**GL:**	8	**Contact:**	grad.	
	Fine:	5%	10 YR 4/2; 10 YR 4/3 in the contact area			Silty clay.						
	Coarse:	95%	Limestone		y		fg		tria		0.5, 0.6	100%

Location:	HS	**Core:**	27	**Liner:**	1, 2	**Depth:**	1.64	**GL:**	9	**Contact:**	grad.	
	Fine:	5%	10 YR 6/6		Silty sand							
	Coarse:	95%	Limestone		y		fg		tria, prol, obl		0.5, 0.6. rare 0.2	70%
			Pottery		y, w, gr		fg		tria		0.4	few fr.
			Limestone		y		mg, cg		tria, obl		0.3. rare 0.6	30%

Location:	HS	**Core:**	27	**Liner:**	2	**Depth:**	1.95	**GL:**	10	**Contact:**	grad.	
	Fine:	10%	10 YR 6/6		Calcite and rare Bohnerz sand, rare silt.							
	Coarse:	90%	Limestone		y		fg		tria		0.7	5%
			Limestone		y, gr, b		mg		prol, obl, tria		0.8; rare 0.3	70%
			Limestone		gr		mg		equ		0.5	2%
			Limestone with gypsum (?) crystals		w, y		mg		obl, tria		0.2, 0.3	23%
The medium gravel is well sorted, generally smaller than 1 cm.												

Location:	HS	**Core:**	27	**Liner:**	2	**Depth:**	2.24	**GL:**	11	**Contact:**	clear	
	Fine:	20%	10 YR 8/2; 10YR 6/6; 10YR 5/6; 10 YR 8/8		Sand with zoning and laminations displaying different colors.							
	Coarse:	80%	Limestone		y		fg		prol, obl, tria		0.6, 0.7	30%
			Limestone		w, gr		mg		tria		0.3 to 0.5	70%

			Bohnerz	b	mg	tria	0.3, 0.4	few fr.		

Location:	HS	**Core:**	27	**Liner:**	2, 3	**Depth:**	3.13	**GL:**	12	**Contact:** clear
	Fine:	10%	10 YR 5/6	Fine to coarse sand of calcite, and Bohnerz, with rare silt.						
	Coarse:	90%	Limestone	y	fg	tria	0.4	5%		
			Quartz	p	fg	tria	0.3	few fr.		
			Bohnerz	b	fg	obl	0.9	3%		
			Limestone	w, gr	mg	tria	0.3	75%		
			Limestone	br	mg	tria	0.4, 0.5	1%		
			Limestone	b	mg	tria	0.7, 0.8	0.75%		
			Chert	nd	mg	tria	0.2	0.25%		
			Limestone	w	cg	tria	0.4	15%		

Location:	HS	**Core:**	27	**Liner:**	3	**Depth:**	3.27	**GL:**	13	**Contact:** sharp
	Fine:	90%	10 YR 5/6	Clayey silt. This main matrix appears to alternate with laminations rich in medium sand and 10 YR 4/3 in color.						
	Coarse:	10%	Limestone	y, gr	fg	tria	0.4, 0.5	5%		
			Bohnerz	b	fg	tria, obl	0.6	5%		
			Limestone	y. gr	mg	tria, obl	0.5 to 0.7	80%		
			Bohnerz	b	mg	tria	0.5	10%		

Location:	HS	**Core:**	27	**Liner:**	3, 4	**Depth:**	4.41	**GL:**	14	**Contact:** clear
	Fine	20%	10 YR 4/4	Sandy silt.						
	Coarse	80%	Limestone	y	fg	tria	0.3, 0.6	5%		
			Bohnerz	b	fg	tria	0.5	2 fr.		
			Limestone	w	mg	tria	0.2 to 0.6	45%		
			Limestone	w	cg	tria	0.4	50%		

Location:	HS	**Core:**	27	**Liner:**	4	**Depth:**	4.56	**GL:**	15	**Contact:** clear
	Fine:	40%	10 YR 6/4	Silty sand (coarse and medium) of Bohnerz and calcite.						
	Coarse:	80%	Limestone	y	fg	tria	0.3, 0.5	22%		
			Cemented aggregate of sand	10 YR 6/4	fg	tria	0.3	3%.		
			Limestone	w	mg	tria	0.4 to 0.8	40%		
			Cemented aggregate of sand	10 YR 6/4	mg	tria	0.6	5%		

Location:	HS	**Core:**	27	**Liner:**	4, 5	**Depth:**	4.68	**GL:**	16	**Contact:** sharp
	Fine:	20%	10 YR 5/6	Silty sand (medium and coarse) of calcite and Bohnerz.						
	Coarse:	80%	Limestone	y	fg	tria	0.5, 0.6	20%		
			Limestone	w	mg	tria	0.6, 0.7	80%		

Location:	HS	**Core:**	27	**Liner:**	5	**Depth:**	4.79	**GL:**	17	**Contact:** sharp
	Fine:	30%	7.5 YR 3/2	Silty sand (coarse and medium) of calcite, Bohnerz and quartz.						

Coarse:	70%	Limestone	y	fg	tria	0.2 to 0.4	19%
		Limestone	y, r	mg	obl, prol	0.5	80%
		Iron-manganese nodules	r	mg	tria	0.6	1%

Location:	HS	**Core:**	27	**Liner:**	5	**Depth:**	4.88	**GL:**	17	**Contact:**	nd
Fine:	30%	10 YR 4/6	Silty sand (coarse and medium) of calcite, Bohnerz and quartz.								
Coarse:	70%	Limestone	y	fg	tria	0.2 to 0.4	19%				
		Quartz	w	fg	tria	0.2, 0.3	1 fr				
		Limestone	y, r	mg	obl, prol	0.5	80%				
		Iron-manganese nodules	r	mg	tria	0.6	1%				
		Quartz	w	mg	tria	0.2, 0.3	1 fr				

Location:	HS	**Core:**	30	**Liner:**	1	**Depth:**	0.50	**GL:**	69	**Contact:**	diff.
Fine:	100%	10 YR 3/3	Silty clay								
Coarse:	0%	/	/	/	/	/	/				

Location:	HS	**Core:**	30	**Liner:**	1	**Depth:**	1.03	**GL:**	70	**Contact:**	grad.
Fine	80%	10 YR 5/6	Clayey silt with coarse sand of calcite. Roots from modern plants, mottled 7.5 YR 4/6								
Coarse	20%	Limestone	y	fg	tria	0.1	30%				
		Limestone	y	mg	tria, obl	0.1	70%				

Location:	HS	**Core:**	30	**Liner:**	1, 2	**Depth:**	2.10	**GL:**	71	**Contact:**	grad.
Fine:	80%	7.5 YR 5/4	Clayey sand – sandy clay. Coarse sand of calcite.								
Coarse:	20%	Limestone	y	fg	tria	0.3, 0.4	20%				
		Limestone	y	mg	tria	0.2, 0.3	80%				

Location:	HS	**Core:**	30	**Liner:**	2	**Depth:**	2.28	**GL:**	72	**Contact:**	diff.
Fine:	80%	5 YR 4/4; starting at - 2.20 m 7.5 Y 4/6	Silty clay.								
Coarse:	20%	Limestone	y	fg	tria	0.2, 0.3	30%				
		Limestone	y	mg	tria	0.1. rare 0.3	70%				

Location:	HS	**Core:**	30	**Liner:**	2, 3	**Depth:**	2.91	**GL:**	73	**Contact:**	grad.
Fine:	80%	10 YR 5/6	Silty clay with medium and coarse sand of calcite and Bohnerz.								
Coarse:	20%	Limestone	y	fg	tria	0.1, 0.2	5%				
		Limestone	y, w	mg	tria	0.2	15%				
		Limestone	y	cg	tria	0.2	80%				

Location:	HS	**Core:**	30	**Liner:**	3	**Depth:**	3.26	**GL:**	74	**Contact:**	clear
Fine:	80%	10 YR 5/6	Clayey silt with coarse sand of calcite.								
Coarse:	20%	Limestone	y	fg	tria	0.1 to 0.3	30%				

			Limestone		y	mg	tria	0.2,0.3	70%	

Particularly in the lower 40 cm of this layer, the gravel is smaller than 2 cm.

Location:	HS	**Core:**	30	**Liner:**	3	**Depth:**	3.31	**GL:**	75	**Contact:** sharp
	Fine:	85%	10 YR 5/6		Silt with coarse and medium sand of calcite.					
	Coarse:	15%	Limestone		y	fg	tria	0.2	70%	
			Limestone		y	mg	tria	0.1,0.2	30%	

Location:	HS	**Core:**	30	**Liner:**	3	**Depth:**	3.46	**GL:**	76	**Contact:** sharp
	Fine:	5%	7.5 YR 4/6		Sandy silty clay.					
	Coarse:	95%	Limestone		y	fg	tria	0.3, 0.4	40%	
			Limestone		y	mg	tria	0.2, 0.3	2%	
			Bohnerz		b	mg	tria	0.4	58%	

Location:	HS	**Core:**	30	**Liner:**	4	**Depth:**	3.75	**GL:**	77	**Contact:** grad
	Fine:	70%	10 YR /46		Silt with rare coarse calcite sand.					
	Coarse:	30%	Limestone		y	fg	tria	0.2, 0.3	20%	
			Limestone		y	mg	tria	0.1, 0.2	80%	

Location:	HS	**Core:**	30	**Liner:**	4	**Depth:**	4.43	**GL:**	78	**Contact:** sharp
	Fine:	80%	10 YR 4/6		Silty clay.					
	Coarse:	20%	Limestone		y	fg	tria	0.2	20%	
			Limestone		y	mg	tria	0.2, 0.3	80%	

Location:	HS	**Core:**	30	**Liner:**	4	**Depth:**	4.53	**GL:**	79	**Contact:** sharp
	Fine:	10%	10 YR 5/4		Silty clay.					
	Coarse:	90%	Limestone		y	fg	tria	0.3	60%	
			Limestone		y	mg	tria	0.2, rare 0.4	40%	

Location:	HS	**Core:**	30	**Liner:**	4	**Depth:**	4.57	**GL:**	80	**Contact:** sharp
	Fine:	10%	nd		Silty clay.					
	Coarse:	90%	Limestone		y	fg	tria	0.2, 0.3	70%	
			Limestone		y	mg	tria	0.3	30%	

Location:	HS	**Core:**	30	**Liner:**	4	**Depth:**	4.88	**GL:**	81	**Contact:** nd
	Fine:	5%	10 YR 5/4		Medium to coarse sand of calcite and Bohnerz, rare silt.					
	Coarse:	95%	Limestone		y, w, b	fg	tria	0.2, 0.3. Rare 0.5 to 0.7	60%	
			Limestone		y, w, b	mg	tria, obl	0.2, 0.3. Rare 0.5, 0.6	40%	

Location:	HS	**Core:**	30	**Liner:**	5	**Depth:**	5.37	**GL:**	82	**Contact:** clear
	Fine:	5%	10 YR 4/4		Sandy silt. Sand of calcite and Bohnerz.					
	Coarse:	95%	Limestone		y	fg	tria	0.2, 0.3	20%	
			Limestone		y	mg	tria	0.4	80%	

Location:	HS	**Core:**	30	**Liner:**	5	**Depth:**	5.68	**GL:**	83	**Contact:**	grad.
	Fine:	80%	2.5 Y 6/4	Clayey silt. Laminations 5 YR 5/6 in color (iron staining?), with rare medium and coarse sand of calcite.							
	Coarse:	20%	Limestone		y	fg	tria		0.3, 0.4		30%
			Limestone		y	mg	tria		0.2 to 0.5		70%
			Down to - 5.47 m, this layer is nearly free of gravel (GL 83a). Deeper than – 5.47 m it is more gravelly.								

Location:	HS	**Core:**	30	**Liner:**	5	**Depth:**	5.75	**GL:**	84	**Contact:**	grad.
	Fine:	10%	10 YR 3/6	Silty sand composed of calcite and quartz.							
	Coarse:	90%	Limestone		y	fg	tria		0.4, 0.5		20%
			Limestone		y	mg	tria		0.3 to 0.5		80%
			Bohnerz		b	mg	tria		0.3, 0.4		few fr.

Location:	HS	**Core:**	30	**Liner:**	5	**Depth:**	5.83	**GL:**	85	**Contact:**	sharp
	Fine:	10%	10 YR 3/3	Silty sand of quartz and Bohnerz.							
	Coarse:	90%	Limestone		y	fg	tria		0.4, 0.5		20%
			Limestone		y	mg	tria		0.3 to 0.5		80%
			Bohnerz		b	mg	tria		0.3, 0.4		few fr.

Location:	HS	**Core:**	30	**Liner:**	5	**Depth:**	5.87	**GL:**	86	**Contact:**	sharp
	Fine:	0%	/	/							
	Coarse:	100%	Limestone		y	cg, pb	nd		nd		100%

Location:	HS	**Core:**	30	**Liner:**	5	**Depth:**	5.97	**GL:**	87	**Contact:**	sharp
	Fine:	5%	10 YR 5/6	Silty sand of quartz and Bohnerz.							
	Coarse:	95%	Limestone		y	fg	tria		0.2, 0.3		10%
			Bohnerz		b	fg	tria		0.3, 0.4		few fr.
			Limestone		y	mg	tria		0.2, 0.3		90%

Location:	HS	**Core:**	30	**Liner:**	5	**Depth:**	6.02	**GL:**	88	**Contact:**	sharp
	Fine:	5%	10 YR 2/2	Silty sand of quartz, Bohnerz and calcite.							
	Coarse:	95%	Limestone		y	fg	tria		0.3		10%
			Limestone		y	mg	tria		0.3, 0.4		90%

Location:	HS	**Core:**	30	**Liner:**	5	**Depth:**	5.87	**GL:**	89	**Contact:**	sharp
	Fine:	2%	7.5 YR 4/4	Silt.							
	Coarse:	98%	Limestone		y	cg, pb	nd		nd		100%

Location:	BS	**Core:**	31	**Liner:**	1	**Depth:**	0.58	**GL:**	257	**Contact:**	clear
	Fine:	25%	nd						nd		
	Coarse:	95%	Limestone		y, w	fg, mg		tria		0.1 to 0.3	100%
			We did not differentiate the upper 5 cm of this layer, which corresponds to a weakly developed A horizon.								

Location:	BS	**Core:**	31	**Liner:**	1	**Depth:**	0.68	**GL:**	258	**Contact:**	sharp
	Fine:	0%	/						/		

	Coarse:	100%	Limestone		w	mg, cg	tria	0.1 to 0.3	100%

Location:	BS	**Core:**	31	**Liner:**	1	**Depth:**	1.22	**GL:**	259	**Contact:** clear
	Fine:	5%	10 YR 7/4		Silt and fine to coarse sand of limestone					
	Coarse:	95%	Limestone		y, w	fg, mg	tria	0.1 to 0.3	100%	

Location:	BS	**Core:**	31	**Liner:**	2	**Depth:**	2.00	**GL:**	260	**Contact:** clear
	Fine:	60%	10 YR 5/4		Silt. Roots from modern vegetation. Possibly secondary calcite pedofeatures or shell fragments (max 2-3 mm in size).					
	Coarse:	40%	Limestone		y, w	fg	tria	0.2	20%	
			Limestone		y, w	mg	tria, obl	0.2	80%	

Location:	BS	**Core:**	31	**Liner:**	2, 3	**Depth:**	3.24	**GL:**	261	**Contact:** diff
	Fine:	95%	10 YR 4/3		Silt. Shell fragmnets.					
	Coarse:	5%	Limestone		y	fg	tria	0.3	10%	
			Limestone		y	mg	tria, obl	0.2, 0.3	90%	
Location:	BS	**Core:**	31	**Liner:**	3, 4	**Depth:**	4.41	**GL:**	262	**Contact:** grad.
	Fine:	95%	10 YR 5/6		Silt. Shell fragmnets.					
	Coarse:	5%	Limestone		y	fg	tria	0.3	10%	
			Limestone		y	mg	tria, obl	0.2, 0.3	90%	

Location:	BS	**Core:**	31	**Liner:**	4	**Depth:**	5.00	**GL:**	263	**Contact:** diff.
	The layer is composed of alternating laminations, GL 263a (down to - 4.86 m), GL 263b (down to - 4.93 m) and again GL 263a (down to – 5.00 m).									
GL 263a	**Fine:**	5%	10 YR 5/4		Medium to coarse sand of calcite and Bohnerz					
	Coarse:	95%	Limestone		y	fg	tria, equ, obl	0.5 to 0.6	10%	
			Limestone		y	mg	tria, obl	0.5 to 0.6	90%	
GL 263a	**Fine:**	95%	10 YR 5/4		Silty sand of calcite and Bohnerz.					
	Coarse:	5%	Limestone		y	fg	obl	0.6, 0.7	100%	

Location:	BS	**Core:**	31	**Liner:**	4	**Depth:**	5.17	**GL:**	264	**Contact:** clear
	Fine:	2%	nd		Silty sand of limestone and Bohnerz. The matrix was too dry, we did not assign a color.					
	Coarse:	98%	Bohnerz		b	fg	obl.	0.4	few fr.	
			Limestone		y	mg	tria	0.3, 0.4	90%	
			Limestone		y	cg	tria	0.3, 0.4	10%	

Location:	BS	**Core:**	31	**Liner:**	5	**Depth:**	5.30	**GL:**	265	**Contact:** clear
	Fine:	5%	10 YR 4/2		Sandy silt - silty sand, containing calcite, quartz, Bohnerz and other iron nodules.					
	Coarse:	95%	Limestone		y	mg	tria, obl	0.4	100%	

Location:	BS	**Core:**	31	**Liner:**	5	**Depth:**	5.52	**GL:**	266	**Contact:** grad.
	Fine:	15%	10 YR 3/2		Sandy silt, similar composition to GL 265.					
	Coarse:	85%	Limestone		y	mg	tria	0.3	8%	

Limestone	b	mg	tria	0.3	90%
Chert	bl	cg	equ	0.3, 0.4	2%

The latter corresponds to a fragment of chert that was broken during the core drilling

Location:	BS	**Core:**	31	**Liner:**	5	**Depth:**	5.75	**GL:**	267	**Contact:**	grad.
	Fine:	15%	10 YR 5/4	Silt with little sand of calcite, quartz, bohnerz and possibly chert.							
	Coarse:	85%	Bohnerz	b	mg	equ	0.6	2%			
			Limestone	b	mg	tria, obl	0.4, 0.3	98%			

Location:	BS	**Core:**	31	**Liner:**	5	**Depth:**	6.10	**GL:**	268	**Contact:**	clear
Similarly to GL 263, GL 268 is composed of alternating beds, GL 268a and GL 268b.											
GL 268a	**Fine:**	5%	10 YR 5/6	Silty clay, also rich in sand							
	Coarse:	95%	Bohnerz	b	mg	equ	0.4, 0.5	5%			
			Limestone	y, b	mg	tria, obl	0.4, 0.5	95%			
GL 268a	**Fine:**	20%	10 YR 5/6	Silty clay, also rich in sand							
	Coarse:	80%	Limestone	y	fg	equ	0.4, 0.5	10%			
			Limestone	y	mg	tria, obl	0.4, 0.5	90%			

Location:	BS	**Core:**	31	**Liner:**	5, 6	**Depth:**	6.30	**GL:**	269	**Contact:**	nd
	Fine:	2%	10 YR 4/6	Silty clay.							
	Coarse:	98%	Limestone	y	fg	equ	0.5 to 0.7	10%			
			Limestone	y, b	mg	tria, obl	0.5 to 0.7	90%			
			Bohnerz	b	mg	equ	0.5 to 0.7	5%			

Location:	BS	**Core:**	32	**Liner:**	1	**Depth:**	0.87	**GL:**	249	**Contact:**	grad.
	Fine:	100%	Upper 13 cm 10 YR 4/3; lower part 10 YR 5/4	Silty clay							
	Coarse:	0%	/	/	/	/	/	/			

Location:	BS	**Core:**	32	**Liner:**	1	**Depth:**	1.22	**GL:**	250	**Contact:**	nd
	Fine:	75%	10 YR 5/6	Silt with rare medium and coarse sand of calcite and Bohnerz.							
	Coarse:	25%	Limestone	y	fg	tria	0.3	73%			
			Bohnerz	b	fg	tria	0.6	2%			
			Limestone	y	mg	tria	0.2	15%			

Location:	BS	**Core:**	32	**Liner:**	2	**Depth:**	1.90	**GL:**	251	**Contact:**	nd
GL 251 is composed of alternating beds, GL 251a and GL 251b. Beds are from 5 to 10 cm thick and the passage from one bed to the lower one is clear											
GL 251a	**Fine:**	95%	10 YR 5/6	Silt with little medium and coarse calcite sand.							
	Coarse:	5%	Limestone	y	fg	tria	0.3, 0.4	100%			
GL 251a	**Fine:**	5%	10 YR 5/6	Silt with little medium and coarse calcite sand.							
	Coarse:	95%	Limestone	y, b	fg	tria	0.3, 0.4	85%			
			Bohnerz	b	fg	tria	0.9	5%			
			Limestone	y, b	mg	tria	0.3, 0.4	15%			

Location:	BS	**Core:**	32	**Liner:**	2	**Depth:**	2.32	**GL:**	252	**Contact:**	clear

Very similar to previous layer. In GL 252 the passage from alternating beds is sharper and gravel-rich beds contain darker silty sand laminations which are 10 YR 3/2 and 4/2 in color.

Location:	BS	**Core:**	32	**Liner:**	3	**Depth:**	2.81	**GL:**	253	**Contact:** grad.
	Fine:	95%	10 YR 5/6		Silty clay					
	Coarse:	5%	Limestone		y	fg	tria	0.2	100%	

Location:	BS	**Core:**	32	**Liner:**	3	**Depth:**	3.11	**GL:**	254	**Contact:** sharp
	Fine:	10%	10 YR 5/6		Silty sand with aggregates of silty sand 10 YR 3/2 and 4/2 in color.					
	Coarse:	90%	Limestone		y, b	fg	tria	0.3	35%	
			Bohnerz		b	mg	tria	0.2, 0.3	5%	
			Limestone		y, b	mg	tria	0.8	60%	

Location:	BS	**Core:**	32	**Liner:**	3, 4	**Depth:**	3.80	**GL:**	255	**Contact:** grad.
	Fine:	98%	10 YR 5/6		Clayey silt.					
	Coarse:	2%	Limestone		y, b	mg	tria	0.3	100%	

Location:	BS	**Core:**	32	**Liner:**	4	**Depth:**	4.20	**GL:**	256	**Contact:** nd
	Fine:	5%	10 YR 5/6		Silty sand.					
	Coarse:	95%	Limestone		y, b	fg	prol, equ	0.8	25%	
			Limestone		y, b	mg	tria, obl	0.4 to 0.8	75%	

Location:	BS	**Core:**	33	**Liner:**	1	**Depth:**	0.17	**GL:**	243	**Contact:** grad.
	Fine:	85%	10 YR 3/3		Silty clay					
	Coarse:	15%	Limestone		y	fg	tria	0.2, 0.3	40%	
			Limestone		y	mg	tria	0.2 to 0.4	60%	
			Iron nodules		b	mg	tria	0.4, 0.3	1 fr.	

Location:	BS	**Core:**	33	**Liner:**	1	**Depth:**	0.67	**GL:**	244	**Contact:** grad.
	Fine:	70%	10 YR 5/8		Silty clay with rare coarse sand of limestone. The matrix is also carchterized by a dark stripe 10 YR 3/2. Ants and roots: mixing.					
	Coarse:	30%	Limestone		y	fg	tria	0.4	15%	
			Limestone		y	mg	tria	0.3, 0.4	85%	

Location:	BS	**Core:**	33	**Liner:**	1	**Depth:**	0.95	**GL:**	245	**Contact:** clear
	Fine:	15%	10 YR 5/6		Silty clay with rare coarse sand of limestone.					
	Coarse:	85%	Limestone		y	fg	tria	0.4	15%	
			Limestone		y	mg	tria	0.3, 0.4	85%	

Location:	BS	**Core:**	33	**Liner:**	1	**Depth:**	1.02	**GL:**	246	**Contact:** clear
	Fine:	10%	10 YR 5/6		Silty clay with rare coarse sand of limestone.					
	Coarse:	90%	Limestone		y	fg	tria	0.4, 0.3	15%	
			Limestone		y	mg	tria	0.2, 0.3	85%	

Location:	BS	**Core:**	33	**Liner:**	1	**Depth:**	1.22	**GL:**	247	**Contact:** diff.

Similar to previous sediment but richer in gravel of limestone (up to coarse-gravel sized). Together with fresh limestone fragments we identified also very weathered limestone gravel.

Location:	BS	**Core:**	33	**Liner:**	1	**Depth:**	1.25	**GL:**	248	**Contact:** clear
	Fine:	10%	10 YR 5/6	Silty clay with rare coarse sand of limestone.						
	Coarse:	90%	Limestone	y	fg	tria	0.4, 0.3	15%		
			Limestone	y	mg	tria	0.2, 0.3	85%		

Location:	BS	**Core:**	33	**Liner:**	2	**Depth:**	1.30	**GL:**	249	**Contact:** nd
	Fine:	60%	10 YR 5/6	Silty clay with rare coarse sand of limestone.						
	Coarse:	40%	Limestone	y	fg	tria	0.3	2%		
			Limestone	y	mg	tria	0.3	15%		
			Limestone	y	mg	tria	0.3, 0.4	83%		

Location:	HF	**Core:**	37	**Liner:**	1	**Depth:**	0.32	**GL:**	200	**Contact:** clear
	Fine:	60%	10 YR 2/1	Silt rich in organic matter (A horizon of modern soil).						
	Coarse:	40%	Limestone	w	fg	tria	0.3	10%		
			Limestone	w	mg	tria	0.3	90%		

Location:	HF	**Core:**	37	**Liner:**	1	**Depth:**	1.02	**GL:**	201	**Contact:** sharp
	GL 201 is composed of 60% of fine fraction and 40% of gravel. In this layer we distinguished two different type of alternating laminations, GL 201a and GL 201b. These laminations differ for matrix color and composition.									
GL 201a	**Fine:**	/	10 YR 5/3	Coarse to fine calcite sand and rare silt.						
	Coarse:	/	Limestone	w	fg	tria, obl, prol	0.5	15%		
			Bohnerz	b	fg	tria, equ, obl	0.6	5%		
			Limestone	w	mg	tria, obl	0.4, 0.3	60%		
			Limestone	w	cg	tria	0.3	20%		
GL 201b	**Fine:**	/	10 YR 6/6	Coarse to fine sand of calcite, quartz and Bohnerz, and rare silt.						
	Coarse:	/	Limestone	w	fg	tria, obl, prol	0.5	15%		
			Bohnerz	b	fg	tria, equ, obl	0.6	5%		
			Limestone	w	mg	tria, obl	0.5	80%		

Location:	HF	**Core:**	37	**Liner:**	1, 2	**Depth:**	1.61	**GL:**	202	**Contact:** grad
	Fine:	70%	10 YR 2/1	Sandy silt, contain organic matter, sand-sized grains of pottery, charcoal and quartz.						
	Coarse:	30%	Limestone	w	fg	tria	0.4	9%		
			Pottery	r	mg	tria	0.3	few fr.		
			Limestone	w	mg	tria, obl	0.3	90%		
			Charcoal	b	fg	nd	nd	1%		
	Pottery and (some) limestone gravel are very weathered. the gravel is well sorted and smaller than 1 cm.									

Location:	HF	**Core:**	37	**Liner:**	2	**Depth:**	1.73	**GL:**	203	**Contact:** clear

	Fine:	98%	Very dark, no comparison with Munsell. Also mottles Glay 1 5/n.			Clayey silt very rare coarse sand of clacite.			
	Coarse:	2%	Limestone	w	fg	tria	0.4	100%	

Location:	HF	**Core:**	37	**Liner:**	2	**Depth:**	1.98	**GL:**	204	**Contact:**	grad
	GL 204 is composed of alternating laminations which differ for the iron-manganese staining of the matrix.										
GL 204a	**Fine:**	100%	5 Y 6/2	Silty sand. Coarse to fine calcite sand.							
	Coarse:	0%	/	/	/	/	/	/			
GL 204b	**Fine:**	100%	10 YR 5/6	Silty and fine sand.							
	Coarse:	0%	/	/	/	/	/	/			

Location:	HF	**Core:**	37	**Liner:**	2	**Depth:**	2.28	**GL:**	205	**Contact:**	grad
	GL 205 is composed of alternating gravel rich (GL 205a) and matrix rich (GL 205b) beds.										
GL 205a	**Fine:**	30%	5 Y 6/2	Silty sand, composed of fine to coarse calcite.							
	Coarse:	70%	Limestone	w	fg	tria, obl	0.3	40%			
			Limestone	w	mg	tria, obl	0.1, 0.2	60%			
GL 205b	**Fine:**	80%	10 YR 5/6 alternating in laminations with 7.5 YR 4/6.	Silt with little calcite sand.							
	Coarse:	20%	Limestone	w	fg	tria, obl	0.3	100%			

Location:	HF	**Core:**	37	**Liner:**	2, 3	**Depth:**	2.66	**GL:**	206	**Contact:**	grad
	GL 206 is very similar to GL 204.										
GL 206a	**Fine:**	100%	5 Y 6/2	Silty sand. Coarse to fine calcite sand.							
	Coarse:	0%	/	/	/	/	/	/			
GL 204b	**Fine:**	100%	10 YR 5/6	Silty and fine sand.							
	Coarse:	0%	/	/	/	/	/	/			

Location:	HF	**Core:**	37	**Liner:**	3	**Depth:**	2.77	**GL:**	207	**Contact:**	grad
	This layer is composed of alternating laminations of silty sand (2.5 Y 5/2; 5/3; 5/4 in color) and clay (10 YR 5/3). Silty sand layers are richer in medium sand of calcite. GL 207 is free of gravel.										

Location:	HF	**Core:**	37	**Liner:**	3	**Depth:**	3.33	**GL:**	208	**Contact:**	clear
	GL 208 is composed of alternating beds, which differ for their matrix. Both bed types display similar gravel.										
GL 208a	**Fine:**	95%	2. 5 Y 6 /3 and 5/2	Silty sand of quartz and calcite.							
	Coarse:	5%	See for GL 208b.								
GL 208b	**Fine:**	95%	10 YR 5/8	Sand of calcite.							
	Coarse:	5%	Limestone	y	fg	tria, obl	0.2	60%			
			Limestone	y	mg	tria	0.3	40%			

Location:	HF	**Core:**	37	**Liner:**	3	**Depth:**	3.66	**GL:**	209	**Contact:**	nd
	Fine:	90%	2.5 Y 6/2	Sandy silt, no more laminations. Sand of calcite.							
	Coarse:	10%	Limestone	y	mg	tria, obl	0.3	100%			

Location:	HF	**Core:**	37	**Liner:**	4	**Depth:**	4.51	**GL:**	210	**Contact:**	clear
	GL 210 is composed of alternating beds, which differ for their matrix. Both bed types display similar gravel.										

GL 210a	**Fine:**	80%	2. 5 Y 6 /2	Silt.						
	Coarse:	20%	See for GL 210b.							
GL 210b	**Fine:**	80%	10 YR 4/6	Sandy silt.						
	Coarse:	20%	Limestone	y	fg	obl	0.1	10%		
			Limestone	y	mg	tria, obl	0.1, 0.2	90%		

Location:	HF	**Core:**	37	**Liner:**	4	**Depth:**	4.88	**GL:**	211	**Contact:** clear
GL 211 is composed of alternating matrix rich (GL 211a) and gravel rich (GL 211b) beds.										
GL 211a	**Fine:**	30%	2.5 Y 6/4	Sand with graded laminations, some aggregates and lenses of sand are 5 YR 4/6 in color.						
	Coarse:	70%	Limestone	y	fg	obl	0.3, 0.2	40%		
			Limestone	y	mg	tria, obl	0.1, 0.2	60%		
GL 211b	**Fine:**	15%	2.5 Y 6/4	Sandy, but richer in coarser sand than GL 211a						
	Coarse:	85%	Limestone	y	fg	obl	0.3, 0.2	60%		
			Limestone	y	mg	tria, obl	0.3	40%		

Location:	HF	**Core:**	37	**Liner:**	5	**Depth:**	5.53	**GL:**	212	**Contact:** clear
	Fine:	60%	5 Y 5/1	Sandy silt, fine to medium sand of calcite and quartz.						
	Coarse:	40%	Limestone	y	fg	tria, obl	0.1	30%		
			Limestone	y	mg	tria, obl	0.2	70%		

Location:	HF	**Core:**	37	**Liner:**	5	**Depth:**	5.68	**GL:**	213	**Contact:** clear
	Fine:	90%	5 Y 4/1	Silt with rare fine sand.						
	Coarse:	10%	Limestone	y	fg	tria, obl	0.2	60%		
			Limestone	y	mg	tria, obl	0.2	40%		

Location:	HF	**Core:**	37	**Liner:**	5	**Depth:**	5.76	**GL:**	214	**Contact:** clear
	Fine:	70%	5 Y 4/1	Silt with rare fine sand.						
	Coarse:	30%	Limestone	y	fg	tria, obl	0.2	30%		
			Limestone	y	mg	tria, obl	0.2	70%		

Location:	HF	**Core:**	37	**Liner:**	5	**Depth:**	5.89	**GL:**	215	**Contact:** clear
	Fine:	100%	5 Y 5/1	Silt, some lenses are 2.5 Y 5/1 but no difference in grain size.						
	Coarse:	0%	/	/	/	/	/	/		

Location:	HF	**Core:**	37	**Liner:**	5, 6	**Depth:**	6.34	**GL:**	216	**Contact:** sharp
	Fine:	60%	2.5 Y 6/2	Silty sand, medium and coarse calcite sand.						
	Coarse:	40%	Limestone	y	fg	tria, obl	0.2, 0.3	10%		
			Limestone	y	mg	tria, obl	0.2, 0.3	90%		

Location:	HF	**Core:**	37	**Liner:**	6	**Depth:**	6.59	**GL:**	217	**Contact:** grad
	Fine:	90%	5 Y 5/2	Silt with very rare fine sand.						
	Coarse:	10%	Limestone	y	fg	tria, obl	0.1, 0.2	10%		
			Limestone	y	mg	tria, obl	0.2, 0.3	90%		

Location:	HF	**Core:**	37	**Liner:**	6	**Depth:**	7.32	**GL:**	218	**Contact:** grad
	Fine:	70%	5 Y 5/2	Silt, richer in medium and coarse sand of calcite than GL 217.						

Coarse:	30%	Limestone	y	fg	tria, obl	0.2	20%
		Limestone	y	mg	tria, obl	0.1, 0.3	80%

Location:	HF	**Core:**	37	**Liner:**	7	**Depth:**	7.37	**GL:**	219	**Contact:**	sharp
	Fine:	70%	5 Y 5/2	Silt with calcite coarse sand.							
	Coarse:	30%	Limestone		y	fg	tria		0.2		20%
			Limestone		y	mg	tria, obl		0.3		80%

Location:	HF	**Core:**	37	**Liner:**	7	**Depth:**	8.39	**GL:**	220	**Contact:**	clear
	GL 220 is composed of beds rich in gravel (GL 220a), alternating with thin laminations (GL 220b), which display a different matrix color.										
GL 220a	**Fine:**	30%	5 Y 5/1	Silt with fine to coarse calcite.							
	Coarse:	70%	Limestone		y	fg	tri		0.3, rare 0.5		20%
			Limestone		y	mg	tria, obl		0.3, rare 0.5		70%
			Limestone		y	cg	tria		0.3		10%
GL 220b	**Fine:**	80%	2.5 Y 4/4	Sandy, but in comparison with GL 211 richer in coarser sand of calcite, quartz and Bohnerz.							
	Coarse:	20%	Limestone		y	fg	tri		0.3, rare 0.5		30%
			Limestone		y	mg	tria, obl		0.3, rare 0.5		70%
			From one of these laminations (at - 8.47 m) we recovered the bone fragmented we used for radiocarbon dating. The matrix of this lamination is darker, 2.5 Y 5/2								

Location:	HF	**Core:**	37	**Liner:**	7	**Depth:**	8.54	**GL:**	221	**Contact:**	grad
	Fine:	5%	5 Y 5/1	Silt.							
	Coarse:	90%	Limestone		y	fg	tria		0.3		15%
			Limestone		y	mg	tria, obl		0.2, 0.3		85%

Location:	HF	**Core:**	37	**Liner:**	8	**Depth:**	9.23	**GL:**	222	**Contact:**	sharp
	GL 222 is composed of beds richer in fine fraction (GL 222a), alternating with beds richer in gravel (GL 222b).										
GL 222a	**Fine:**	60%	5 Y 4/2	Silt with fine to medium sand of quartz and Bohnerz.							
	Coarse:	40%	Limestone		y	fg	tri		0.3.		5%
			Limestone		y	mg	tria		0.3, 0.4		95%
GL 222b	**Fine:**	5%	5 Y 5/1	Sandy silt. Fine to coarse calcite and Bohnerz sand.							
	Coarse:	95%	Limestone		y	fg	tri, obl		0.3		20%
			Limestone		y	mg	tria, obl		0.3		80%

Location:	HF	**Core:**	37	**Liner:**	8	**Depth:**	9.55	**GL:**	223	**Contact:**	clear
	GL 223 displays bed types comparable with those of GL 222. As main difference, the gravel rich beds of GL 223 (GL 223b) are richer in coarse calcite sand.										
GL 222a	**Fine:**	15%	5 Y 4/1	Silt with fine to medium sand of quartz and Bohnerz.							
	Coarse:	85%	Limestone		y	fg	tri		0.3.		10%
			Limestone		y	mg	tria		0.3, 0.4		90%
GL 222b	**Fine:**	5%	5 Y 5/2	Sandy silt. Fine to coarse calcite sand.							
	Coarse:	95%	Limestone		y	fg	tri, obl		0.2, 0.3		30%
			Limestone		y	mg	tria		0.3		70%

Location:	HF	**Core:**	37	**Liner:**	8	**Depth:**	9.73	**GL:**	224	**Contact:**	grad
	Fine:	40%	5 Y 4/2	Silt with medium and coarse sand of clacite.							
	Coarse:	60%	Limestone		y	fg		tria		0.2	60%
			Limestone		y	mg		tria		0.3, 0.4	40%
			Gravel is usually smaller than 1 cm.								

Location:	HF	**Core:**	37	**Liner:**	8	**Depth:**	9.76	**GL:**	225	**Contact:**	nd
	Fine:	5%	5 Y 4/1	Sandy silt. Medium and fine sand of calcite and quartz.							
	Coarse:	95%	Limestone		y	fg		tria		0.4	10%
			Limestone		y	mg		tria		0.4	90%

Location:	HF	**Core:**	38	**Liner:**	1	**Depth:**	0.67	**GL:**	232	**Contact:**	grad
	Fine:	5%	10 YR 3/1	Silt with medium and coarse calcite sand.							
	Coarse:	95%	Limestone		y	fg		tria		0.3	40%
			Limestone		y	mg		tria		0.3	60%

Location:	HF	**Core:**	38	**Liner:**	1	**Depth:**	0.89	**GL:**	233	**Contact:**	sharp
	Fine:	5%	10 YR 5/4	Silt with medium and coarse calcite sand.							
	Coarse:	95%	Limestone		y	fg		tria		0.3	30%
			Limestone		y	mg		tria		0.2, 0.1	70%

Location:	HF	**Core:**	38	**Liner:**	1	**Depth:**	1.00	**GL:**	234	**Contact:**	sharp
	Fine:	0%	/	/							
	Coarse:	100%	Limestone		y	fg, mg, cg		tria		0.3	100%

Location:	HF	**Core:**	38	**Liner:**	1	**Depth:**	1.22	**GL:**	235	**Contact:**	nd
	Fine:	5%	10 YR 6/4	Silty sand, fine to medium calcite sand.							
	Coarse:	95%	Limestone		y	fg		tria		0.3	20%
			Limestone		y	mg		tria		0.3, 0.2	80%

Location:	HF	**Core:**	38	**Liner:**	2	**Depth:**	2.00	**GL:**	236	**Contact:**	grad.
	Fine:	10%	10 YR 6/4	Silty sand, fine to medium calcite sand.							
	Coarse:	90%	Limestone		y	fg		tria		0.3	20%
			Limestone		y	mg		tria		0.3, 0.2	80%

Location:	HF	**Core:**	38	**Liner:**	2	**Depth:**	2.44	**GL:**	237	**Contact:**	nd
	Fine:	5%	10 YR 6/4	Silty sand, fine to medium calcite sand.							
	Coarse:	95%	Limestone		y	fg		tria, obl		0.3	10%
			Limestone		y	mg		tria		0.2	90%

Location:	HF	**Core:**	38	**Liner:**	3	**Depth:**	3.66	**GL:**	238	**Contact:**	nd
	Fine:	0%	/	/							
	Coarse:	100%	Limestone		y	fg		tria		0.3, 0.4	30%
			Limestone		y	mg		tria		0.3, 0.2	50%
			Limestone		y	cg		tria		0.3, 0.4	20%

Location:	HF	**Core:**	38	**Liner:**	4	**Depth:**	4.49	**GL:**	239	**Contact:**	clear

Fine:	5%	10 YR 6/3. In the upper part 5 Y 4/3	Silty sand, fine to medium calcite sand.						
Coarse:	95%	Limestone	y	fg	tria	0.4	80%		
		Limestone	y	mg	tria	0.3	20%		

Location:	HF	**Core:**	38	**Liner:**	4	**Depth:**	4.61	**GL:**	240	**Contact:**	nd
Fine:	0%	/	/								
Coarse:	95%	Limestone		y	fg	tria	0.3	10%			
		Limestone		y	mg	tria	0.3	90%			

Location:	HF	**Core:**	38	**Liner:**	4	**Depth:**	4.88	**GL:**	241	**Contact:**	nd
Fine:	5%	10 YR 7/6	Silty sand, fine to medium calcite sand.								
Coarse:	95%	Limestone		y	fg	tria	0.3	20%			
		Limestone		y	mg	tria	0.2	70%			
		Limestone		y	cg	tria	0.3	10%			

Location:	HF	**Core:**	38	**Liner:**	5	**Depth:**	6.10	**GL:**	242	**Contact:**	nd

In this liner we recovered fine and medium angular (0.2, 0.3) limestone gravel. During sediment recovery we hit an aquifer, the fine fraction escaped from the liner and part of the latter got broken. Therefore GL 242 cannot be regarded as representative. In the upper part of the liner we observed rare aggregates of silty sand that appear 2.5 Y 7/1 (completely dry) and 2.5 Y 5/2 (wet).

Location:	HF	**Core:**	39	**Liner:**	1	**Depth:**	0.60	**GL:**	226	**Contact:**	mixed
Fine:	30%	nd	Soil, not described								
Coarse:	70%	Limestone		w	fg	tria	0.3	15%			
		Limestone		w	mg	tria	0.2	85%			

Location:	HF	**Core:**	39	**Liner:**	1, 2	**Depth:**	2.44	**GL:**	227	**Contact:**	nd
Fine:	10%	10 YR 6/6. Lowermost 20 cm are 10 YR 6/4	Silt with rare medium and coarse calcite sand. Down to - 1.80 m root from modern vegetation.								
Coarse:	90%	Limestone		w	fg	tria	0.4	10%			
		Limestone		w	mg	tria	0.1 to 0.4	90%			

Location:	HF	**Core:**	39	**Liner:**	3	**Depth:**	3.19	**GL:**	228	**Contact:**	diff.
Fine:	20%	10 YR 7/1	Silt with medium and coarse calcite sand.								
Coarse:	80%	Limestone		w	fg	tria	0.4	10%			
		Limestone		w	mg	tria	0.1 to 0.4	90%			

Location:	HF	**Core:**	39	**Liner:**	3, 4	**Depth:**	4.41	**GL:**	229	**Contact:**	sharp
Fine:	20%	10 YR 5/3	Silt with medium and coarse calcite sand.								
Coarse:	80%	Limestone		w	fg	tria	0.3	10%			
		Limestone		w	mg	tria	0.1, 0.2	90%			

Location:	HF	**Core:**	39	**Liner:**	4	**Depth:**	4.51	**GL:**	230	**Contact:**	sharp
Fine:	0%	/	/								

Coarse:	100%	Limestone	w	cg, pb	nd	nd	100%	

Location:	HF	**Core:**	39	**Liner:**	4	**Depth:**	4.88	**GL:**	231	**Contact:**	nd
	Fine:	20%	10 YR 7/3	Silt with medium and coarse calcite and Bohnerz sand.							
	Coarse:	80%	Limestone	w	fg	tria, prol	0.2, 0.3	10%			
			Limestone	w	mg	tria	0.1, 0.2	90%			

References

Bosellini, A., Mutti, E., Ricci Lucchi, F., 1989. Rocce e successioni sedimentarie, Torino.

Chilingar, G.V., Bissel, H.J., Fairbridge, R.W., 1967. Carbonate rocks. Elservier, Amsterdam.

Fitzpatrick, E. A., 1983. Soils. Their Formation, Classification and Distribution. Hong Kong.

Stoops, G., 2003. Guidelines for Analysis and Description of Soil and Regolith Thin Sections. Soil Science Society of America, Inc. Madison.

Vos, C., Don, A., Prietz, R., Heidkamp, A., Freibauer, A., 2016. Field-based soil-texture estimates could replace laboratory analysis. Geoderma 267, 215-219.